Multiscale Modeling and Characterization of the Elastic Behavior of Anisotropic Thin Films

Elia Zgheib

Thèse
de doctorat
de l'UTT

Elia ZGHEIB

Multiscale Modeling and Characterization of the Elastic Behavior of Anisotropic Thin Films

Champ disciplinaire :
Sciences pour l'Ingénieur

2020TROY0023 **Année 2020**

Thèse en cotutelle avec Université Libanaise - Beyrouth - Liban

Université Libanaise

utt
UNIVERSITÉ DE TECHNOLOGIE
TROYES

THESE

pour l'obtention du grade de

DOCTEUR
de l'UNIVERSITE DE TECHNOLOGIE DE TROYES

EN SCIENCES POUR L'INGENIEUR

Spécialité : MATERIAUX, MECANIQUE, OPTIQUE, NANOTECHNOLOGIE

présentée et soutenue par

Elia ZGHEIB

le 1er décembre 2020

Multiscale Modeling and Characterization of the Elastic Behavior of Anisotropic Thin Films

JURY

M. Frédéric JACQUEMIN	PROFESSEUR DES UNIVERSITES	Président
M. Grégory ABADIAS	PROFESSEUR DES UNIVERSITES	Rapporteur
Mme Shabnam ARBAB CHIRANI	PROFESSEURE DES UNIVERSITES	Rapporteure
M. Ahmed ELMARAKBI	PROFESSOR	Examinateur
M. Jérôme FAVERGEON	PROFESSEUR DES UNIVERSITES	Examinateur
M. Manuel FRANÇOIS	PROFESSEUR DES UNIVERSITES	Examinateur
M. Khaled KHALIL	PROFESSEUR DES UNIVERSITES	Directeur de thèse
M. Akram ALHUSSEIN	PROFESSEUR ASSOCIE UTT	Directeur de thèse

Personnalité invitée

M. Mohamed Fares SLIM	DOCTEUR

“Dare to know!

Have the courage to use your own intelligence.”

– **Immanuel Kant**

To my mother

To my father

To my sisters

To my love

Acknowledgments

My profound gratitude and recognition are expressed, foremost, to my three academic supervisors, **Mr. Akram Alhussein**, Associate Professor at the University of Technology of Troyes, **Mr. Khaled Khalil**, Professor at the Lebanese University, and **Mr. Manuel François**, Professor at the University of Technology of Troyes. I would like to warmly thank them for believing in my potential and providing me with the right tools to strive in using my talents and curiosity during these three years. I revere their eminent support and most importantly, their humanitarian and professional values, which were reflected throughout the thesis work. Their equanimity and constant motivation inspired me to dare to aim high. Their erudite work was undoubtedly key to face all the challenges during the research time of the thesis. For the past three years, they have never stopped pushing me to deepen my knowledge in this field, so they constantly offered me to attend several conferences and workshops, which helped me to open up to the worldwide development in my field of research.

Moreover, I would like to profoundly thank **Prof. Manuel François** for sharing with me scientific culture, competences and experience. His hard questions incented me to widen my research from various perspectives. This thesis could not be the same without the presence of a mentor and a friend, **Dr. Mohamed Fares Slim**. When faced by negative experimental results, he was my intellectual bolster. My sincere thanks to the person who never felt tired to provide his energy and time for new solutions. Additionally, I would like to thank **Prof. Benoît Panicaud** for his support in further scientific consultations and discussions.

I would like to thank **Mrs. Shabnam Arbab Chirani**, Professor at the Research Institute Dupuy de Lôme and **Mr. Grégory Abadias**, Professor at the University of Poitiers, for the honor they gave it to me to evaluate my work. I also want to thank **Mr. Jérôme Favergeon**, Professor at the University of Technology of Compiègne, **Mr. Ahmed Elmarakbi**, Professor at Northumbria University in the United Kingdom, and **Mr. Frédéric Jacquemin**, Professor at the University of Nantes, for accepting to be members of my Ph.D. examination committee.

To the academic institutions, University of Technology of Troyes (UTT) and Lebanese University (LU) and their doctoral schools, I will always appreciate the frame you built and the opportunity you provided me to do my Ph.D. I am proud to be part of these two communities,

where intelligence and hard work are both appreciated. My special thanks go to **Zeinab Ibrahim** (LU), **Isabelle Leclercq** (UTT) and **Pascale Denis** (UTT) for their administrative efforts and advice.

My sincere gratitude goes to my LASMIS colleagues at the UTT antenna in Nogent, with whom I have lived amazing and unforgettable moments during my time there. I affirm my belonging to a family of everlasting connections with **Florent Uny**, **Imane Bouabibsa**, **Alexis De Monteynard**, **Thibaut Perrin**, **Guillaume Raine**, **Sofiane Achache**, **Sandrine Sanchette**, **Christopher Swan**, **Karima Aoudia**, **Sébastien Remy**, **Mohamed El Garah**, **Fabrice Parent**, **Alexandre Delblouwe**, **Ioana Fechete**, **Mohamed Amine Filali**, **Nathan Liebgott**, **Maoxiang Zhu**, **Kamel Ouari**, **Elias Kaady**, **Ahlam Belgroune**, **Fanny Perrot and Frédéric Sanchette**. I will never forget you, **Marie**. I will always call you the "Jill of all trades", all my respect.

Thanks to **Issam Lakdhar**, with whom I laughed, cried, suffered and enjoyed unforgettable moments throughout my three years working on my thesis. Thanks to him, Nogent is not just the place where I complete my PhD, rather it is also the place where I met a true brother and had the chance to engage with his rap songs world and master the Tunisian dialect. Thanks for making Nogent very special to me. I would also like to thank **Father Vincent Cardot** and **Father Stéphane Bredelet** for their spiritual support. I value every person I have met in this small yet generous village, Nogent.

I express my deepest gratitude to my parents, **Dolly Salameh** and **Semaan Zgheib**, and my two sisters, **Myriam Zgheib** and **Marla Zgheib**, for supporting me through adversity times, and believing in my potential. Even from miles away, I felt their presence, and got their efforts in helping me to seek what I am passionate about. I am very lucky to have a family that always pushes me to march into the right career and spiritual paths. A tremendous thank to my mother who always gives without counting the cost and who made my journey impressively more pleasant, Thank you! I will forever owe my achievements to my dedicated, caring and thoughtful family.

Finally, I owe many thanks to my very special person, **Marleine Tamer**, for her true love and big support. Thanks for all the advice and for always showing me new directions when faced by challenges. Thank you for making the three years of my thesis work easier for me. I am grateful to have you by my side.

List of abbreviations

AFAM	Atomic Force Acoustic Microscopy
AISI	American Iron and Steel Institute
Al	Aluminum
Ar	Argon
Au	Gold
bcc	Body-Centered Cubic
BLS	Brillouin Light Scattering
C	Carbon
CGM	Crystallite Group Method
CLBT	Classical Laminated Beam Theory
Co	Cobalt
Cr	Chromium
CR-AFM	Contact Resonance Atomic Force Microscopy
CSM	Continuous Stiffness Measurement
Cu	Copper
CVD	Chemical Vapor Deposition
DC	Direct Current
Dev-CLBT	Developed Classical Laminated Beam Theory
DLC	Diamond-Like Carbon
DV	Diffracting Volume
EB-PVD	Electron Beam Physical Vapor Deposition
ECs	Elasticity Constants
EMAR	Electro-Magnetic Acoustic Resonance
Ext-PM	Extended Pautrot’s Model
Ext-Slim	Extended Slim
FEM	Finite Element Model
FF	Free Free
FFT	Fast Fourier Transform
FRCB	Flexural Rigidity of a Composite Beam
GLAD	GLancing Angle Deposition

GUM	Guide to the expression of Uncertainty in Measurement
hcp	Hexagonal Closed Packed
IET	Impulse Excitation Technique
JCGM	Joint Committee for Guides in Metrology
KE	Kröner-Eshelby
MEMS	Electro Mechanical Micro Systems
min	Minutes
Nb	Niobium
NI	NanoIndentation
O-H	Ortho-Hexagonal
OSG	OrganoSilicate Glass
PECVD	Plasma-Enhanced Chemical Vapor Deposition
PLU	Picosecond Laser Ultrasonics
PVD	Physical Vapor Deposition
RF	Radio Frequency
RFDA	Resonance Frequency and Damping Analysis
rpm	Revolutions Per Minute
RVE	Representative Volume Element
RUS	Resonant Ultrasound Spectroscopy
sccm	Standard Cubic Centimeter per Minute
SCECs	Single-Crystal Elasticity Constants
SEM	Scanning Electron Microscopy
Si	Silicon
SZM	Structure Zone Model
Ta	Tantalum
Ti	Titanium
TNTZ	Titanium-Niobium-Tantalum-Zirconium alloy
IVM	International Vocabulary of Metrology
V	Vanadium
W	Tungsten
XEC	X-ray Elasticity Constants
XRD	X-Ray Diffraction
YSZ	Yttria-Stabilized Zirconia

Summary

Preface

New processes for obtaining materials in the form of thin films were developed in order to deal with various technological and economic constraints imposed in the industrial society. Today, these coatings are widely used in many fields such as mechanics, electronics, optics, chemical and aeronautic industries, etc. A coating acts as a protective film in order to protect, for example, a mechanical part and improve its performance. The thickness of these coatings varies from a few nanometers to a few hundred micrometers. Besides, these thin films can be used individually as a single layer or in multilayers, depending on the required applications. These coatings can be produced by different techniques, among which are given as examples: Physical Vapor Deposition (PVD), Chemical Vapor Deposition (CVD) and thermal spraying. In this thesis, we will particularly focus on thin films produced by magnetron sputtering (one of the PVD techniques).

A thin film produced by magnetron sputtering is generally multiphased, textured, porous and has an ellipsoidal grain shape [Liu 2018, Slim 2019]. Besides, the microstructural properties (structure, texture, morphology and porosity) depend on the deposition parameters [Ait-Djafer 2015, Zhang 2017]. However, these microstructural properties can influence the physical and mechanical properties of the film and thus can provide anisotropic behavior to the film. In order to ensure the performance of the mechanical parts, it is necessary to control the properties of the coated components. Indeed, we will be particularly interested in the elastic properties of thin films produced by magnetron sputtering.

Predicting the elastic behavior of coatings requires a perfect knowledge of the elasticity constants of the film, which depend on its microstructural properties. The identification of the elasticity constants is important in the field of engineering, in the choice of material and in the dimensioning of structures. Since thin films deposited by magnetron sputtering are often anisotropic, the knowledge of the anisotropic elasticity constants is necessary to predict the elastic behavior of the material. The elasticity constants allow us also to predict the residual stresses generated during the deposition process.

This thesis aims to determine the macroscopic elasticity constants of anisotropic thin films. Different methodologies will be proposed to determine the elasticity constants of thin

films having anisotropic elastic behavior. Two different approaches will be used in this work. A macroscopic approach consists in determining the elasticity constants of a film by vibrational measurements using the Impulse Excitation Technique (IET). A microscopic approach consists of determining the elasticity constants of a film by taking into account its microstructural properties (porosity, morphological and crystallographic textures). The crystallographic texture will be obtained by X-ray diffraction. The porosity will be measured by image analysis. The morphological texture will be observed by scanning electron microscopy.

This manuscript is therefore composed of five chapters.

The first chapter will present generalities on elasticity and its interest in engineering. The compliance and rigidity tensors of generally anisotropic materials and some others with particular symmetries will be illustrated. The determination of elasticity constants from the rigidity tensors will also be presented. Then, we will introduce several characterization techniques used to determine the elasticity constants of thin films by indicating the different problems encountered. Among the different techniques, the Impulse Excitation Technique will be chosen to measure the macroscopic elasticity constants of our films. From a literature synthesis, we will show that thin films produced by magnetron sputtering are often porous, polycrystalline, textured, multiphased and their elastic behavior depends on the deposition conditions through the microstructure. Therefore, the characterization of a thin film at the microscopic scale is performed by taking into account its microstructural properties. In order to characterize the anisotropy of thin films, two approaches will be developed during this work. The impulse excitation technique and the X-ray diffraction will be used for macroscopic and microscopic elastic characterizations, respectively.

The second chapter will be dedicated to the development of new models to determine the Young's and shear moduli of multilayer coatings, for any thickness, and mechanical and physical properties of the substrate and films. These models will be validated by comparing their results to those of a finite element model taken as a reference.

In the third chapter, the mechanical models (Ext-PM, Dev-CLBT and Ext-Slim) developed will be applied to titanium and niobium films deposited in multilayers. The elasticity constants of each film assumed isotropic, will be determined by means of the Impulse Excitation Technique. Then, the reduced moduli determined by this technique and nanoindentation will be compared.

The fourth chapter is divided into two parts. The first part will be devoted to the development of a model to determine the elasticity constants of anisotropic films. The validity range of the developed model will be determined by comparing its results with those of a finite element model taken as a reference. The second part will focus on the macroscopic elastic characterization of anisotropic titanium films, deposited by magnetron sputtering at oblique incidence. The elasticity constants of each deposited film will be correlated with the morphology, the structure, the texture and the glancing angle of each film. This chapter develops the first methodology for macroscopic elastic characterization of anisotropic thin films.

Finally, the fifth chapter will focus on the second methodology for characterizing anisotropic films. We will start with a brief introduction to X-ray diffraction. Then we will formulate the effective stiffness tensor and the microscopic strain measured by X-ray diffraction within the framework of the Kröner-Eshelby micromechanical model [Eshelby 1957]. Then, using the microstructural properties obtained by X-ray diffraction and the self-consistent model, the macroscopic elasticity constants of the porous, textured and single-phase titanium films sputter-deposited at oblique incidence will be determined. This methodlogy will allow us to have the first set of values of the macroscopic elasticity constants of GLAD films, which are not been determined in the literature. Finally, we will study the effect of porosity and morphological and crystallographic textures on the macroscopic elasticity constants and the microscopic behavior of single-phase Ti_{α} titanium films.

Chapter I

Introduction to the elasticity of thin films

I.1. Anisotropy and elastic symmetries: Brief overview

The elastic behavior of any material is defined by a compliance tensor S_{ijkl} or a stiffness tensor C_{ijkl}, which links the stress to the elastic strain. These are fourth-rank tensors, containing 81 Cartesian components in an orthonormal base (x_1, x_2, x_3) [Vannucci 2018]. According to Hooke's law, the linear relations between the stress σ and strain ε tensors are written for all the materials as follows [Vannucci 2018]:

$$\sigma_{ij} = C_{ijkl}\,\varepsilon_{ij} \tag{I.1}$$

$$\varepsilon_{ij} = S_{ijkl}\,\sigma_{ij} \tag{I.2}$$

with i, j, k and $l \in \{1, 2, 3\}$.

The stiffness and compliance tensors are represented by second-rank symmetric tensors with 3×3 components in a three-dimensional space $\mathbb{R}^3$ and thus they have only 6 independent components. These six components can be rearranged into a column vector. Due to the symmetry of the stress and strain tensors, the symmetries in the stiffness and compliance tensors are:

$$C_{ijkl} = C_{klij} \quad S_{ijkl} = S_{klij} \tag{I.3}$$

$$C_{ijkl} = C_{jikl} = C_{ijlk} = C_{jilk} \quad S_{ijkl} = S_{jikl} = S_{ijlk} = S_{jilk} \tag{I.4}$$

The 81 components of the compliance and stiffness tensors can then be reduced to 36 independent components. These components can then be rearranged into a second-rank symmetric tensor with 6×6 components. It can therefore be easily represented by a 6×6 symmetric square matrix.

According to the Kelvin's notation [Kelvin 1856], Eqs. (I.1) and (I.2) can be written as follows:

$$\begin{Bmatrix} \sigma_{11} \\ \sigma_{22} \\ \sigma_{33} \\ \sqrt{2}\sigma_{23} \\ \sqrt{2}\sigma_{31} \\ \sqrt{2}\sigma_{12} \end{Bmatrix} = \begin{bmatrix} C_{1111} & C_{1122} & C_{1133} & \sqrt{2}C_{1123} & \sqrt{2}C_{1131} & \sqrt{2}C_{1112} \\ C_{2211} & C_{2222} & C_{2233} & \sqrt{2}C_{2223} & \sqrt{2}C_{2231} & \sqrt{2}C_{2212} \\ C_{3311} & C_{3322} & C_{3333} & \sqrt{2}C_{3323} & \sqrt{2}C_{3331} & \sqrt{2}C_{3312} \\ \sqrt{2}C_{2311} & \sqrt{2}C_{2322} & \sqrt{2}C_{2333} & 2C_{2323} & 2C_{2331} & 2C_{2312} \\ \sqrt{2}C_{3111} & \sqrt{2}C_{3122} & \sqrt{2}C_{3133} & 2C_{3123} & 2C_{3131} & 2C_{3112} \\ \sqrt{2}C_{1211} & \sqrt{2}C_{1222} & \sqrt{2}C_{1233} & 2C_{1223} & 2C_{1231} & 2C_{1212} \end{bmatrix} \begin{Bmatrix} \varepsilon_{11} \\ \varepsilon_{22} \\ \varepsilon_{33} \\ \sqrt{2}\varepsilon_{23} \\ \sqrt{2}\varepsilon_{31} \\ \sqrt{2}\varepsilon_{12} \end{Bmatrix} \tag{I.5}$$

$$\begin{Bmatrix} \varepsilon_{11} \\ \varepsilon_{22} \\ \varepsilon_{33} \\ \sqrt{2}\varepsilon_{23} \\ \sqrt{2}\varepsilon_{31} \\ \sqrt{2}\varepsilon_{12} \end{Bmatrix} = \begin{bmatrix} S_{1111} & S_{1122} & S_{1133} & \sqrt{2}S_{1123} & \sqrt{2}S_{1131} & \sqrt{2}S_{1112} \\ S_{2211} & S_{2222} & S_{2233} & \sqrt{2}S_{2223} & \sqrt{2}S_{2231} & \sqrt{2}S_{2212} \\ S_{3311} & S_{3322} & S_{3333} & \sqrt{2}S_{3323} & \sqrt{2}S_{3331} & \sqrt{2}S_{3312} \\ \sqrt{2}S_{2311} & \sqrt{2}S_{2322} & \sqrt{2}S_{2333} & 2S_{2323} & 2S_{2331} & 2S_{2312} \\ \sqrt{2}S_{3111} & \sqrt{2}S_{3122} & \sqrt{2}S_{3133} & 2S_{3123} & 2S_{3131} & 2S_{3112} \\ \sqrt{2}S_{1211} & \sqrt{2}S_{1222} & \sqrt{2}S_{1233} & 2S_{1223} & 2S_{1231} & 2S_{1212} \end{bmatrix} \begin{Bmatrix} \sigma_{11} \\ \sigma_{22} \\ \sigma_{33} \\ \sqrt{2}\sigma_{23} \\ \sqrt{2}\sigma_{31} \\ \sqrt{2}\sigma_{12} \end{Bmatrix} \tag{I.6}$$

Eqs. (I.5) and (I.6) can be written with index contraction. The orders of indices established by the Kelvin's notation are:

$$11 \rightarrow 1, \qquad 22 \rightarrow 2, \qquad 33 \rightarrow 3 \tag{I.7}$$

$$32 \text{ or } 23 \rightarrow 4, \qquad 31 \text{ or } 13 \rightarrow 5, \qquad 21 \text{ or } 12 \rightarrow 6 \tag{I.8}$$

After index contraction, Eqs. (I.5) and (I.6) are written in the following form:

$$\begin{Bmatrix} \sigma_1 \\ \sigma_2 \\ \sigma_3 \\ \sigma_4 \\ \sigma_5 \\ \sigma_6 \end{Bmatrix} = \begin{bmatrix} C_{11} & C_{12} & C_{13} & C_{14} & C_{15} & C_{16} \\ C_{21} & C_{22} & C_{23} & C_{24} & C_{25} & C_{26} \\ C_{31} & C_{32} & C_{33} & C_{34} & C_{35} & C_{36} \\ C_{41} & C_{42} & C_{43} & C_{44} & C_{45} & C_{46} \\ C_{51} & C_{52} & C_{53} & C_{54} & C_{55} & C_{56} \\ C_{61} & C_{62} & C_{63} & C_{64} & C_{65} & C_{66} \end{bmatrix} \begin{Bmatrix} \varepsilon_1 \\ \varepsilon_2 \\ \varepsilon_3 \\ \varepsilon_4 \\ \varepsilon_5 \\ \varepsilon_6 \end{Bmatrix} \tag{I.9}$$

$$\begin{Bmatrix} \varepsilon_1 \\ \varepsilon_2 \\ \varepsilon_3 \\ \varepsilon_4 \\ \varepsilon_5 \\ \varepsilon_6 \end{Bmatrix} = \begin{bmatrix} S_{11} & S_{12} & S_{13} & S_{14} & S_{15} & S_{16} \\ S_{21} & S_{22} & S_{23} & S_{24} & S_{25} & S_{26} \\ S_{31} & S_{32} & S_{33} & S_{34} & S_{35} & S_{36} \\ S_{41} & S_{42} & S_{43} & S_{44} & S_{45} & S_{46} \\ S_{51} & S_{52} & S_{53} & S_{54} & S_{55} & S_{56} \\ S_{61} & S_{62} & S_{63} & S_{64} & S_{65} & S_{66} \end{bmatrix} \begin{Bmatrix} \sigma_1 \\ \sigma_2 \\ \sigma_3 \\ \sigma_4 \\ \sigma_5 \\ \sigma_6 \end{Bmatrix} \tag{I.10}$$

The Voigt's notation [Voigt 1910, François 2009] is not symmetric in terms of stress and strain and the contraction scheme of stiffness and compliance tensors is not the same. Kelvin's notation does not have these drawbacks. Even though, the two notations are equivalent [François 2009]. Kelvin's notation is preferred in this work. It gives a representation of

elasticity by matrices, $[C]$ and $[S]$, representing second-rank symmetric tensors in $\mathbb{R}^6$, which is not the case with the Voigt's notation [Mehrabadi 1990]. For instance, this fact helps the rotation of the matrices owing to the transferring from fourth-rank tensors in $\mathbb{R}^3$, to second-rank tensors in $\mathbb{R}^6$.

The stiffness matrix can be subdivided into various parts describing a particular effect. The different mechanical effects are presented in Fig. I.1. The Poisson's and Chentsov's effects shown on this figure correspond respectively to the shearing strains produced by a normal stress and the coupling between a shear stress and the shearing strains in orthogonal planes. A similar partition is also possible for the compliance matrix $[S]$.

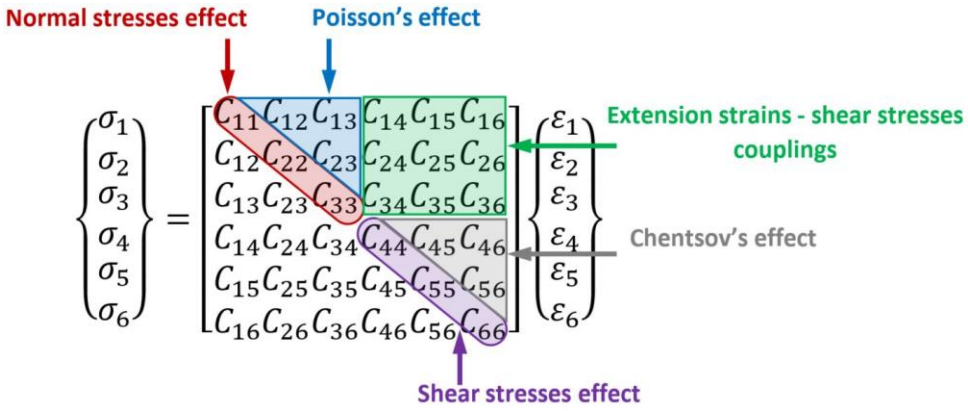

Fig. I.1. The different mechanical effects of the stiffness matrix.

I.1.1. Anisotropic elasticity

An elastically anisotropic material has different elastic properties depending on the direction (single-crystal, polycrystals with oriented morphology, texture, multiphase, composite, wood, multilayers, etc.). Thanks to the symmetries of the stress and strain tensors, the stiffness and compliance tensors contain 21 instead of 36 independent components. The material having the lowest symmetry is known as triclinic material with a general form of anisotropy. Matrix $[C]$ appears hence as:

$$[C] = \begin{bmatrix} C_{11} & C_{12} & C_{13} & C_{14} & C_{15} & C_{16} \\ & C_{22} & C_{23} & C_{24} & C_{25} & C_{26} \\ & & C_{33} & C_{34} & C_{35} & C_{36} \\ & & & C_{44} & C_{45} & C_{46} \\ & sym & & & C_{55} & C_{56} \\ & & & & & C_{66} \end{bmatrix} \tag{I.11}$$

I.1.2. The elasticity of material with hexagonal symmetry

In the case of a material with hexagonal symmetry, the number of independent components is reduced to 5. This material presents an axis of cylindrical symmetry and is called *transversely isotropic*. Many materials belong to this class, like for instance composites, laminated steel and wood. The stiffness tensor is written as follows:

$$[C] = \begin{bmatrix} C_{11} & C_{12} & C_{13} & 0 & 0 & 0 \\ & C_{11} & C_{13} & 0 & 0 & 0 \\ & & C_{33} & 0 & 0 & 0 \\ & & & C_{44} & 0 & 0 \\ & sym & & & C_{44} & 0 \\ & & & & & C_{11}-C_{12} \end{bmatrix} \tag{I.12}$$

I.1.3. The elasticity of material with cubic symmetry

By considering a material with cubic symmetry, the number of independent components is reduced to only three, since the crystalline system presents a high symmetry. The stiffness tensor is then written as follows:

$$[C] = \begin{bmatrix} C_{11} & C_{12} & C_{12} & 0 & 0 & 0 \\ & C_{11} & C_{12} & 0 & 0 & 0 \\ & & C_{11} & 0 & 0 & 0 \\ & & & C_{44} & 0 & 0 \\ & sym & & & C_{44} & 0 \\ & & & & & C_{44} \end{bmatrix} \tag{I.13}$$

I.1.4. Isotropic elasticity

An elastically isotropic material has the same elastic properties in all directions. It represents highest level of symmetry. In this case, only two independent components C_{11} and C_{12} are sufficient to characterize the elastic behavior of the material, as follows:

$$[C] = \begin{bmatrix} C_{11} & C_{12} & C_{12} & 0 & 0 & 0 \\ & C_{11} & C_{12} & 0 & 0 & 0 \\ & & C_{11} & 0 & 0 & 0 \\ & & & C_{11}-C_{12} & 0 & 0 \\ & sym & & & C_{11}-C_{12} & 0 \\ & & & & & C_{11}-C_{12} \end{bmatrix} \tag{I.14}$$

I.1.5. The engineering constants of elasticity

The engineers usually prefer to use the so-called *elasticity constants* instead of the elastic stiffness and compliance matrix components, C_{ij} and S_{ij} respectively. These elasticity constants must represent all the mechanical effects in a stressed material. They are defined as a function of the C_{ij} or S_{ij}. Several elasticity constants were defined in the literature, among which, Young's modulus, shear modulus, Poisson's ratio, Chentsov's ratio, etc.

Young's modulus measures the extension stiffness along the direction of one of the three axes. The mechanical meaning of the shear modulus is completely analogous to that of the Young's modulus but in shear stress and strain instead of normal ones. The Poisson's ratios measure the Poisson's effect i.e. the deformation in a direction transversal to that of the normal stress. These elasticity constants can be defined from the following expressions:

$$E_i = \frac{1}{S_{ii}} \qquad i = 1, 2, 3 \tag{I.15}$$

$$G_{ij} = \frac{1}{2\,S_{kk}} \qquad i, j = 1, 2, 3, \qquad i \neq j, \qquad k = 4, 5, 6 \tag{I.16}$$

$$\nu_{ij} = -\frac{S_{ji}}{S_{ij}} \qquad \frac{\nu_{ij}}{E_i} = \frac{\nu_{ji}}{E_j} \qquad i, j = 1, 2, 3 \tag{I.17}$$

Where E, G and ν are Young's modulus, shear modulus and Poisson's ratio respectively. The elasticity constants can be expressed as a function of the components of the stiffness matrix C_{ij} by inverting the compliance matrix: $[C] = [S]^{-1}$.

The elasticity constants are very important physical quantities in the field of engineering. The prediction of the elastic behavior of a material is important when the material is subjected to different types of loading. Several analytical and numerical models were developed using the elastic properties of materials in order to design structures, to predict the lifetime of their constitutive materials and to have a safe operation of the stressed structure. Furthermore, in the mechanical field, the elastic behavior is used as a criterion to choose the most suitable material for a well-defined application. In the next section, some methods of measuring the elasticity constants will be presented with their corresponding issues.

I.2. Methods of measuring the elasticity constants of thin films with the corresponding issues

Several methods were developed to determine the elasticity constants of bulk and coated materials. They can be classified into two groups: static and dynamic techniques.

I.2.1. Static techniques

I.2.1.1. Tensile test

The tensile test is one of the first static (or, more precisely, quasi-static) techniques used to determine several mechanical characteristics of a material, such as Young's modulus, Poisson's ratio, yield strength, etc. It allows the prediction of the mechanical behavior, which can be used for structure calculation.

For thin film application, several studies have used the tensile test to determine the Young's modulus of different types of films [Hollman 1997, Chen 2009, Huang 2013, He 2016]. Hollman et al. [Hollman 1997] have noted that the tensile test is highly dependent on the residual compressive stresses in the film. Chen et al. [Chen 2009] found that the external load should be applied only on the substrate such that the film is loaded indirectly through displacement continuity. By determining the 3D elastic stress field in a composite structure, the elastic properties of thin films are accurately calculated with proper gripping and stress concentration. Huang et al. [Huang 2013] found a good agreement between the moduli extracted from the tensile loading and those obtained by nanoindentation for multilayered ZrCu/Cu thin films. In order to improve the quality of the results, Gong et al. [Gong 2014] delimited the test sample into three zones: two coated zones with different thicknesses and uncoated one. This decomposition enabled to simultaneously obtain the substrate and film strains, to study the relationship between the thickness of the films and their elasticity constants and to reduce the experimental error.

For small-scale tensile testing, the strain measurement must be performed in situ to prevent the gripping problems and tester compliance that make the strain values unreliable [Huang 2000]. For this reason, different in-situ methods were combined with tensile testing, such as interferometric strain/displacement gauge [Sharpe 1997], speckle interferometry [Read 2001], X-ray diffraction (XRD) [Faurie 2005, Geandier 2010, Djaziri 2014] or laser diffraction [Huang 2000]. Sharpe et al. [Sharpe 1997] have used an interferometric strain/displacement

gauge, which is a non-contacting optical technique to measure the strain on brittle polysilicon thin films. The Young's modulus is then calculated from the slope of the experimental stress-strain curve.

The tensile test is one of the most techniques used to characterize the elastic behavior of materials but its application in the case of thin films remains restrictive because of the various problems encountered during the test (film delamination, film cracking during the test, stress concentration and gripping problem, etc.). It is also interesting to note that the sensitivity of this method decreases when the ratio between the substrate and film thicknesses increases owing to decreasing in the film sensitivity to the applied load. Consequently, this method is not suitable for the elastic characterization of thin films of few micrometers in thickness.

I.2.1.2. Bending test

The bending test also appears to be the most popular technique used, particularly for testing brittle materials, such as ceramics. For small-scale tests, this method is often easier to be implemented than the tensile one. Several works have used bending test to determine the Young's modulus of thin films. Rouzaud et al. [Rouzaud 1995] have performed a three-point bending test to determine the Young's modulus of C, W, CrC, and TiN coatings. Kraft et al. [Kraft 1998] and Schalko [Schalko 2011] have also determined the Young's modulus and the internal tensile strength of thin films using bending tests. Mendels et al. [Mendels 2005] have performed four-point bending micro-tests to determine the Young's modulus of a Ti/TiN multilayer coating. Dong et al. [Dong 2013] have performed bending tests to micro-beams using a nanoindenter and have determined the Young's modulus of a SiON film used in electromechanical microsystems (MEMS). Grieseler et al. [Grieseler 2016] have carried out in-situ bending tests in a scanning electron microscope. The problems encountered with this test are the same as those encountered with the tensile test, due to the high level of applied loading during the test.

I.2.1.3. Nanoindentation test

Among many techniques available to assess the film Young's modulus, NanoIndentation (NI) technique is applied frequently for this purpose. It was developed to characterize different types of materials and particularly thin films. This static test is often used to determine the mechanical properties, such as hardness, elastic and elastoplastic properties.

Chen et al. [Chen 2005] have performed NI tests on W and Al films deposited on two different types of substrates and found that the type of substrate used influences the measured modulus. Gerthoffer et al. [Gerthoffer 2017] have used NI to determine the Young's modulus of a Mo film for energy applications. NI measurements were performed on the cross-sectional and the surface of ZrO films obtained by EB-PVD [Lugscheider 2001]. A significant difference between the values was observed, they were between 10 *GPa* and 160 *GPa* for the measurements performed on the surface and between 20 *GPa* and 120 *GPa* for the measurements made on the cross-section. TiC films of 2 μm thick were deposited on different Ti, Cr and Mo sub-layers by magnetron sputtering [Feng 1998]. The authors found that the films Young's moduli determined by NI depend on the sub-layer used. The measured values varied between 400 *GPa* and 500 *GPa*.

Furthermore, a coupling between the experimental results and the numerical simulations was performed [Zhao 2011, Isselé 2012, Pandure 2014] in order to overcome the effect of the substrate. This coupling can be used to extract mechanical properties like hardness, Young's modulus, optimal thickness, etc. Gamonpilas et al. [Gamonpilas 2004] have determined the indentation behavior of various coated structures by using a combination of dimensional and finite element analyses. The effect of substrate properties on the elastic behavior of the films was investigated. The results revealed that the indentation experiments should be carried out up to a maximum depth of 5 % of the film thickness to avoid any influence from the substrate. This rule is applicable when the yield strength and Young's modulus ratios between the coating and the substrate $\sigma_{y,c}/\sigma_{y,s}$ and E_c/E_s are higher than 10 and 0.1 respectively. If $\sigma_{y,c}/\sigma_{y,s} < 10$, the maximum depth becomes 10 % of the film thickness. Saha et al. [Saha 2002] have evaluated by NI the effect of Al, glass, Si and sapphire substrates on the mechanical properties of Al and W thin films. They found that the elastic modulus of thin films is strongly affected by the substrate because the elastic field under the indenter is extended into the substrate, especially when the film thickness is small.

Although the nanoindentation test is one of the most frequently used techniques to determine the elasticity constants of thin films, the results of this test are influenced by the elastic interaction between the substrate and the film. In addition, since the majority of thin films are anisotropic, the Young's modulus determined by nanoindentation is a combination of the in-plane and out-of-plane Young's moduli. It also assumes that the Poisson's ratio of the tested film is known, which is not always true.

I.2.2. Dynamic techniques

I.2.2.1. Resonant Ultrasound Spectroscopy

Resonant Ultrasound Spectroscopy (RUS) is one of the non-destructive testing methods. The technique principle is based on the propagation velocity of an ultrasonic wave within a material, which is directly related to the elastic properties of the material. These specific velocity measurements can be performed by using contact or immersion measurement methods.

Several researchers [Lima 2005, Tan 2010, Sedmák 2013] have used the ultrasonic method to determine the elasticity constants of coatings obtained by thermal spray. Thomasovà et al. [Thomasovà 2015] have determined the Young's modulus of a NiTi thin film produced by magnetron sputtering using the ultrasonic method. The ultrasonic characterization of elastic anisotropy in plasma-sprayed alumina coatings was also performed by this method [Parthasarathi 1995]. Another alternative of this method consists in measuring the ultrasonic wave propagation velocity at the surface. Hurley et al. [Hurley 2001] and Schneider et al. [Schneider 1997] have determined respectively the elasticity constants of anisotropic TiN and Young's modulus of DLC films with the same method.

The advantage of employing the RUS technique for coatings is that small amplitude excitations are sufficient for the measurements. Furthermore, the ability to calculate the entire stiffness matrix from a single spectrum is a distinct advantage of this method. Despite the non-destructive nature and all other advantages, this technique has not been considered for thin films that have complex microstructures. The results may be influenced by the texture and structural defects present within the material. The non-linearity and anelasticity in the elastic properties of textured thin films make it difficult to determine uniquely the microstructure-dependent linear elastic properties except when the material is subjected to small strains [Liu 2008]. Ledbetter et al. [Ledbetter 1988] have noted that an anisotropic distribution of dislocations in a material can influence the measurements of the elasticity constants.

I.2.2.2. Impulse Excitation Technique

The Impulse Excitation Technique (IET) consists in exciting a sample (beam, cylinder, disc, etc.) by a striker and let it freely vibrate without any constraint. The signal generated by these mechanical vibrations is recorded using a microphone or a transducer. This signal is then analyzed to extract the resonant frequencies of the vibrated sample by Fast Fourier Transform

(FFT). The measured resonant frequencies are used to determine the elasticity constants of the tested material using elasticity expressions. These expressions involve the dimensions and density of the sample.

This technique has been used by several researchers to determine the elastic constants of different materials, such as metals, composites, ceramics, polymers, glass, porous materials, coatings, etc. [Atri 1999, Schrooten 1999, Radovic 2004, Gadaud 2004, Gadaud 2009, Hauert 2009, Vasechko 2016] and over a wide range of temperatures [Peraud 1997, Gadaud 2009, Raj 2009; Patel 2018]. Peraud et al. [Peraud 1997], Etienne et al. [Etienne 2004] and Sanchette et al. [Sanchette 1999] have determined the Young's modulus of different thin films with this technique, respectively: $\sim 2\ \mu m$ thick SiC and NiTi, 0.2 μm thick TiN, and 10 μm thick AlTiN and AlCrN. Gadaud et al. [Gadaud 2009] have measured the shear modulus of NiO thin films having two different thicknesses (40 μm and 60 μm). Slim et al. [Slim 2017b] have determined the Young's and shear moduli of 2.88 μm thick W film deposited by magnetron sputtering. López-Puerto et al. [López-Puerto 2014] have determined the Young's moduli of 200 *nm* thick Al and 250 *nm* thick Au films in an Al/Au/Kapton multilayer composite using the same technique.

Other authors [Grüter 2010, Ma 2012] have employed the IET to simultaneously measure the density and Young's modulus of thin films. The proposed method requires the use of a beam composed of three layers (substrate + film 1+ film 2) in order to attribute one analytical expression for each film. Ma et al. [Ma 2012] have used this method to simultaneously measure the Young's modulus and density of Ni film deposited on Si cantilever beam. Furthermore, it has been shown recently that Young's modulus and density of thin films can also be simultaneously determined by measuring the in-plane and out-of-plane resonant frequencies [Ilic 2010]. However, the in-plane excitation is difficult to be achieved in practice. On the other hand, another non-destructive method was proposed to simultaneously determine the Young's modulus and either the density or the thickness of thin films [Stachiv 2014]. It consists in detecting the resonant frequency shifts of coated and uncoated resonators caused by an attached mass. Thanks to the well-established resonance-based mass sensors, film properties can be determined even if no shift of the resonant frequency was found.

This non-destructive technique is easily usable without any expensive equipment required. The advantage of this technique is that very low-stress levels are generated compared to the yield strength of most materials owing to very small strains generated during the test. The

IET is qualified as a promising alternative for the characterization of the elastic behavior of thin films.

I.2.3. Other techniques

Other experimental techniques were used to determine the elasticity constants of thin films, namely atomic force microscopy, bulge test, Brillouin light scattering, surface acoustic wave spectroscopy, picosecond ultrasonic method, and ellipsometric porosimetry.

The Atomic Force Microscopy (AFM) was used to determine the Young's modulus of different types of thin films. For example, Kim et al [Kim 2009] have used force modulation AFM to obtain Young's modulus maps at a cross-section of a 150 *nm* thick film of UV cured OrganoSilicate Glass (OSG). Enhanced AFM techniques were used to determine the Young's modulus, namely Atomic Force Acoustic Microscopy (AFAM) and Contact Resonance Atomic Force Microscopy (CR-AFM). Kopycinska-Müller et al. [Kopycinska-Müller 2013] have used AFAM method to determine the Young's modulus of nanoporous OSG thin films. Stan et al. [Stan 2009] have used CR-AFM technique to determine the Young's modulus of 500 *nm* thick of low-*k* dielectric thin films. The CR-AFM method allows us to determine the effective tip-sample contact stiffness from the analysis of the vibrations of an AFM cantilever excited by an ultrasonic source placed below the sample [Rabe 2006]. Kaman [Kaman 2014] have determined the Young's modulus of a chalcogenide film by measuring the force curves using an atomic force microscope.

Sungwoo et al. [Sungwoo 2005] have determined the Young's modulus and Poisson's ratio of Si film using the hole drilling method at a microscopic scale. The nanometric strains generated by the film under different loads were measured by image correlation obtained by atomic force microscopy. Cianci et al. [Cianci 2007] have determined the Young's modulus of thin silicon nitride film deposited by dual-frequency PECVD, by measuring the deflection of a circular membrane as a function of the load applied by means of a profilometer. Colombi et al. [Colombi 2013] have determined the Young's moduli of a series of amorphous titanium dioxide films, varying the thickness between 10 *nm* and 125 *nm* by extracting the resonance frequencies of polymer microbeams.

Vlassak et al. [Vlassak 1992] have determined the Young's modulus and Poisson's ratio of silicon nitride films using the bulge test. Martins et al. [Martins 2009] have performed the bulge test to determine Young's modulus and Poisson's ratio of very thin Si_3N_4 dielectric films

for micro-electro-mechanical systems. Bulge test was also used to determine the Young's modulus of Cu and Cu-Ni textured films [Tsakalakos 1981].

Apreutesei et al. [Apreutesei 2017] have determined the elasticity constants of metallic glass films using Brillouin Light Scattering (BLS). Chapelon et al. [Chapelon 2006] have determined the Young's modulus of porous a-SiOC:H films deposited by PECVD, using picosecond ultrasonic method. Abadias et al. [Abadias 2020] have determined the elasticity constants of cubic epitaxial TaN films deposited by reactive magnetron sputtering. They have determined c_{44} and c_{12} from the BLS method and c_{11} from the Picosecond Laser Ultrasonics (PLU) method for the $\delta - Ta_xN$ single cubic phase embedded in the film. The elasticity constants of Ta_α and Ta_β thin films were also determined by combining the BLS and PLU methods [Abadias 2019a]. The ellipsometric porosimetry [Mogilnikov 2002] and the Drum head test [Heinen 1995] were also used to determine the Young's modulus of thin films.

I.3. Microstructural properties of thin films deposited by magnetron sputtering: correlation and dependence on deposition conditions

I.3.1. Young's modulus

Shaochen et al. [Shaochen 2018] have determined the hardness and Young's modulus of ZrN films deposited by magnetron sputtering on zirconium alloy substrates at different working pressures. They have found that the best mechanical properties were obtained at a working pressure of 0.7 *Pa* (H = 16 *GPa* and E = 193.5 *GPa*). Bao et al. [Bao 2018] have measured by nanoindentation the Young's modulus of a 1.5 μm thick SiC film deposited at different working pressures by magnetron sputtering on a Zircaloy-4 (zirconium alloy) substrate. They have found that Young's modulus decreased from 214 *GPa* to 100 *GPa* by increasing the working pressure from 0.4 *Pa* to 2.4 *Pa* (Fig. I.2). Achache et al. [Achache 2016] have reported that Young's modulus of TNTZ superelastic films produced by magnetron sputtering depends on the working pressure and the substrate bias voltage. Using nanoindentation tests, they have shown that Young's modulus is inversely proportional to the working pressure; it reduced from 104 *GPa* to 89 *GPa* with increasing the pressure from 0.2 *Pa* to 2 *Pa*. The bias voltage differently influenced the film Young's modulus. It slightly

increased from 104 *GPa* to 108 *GPa* with increasing the substrate bias voltage from 0 *V* to -200 *V* and it reduced to 98 *GPa* for the film deposited at -300 *V* bias voltage.

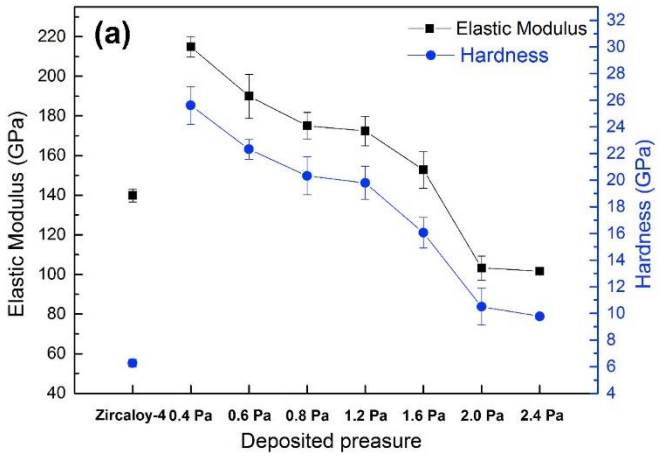

Fig. I.2. Evolution of the hardness and Young's modulus of SiC films deposited at different working pressures [Bao 2018].

Ait-Djafer et al. [Ait-Djafer 2015] have deposited 1 μm thick TiAlN thin films using the reactive magnetron sputtering and evaluated the effect of the substrate bias voltage and the working pressure on the Young's modulus measured by NI technique. They have reported that the elastic modulus increased from 311 *GPa* to 480 *GPa* by increasing the bias voltage from 0 *V* to -60 *V*. They also found that Young's modulus reduced from 311 *GPa* to 205 *GPa* by increasing the working pressure from 2 *Pa* to 5 *Pa*. Choudhary et al. [Choudhary 2015] have also studied the effect of the substrate bias voltage on AlN films produced by magnetron sputtering. They have reported an increase in the Young's modulus value, measured by nanoindentation, from 100 *GPa* to 215 *GPa* with the increase of bias voltage from 0 *V* to -100 *V*. Bramowicz et al [Bramowicz 2016] have deposited hydroxyapatite coatings of 450 *nm* thick with Radio Frequency (RF) magnetron sputtering at different temperatures. They have found that the film Young's modulus, measured by nanoindentation, reduced from 170 *GPa* to 80 *GPa* with increasing the deposition temperature from 400 ℃ to 800 ℃.

Zhang et al [Zhang 2017] have studied the influence of the deposition temperature on the Young's modulus of CrB_2 films of ~ 1 μm thickness, deposited by magnetron sputtering on Si substrates. The NI measurements showed that varying the deposition temperature between 100 ℃ and 400 ℃ led to an increase in the Young's modulus from 425 *GPa* to 525 *GPa*. Abegunde et al. [Abegunde 2020] have investigated, by NI measurements, the evolution of Young's modulus of TiC films deposited by RF magnetron sputtering as a function of RF

power, temperature and deposition time. They have noted that by increasing the RF power from 150 *W* to 200 *W*, the Young's modulus decreased and then increased with a power up to 250 *W*. These results were found similar for films deposited at 80 ℃, 90 ℃ and 100 ℃.

I.3.2. Morphology

Chawla et al. [Chawla 2009] have examined the morphology of Ti films deposited at 100 °C with constant working pressure and varying the sputtering power from 50 *W* to 150 *W*. With increasing power, they have noticed that the density of the film has increased. They also examined the morphology of the films deposited at constant pressure, 50 *W* power and different substrate temperatures varied from 100 ℃ to 500 ℃. The morphology of the grains changed by increasing the substrate temperature and became denser.

By varying the working pressure between 0.1 *Pa* and 1.6 *Pa*, Bao et al. [Bao 2018] have noticed that the SiC films deposited at low pressure below 0.3 *Pa* were cracked and delaminated from the substrate. The films deposited at 0.4 *Pa* were dense and those deposited at a pressure above 0.8 *Pa* presented a columnar growth. Zhang et al. [Zhang 2017] reported that the deposition temperature of CrB_2 thin film influenced its morphology. A fine and dense structure at 100 °C. Beyond 100 ℃ and up to 400 ℃, the deposited films showed columnar growth. Achache et al. [Achache 2016] have shown that by varying the working pressure between 0.5 *Pa* and 2 *Pa*, the TNTZ deposited films presented columnar growth. By reducing the pressure to 0.2 *Pa*, they have obtained dense films. In addition, the films deposited at 0.2 *Pa* with high bias voltage varied between -100 *V* and -300 *V* presented a crater-like surface.

I.3.3. Structure

Thin films produced by magnetron sputtering are generally polycrystalline and composed of different phases. Since magnetron sputtering is an out of equilibrium deposition process, it favors the formation of metastable phases, such as W_β in tungsten films [Shen 2000, Girault 2013, Slim 2017b], Ti_β in Ti-17 films [Liu 2018] and Ta_β in tantalum films [Javed 2010, Colin 2017]. Pfeiler et al. [Pfeiler 2007] have reported the presence of different phases within the Ti-Al-V-N films. With increasing the bias voltage, the fraction of the hcp phase decreased and then disappeared at -160 *V* (Fig. I.3).

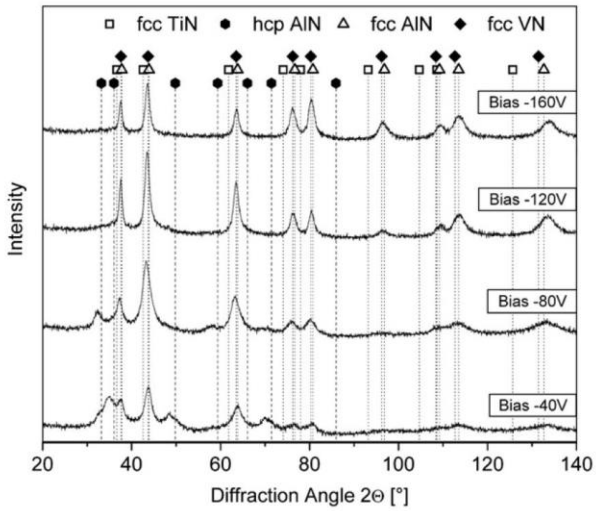

Fig. I.3. X-ray diffraction patterns of Ti-Al-V-N coatings deposited at different bias voltages [Pfeiler 2007].

Ait-Djafer et al. [Ait-Djafer 2015] have reported that the presence of different phases within TiAlN films depends on the working pressure and the bias voltage of the substrate. Liu et al. [Liu 2018] noticed the presence of the two phases α and β of titanium in Ti-17 films. They found that the evolution of the phases within their films depends on the substrate temperature.

I.3.4. Texture

Thin films elaborated by magnetron sputtering are generally textured. Their texture depends on the deposition parameters. Zhang et al. [Zhang 2013] have noted a change in the texture, depending on the thickness of TiN films deposited by magnetron sputtering. They have reported a change from (002) to (111) texture by increasing the film thickness from 286 *nm* to 2357 *nm*. Chaabani et al. [Chaabani 2017] have studied the effect of the target-to-substrate distance on the texture of strontium barium titanate ($BaSrTiO_3$) films. They have noticed a change from (111) to (100) texture by increasing this distance from 5 *cm* to 10 *cm*. Achache et al. [Achache 2016] have shown the texture changes as a function of substrate bias voltage and deposition pressure. Sharma et al. [Sharma 2016] have studied the crystallographic texture of Ni-Mn-Ga based thin films obtained by magnetron sputtering at different sputtering powers (Fig. I.4).

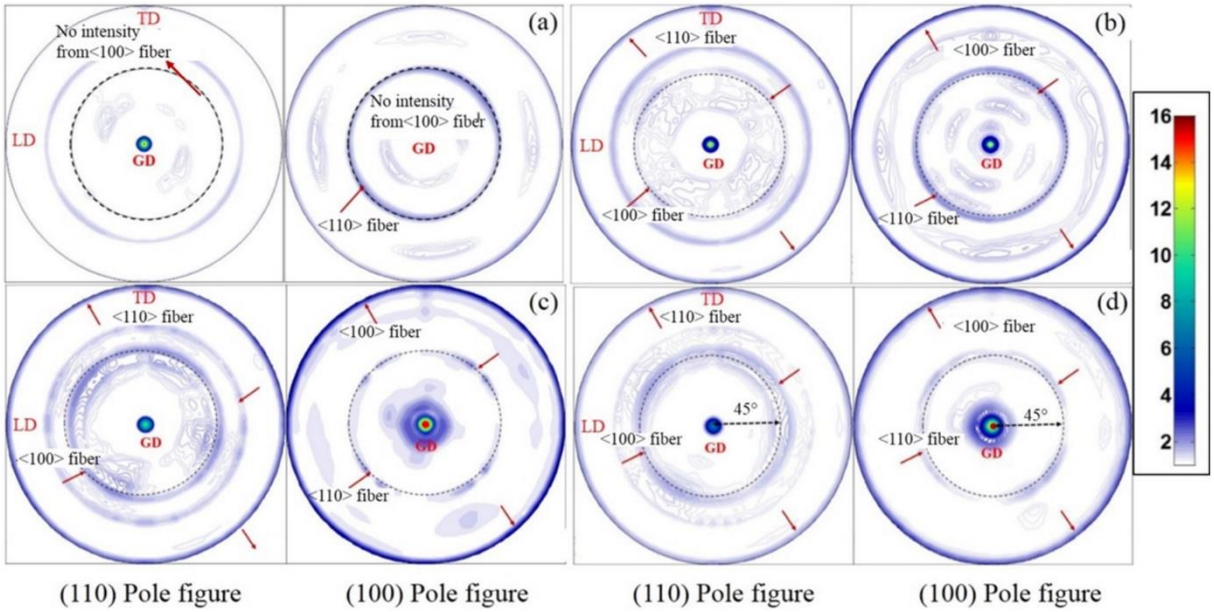

Fig. I.4. (110) and (100) measured pole figures for Ni-Mn-Ga based films deposited at: a) 30 *W*, b) 50 *W*, c) 70 *W* and d) 90 *W* [Sharma 2016].

Liu et al. [Liu 2016] have studied the effect of substrate temperature on the texture of Ti6Al4V films obtained by magnetron sputtering. They have noticed a change in film texture by increasing the temperature from 100 ℃ to 400 ℃ while above 500 ℃, the film has no longer a texture. Zhang et al. [Zhang 2017] have noted that the texture of the CrB_2 films deposited by magnetron sputtering depends on the substrate temperature. They have reported that films obtained at temperatures below 300 ℃ did not have preferential orientations and that above 300 ℃, a (001) preferential orientation appeared. The effects of sputtering power, substrate temperature and working pressure on the texture of Ti films were determined using XRD analysis [Chawla 2009]. The Ti films exhibit an initial (100) preferred orientation but the (002) and (101) orientations were observed with the increasing of the sputtering power and substrate temperature, respectively.

Moreover, several studies have examined the evolution of the film texture as a function of the substrate inclination angle α. Abadias et al. [Abadias 2019b] have determined the texture of HfN films deposited at oblique angle deposition conditions. With increasing α above 35°, the development of biaxial texture with double in-plane alignment was noticed (Fig. I.5).

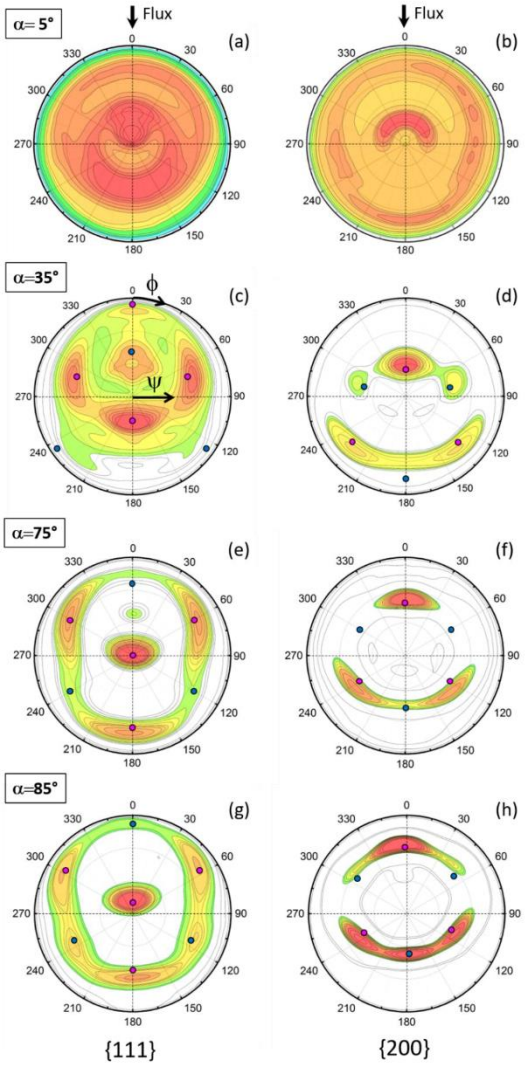

Fig. I.5. {111} (a, c, e, g) and {200} (b, d, f, h) X-ray diffraction pole figures of oblique angle deposition HfN films at different substrate inclination angles [Abadias 2019b].

I.3.5. Residual stresses

The residual stresses generated in films during the deposition process, by magnetron sputtering, depend on different parameters e.g. working pressure, bias voltage, substrate temperature, substrate inclination, film thickness, etc. Escobar et al. [Escobar 2015] reported the influence of substrate temperature on the evolution of residual stresses in TiZrN thin films. They found that all films presented residual compressive stresses decreased from -2.8 *GPa* at floating temperature to -1.05 *GPa* at 200 ℃. Pfeiler et al. [Pfeiler 2007] have determined the Young's modulus, hardness and residual stress of Ti-Al-V-N coatings as a function of the bias voltage (Fig. I.6). The residual compressive stress increased from around -0.4 *GPa* at -40 *V* up

to -1.5 *GPa* at -80 *V*. However, it remained more or less constant for the higher voltages between -80 *V* and -160 *V* (Fig. I.6).

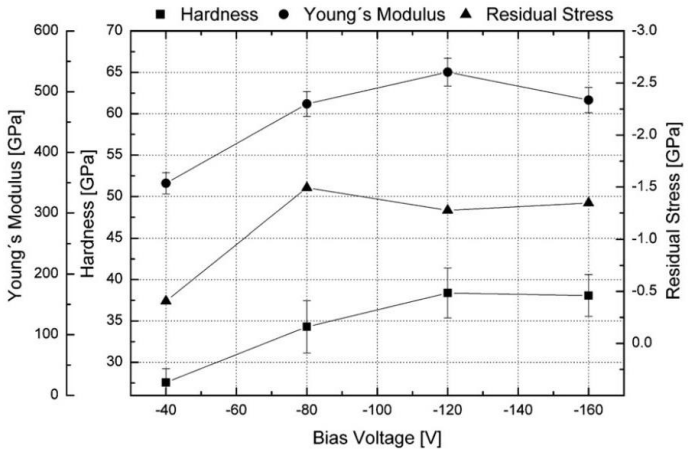

Fig. I.6. The residual stress, Young's modulus and hardness of Ti-Al-V-N coatings versus bias voltage [Pfeiler 2017].

Furthermore, several studies have examined the evolution of the residual stress as a function of the deposition angle (α). Siad et al. [Siad 2016] have evaluated the residual stress of Al, Ti and Cr thin films prepared by the glancing angle deposition method. The residual stress was calculated by Stoney's formula using the wafer curvature technique. They found that the absolute values of the residual stress in Ti and Cr films suddenly dropped to lower values with the change of substrate inclination from 45° to 60° (Fig. I.7). This significant reduction was explained by the increase of film porosity. From Fig. I.7, we can also see the transition from compressive to tensile stress in Al film.

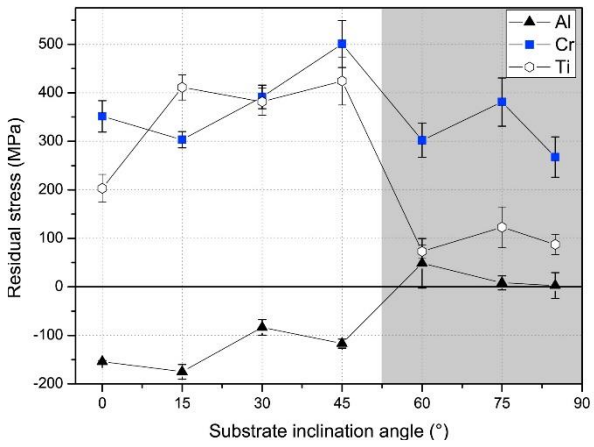

Fig. I.7. Evolution of the residual stress of Al, Ti and Cr thin films as a function of the substrate inclination angle [Siad 2016].

Recently, Abadias et al. [Abadias 2019b] have determined the residual stress of polycrystalline HfN thin films deposited by magnetron sputtering at 300 ℃ with oblique incidence. They have found that the residual stress changed from -5 *GPa* strongly compressive at 5° of inclination to slightly tensile for an inclination higher than 35°. The residual stress was measured by X-ray diffraction.

From this short literature review, it can be seen that thin films deposited by magnetron sputtering are generally multiphase, polycrystalline, textured, porous and present grains with columnar morphology. These characteristics provide them an anisotropic elastic behavior. In addition, their elastic properties, morphologies, structures and crystallographic orientations depend mainly on the deposition conditions. Therefore, in order to control the elastic behavior of thin films obtained by magnetron sputtering, their elasticity constants should be evaluated.

I.4. Methodology for measuring the elasticity constants

As we have seen from the previous section, one can conclude that the macroscopic characterization of the elasticity constants of thin films obtained by magnetron sputtering is insufficient to predict their elastic behavior. Therefore, the microscopic characterization of the elasticity constants of thin films is essential, along with the macroscopic one, to have a better assessment of the elastic behavior of thin films. It goes through the determination of the film X-ray elasticity constants (XEC) and thus the assessment of stresses within the deposited film.

The XRD gives us a mesoscopic quantity: the strain $\varepsilon_{\phi,\psi}$ in the measurement direction that corresponds to the average of the strains of the crystallites in the diffraction position. This experimental quantity is specific to crystallites diffracted. Therefore, the macroscopic stress cannot be related to the strain of the diffracting volume via the macroscopic elasticity constants of the effective material. In order to study the stresses in polycrystalline materials, the macroscopic stresses were related to the elastic strains measured by diffraction using the XEC $F_{ij}(hkl,\phi,\psi)$ [Hauk 1997] as follows:

$$\varepsilon_{\phi,\psi}^{\{hkl\}} = F_{ij}(hkl,\phi,\psi)\ \sigma_{ij}^{I} \tag{I.18}$$

Where h, k and l are Miller's indices. $\varepsilon_{\phi,\psi}^{\{hkl\}}$ represents the average strain measured on a family of planes $\{hkl\}$ in the measurement direction defined by the tilt ψ and azimuth ϕ angles. σ_{ij}^{I} represents the macroscopic stress.

These XEC can be defined as the average of the elasticity constants of the diffracted crystallites [Dölle 1979]. The XEC can be determined experimentally or from the SCECs using a micromechanical model (Reuss, Voigt, Kröner-Eshelby, etc.). These models were applied to determine the XEC of isotropic and textured materials [Barral 1987, Baczmanski 2003]. The XEC were also determined experimentally by XRD or neutrons diffraction under applied loading [Hayakawa 1985, Gnäupel-Herold 1998, Howard 1999, Fréour 2005, Martinschitz 2006, Gnäupel-Herold 2012].

In the following sections, several methodologies, developed in the literature, are presented based on different scale approaches.

I.4.1. Macroscopic approaches

The elasticity constants of isotropic or anisotropic materials can be determined using dynamic techniques. Two different methodologies were used in the literature. The first one consists in coupling numerical simulations to experimental measurements by minimizing different error functions [Nieves 2003, Maletta 2004, Bruno 2006, Alfano 2007, Pagnotta 2009, Gogu 2010, Barkanov 2015]. Using different optimization methods, such as simplex, gradient, least squares and genetic algorithms, the elasticity constants of anisotropic plates of any shape converge after several iterations. Using the IET, this methodology requires several frequency modes (from 4 and up to 10 modes) in order to obtain reliable solutions. Examples of a flow chart and a measurement system that allow the detection of all the resonant frequencies of a sample and thus the identification of elasticity constants are shown in Fig. I.8.

a) b)

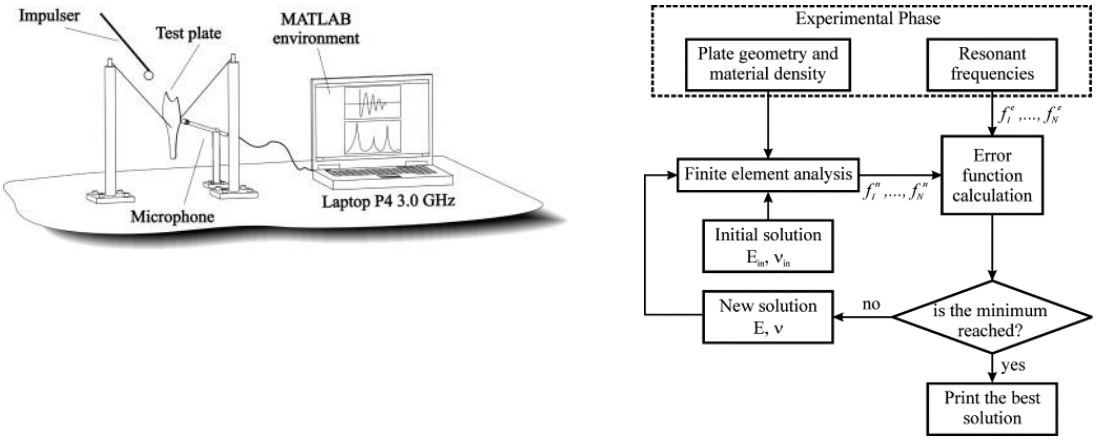

Fig. I.8. Schematic representation of a) the measurement system of the elasticity constants and b) the flow chart used for elasticity constants identification [Pagnotta 2009].

The second methodology proposed in the literature consists of measuring the resonant frequencies of the tested sample using the vibrational technique. Then, these measured frequencies are correlated to the elasticity constants of the sample through a suitable model [ASTM 2015].

In the case of thin films, the principle of the measurement is to perform a two-steps frequency measurement before and after deposition. The resonance frequencies of the substrate and the composite beam (Substrate + film), the elasticity constants of the substrate and the properties (mass, dimensions, density) of the substrate and film were used to determine the elasticity constants of the film through mechanical models. The existing mechanical models in the literature for the determination of the Young's modulus are based on two different theories: the flexural rigidity of a composite beam (FRCB) and the classical laminated beam theory (CLBT) [Slim 2017a]. Based on the Hamilton's principle, the shear modulus of thin films can be determined using IET [Gadaud 2009, Slim 2017b].

I.4.2. Microscopic approaches

The prediction of the elastic behavior of anisotropic material requires a perfect knowledge of the corresponding elasticity constants that depend on the microstructural properties of the material. Its elastic response should also be described at the microscopic scale. For instance, the determination of the residual stress issued from any process requires the knowledge of the Single-Crystal Elasticity Constants (SCECs) of the different phases embedded in a material [Hauk 1997].

The SCECs can be determined experimentally either directly on single-crystal specimens [Tanaka 1996, Leisure 1997, Sedlak 2005, Migliori 2005] or indirectly on macroscopic polycrystalline specimens. The second method can be applied by measuring the microscopic strain response by diffraction under applied loading [Hayakawa 1985, Singh 1998, Gnäupel-Herold 1998, Howard 1999, Fréour 2005, Faurie 2005, Talling 2008, Efstathiou 2010, Patel 2014, Slim 2019]. It can also be applied by means of Resonant Ultrasound Spectroscopy (RUS) combined with Electro-Magnetic Acoustic Resonance (EMAR) and the crystallographic orientations [Tane 2013, Tane 2017] or by Picosecond Laser Ultrasonic (PLU) and Brillouin Light Scattering (BLS) techniques [Abadias 2019a]. Efstathiou et al. [Efstathiou 2010] have determined the SCECs of the studied crystal (β21s) by minimizing the difference between the experimental data and those simulated by a virtual finite element model of a titanium

polycrystal. The single-crystal elasticity tensor of a cubic phase (Section I.1.3) can be described using three independent constants (c_{11}, c_{12}, c_{44}). Slim et al. [Slim 2019] have calculated the SCECs of the W_β cubic phase through an inverse procedure using at least three independent experimental quantities. They determined two macroscopic quantities (E_x, G_{yz}) using the IET and one quantity by strain measurement under applied loading. Then, they expressed them as a function of single-crystal stiffness tensor using the KE self-consistent micromechanical model. Then, the SCECs were calculated by minimizing an objective function defined as the difference between the experimental and the calculated quantities.

The macroscopic elastic behavior of anisotropic materials can be predicted from the single-crystal elasticity constants using different scale-transition models, such as Voigt [Voigt 1910], Reuss [Reuss 1929], Neerfeld-Hill [Neerfeld 1942, Hill 1952], self-consistent of Kröner-Eshelby [Eshelby 1957, Kröner 1958], Vook-Witt [Vook 1965, Witt 1968], normalized self-consistent [Li 1999], Hashin-Shtrikman [Hashin 1962] and Mori-Tanaka [Mori 1973] models. Mori-Tanaka model is equivalent to one of Hashin and Shtrikman's models in the elastic regime. Table I.1 summarizes different methodologies used to determine the single-crystal or polycrystals elasticity constants of different types of materials, found in the literature.

Table I.1
Summary of different methodologies used to determine the elasticity constants of a single-crystal or polycrystals of different types of materials.

Material	Modeling	Experimental description	Reference
SCECs in Fe-31Ni alloy	Self-consistent model of Kröner-Eshelby	Young's modulus was determined using four-points bending test. XEC were determined using XRD under applied four-points bending loads.	[Hayakawa 1985]
SCECs in Al, Cu and Steel.	Self-consistent model of Kröner-Eshelby	XEC were determined using neutron diffraction under applied uniaxial tensile and compressive loads.	[Gnäupel-Herold 1998]
Polycrystalline Cu, TiN, Zn and Al_2O_3	Self-consistent model of Kröner-Eshelby	The texture was taken into account by calculating the Orientation Distribution Functions (ODF).	[Hendrix 1998]
SCECs in Ni-Cr-Fe and Ti-Al-V alloys and cubic zirconia	Reuss and Voigt-Reuss-Hill approximations	XEC were determined using neutron diffraction under applied uniaxial tensile and loads.	[Howard 1999]
SCECs of Au (fcc) and Nb (bcc) thin films	Vook-Witt and Inverse Vook-Witt models	The elastic strain measurements were performed using XRD under applied tensile loads.	[Welzel 2003]
SCECs of Ti_β phase in polycrystalline Ti-17 alloy	Inverse self-consistent model	XEC were determined using XRD under applied bending loads.	[Fréour 2005]

SCECs in Au thin films	Voigt and Reuss models	The elastic strain measurements were performed using XRD under applied tensile loads.	[Renault 2003]
SCECs in Cu and CrN thin films	Neerfeld-Hill model	The elastic strain measurements were performed using XRD under applied tensile loads.	[Martinschitz 2009]
SCECs in Au thin films	Reuss model	The elastic strain measurements were performed by XRD using synchrotron radiation under applied tensile loads.	[Faurie 2005]
SCECs of β21s in Ti polycrystal	Finite element model	Coupling high-energy XRD tests under imposed loading and crystal-based finite element modeling. The texture was taken into account by calculating the Orientation Distribution Functions (ODF).	[Efstathiou 2010]
Polycrystals with cubic and hexagonal symmetries	Self-consistent model of Kröner-Eshelby	Simulation	[Hounkpati 2014a]
Al-SiC and Zn-Cd polycrystals	Normalized self-consistent model	Simulation	[Hounkpati 2014b, Hounkpati 2015]
SCECs of W_β phase in W thin film	Self-consistent model of Kröner-Eshelby	The elastic strain measurements were performed using XRD under applied bending loads.	[Slim 2019]
SCECs from as-cast Fe-3% Si polycrystals	Finite element simulations	Spherical nanoindentation and orientation measurements	[Patel 2014]
SCECs of W_β phase in W thin film	Density functional theory	Picosecond ultrasonic	[Nagakubo 2020]
SCECs of Ta_α and Ta_β phase in Ta thin film	Density functional theory	Picosecond laser ultrasonic and Brillouin light scattering	[Abadias 2019a]
SCECs of $Mg_{85}Zn_6Y_9$ in Mg-Zn-Y alloy	Hashin-Shtrikman, Inverse self-consistent and Inverse Voigt-Reuss-Hill approximations	Resonant ultrasound spectroscopy and the crystallographic orientations	[Tane 2013]
SCECs of Cu, Mg and AZ31	Hashin-Shtrikman, Inverse self-consistent and Inverse Voigt-Reuss-Hill approximations	Resonant ultrasound spectroscopy and the crystallographic orientations	[Tane 2017]

In this context, this thesis aims to propose methodologies allowing the elastic characterization of anisotropic thin films at two different scales (Fig. I.9). The Impulse Excitation Technique (IET) is chosen, regarding its advantages compared with other techniques (Section I.2.2.2), in order to characterize macroscopically thin films. For the microscopic elastic characterization of thin films, the X-ray diffraction is chosen, thanks to its selective nature, to determine the different microstructural properties of the films. The microscopic approach will allow the determination of the elastic behavior of anisotropic thin films by taking into account its corresponding microstructural properties (phases, morphological texture, crystallographic

texture and porosity). These methods will be applied first to thin films in multilayer with isotropic behavior (Chapter II and Chapter III) and then to thin films with anisotropic behavior deposited at oblique incidence (Chapter IV and Chapter V).

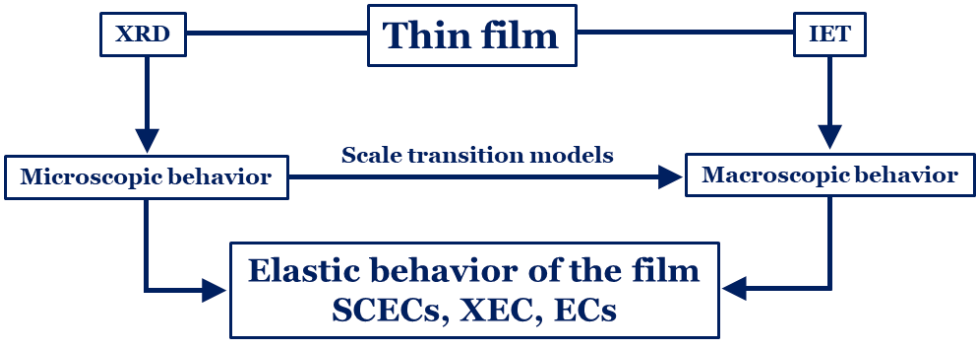

Fig. I.9. Schematic representation of the methodology adopted for the characterization of the elastic behavior of thin films.

I.5. Conclusions

In this first chapter, some generalities on elasticity were briefly introduced with its interest in engineering. The compliance and stiffness tensors of generally anisotropic materials and some others with particular symmetries were illustrated. The determination of the elasticity constants from the compliance and stiffness tensors was also presented.

The experimental methods that are mostly used to determine the elasticity constants of materials were presented. The corresponding issues encountered in the case of thin films were addressed. Several studies show that the elastic behavior of thin films depends on the deposition parameters (Section I.3). Furthermore, a thin film is generally polycrystalline, textured, maybe porous with columnar morphology, and composed of different phases, which give it an anisotropic elastic behavior. Therefore, a multiscale characterization of these elasticity constants is required to predict the anisotropic elastic behavior of thin films.

In order to characterize the anisotropy of thin films, two approaches will be developed during this work. The Impulse Excitation Technique (IET) and the X-ray Diffraction (XRD) will be used for macroscopic and microscopic elastic characterizations, respectively.

Chapter II

Analytical development for the determination of the elasticity constants of multilayer coatings

II.1. Introduction

The Impulse Excitation Technique (IET) is a non-destructive technique that can be easily used to determine the elasticity constants of different types of materials [Atri 1999, Radovic 2004, Gadaud 2004, Gadaud 2009]. Thanks to its high precision and the negligible stress generation, the IET can be used as a new alternative method to determine the Young's and shear moduli of thin films. Several mechanical models were developed to determine the Young's modulus of coatings using the IET. The first one was initiated by Berry [Berry 1975] and then other models were developed based on various theories [Mazot 1998, Gadaud 2004, López-Puerto 2014]. To guide the user in his choice, Slim et al. [Slim 2017a] have studied the difference between the models and their validity range. It can also be mentioned that the Hamilton's principle was applied in the literature to determine coating shear modulus using the IET [Gadaud 2009, Slim 2017b].

For multilayer coatings, several models were developed to determine the Young's modulus of each layer based on the Flexural Rigidity of a Composite Beam (FRGB) [Cho 1999] or the Classical Laminated Beam Theory (CLBT) [López-Puerto 2014]. In these studies, the models were developed by assuming that the thickness of the coating is negligible compared to the thickness of the substrate. Therefore, the determination of the shear modulus of each layer in multilayer coatings cannot be expressed in a closed-form analytical expression. Moreover, concerning the vibrational mode, a lack of information concerning the determination of Young's modulus using different modes measured by IET motivates us to carry out a thorough study and to develop new models, which allow the determination of the elasticity constants of each layer in multilayer coatings.

This chapter aims to extend the previous works by developing new models allowing the determination of the Young's and shear moduli of layers whatever the thickness and the mechanical and physical properties of the substrate and the deposited layers. In order to guide our choice of model, we will proceed as follows: Firstly, the mechanical models existing in the literature are presented for the determination of Young's and shear moduli of a thin film. Then, new models are developed for determining the elasticity constants of multilayer coatings. In the last section, a comparison between the analytical models existing in the literature, the developed models and a developed finite element model (FEM) is performed. This comparison allows us to identify the most reliable model among the analytical models taking the FEM as a reference.

II.2. Review of the analytical models proposed for determining Young's modulus of coatings in a bilayer structure

II.2.1. Theoretical background

For the analysis of the flexural vibrations of a uniform isotropic beam, the Euler-Bernoulli equation is considered, neglecting the effects of shear and rotational inertia. The motion of a beam subjected to flexural vibrations can be described by the following differential equation [Rao 2006]:

$$\rho S \frac{\partial^2 w(x,t)}{\partial t^2} + \frac{\partial^2}{\partial x^2}\left(E I_y \frac{\partial^2 w(x,t)}{\partial x^2} \right) = 0 \qquad \text{(II.1)}$$

Where ρ is the density, $w(x,t)$ is the displacement along the z-axis of a given point belonging to the excited structure as a function of its position x and time t (Fig. II.1), E is the Young's modulus, I_y is the second moment of area with respect to the z-axis of the cross-section and S is the cross-sectional area.

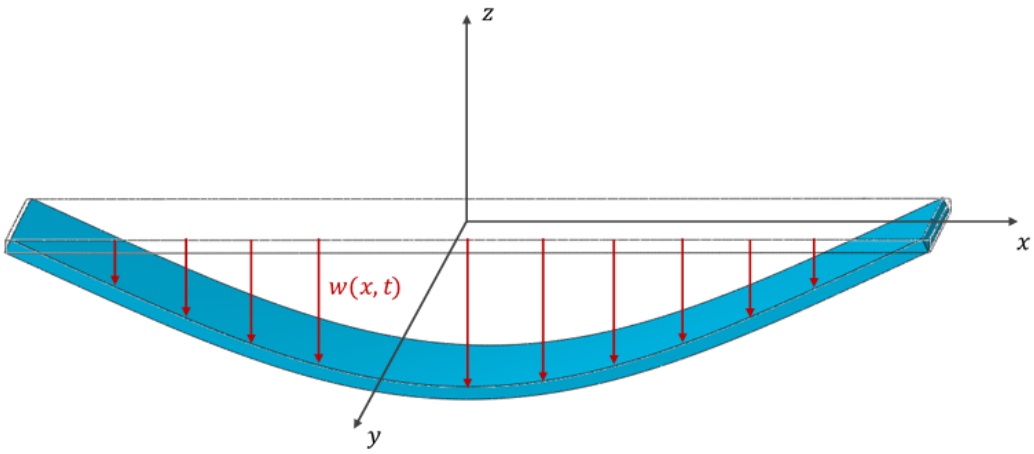

Fig. II.1. Schematic representation of a beam subjected to flexural vibrations.

This differential equation (Eq. (II.1)) can be solved analytically to determine the modal shapes and the natural frequencies of the vibration modes. In the case of IET, free-free (FF) boundary conditions are generally adopted and the characteristic equation corresponding to these boundary conditions is [Rao 2006]:

$$cos\, X_n\, cosh\, X_n - 1 = 0 \tag{II.2}$$

Where X_n is the eigenfrequency corresponding to the n^{th} vibration mode. Using Newton-Raphson method [Walter 2015], Eq. (II.2) was solved and the values of X_n for the first four modes were determined:

$$\begin{pmatrix} X_1 \\ X_2 \\ X_3 \\ X_4 \end{pmatrix} = \begin{pmatrix} 4.73004 \\ 7.85320 \\ 10.9956 \\ 14.1371 \end{pmatrix} \tag{II.3}$$

Thus, the resonance frequencies can be determined from the following equation [Rao 2006]:

$$F^{(n)} = \frac{X_n^2}{2\pi L^2}\sqrt{\frac{EI_y}{\rho S}} \tag{II.4}$$

Where $F^{(n)}$ is the resonance frequency of the n^{th} mode and L is the length of the beam. By inverting Eq. (II.4), the corresponding Young's modulus can be determined from the following expression:

$$E = \left(\frac{2\pi L^2}{X_n^2}\right)^2 \frac{\rho S}{I_y} \left(F^{(n)}\right)^2 \tag{II.5}$$

The IET can be used to determine the Young's modulus, in the case of a FF beam with a rectangular cross-section, according to the following equation [ASTM 2015]:

$$E = k_1 \rho \frac{L^4}{h^2} T_f \left(F^{(1)}\right)^2 \tag{II.6}$$

Where $k_1 \approx 0.9465$, $F^{(1)}$ is the fundamental resonance frequency, h is the thickness. T_f is a geometrical correction factor introduced to take into account the shear and rotary inertia effects, which are not considered in the Euler-Bernoulli theory [ASTM 2015]:

$$T_f = 1 + 6.585(1 + 0.0752\nu + 0.8109\nu^2)\left(\frac{h}{L}\right)^2 - 0.868\left(\frac{h}{L}\right)^4 - \left[\frac{8.34(1 + 0.2023\nu + 2.173\nu^2)\left(\frac{h}{L}\right)^4}{(1 + 6.338(1 + 0.1408\nu + 1.536\nu^2)\left(\frac{h}{L}\right)^2}\right] \quad \text{(II.7)}$$

Where ν is Poisson's ratio. In the case of $h/L \leq 0.05$, Eq. (II.7) can be simplified into the following expression:

$$T_f = 1 + k_2\left(\frac{h}{L}\right)^2 \quad \text{(II.8)}$$

Where $k_2 \approx 6.585$.

In the following sections, a composite beam (substrate + coating) with a rectangular cross-sectional area will be considered. The principle of the measurement is to perform a two-steps frequency measurement before and after deposition. Using the resonance frequencies of the substrate and the composite beam and knowing the density of both substrate and coating and their dimensions, the elasticity constants of the substrate and the film can be determined through mechanical models. The existing mechanical models in the literature are based on two different theories: the flexural rigidity of a composite beam (FRCB) and the classical laminated beam theory (CLBT).

II.2.2. Models based on the Flexural Rigidity of a Composite Beam

The FRCB theory assumes that the coatings are perfectly homogeneous and adherent to the substrate allowing a continuity in terms of deformations between the substrate and the coating. With these assumptions, the flexural rigidity of the entire composite beam can be expressed as the sum of the flexural rigidity of each layer (Eq. (II.9)) [Gere 2003]. Moreover, the product $\rho_t S_t$ is expressed as the summation of the corresponding product of each layer (Eq. (II.10)) [Gere 2003]:

$$E_t I_t = \sum_{k=0}^{N} E_k I_k \quad \text{(II.9)}$$

$$\rho_t S_t = \sum_{k=0}^{N} \rho_k S_k \tag{II.10}$$

Where the subscripts "0", "*k*", "*t*" and "*N*" correspond to substrate, k^{th} layer, whole beam and the total number of layers of coating, respectively. By substituting Eq. (II.9) and Eq. (II.10) into Eq. (II.4), we obtain the n^{th} resonance frequency of the composite beam as follows:

$$F_N^{(n)} = \frac{X_n^2}{2\pi L^2}\sqrt{\frac{E_t I_t}{\rho_t S_t}} \tag{II.11}$$

Many models were developed [Berry 1975, Whiting 1995, Mazot 1998, Gadaud 2004] with analytical expressions for a FF composite beam (substrate + coating) with a rectangular cross-sectional area to determine the Young's modulus of a single layer coating ($N = 1$). Some of these models like Berry and Lopez's models [Berry 1975, Mazot 1998] assumed that the neutral axis remains fixed after deposition (it always corresponds to the mid-plane of the substrate cross-section). With this assumption, no shifting of the neutral surface is considered and a systematic error increases with the film thickness. However, Pautrot's model [Whiting 1995, Mazot 1998, Gadaud 2004] was developed in order to take into account the shift of the neutral axis after deposition (Fig. II.2(a)). The second moments of area of the substrate and the coating were expressed as a function of the shift e_1 presented in Fig. II.2. This shift can be determined using the equilibrium of the axial forces [Gere 2003] generated during pure bending (Fig. II.2(b)) as follows:

$$\int_{-\frac{b}{2}}^{\frac{b}{2}}\int_{-h_0+e_1}^{e_1} \sigma_0 \, dS_0 + \int_{-\frac{b}{2}}^{\frac{b}{2}}\int_{e_1}^{e_1+h_1} \sigma_1 \, dS_1 = 0 \tag{II.12}$$

$$\int_{-h_0+e_1}^{e_1} E_0 \, z \, dz + \int_{e_1}^{e_1+h_1} E_1 \, z \, dz = 0 \tag{II.13}$$

$$e_1 = \frac{E_0 h_0^2 - E_1 h_1^2}{2E_0 h_0 + 2E_1 h_1} \tag{II.14}$$

$$I_0 = \frac{bh_0^3}{12} + bh_0\left(\frac{h_0}{2} - e_1\right)^2 \quad \text{(II.15)}$$

$$I_1 = \frac{bh_1^3}{12} + bh_1\left(e_1 + \frac{h_1}{2}\right)^2 \quad \text{(II.16)}$$

Where b is the width of the cross-section, h_0 is the substrate thickness, h_1 is the film thickness and σ_0 and σ_1 are the stresses in the substrate and the coating respectively.

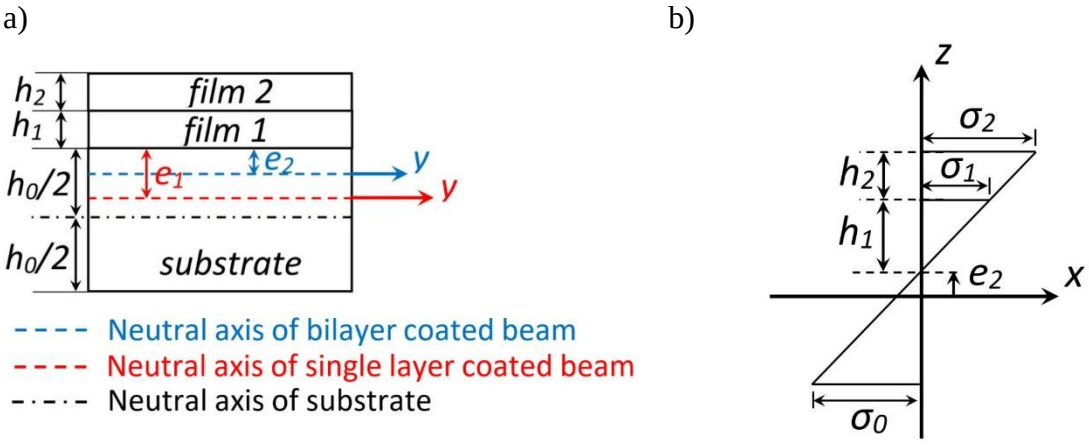

Fig. II.2. Schematic representation of the shift of the neutral axis: a) cross-sectional view, b) stress distribution in a three-layer composite beam.

By substituting Eq. (II.15) and Eq. (II.16) into Eq. (II.11), we obtain the analytical expression developed by Pautrot et al. expressing the ratio of the frequencies of the substrate and the coated substrate [Whiting 1995, Mazot 1998, Gadaud 2004]:

$$(R_{F1})^2 = \frac{(R_{E1}R_{h1}^3 + 1)\,(R_{E1}R_{h1} + 1) + 3R_{E1}R_{h1}(R_{h1} + 1)^2}{(R_{\rho 1}R_{h1} + 1)(R_{E1}R_{h1} + 1)} \quad \text{(II.17)}$$

With:

$$R_{h1} = \frac{h_1}{h_0} \quad \text{(II.18)}$$

$$R_{\rho 1} = \frac{\rho_1}{\rho_0} \quad \text{(II.19)}$$

$$R_{E1} = \frac{E_1}{E_0} \quad \text{(II.20)}$$

$$R_{F1} = \frac{F_1}{F_0} \tag{II.21}$$

Where F_1 is the flexural resonance frequency of the whole bilayer beam and F_0 is the flexural resonance frequency of the uncoated substrate.

Then, by inverting Eq. (II.17), the Young's modulus of the coating can be calculated using the following expression:

$$\begin{aligned} E_1 = \frac{E_0}{2R_{h1}^4}\Big[&\left(R_{h1} + R_{\rho 1}R_{h1}^2\right)\left(R_{f1}\right)^2 - 4R_{h1}^3 - 6R_{h1}^2 - 4R_{h1} \\ &+ \Big(4R_{h1}^4\left[\left(1 + R_{h1}R_{\rho 1}\right)(R_{F1})^2 - 1\right] \\ &+ \left[4R_{h1}^3 + 6R_{h1}^2 + 4R_{h1} - \left(R_{h1} + R_{\rho 1}R_{h1}^2\right)(R_{F1})^2\right]^2\Big)^{0.5}\Big] \end{aligned} \tag{II.22}$$

Whiting et al. [Whiting 1995] have provided a simplified expression for a more direct calculation of the film elastic modulus with further simplification related to the thin film geometry as:

$$E_1 = \frac{E_0}{3}\left[\frac{2R_{F1} + R_{\rho 1}R_{h1} - 2}{R_{h1}}\right] \tag{II.23}$$

Where $R_{h1} << 1$ so that the terms containing powers of R_{h1} greater than one may be neglected. The more general equation, Eq. (II.22), will be employed in this work to increase the accuracy. Note that all the models discussed above, for the resonance frequencies of a bilayer beam (substrate + coating), are based on FRCB of isotropic materials and they neglect material anisotropy and damping contributions, such as material viscoelasticity or other hysteretic effects [Gamboa 2016].

II.2.3. Model based on the Classical Laminated Beam Theory

A simplified one-dimensional (1D) model based on CLBT is proposed herein to determine the Young's modulus of an individual thin film. It fulfills Kirchhoff's law [Hyer 2009] and it is applicable for one, two and multiple layers [Hanada 1989, Ying 2010]. This theory assumes that the beam is symmetrical about the mid-surface of the composite beam with respect to the z-axis (Fig. II.3) and neglects the effect of shear deformations with no coupling

between bending and extension [Hyer 2009, López-Puerto 2014]. These two assumptions are not respected in most cases where the film is deposited on one side of the substrate. However, the model can be used as an approximation in the case of an asymmetric beam of several thin films deposited on a thicker substrate. Certainly, the higher the ratio of Young's moduli and the thicknesses ratio, the higher the error associated with this model is [López-Puerto 2014, Slim 2017a].

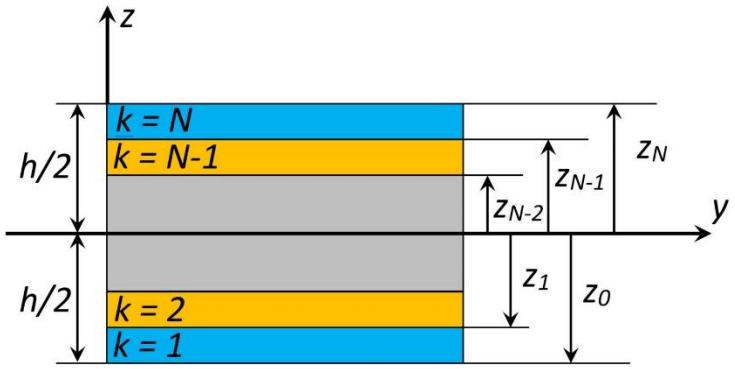

Fig. II.3. Schematic view of a symmetrical laminated beam.

In the case of a beam subjected to FF boundary conditions, the frequency ratio of the laminated beam is expressed as follows [López-Puerto 2014]:

$$(R_{F1})^2 = \frac{12\rho_0}{E_0 h_0^2}\left(\frac{1}{d_{11}\,(\rho_0 h_0 + \rho_1 h_1)}\right) \tag{II.24}$$

In the case of a single layer coating:

$$d_{11} = \frac{\dfrac{E_0 K_0}{1-\nu_0^2} + \dfrac{E_1 K_1}{1-\nu_1^2}}{\left[\dfrac{E_0 K_0}{1-\nu_0^2} + \dfrac{E_1 K_1}{1-\nu_1^2}\right]^2 - \left[\dfrac{\nu_0 E_0 K_0}{1-\nu_0^2} + \dfrac{\nu_1 E_1 K_1}{1-\nu_1^2}\right]^2} \tag{II.25}$$

Where K_0 and K_1 are functions of the layer thicknesses h_0 and h_1 and are defined as:

$$K_0 = \frac{h_0}{4}\left(\frac{h_0^2}{3} + h_1^2\right) \tag{II.26}$$

$$K_1 = \frac{h_1}{4}\left(\frac{h_1^2}{3} + h_0^2\right) \tag{II.27}$$

II.2.4. Models usage with application

In the previous section, the models developed to determine the Young's modulus of a coating in a bilayer structure using the IET were presented. Many researchers have used the IET to test samples of various films with different thicknesses. For instance, Kim et al. [Kim 1997] have used Pautrot's model to determine the Young's modulus of titanium (Ti) film deposited, by radio frequency (RF) magnetron sputtering, on silicon (Si) wafer specimens with different geometries. They have shown that the IET gives accurate results compared to a static method based on beam bending under a dead weight. Peraud et al. [Peraud 1997] have used Berry's model to determine the Young's modulus of 2.2 μm thin silicon carbide (SiC) and 2.5 μm thin nickel-titanium alloy (NiTi) layers performed by the Dynamic Ion Mixing (DIM) method. They have shown that IET allows us to determine the Young's modulus of very thin coatings. Mazot et al. [Mazot 1998] have reported that the Young's modulus calculated using Berry and Lopez's models begins to diverge from a thickness ratio R_h equal to 0.1. The difference between the models also becomes significant in the case of high R_E and R_ρ.

Cho et al. [Cho 1999] have evaluated the Young's modulus of different metallic films: Ni, Co, Cr and Ti thin films deposited by RF magnetron sputtering with different thicknesses on Si wafers. In terms of film thickness variation, they found that the Young's modulus of Ni films decreases as the thickness of the film increases. For Cr and Co films, they did not find any significant difference. Etienne et al. [Etienne 2004] have used Pautrot's model and determined the Young's modulus of titanium nitride (TiN) of 0.2 μm of thickness elaborated by ion implantation. Bellan et al. [Bellan 2004] have evaluated the elasticity constants of 35 μm thick SiC and 95 μm thick Pyrolytic Carbon (PyC) films elaborated by Chemical Vapor Deposition (CVD). They have shown that IET gives good and accurate results. The crystalline thin films are also used in the nanometric range, such as in nano and microelectronic devices [Williams 1992, Ziegele 1997, Romero 2003, Deng 2005]. Hoy-Benítez et al. [Hoy-Benítez 2012] have tested bilayer beams in a cantilever configuration and they measured the Young's modulus of gold (Au) films of 100 *nm* thickness deposited on polysulfone (PSF) substrates of 130 μm of thickness. They found similar results to those reported in the literature.

Several researches have already been performed using the CLBT model in order to determine the Young's modulus of thin films [López-Puerto 2014, Slim 2017a]. By comparing the CLBT model to a FEM, López-Puerto et al. found that the CLBT model is limited to a film

thickness of 250 *nm* (R_{h1} < 0.002). A recent study [Slim 2017a] shows that the minimal error zone associated with the CLBT model is centered at Young's modulus ratio equal to 1. This is due to the assumption of symmetry on which is based the CLBT model. It found that Pautrot's model presents results, which are the closest to FEM. In order to identify the most suitable model for determining the Young's modulus, a parametric comparison between the analytical models and a FEM was made [Slim 2017a]. It noticed that Pautrot's model is the most suitable model to determine the Young's modulus. The good agreement between Pautrot's model and FEM confirms that the shift of the neutral axis after deposition is an important factor affecting the solution, and it should be taken into account in the development. It was applied to determine the Young's modulus of Al and W thin films by means of the IET [Slim 2017a, Slim 2017b].

II.3. Review of the analytical models proposed for determining shear modulus of coatings in a bilayer structure

II.3.1. Theoretical background

The torsional equation of beams with a rectangular cross-section was developed by Timoshenko and Goodier [Timoshenko 1951] and Spinner and Tefft [Spinner 1961]. The differential equation that describes the motion of a beam with a rectangular cross-section, subjected to torsional vibrations (Fig. II.4) can be written as follows [Rao 2006]:

$$\rho I_p \frac{\partial^2 \theta(x,t)}{\partial t^2} - \frac{\partial^2}{\partial t \partial x}\left(\rho I_\psi \frac{\partial^2 \theta(x,t)}{\partial x \partial t}\right) - \frac{\partial}{\partial x}\left(C \frac{\partial \theta(x,t)}{\partial x}\right) + \frac{\partial^2}{\partial x^2}\left(E I_\psi \frac{\partial^2 \theta(x,t)}{\partial x^2}\right) = 0 \quad \text{(II.28)}$$

Where ρ is the density, $\theta(x,t)$ is the angular displacement of a given point depending on its position *x* and time *t*, *E* is the Young's modulus. The parameter I_ψ is defined by:

$$I_\psi = \int_S \psi(y,z)^2 dS \quad \text{(II.29)}$$

Where $\psi(y,z)$ is known as the warping function describing the warping of the beam section. The polar moment of inertia of the cross-section I_p is defined by:

$$I_p = \int_S (y^2 + z^2) dS = \frac{hb^3 + bh^3}{12} \tag{II.30}$$

The torsional rigidity C of a rectangular cross-section is defined by:

$$C = \iint_S G\left[\left(\frac{\partial \psi}{\partial y} - z\right)^2 + \left(\frac{\partial \psi}{\partial z} + y\right)^2\right] dS \tag{II.31}$$

With G the shear modulus.

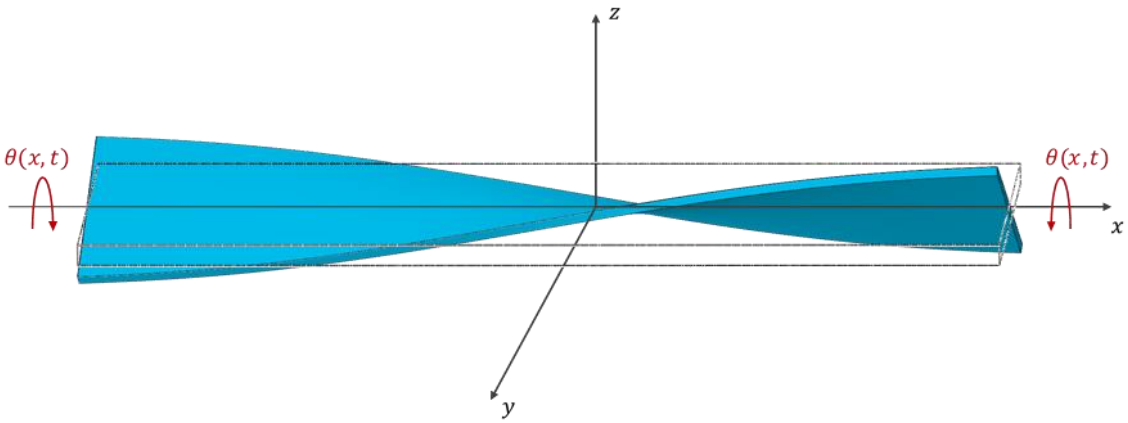

Fig. II.4. Schematic representation of a beam subjected to torsional vibrations.

In the case of a free-free beam with a rectangular cross-section, the shear modulus can be determined from the following equation [ASTM 2015]:

$$G = 4\rho R L^2 T^2 \tag{II.32}$$

Where T is the fundamental torsional resonance frequency of the beam and R is the shape factor that takes into account the warping of the beam. R is expressed as a function of the dimensions of the beam as follows:

$$R = \left[\frac{1 + \left(\frac{b}{h_0}\right)^2}{4 - 2.521\frac{h_0}{b}\left(1 - \frac{1.991}{e^{\pi\frac{b}{h_0}} + 1}\right)}\right] \cdot \left[1 + \frac{0.00851 b^2}{L^2}\right] - 0.060\left(\frac{b}{L}\right)^{\frac{3}{2}}\left(\frac{b}{h_0} - 1\right)^2 \tag{II.33}$$

II.3.2. Models based on Hamilton's principle

II.3.2.1. Homogeneous beam (uncoated substrate)

The existing mechanical models in the literature for torsional vibrations are based on Hamilton's principle [Berdichevsky 2009]. This principle lies in the minimization of the Lagrangian of the system, which is expressed as a function of the kinetic and potential energies of the structure subjected to vibrations.

In the case of a beam with a rectangular cross-section subjected to torsional vibrations, the warping function $\psi(y,z)$ is used to denote the axial displacement. However, for beams satisfying the condition $h_0 \ll b$, the warping function should be simplified and this depends only on y as [Timoshenko 1951, Laroze 1974, Rao 2006]:

$$u = z\,\psi(y)\frac{\partial\theta(x,t)}{\partial x} \tag{II.34}$$

The other two displacement components can be expressed as follows:

$$v = -z\,\theta(x,t) \tag{II.35}$$

$$w = y\,\theta(x,t) \tag{II.36}$$

The strain components can be defined from the displacement components mentioned above as follows:

$$\varepsilon_{xx} = \frac{\partial u}{\partial x} = z\,\psi(y)\frac{\partial^2\theta}{\partial x^2} \tag{II.37}$$

$$\varepsilon_{xy} = \frac{\partial u}{\partial y} + \frac{\partial v}{\partial x} = \left(\frac{\partial\psi}{\partial y} - 1\right) z\frac{\partial\theta}{\partial x} \tag{II.38}$$

$$\varepsilon_{xz} = (\psi + y)\frac{\partial\theta}{\partial x} \tag{II.39}$$

When $L \gg h_0$, the strain component along the x-axis can be neglected. Besides, the Lagrangian of a homogeneous beam can be written as a function of the kinetic and potential energies of the beam (uncoated substrate) as follows [Géradin 1994, Gadaud 2009, Slim 2017b, Slim 2018]:

$$L = \frac{1}{2}\int_{-\frac{L}{2}}^{\frac{L}{2}}\int_{-\frac{b}{2}}^{\frac{b}{2}}\int_{-\frac{h_0}{2}}^{\frac{h_0}{2}} G_0\left(\frac{\partial\theta}{\partial x}\right)^2\left[\left(\frac{\partial\psi}{\partial y}-1\right)^2 z^2+(\psi+y)^2\right]dx\,dy\,dz - \int_{-\frac{L}{2}}^{\frac{L}{2}}\int_{-\frac{b}{2}}^{\frac{b}{2}}\int_{-\frac{h_0}{2}}^{\frac{h_0}{2}} \rho_0(2\pi T_0)^2\theta^2(y^2+z^2)\,dx\,dy\,dz \quad \text{(II.40)}$$

Applying Hamilton's principle, which is based on the minimization of the Lagrangian of the system, the warping function as well as the torsional resonance frequency of the beam can be determined [Gadaud 2009, Slim 2017b, Slim 2018]:

$$\psi(y) = -y + \frac{h_0 \sinh\left(\frac{2\sqrt{3}y}{h_0}\right)}{\sqrt{3}\cosh\left(\frac{\sqrt{3}b}{h_0}\right)} \quad \text{(II.41)}$$

$$T_0 = \frac{1}{2L}\sqrt{\frac{K_{t1}}{K_{t2}}}\sqrt{\frac{G_0}{\rho_0}} \quad \text{(II.42)}$$

With:

$$K_{t1} = \frac{h_0^3}{3}\left[b - \frac{h_0}{\sqrt{3}}\tanh\left(\frac{\sqrt{3}b}{h_0}\right)\right] \quad \text{(II.43)}$$

$$K_{t2} = \frac{bh_0}{12}(b^2+h_0^2) \quad \text{(II.44)}$$

In the case of torsional vibrations of a bilayer beam, the principle of the measurement is the same as for the case of flexural vibrations. Two torsional frequency measurements are performed: the first one for the substrate before deposition and the second one for the bilayer structure (substrate + coating). Then, using a mechanical model that involves the ratios between the two resonance frequencies, the Young's moduli, densities and dimensions of the substrate and the film, and the shear modulus of the uncoated substrate, we can retrieve the value of the shear modulus of the deposited film.

II.3.2.2. Gadaud's model

By applying the Hamilton's principle, Gadaud et al. [Gadaud 2009] have developed an analytical model (Eq. (II.45)) in order to determine the shear modulus of the film deposited on a beam substrate with a rectangular cross-section using the IET:

$$(R_{T1})^2 \approx \frac{1 + R_{G1}R_{h1}\left(3 - \frac{h_0}{b\sqrt{3}}\right)}{1 + R_{\rho 1}R_{h1}\left(\frac{b^2 + 3h_0^2}{b^2 + h_0^2}\right)} \tag{II.45}$$

With:

$$R_{T1} = \frac{T_1}{T_0} \tag{II.46}$$

Where T_1 is the fundamental torsional resonance frequency of the whole bilayer beam and T_0 is the fundamental torsional resonance frequency of the uncoated substrate.

This model supposes that the thickness of the coating is very small, compared to that of the substrate. In addition, this model does not take into account the shift of the neutral axis due to the coating (Fig. II.2). Therefore, the error derived from Gadaud's model (Eq. (II.45)) increases with the rise of the thickness, density, Young's and shear moduli ratios because of this assumption.

II.3.2.3. Slim's model

After deposition, the neutral axis does not remain at the mid thickness of the substrate due to the addition of different film material. In order to decrease the error derived from Gadaud's model (Eq. (II.45)), Slim et al. [Slim 2017b] have developed an enhanced model that takes into account the shift of the neutral axis after deposition. The shift e_1 (Eq.(II.14)) is integrated for the determination of the torsional resonance frequency of the composite beam (substrate + coating). The Lagrangian of the composite system, to be minimized, can then be written as follows [Slim 2017b]:

$$
\begin{aligned}
L = \frac{1}{2}\int_{-\frac{L}{2}}^{\frac{L}{2}}\int_{-\frac{b}{2}}^{\frac{b}{2}}\int_{-h_0+e_1}^{e_1} G_0\left(\frac{\partial\theta}{\partial x}\right)^2\left[\left(\frac{\partial\psi}{\partial y}-1\right)^2 z^2+(\psi+y)^2\right]dx\,dy\,dz \\
+\frac{1}{2}\int_{-\frac{L}{2}}^{\frac{L}{2}}\int_{-\frac{b}{2}}^{\frac{b}{2}}\int_{e_1}^{e_1+h_1} G_1\left(\frac{\partial\theta}{\partial x}\right)^2\left[\left(\frac{\partial\psi}{\partial y}-1\right)^2 z^2+(\psi+y)^2\right]dx\,dy\,dz \\
-\int_{-\frac{L}{2}}^{\frac{L}{2}}\int_{-\frac{b}{2}}^{\frac{b}{2}}\int_{-h_0+e_1}^{e_1} \rho_0(2\pi T_1)^2\theta^2(y^2+z^2)\,dx\,dy\,dz \\
-\int_{-\frac{L}{2}}^{\frac{L}{2}}\int_{-\frac{b}{2}}^{\frac{b}{2}}\int_{e_1}^{e_1+h_1} \rho_1(2\pi T_1)^2\theta^2(y^2+z^2)\,dx\,dy\,dz
\end{aligned}
\tag{II.47}
$$

Applying Hamilton's principle as for the case of the uncoated substrate, the torsional resonance frequency ratio can be written [Slim 2017b, Slim 2018]:

$$
R_{T1} = \left[\frac{\rho_0\, b\,(h_0^2+b^2)}{3\,G_0\,h_0^2\left(b-\frac{h_0}{\sqrt{3}}\tanh\left[\frac{\sqrt{3}\,b}{h_0}\right]\right)}\right]^{0.5}\left[\frac{\left[A\left(3bCH_3(h_0E_0+h_1\,E_1)-H_4\sqrt{3A}\right)\right]}{\left[\left(bCH_3(h_0E_0+h_1E_1)(H_1\rho_0h_0+H_2\rho_1h_1)\right)\right]}\right]^{0.5} \tag{II.48}
$$

Where:

$$
\begin{aligned}
A = E_0^2h_0^5G_0 + E_1^2h_1^5G_1 + E_0h_0^4h_1(2E_1G_0+3E_0G_1) + E_1h_0h_1^4(2E_0G_1+3E_1G_0) \\
+ 2h_0^3h_1^2(3E_0^2G_1+2E_1^2G_0) + 2h_0^2h_1^3(2E_0^2G_1+3E_1^2G_0)
\end{aligned}
\tag{II.49}
$$

$$
B = 2\sqrt{3}\;b\;C\;(E_0\;h_0+E_1\;h_1) \tag{II.50}
$$

$$
C = \sqrt{G_0\;h_0+G_1\;h_1} \tag{II.51}
$$

$$
H_1 = 3h_0^3E_0^2(h_0+2h_1)+E_1h_1(b^2+h_1^2)(2h_0E_0+E_1h_1)+E_0^2h_0^2(b^2+4h_1^2) \tag{II.52}
$$

$$
H_2 = 3h_1^3E_1^2(h_1+2h_0)+E_0h_0(b^2+h_0^2)(2h_1E_1+E_0h_0)+E_1^2h_1^2(b^2+4h_0^2) \tag{II.53}
$$

$$
H_3 = \frac{B}{e^{\sqrt{A}}+1} \tag{II.54}
$$

$$
H_4 = \frac{B}{e^{\sqrt{A}}-1} \tag{II.55}
$$

Using Eq. (II.48) to Eq. (II.55), the shear modulus of an isotropic thin film can be determined.

II.3.3. Models usage with application

Gadaud et al. [Gadaud 2009] used their model (Eq. (II.45)) with IET to test several bulk isotropic materials. In addition, the model was applied to determine the shear modulus of NiO oxides layers grown on Ni substrates. The validation of this model was performed by comparing the Poisson's ratio deduced from the literature to the one calculated from the measured Young's and shear moduli assuming isotropic behavior of the coating. A coherence in terms of Poisson's ratio was obtained [Gadaud 2009].

Besides, Slim's model [Slim 2017b] was applied to determine the shear modulus of tungsten films deposited on glass substrates. A good agreement between the obtained shear modulus and the ones reported in the literature was obtained. It was concluded that the difference between the Poisson's ratios of two different tested samples measured by IET is lower than the measurement uncertainties. This difference was due to the measurement uncertainty on the elasticity constants and to the presence of a W_β phase in the film structure.

In the following section, an analytical development applied to multilayer-coated beams will be presented. The new models were developed by describing the behavior of multilayer beams in flexural and torsional vibration modes. They were developed based on the theories presented above, taking into account the shift of the neutral axis after coating deposition.

II.4. Development of new analytical models to determine the elasticity constants of coatings in a multilayer structure

A composite beam with rectangular cross-sectional area and a total thickness h_t constituted of a substrate and N dissimilar coatings is considered (Fig. II.5(a)). Each layer is indicated by the index k (k = 1, …, N) as shown in Fig. II.5(b). The index k = 0 denotes the naked substrate. In the case of a multilayer structure, the vibrational measurements are conducted sequentially, first for the substrate, then after each deposited film. This order of measurements requires the determination of the elasticity constants of the k^{th} film (k > 0) before depositing the following one $(k+1)^{th}$. Using the sample frequencies, the density and dimensions of the substrate and the coating, the elasticity constants of the substrate and each film can be

determined through mechanical models. Two mechanical models were developed to determine the Young's modulus of each film in a multilayer structure. They are based on two different theories: the flexural rigidity of a composite beam (FRCB) and the classical laminated beam theory (CLBT). In addition, based on Hamilton's principle, a new model was developed to determine the shear modulus of each film.

a) b)

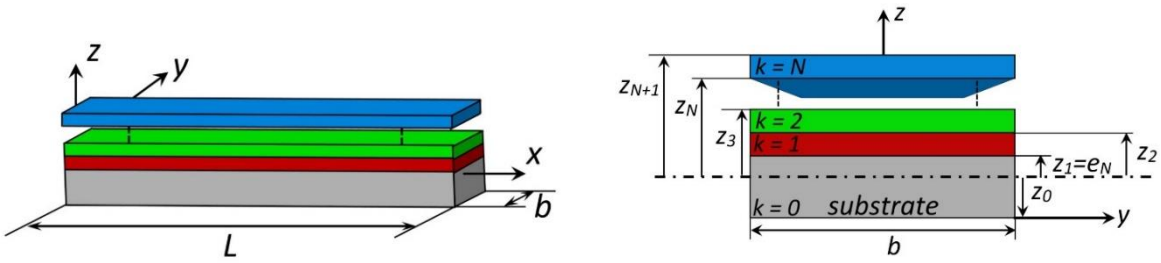

Fig. II.5. Schematic representation of a multilayer beam: a) free configuration of a multilayer beam and b) The z-coordinates of each layer in a cross-sectional view.

II.4.1. Extended Pautrot's model (Ext-PM)

As Pautrot's model is approved to reliably determine the Young's modulus of single-layer coatings, it was extended to develop the new model, where the neutral axis will shift after each layer deposited. This shift can be generalized for any number "*N*" of isotropic layers using a generalized equation of equilibrium of the axial forces as follows:

$$\sum_{k=0}^{N} \iint \sigma_k dS_k = \int_{-h_0+e_N}^{e_N} E_0\, z\, dz + \sum_{k=1}^{N} \int_{Z_1}^{Z_2} E_k\, z\, dz = 0 \tag{II.56}$$

With:

$$Z_1 = e_N + \delta_k \sum_{j=1}^{k-1} h_j \qquad \delta_k = \begin{cases} 0 & if\ k = 1 \\ 1 & if\ k \neq 1 \end{cases} \quad (k = 1, \dots, N)$$
$$Z_2 = Z_1 + h_k \tag{II.57}$$

By integrating Eq. (II.56) and applying the static equilibrium of a beam in pure bending, the generalized shift e_N becomes:

$$e_N = \frac{E_0 h_0^2 - \sum_{i=1}^{N} E_i h_i \left[h_i + 2\delta_i \sum_{j=2}^{i} h_{j-1}\right]}{2 \sum_{i=0}^{N} E_i h_i} \tag{II.58}$$

Developing Eq. (II.11) by taking into consideration the shift (e_2) of a bi-coated beam (N = 2) in the expressions of second moments of inertia of both substrate and coating of Eq. (II.9), we obtain the new analytical expression developed herein, expressing the ratio of the frequencies of the substrate and the bi-coated substrate:

$$(R_{F2})^2 = \frac{1 + (R_{h1}^2 R_{E1})^2 + (R_{h2}^2 R_{E2})^2 + 2X_1 R_{E1} R_{h1} + 2X_2 R_{E2} R_{h2}}{(1 + R_{h1} R_{\rho 1} + R_{h2} R_{\rho 2})(1 + R_{E1} R_{h1} + R_{E2} R_{h2})} \quad \text{(II.59)}$$

With:

$$R_{h2} = \frac{h_2}{h_0} \quad \text{(II.60)}$$

$$R_{\rho 2} = \frac{\rho_2}{\rho_0} \quad \text{(II.61)}$$

$$R_{E2} = \frac{E_2}{E_0} \quad \text{(II.62)}$$

$$R_{F2} = \frac{F_2}{F_0} \quad \text{(II.63)}$$

$$X_1 = 2 + 6R_{h1}(R_{h1} + R_{h2} + 1) + R_{h2}(3 + 2R_{h2}) \quad \text{(II.64)}$$

$$X_2 = R_{E2} R_{h2}(2R_{h1}^2 + 3R_{h1} R_{h2} + 2R_{h2}^2) + 2R_{h1}^2 + 3R_{h1} + 2 \quad \text{(II.65)}$$

Knowing the thicknesses and the densities of the substrate and the two films, the Young's moduli of the substrate and the first film, and by inverting Eq. (II.59), the Young's modulus of the second film is determined using the following equation:

$$E_2 = \frac{-b_1 + \sqrt{b_1^2 - 4a_1 c_1}}{2a_1} \quad \text{(II.66)}$$

Where:

$$a_1 = R_{h2}^4 \quad \text{(II.67)}$$

$$b_1 = 4R_{h2}^3(1 + R_{E1}R_{h1}) + R_{h2}^2\left[6 - R_{\rho 2}\left(R_{f2}\right)^2 + 6R_{h1}(2 + R_{E1}R_{h1})\right] + R_{h2}\left[4 - \left(R_{f2}\right)^2 + 4R_{h1}^2(3 + R_{E1}R_{h1}) + R_{h1}\left[12 - R_{\rho 1}(R_{F2})^2\right]\right] \quad \text{(II.68)}$$

$$c_1 = 1 - (1 + R_{E1}R_{h1})\left(1 + R_{\rho 1}R_{h1} + R_{\rho 2}R_{h2}\right)(R_{F2})^2 + R_{E1}R_{h1}(4 + 6R_{h1} + 4R_{h1}^2 + R_{E1}R_{h1}^3) \quad \text{(II.69)}$$

II.4.2. Enhancement of the CLBT model (Dev-CLBT)

As in the case of single-layer coated beams, the CLBT model can be used to determine the Young's modulus of the k^{th} layer (E_k) if the elastic modulus of the (k-1)th, (k-2)th, …, 1st layers are known. For instance, in a bi-coated isotropic beam structure, the 3×3 bending stiffness matrix D_{ij} is defined in Eq. (II.70) with N = 2 [Hyer 2009]:

$$D_{ij} = \int_{z_{k-1}}^{z_k} \bar{Q}_{ij}^{(k)} z^2 dz = \frac{1}{3}\sum_{k=1}^{N+1} \bar{Q}_{ij}^{(k)}(z_k^3 - z_{k-1}^3) \qquad \begin{cases} i,j = 1,2\ or\ 6 \\ k = 1,\dots,N+1 \end{cases} \quad \text{(II.70)}$$

Where z_k is the coordinate of the k^{th} layer and $\bar{Q}_{ij}^{(k)}$ are the transformed reduced stiffness elements. $\bar{Q}_{ij}^{(k)}$ are a function of the reduced stiffness including information on elastic modulus, Poisson's ratio, and the orientation (θ_k) of the k^{th} layer [Hyer 2009, López-Puerto 2014]. Working with the x-y axes as principal axes for both substrate and film leads to obtain a zero-layer orientation (θ_k = 0) [López-Puerto 2014].

The enhancement of the CLBT model is performed herein for "N" dissimilar layers; assuming that the neutral axis will shift after deposition using the shift of Eq. (II.58) and the following new 3×3 bending stiffness matrix:

$$D'_{ij} = \int_{-h_0+e_N}^{e_N} \bar{Q}_{ij}^{(0)} z^2 dz + \sum_{k=1}^{N} \int_{Z_1}^{Z_2} \bar{Q}_{ij}^{(k)} z^2 dz \qquad (i,j = 1,2\ or\ 6) \quad \text{(II.71)}$$

Where Z_1 and Z_2 are given in Eq. (II.57). For isotropic substrate and film materials, the stiffness elements become:

$$\bar{Q}_{11}^{(k)} = \bar{Q}_{22}^{(k)} = Q_{11}^{(k)} = Q_{22}^{(k)} = \frac{E_k}{1-(\nu_k)^2} \tag{II.72}$$

$$\bar{Q}_{12}^{(k)} = Q_{12}^{(k)} = \frac{\nu_k E_k}{1-(\nu_k)^2} \tag{II.73}$$

$$\bar{Q}_{16}^{(k)} = \bar{Q}_{26}^{(k)} = 0 \tag{II.74}$$

$$\bar{Q}_{66}^{(k)} = Q_{66}^{(k)} = \frac{E_k}{2\,(1+\nu_k)} \tag{II.75}$$

Where E_k and υ_k are respectively the Young's modulus and Poisson's ratio of the k^{th} layer. The flexural moment per unit width M_y, producing transverse *w* deflections can be expressed in terms of the curvature as [Hyer 2009]:

$$M_y = -\frac{1}{d_{11}^N}\frac{\partial^2 w}{\partial x^2} \tag{II.76}$$

Where d_{11} is the (1,1) element of the bending matrix $[d]=[D]^{-1}$. For a symmetrical laminated beam, d_{11} can be expressed as:

$$d_{11}^{(N)} = \frac{D_{22}}{det[D]} \tag{II.77}$$

$$det[D] = D_{11}D_{22} - D_{12}^2 \tag{II.78}$$

Where $det[D]$ is the determinant of the matrix D_{ij}. The vibrating laminated beam subjected to a flexural moment M_y with transverse displacements *w* can be expressed, according to CLBT, by the following equation [López-Puerto 2014]:

$$\frac{\partial^2 M_y}{\partial x^2} = \rho_{eff}^{(N)}\frac{\partial^2 w}{\partial t^2} \tag{II.79}$$

Where ρ_{eff} is the weighted area density (in kg/m^2) expressed as:

$$\rho_{eff}^{(N)} = \int_{-(\sum_{k=0}^{N} h_k)/2}^{(\sum_{k=0}^{N} h_k)/2} \rho_k dz = \sum_{k=0}^{N} \rho_k h_k \tag{II.80}$$

By substituting Eq. (II.76) into Eq. (II.79), the following differential equation of the transverse vibration of a symmetric laminated beam is obtained:

$$\frac{1}{d_{11}^{(N)} \rho_{eff}^{(N)}} \frac{\partial^4 w}{\partial x^4} + \frac{\partial^2 w}{\partial t^2} = 0 \tag{II.81}$$

Where the term d_{11} contains the properties of each layer (Young's modulus, Poisson's ratio and thickness). Notice that Eq. (II.81) has the same form as Eq. (II.1) for a homogeneous isotropic beam when carrying out the following transformations:

$$E_0 \rightarrow \frac{12}{h_0^3 d_{11}^{(N)}} \tag{II.82}$$

$$\rho_0 \rightarrow \frac{\rho_{eff}^{(N)}}{h_0} \tag{II.83}$$

By substituting Eqs. (II.82) and (II.83) into Eq. (II.4), the resonance frequencies of a laminated beam can be expressed as:

$$F_N^{(n)} = \frac{X_n^2}{2\pi L^2} \sqrt{\frac{1}{d_{11}^{(N)} \rho_{eff}^{(N)}}} \tag{II.84}$$

The frequency ratio becomes:

$$\left(R_{F(N)}\right)^2 = \frac{12\rho_0}{E_0 h_0^2} \left(\frac{1}{d_{11}^{(N)} \rho_{eff}^{(N)}} \right) \tag{II.85}$$

Using Eq. (II.85) with N = 1, we can obtain the frequency ratio for a single layer coated beam (Eq. (II.24)). Inverting the new sub-matrix D'_{ij} of Eq. (II.71) for the case of a bi-coated (N = 2) isotropic beam and applying the expression of d_{11} from Eq. (II.77), the newR_0, R_1 and R_2 functions of the thicknesses and the shift e_2, are determined as:

$$d_{11}^{(2)} = \frac{\frac{E_0 R_0}{1-\nu_0^2} + \frac{E_1 R_1}{1-\nu_1^2} + \frac{E_2 R_2}{1-\nu_2^2}}{\left[\frac{E_0 R_0}{1-\nu_0^2} + \frac{E_1 R_1}{1-\nu_1^2} + \frac{E_2 R_2}{1-\nu_2^2}\right]^2 - \left[\frac{\nu_0 E_0 R_0}{1-\nu_0^2} + \frac{\nu_1 E_1 R_1}{1-\nu_1^2} + \frac{\nu_2 E_2 R_2}{1-\nu_2^2}\right]^2} \quad \text{(II.86)}$$

With:

$$R_0 = \frac{h_0^3}{3} - e_2 h_0^2 + e_2^2 h_0 \quad \text{(II.87)}$$

$$R_1 = \frac{h_1^3}{3} + e_2 h_1^2 + e_2^2 h_1 \quad \text{(II.88)}$$

$$R_2 = \frac{h_2^3}{3} + (e_2 + h_1)(e_2 + h_1 + h_2)h_2 \quad \text{(II.89)}$$

The frequency ratio of a laminated beam is expressed using Eq. (II.85) with the new expressions of D'_{ij} and d_{11} from Eq. (II.71) and Eq. (II.86), respectively. This expression is an implicit function. Therefore, in order to determine the solution, an iteration loop is applied using bisection method [Walter 2015]. The unknown elastic modulus of the second film (E_2) is then found.

For bilayer coatings, López-Puerto et al. [López-Puerto 2014] proved that the solution depends on the stacking sequence selected (Au / Al / Kapton or Al / Au / Kapton) because the lack of symmetry can lead to large errors (> 1.3%) in the prediction of the frequency of a multi-coated beam using CLBT. Therefore, the developed models, based on the two different theories (FRCB and CLBT), will be examined by comparing them to a numerical model based on Finite Element Model (FEM) in order to quantitatively analyze the difference between them. An outline of the analytical models proposed in the literature and the models developed in the present chapter is presented in Table II.1.

Table II.1
Summary of the analytical models.

Model	Theory	Nb. of layers	Assumptions
Lopez [Mazot 1998]	FRCB	Bilayer	Isotropy
Berry [Berry 1975]	FRCB	Bilayer	Simplification of Lopez's model
Pautrot [Gadaud 2004]	FRCB	Bilayer	Isotropy & Shift
Whiting [Whiting 1995]	FRCB	Bilayer	Simplification of Pautrot's model
CLBT [López-Puerto 2014]	CLBT	Multilayer	Symmetry & Anisotropy
Extended Pautrot (Ext-PM) [Present Work]	FRCB	Multilayer	Isotropy & Shift
Developed CLBT (Dev-CLBT) [Present Work]	CLBT	Multilayer	Symmetry, Anisotropy & Shift

II.4.3. Extended Slim's model (Ext-Slim)

Hamilton's principle can also be applied for isotropic multilayer beam by extending Slim's model. The same development as that performed for a single layer coated beam was applied to obtain an extension to a multilayer beam. This extension allowed us to determine the shear modulus of each film.

For multilayer beam subjected to torsional vibrations, the Lagrangian is expressed as:

$$
\begin{aligned}
L = \frac{1}{2}\int_{-\frac{L}{2}}^{\frac{L}{2}}\int_{-\frac{b}{2}}^{\frac{b}{2}}\int_{-h_0+e_N}^{e_N} G_0\left(\frac{\partial\theta}{\partial x}\right)^2\left[\left(\frac{\partial\psi}{\partial y}-1\right)^2 z^2+(\psi+y)^2\right]dx\,dy\,dz \\
+\frac{1}{2}\sum_{k=1}^{N}\int_{-\frac{L}{2}}^{\frac{L}{2}}\int_{-\frac{b}{2}}^{\frac{b}{2}}\int_{Z_1}^{Z_2} G_k\left(\frac{\partial\theta}{\partial x}\right)^2\left[\left(\frac{\partial\psi}{\partial y}-1\right)^2 z^2+(\psi+y)^2\right]dx\,dy\,dz \\
-\int_{-\frac{L}{2}}^{\frac{L}{2}}\int_{-\frac{b}{2}}^{\frac{b}{2}}\int_{-h_0+e_N}^{e_N}\rho_0(2\pi T_N)^2\theta^2(y^2+z^2)\,dx\,dy\,dz \\
-\sum_{k=1}^{N}\int_{-\frac{L}{2}}^{\frac{L}{2}}\int_{-\frac{b}{2}}^{\frac{b}{2}}\int_{Z_1}^{Z_2}\rho_k(2\pi T_k)^2\theta^2(y^2+z^2)\,dx\,dy\,dz
\end{aligned}
\tag{II.90}
$$

Where Z_1 and Z_2 are given in Eq. (II.57). By integrating Eq. (II.90) with respect to the z-axis and applying it to a bilayer coating beam (N = 2), we obtain:

$$
\begin{aligned}
L = & \frac{1}{2}\int_{-\frac{L}{2}}^{\frac{L}{2}}\int_{-\frac{b}{2}}^{\frac{b}{2}} G_0\left(\frac{\partial\theta}{\partial x}\right)^2\left[R_0\left(\frac{\partial\psi}{\partial y}-1\right)^2+h_0(\psi+y)^2\right]dx\,dy \\
& +\frac{1}{2}\int_{-\frac{L}{2}}^{\frac{L}{2}}\int_{-\frac{b}{2}}^{\frac{b}{2}} G_1\left(\frac{\partial\theta}{\partial x}\right)^2\left[R_1\left(\frac{\partial\psi}{\partial y}-1\right)^2+h_1(\psi+y)^2\right]dx\,dy \\
& +\frac{1}{2}\int_{-\frac{L}{2}}^{\frac{L}{2}}\int_{-\frac{b}{2}}^{\frac{b}{2}} G_2\left(\frac{\partial\theta}{\partial x}\right)^2\left[R_2\left(\frac{\partial\psi}{\partial y}-1\right)^2+h_2(\psi+y)^2\right]dx\,dy \\
& -\int_{-\frac{L}{2}}^{\frac{L}{2}}\int_{-\frac{b}{2}}^{\frac{b}{2}} \rho_0(2\pi T_2)^2\theta^2(h_0\,y^2+R_0)\,dx\,dy \\
& -\int_{-\frac{L}{2}}^{\frac{L}{2}}\int_{-\frac{b}{2}}^{\frac{b}{2}} \rho_1(2\pi T_2)^2\theta^2(h_1\,y^2+R_1)\,dx\,dy \\
& -\int_{-\frac{L}{2}}^{\frac{L}{2}}\int_{-\frac{b}{2}}^{\frac{b}{2}} \rho_2(2\pi T_2)^2\theta^2(h_2\,y^2+R_2)\,dx\,dy
\end{aligned}
\tag{II.91}
$$

Where R_0, R_1 and R_2 are given in Eqs. (II.87), (II.88) and (II.89) respectively. The Hamilton's principle implies that the warping function $\psi(y)$ should minimize the potential energy of the system. The variation of the corresponding potential energy should be zero:

$$
\begin{aligned}
\delta\pi_p = & \frac{1}{2}\delta\left[\int_{-\frac{L}{2}}^{\frac{L}{2}} G_0\left(\frac{\partial\theta}{\partial x}\right)^2 dx \int_{-\frac{b}{2}}^{\frac{b}{2}}\left[R_0\left(\frac{\partial\psi}{\partial y}-1\right)^2+h_0(\psi+y)^2\right]dy\right] \\
& +\frac{1}{2}\delta\left[\int_{-\frac{L}{2}}^{\frac{L}{2}} G_1\left(\frac{\partial\theta}{\partial x}\right)^2 dx \int_{-\frac{b}{2}}^{\frac{b}{2}}\left[R_1\left(\frac{\partial\psi}{\partial y}-1\right)^2+h_1(\psi+y)^2\right]dy\right] \\
& +\frac{1}{2}\delta\left[\int_{-\frac{L}{2}}^{\frac{L}{2}} G_2\left(\frac{\partial\theta}{\partial x}\right)^2 dx \int_{-\frac{b}{2}}^{\frac{b}{2}}\left[R_2\left(\frac{\partial\psi}{\partial y}-1\right)^2+h_2(\psi+y)^2\right]dy\right] = 0
\end{aligned}
\tag{II.92}
$$

By solving Eq. (II.92) as for the case of a single-layer coated beam [Gadaud 2009, Slim 2018], the warping function $\psi(y)$ can be determined:

$$\psi(y) = -y + \frac{\sqrt{A'}\exp\left[\frac{B'}{\sqrt{A'}}\left(\frac{1}{2}-\frac{y}{b}\right)\right]\left(-1+\exp\left[\frac{2B'}{b\sqrt{A'}}y\right]\right)}{\sqrt{3}\,C'\left(1+\exp\left[\frac{B'}{\sqrt{A'}}\right]\right)E_t h_t} \tag{II.93}$$

With:

$$A' = A_{1,1} + A_{0,1} + A_{0,2} + A_{1,2} + A_{0,1,2} + A_{0,2,1} \tag{II.94}$$

$$A_{1,1} = E_0^2 h_0^5 G_0 + E_1^2 h_1^5 G_1 + E_2^2 h_2^5 G_2 \tag{II.95}$$

$$\begin{aligned} A_{0,1} = {} & E_0 h_0^4 h_1 (2E_1 G_0 + 3E_0 G_1) + 2h_0^3 h_1^2 (3E_0^2 G_1 + 2E_1^2 G_0) \\ & + 2h_0^2 h_1^3 (2E_0^2 G_1 + 3E_1^2 G_0) + E_1 h_0 h_1^4 (2E_0 G_1 + 3E_1 G_0) \end{aligned} \tag{II.96}$$

$$\begin{aligned} A_{0,2} = {} & E_0 h_0^4 h_2 (2E_2 G_0 + 3E_0 G_2) + 2h_0^3 h_2^2 (3E_0^2 G_2 + 2E_2^2 G_0) \\ & + 2h_0^2 h_2^3 (2E_0^2 G_2 + 3E_2^2 G_0) + E_2 h_0 h_2^4 (2E_0 G_2 + 3E_2 G_0) \end{aligned} \tag{II.97}$$

$$\begin{aligned} A_{1,2} = {} & E_1 h_1^4 h_2 (2E_2 G_1 + 3E_1 G_2) + E_2 h_1 h_2^4 (2E_1 G_2 + 3E_2 G_1) \\ & + 2h_1^3 h_2^2 (2E_2^2 G_1 + 3E_1^2 G_2) + 2h_2^3 h_1^2 (2E_1^2 G_2 + 3E_2^2 G_1) \end{aligned} \tag{II.98}$$

$$\begin{aligned} A_{0,1,2} = {} & 4h_0 h_1^3 h_2 (3E_0 E_1 G_2 + 3E_1 E_2 G_0 - E_0 E_2 G_1) \\ & + 4h_0 h_1 h_2^3 (3E_2^2 G_0 + 2E_1 E_0 G_2) + 4h_0^3 h_1 h_2 (3E_0^2 G_2 + 2E_1 E_2 G_0) \end{aligned} \tag{II.99}$$

$$\begin{aligned} A_{0,2,1} = {} & 6h_0 h_1^2 h_2^2 (E_1 E_2 G_0 - E_0 E_2 G_1 + 3E_0 E_1 G_2 + 2E_2^2 G_0) \\ & + 6h_0^2 h_1 h_2^2 (E_0 E_1 G_2 - E_0 E_2 G_1 + E_1 E_2 G_0 + 2E_0^2 G_2 + 2E_2^2 G_0) \\ & + 6h_0^2 h_1^2 h_2 (E_0 E_1 G_2 - E_0 E_2 G_1 + 3E_1 E_2 G_0 + 2E_0^2 G_2) \end{aligned} \tag{II.100}$$

$$B' = 2\sqrt{3}\, b\, C'(E_t h_t) \tag{II.101}$$

$$C' = \sqrt{\sum_{k=0}^{N} G_k h_k} \tag{II.102}$$

$$E_t h_t = \sum_{k=0}^{N} E_k h_k \tag{II.103}$$

Replacing Eq. (II.93) into Eq. (II.91) and by integrating with respect to the y-axis, the torsional resonance frequency for a bilayer-coated beam can be determined:

$$T_2 = \frac{1}{2\sqrt{3}\,L}\operatorname{sech}\left[\frac{B'}{2\sqrt{A'}}\right]\frac{A'(B')^2}{B'(bC')^2(E_t h_t)}\left[\frac{B' + B'\cosh\left[\frac{B'}{\sqrt{A'}}\right] - 2\sqrt{A'}\sinh\left[\frac{B'}{\sqrt{A'}}\right]}{(H'_1\rho_1 + H'_2\rho_2 - H'_3\rho_0) + 2b^2(\rho_t h_t)(E_t h_t)^3}\right]^{0.5} \quad \text{(II.104)}$$

Where:

$$\rho_t h_t = \sum_{k=0}^{N} \rho_k h_k \quad \text{(II.105)}$$

$$H'_1 = (E_1 h_1^2 + E_2 h_2(2h_1 + h_2) - E_0 h_0^2)^3 + (E_1 h_1^2 + E_0 h_0(2h_1 + h_0) - E_2 h_2^2)^3 \quad \text{(II.106)}$$

$$H'_2 = (E_0 h_0(2(h_1 + h_2) + h_0) + E_1 h_1(h_1 + 2h_2) + E_2 h_2^2)^3 - (E_1 h_1^2 + E_0 h_0(2h_1 + h_0) - E_2 h_2^2)^3 \quad \text{(II.107)}$$

$$H'_3 = (E_1 h_1^2 + E_2 h_2(2h_1 + h_2) - E_0 h_0^2)^3 - (E_2 h_2(2h_0 + 2h_1 + h_2) + E_1 h_1(h_1 + 2h_0) + E_0 h_0^2)^3 \quad \text{(II.108)}$$

The corresponding torsional frequency ratio becomes:

$$R_{T2} = T_2\sqrt{\frac{\rho_0}{G_0}}\left[\frac{12\,h_0^2\left(b - \frac{h_0\tanh\left[\frac{\sqrt{3}b}{h_0}\right]}{\sqrt{3}}\right)}{b(h_0^2 + b^2)}\right]^{-0.5} \quad \text{(II.109)}$$

The variety of choices made by the authors and the lack of information on the domain of validity of each model do not allow a global view of the technique. In order to check the reliability of the various formulations and to identify the most suitable model, a parametric comparison between the analytical expressions and a FEM will be made in the following section.

II.5. Comparison between the analytical models and a Finite Element Model

II.5.1. Numerical simulation

Finite Element Analysis (FEA) was carried out using the commercial finite element code ABAQUS [Abaqus 2016] in order to determine the frequencies in the flexural and torsional modes of the naked substrate, the bilayer and the three-layered beams. The beam has a length L of 70 *mm*, width b of 20 *mm* and thickness h_0 of 1 *mm* with a rectangular cross-section.

Two different finite element models were constructed by bonding the coatings on the substrate already created through one of the two different functions: tie or partition; that gives no significant differences in the "*n*" modes of frequency extracted. The first model presents a single layer coated beam with a film thickness h_1 that was varied from 0 to 1 *mm*. The second one presents a bi-coated beam with a first film thicknesses h_1 of 4 μm ($R_{h1} = 4 \times 10^{-3}$) and 100 μm ($R_{h1} = 0.1$) and a second film with a thickness h_2 that varied from 0 to 0.55 *mm*.

To mesh the structure, C3D20 quadratic element was used since it presents an excellent behavior for linear elastic calculations. A mesh convergence study of the first four frequency modes was performed to determine the mesh density at which the values of the first four resonance frequencies converge. By varying the number of elements in all three directions, the element size of 0.35×0.27×0.5 mm^3 was chosen for the substrate that led to invariant frequency values even with the smallest elements.

Considering the beam dimensions mentioned in the first paragraph, it gives 30,000 elements: 200 in the length direction, 75 in the width and 2 in the thickness. For a multilayer beam with $R_{h1} > 0.5$, one element through the film thickness was used (Fig. II.6(a)). For beam geometries whose substrate was significantly thicker than the first film ($R_{h1} \leq 0.5$), a variable element size through thickness was applied as shown in Fig. II.6(b) to avoid the alteration of the frequency values. This mesh principle takes into account the effect of abrupt change in the size of the element at the film/substrate interface avoiding the cutoffs of the propagated waves that disturb the solution [Massabò 2017]. Free boundary conditions were applied to the structure and the resonance frequencies of the composite beam were extracted using the

ABAQUS\Implicit Lanczos eigensolver. These configurations were chosen as a reference to validate the analytical models presented in Section II.4.

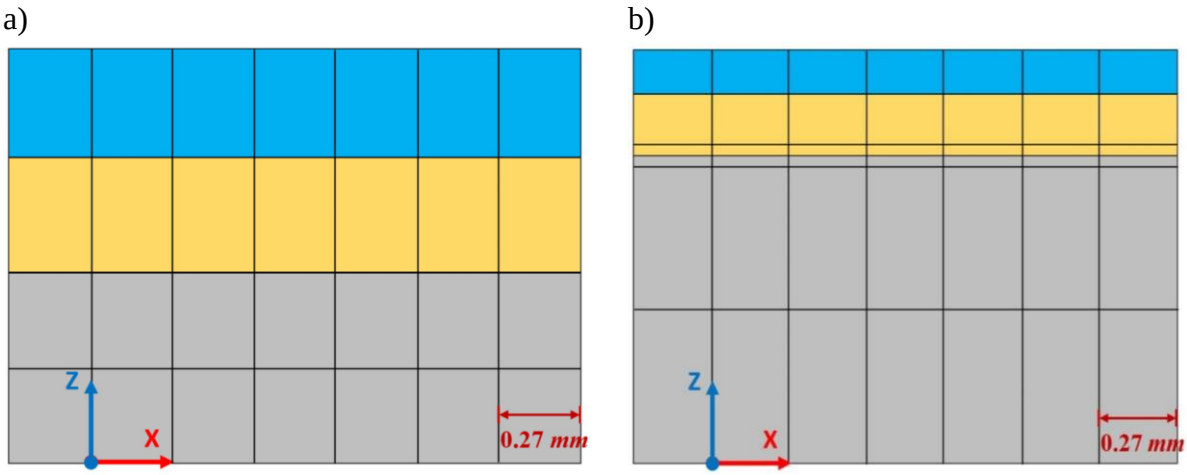

Fig. II.6. Cross-section of FEM with the meshing configuration: a) $R_{h1} > 0.5$, b) $R_{h1} \leq 0.5$.

II.5.2. Flexural mode

In order to identify the most suitable model, a parametric comparison of the analytical models with the FEM was done with a combination of different Young's moduli and density ratios. Four combinations of different materials were chosen to operate at the extreme border where the former models remain invalid [Berry 1975, Mazot 1998, López-Puerto 2014]. Moreover, these combinations allow us to have a large and small shift of the neutral axis. The materials used are presented in Table II.2. The first four flexural vibration modes of a FF multilayered beam are presented in Fig. II.7.

Table II.2
Materials properties used for comparison.

Material	**Specific mass** $(\mathbf{kg/m^3})$	**Young's modulus** (**GPa**)	**Shear modulus** (**GPa**)
Aluminum (Al)	2700	68	24.8
Niobium (Nb)	8600	103	37.5
Titanium (Ti)	4500	116	43.3
Tungsten (W)	19300	400	156.3
AISI316	8000	193	76.3
Silicon (Si)	2330	112.4	43.9
Kapton	1420	3.64	1.4
Gold (Au)	19320	69.1	24.3

a)

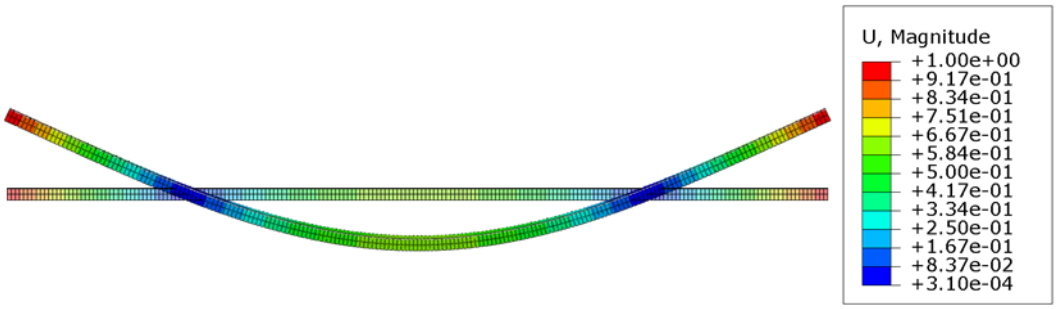

b)

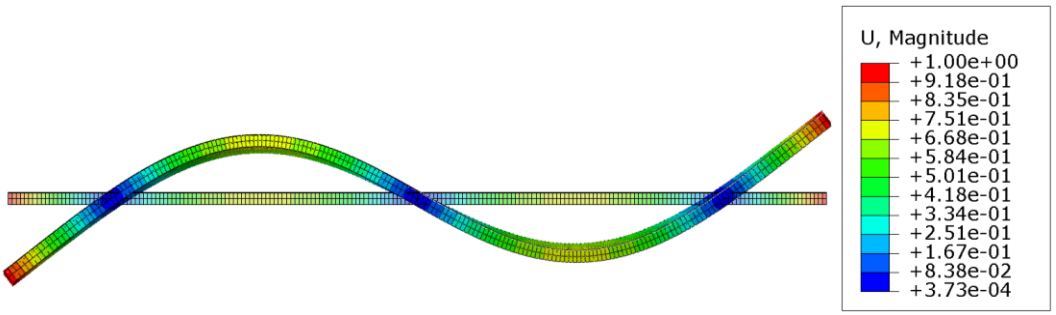

c)

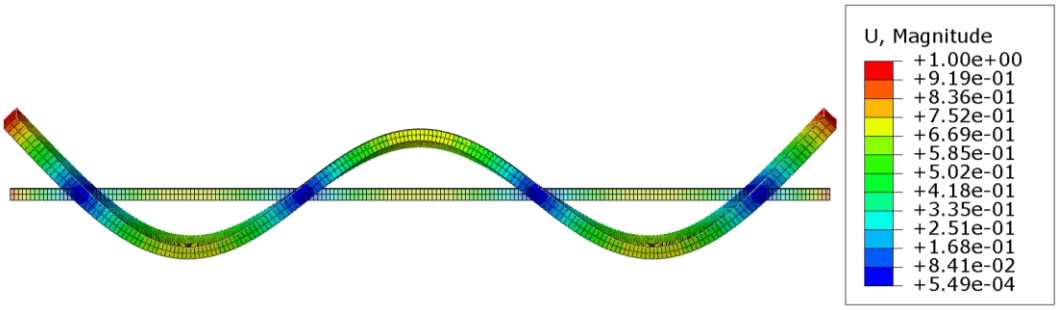

d)

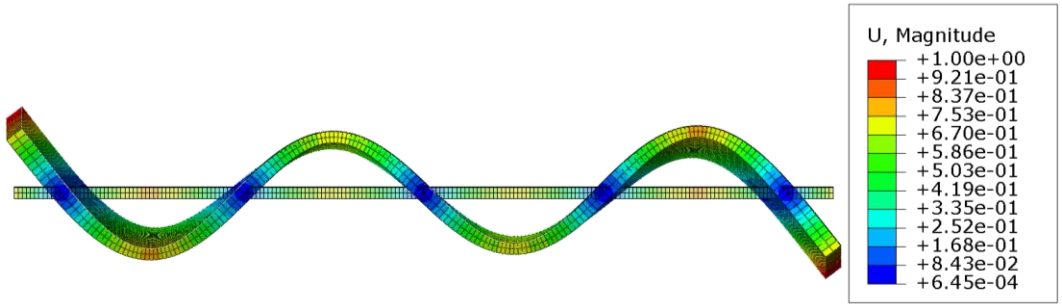

Fig. II.7. Deformed flexural vibrating beam: a) mode I, b) mode II, c) mode III and d) mode IV. The colors indicate the vertical displacement (in *mm*).

For a bilayer beam (substrate + film), the evolution of the frequency ratio R_{F1} as a function of the thickness, density and Young's modulus ratios, is presented in Fig. II.8 with the thickness ratio R_{h1} varying from 0 to 1. The ratios were chosen to cover a large range of materials used for surface coatings. A good agreement can be noted between the developed model (Dev-CLBT, Eq. (II.85)), Pautrot's model (Eq. (II.17)) and the FEM, for any R_{h1}, R_{E1} and $R_{\rho 1}$ ratios. The good reliability of Pautrot's model was already shown in a previous work [Slim 2017a]. As can be seen, the good agreement of the Dev-CLBT model shows that the influence of symmetry becomes negligible when taking into account the shift of the neutral axis after the deposition of the first film. For thickness ratios R_{h1} < 0.1, all models give approximately the same result. For thicker films (R_{h1} > 0.1), the discrepancies between the different models increase due to the different assumptions on which is based each model. For small values of R_{E1} and R_{h1}, Lopez model [Mazot 1998] is the closest to the Pautrot, Dev-CLBT and FEM results since the effect of the shift is negligible. For other configurations, CLBT model is the closest because of the symmetry assumption, leading to an optimum error centered at R_{E1} equal to 1 [Slim 2017a].

a) b)

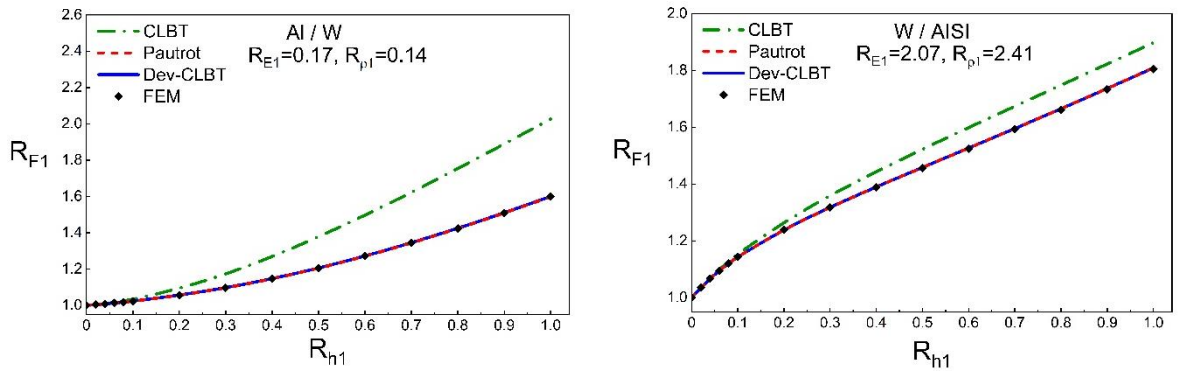

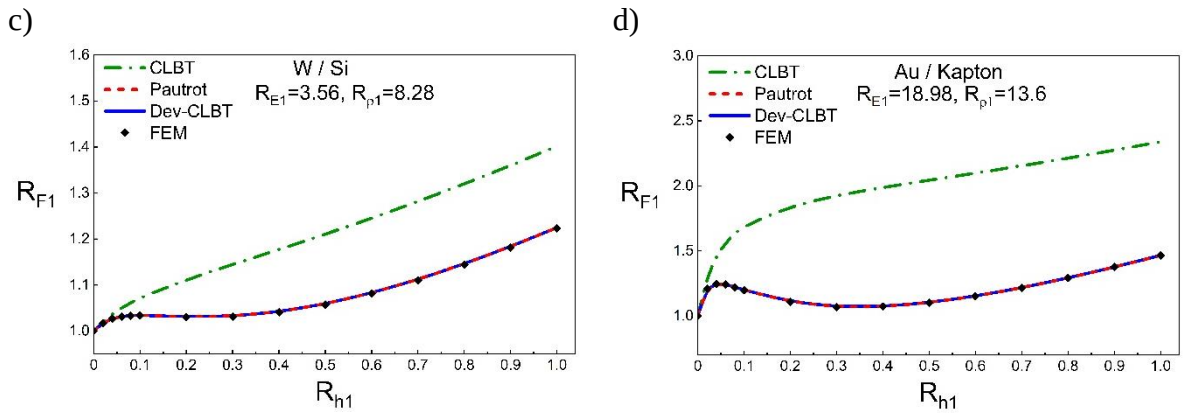

Fig. II.8. Comparison between analytical and numerical models for bilayer isotropic beam (substrate + film) for different Young's moduli and density ratios: a) R_{E1}=0.17, $R_{\rho 1}$=0.14, b) R_{E1}=2.07, $R_{\rho 1}$=2.41, c) R_{E1}=3.56, $R_{\rho 1}$=8.28, and d) R_{E1}=18.98, $R_{\rho 1}$=13.6.

For a three-layered beam (substrate + bilayer films), another comparison was done with different Young's moduli R_{E2} and density $R_{\rho 2}$ ratios. Fig. II.9 presents the evolution of the frequency ratio R_{F2} as a function of the thickness ratio R_{h2} that varied from 0 to 0.55 with two different values of R_{h1} equal to 0.004 and 0.1. A good agreement is noticed between the developed model (Dev-CLBT, Eq. (II.85)), the extended Pautrot's model (Ext-PM, Eq. (II.59)) and the FEM. As for the case of a bilayer beam, we can clearly see the divergence of the CLBT model. This difference between the models increases with the thickness ratio R_{h2}.

The three models (Ext-PM, Dev-CLBT and FEM) predict very similar resonance frequencies for bilayer and three-layered beams. FEM is a numerical approach, which takes into account the slenderness* of the beam, and thus it can be considered as a reference to check analytical models. The difference between FEM and the two analytical models remains lower than 0.2% in the range of the tested ratios (R_h, R_E and R_ρ), which is negligible. This good agreement means that, at least in the range explored in the present study, the rotatory and the shear effects are sufficiently corrected by the T_f factor in Eq. (II.7) or Eq. (II.8) of the substrate and are negligible in the numerical model for the first harmonic mode. It is interesting to note that, in Fig. II.9(c), (d), and (e), the frequency variation versus R_{h2} tends to stabilize which means that, for these configurations, the obtained modulus is not very sensitive to the film thickness. Consequently, the two models are validated and can be used for the prediction of the

* *The propensity of a beam to buckle. It is represented by the quotient between the height and the width of a beam.*

resonance frequencies. In the next chapter, the two models will be used to determine the Young's modulus of each film in a multilayer beam.

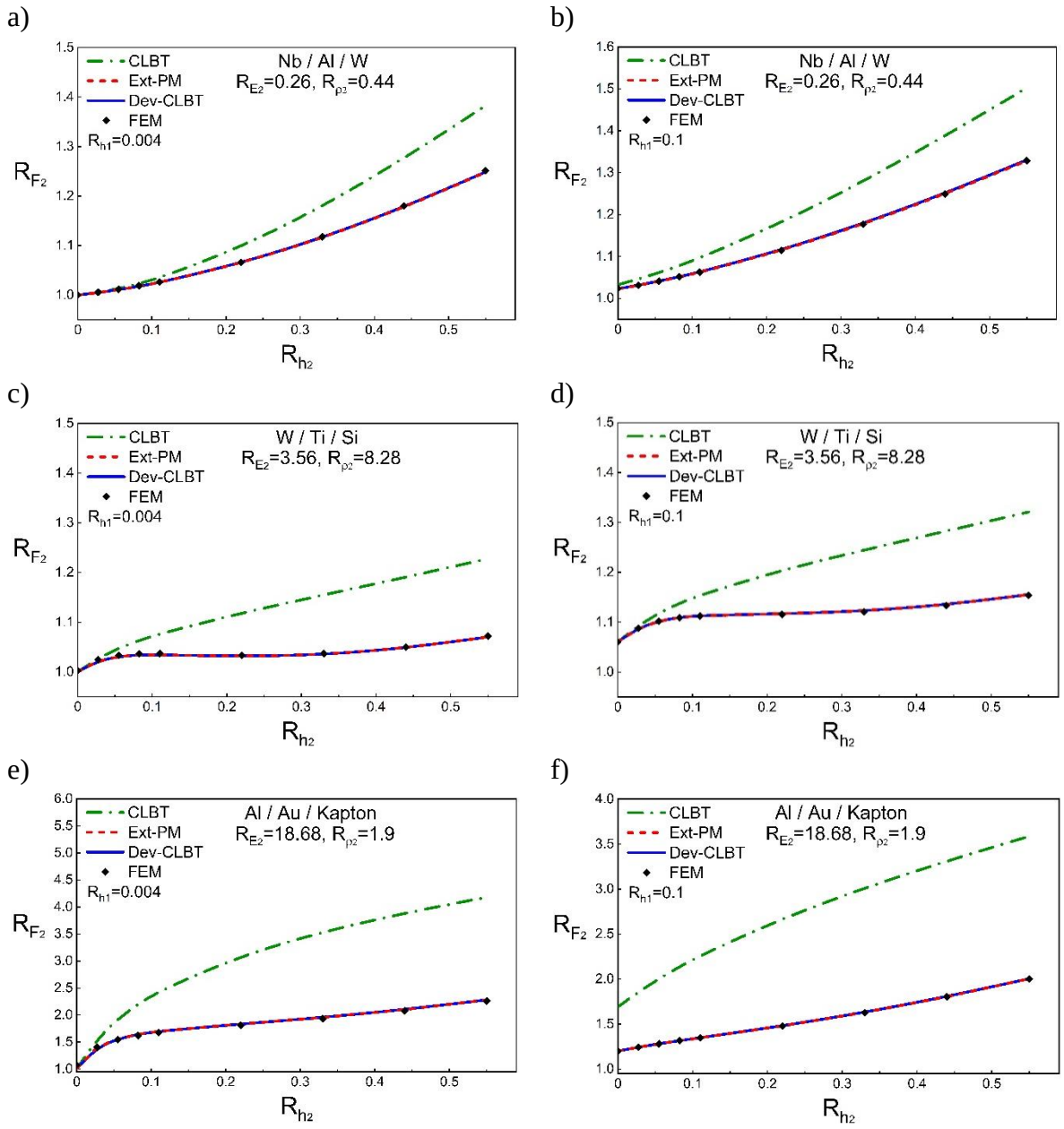

Fig. II.9. Comparison between analytical and numerical models for a multilayer beam comprising three isotropic materials for different Young's moduli and density ratios: a) R_{h1}=0.004, R_{E2}=0.26, $R_{\rho 2}$=0.44, b) R_{h1}=0.1, R_{E2}=0.26, $R_{\rho 2}$=0.44, c) R_{h1}=0.004, R_{E2}=3.56, $R_{\rho 2}$=8.28, d) R_{h1}=0.1, R_{E2}=3.56, $R_{\rho 2}$=8.28, e) R_{h1}=0.004, R_{E2}=18.68, $R_{\rho 2}$=1.9, and f) R_{h1}=0.1, R_{E2}=18.68, $R_{\rho 2}$=1.9.

II.5.3. Torsional mode

In order to check the reliability of the developed formulation (Ext-Slim) for the shear modulus determination, a comparison between the developed model (Eq. (II.109)) and the FEM was performed. The comparison was done with a combination of four different shear moduli R_G and density R_ρ ratios. Fig. II.10 presents the first torsional vibration mode of a FF multilayered beam.

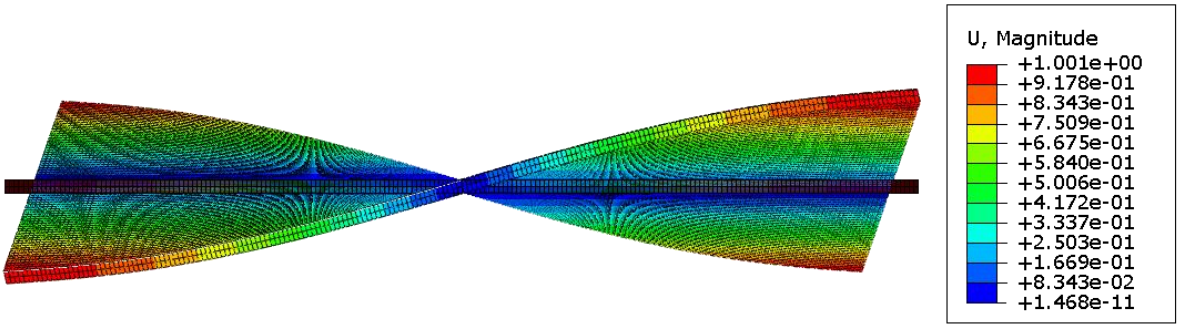

Fig. II.10. Deformed fundamental torsional vibrating beam. The colors indicate the vertical displacement (in *mm*).

For a bilayer beam (substrate + film), the evolution of the frequency ratio R_{T1} as a function of the thickness R_{h1}, density $R_{\rho 1}$ and Young's modulus R_{E1} ratios, is presented in Fig. II.11 with the thickness ratio R_{h1} varying from 0 to 1. In the same studied cases as for the flexural mode, we can see a good agreement between the formulation of Slim's model (Eq. (II.48)) and the finite element calculations. The good reliability of Slim's model was already shown in a previous work [Slim 2017b].

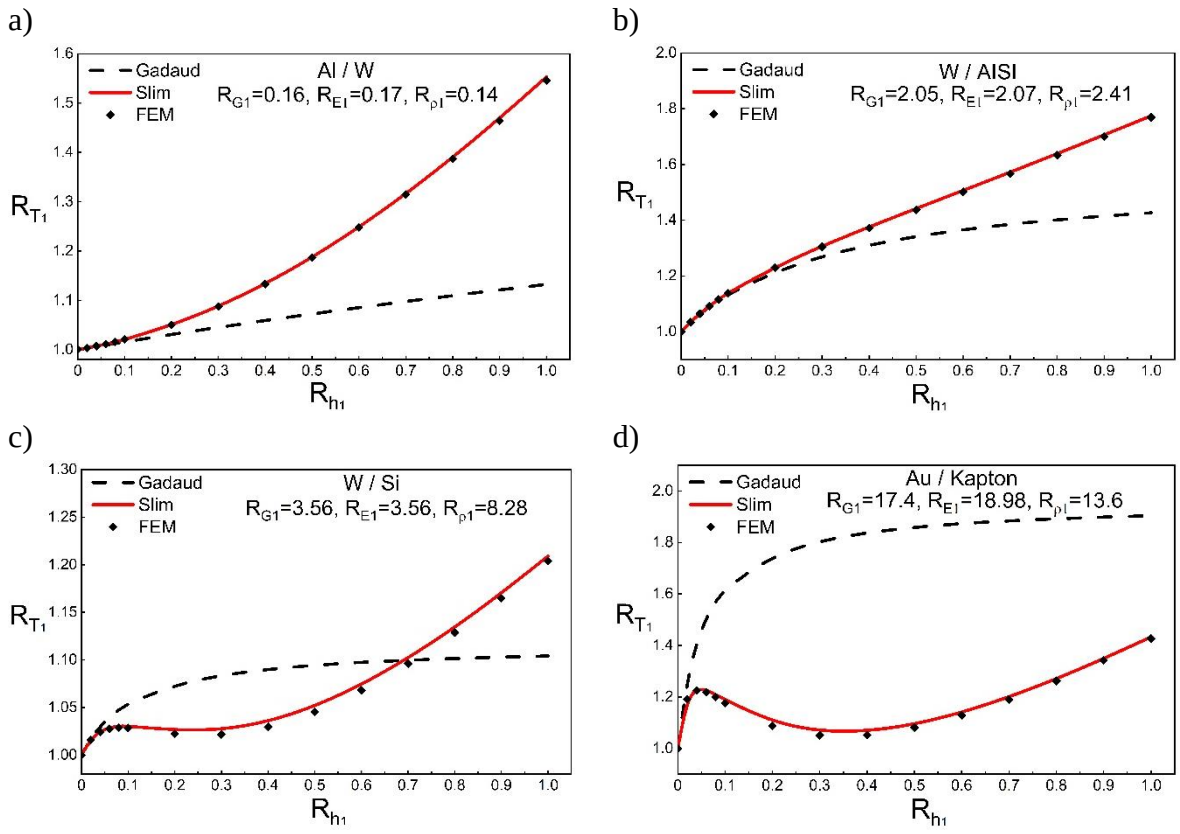

Fig. II.11. Comparison between analytical and numerical models for torsional bilayer beam: a) R_{G1}=0.16, R_{E1}=0.17, $R_{\rho 1}$=0.14, b) R_{G1}=2.05, R_{E1}=2.07, $R_{\rho 1}$=2.41, c) R_{G1}=3.56, R_{E1}=3.56, $R_{\rho 1}$=8.28, and d) R_{G1}=17.4, R_{E1}=18.98, $R_{\rho 1}$=13.6.

Another comparison was done with different shear moduli R_{G2} and density $R_{\rho 2}$ ratios for a three-layered beam (substrate + bilayer films). Fig. II.12 presents the evolution of the frequency ratio R_{T2} as a function of the thickness ratio R_{h2} that varies from 0 to 0.55 with R_{h1} equal to 0.1. A good agreement was noticed between the extended Slim's model (Ext-Slim, Eq. (II.109)) and the FEM for any R_{G2}, R_{E2}, $R_{\rho 2}$ and R_{h2}.

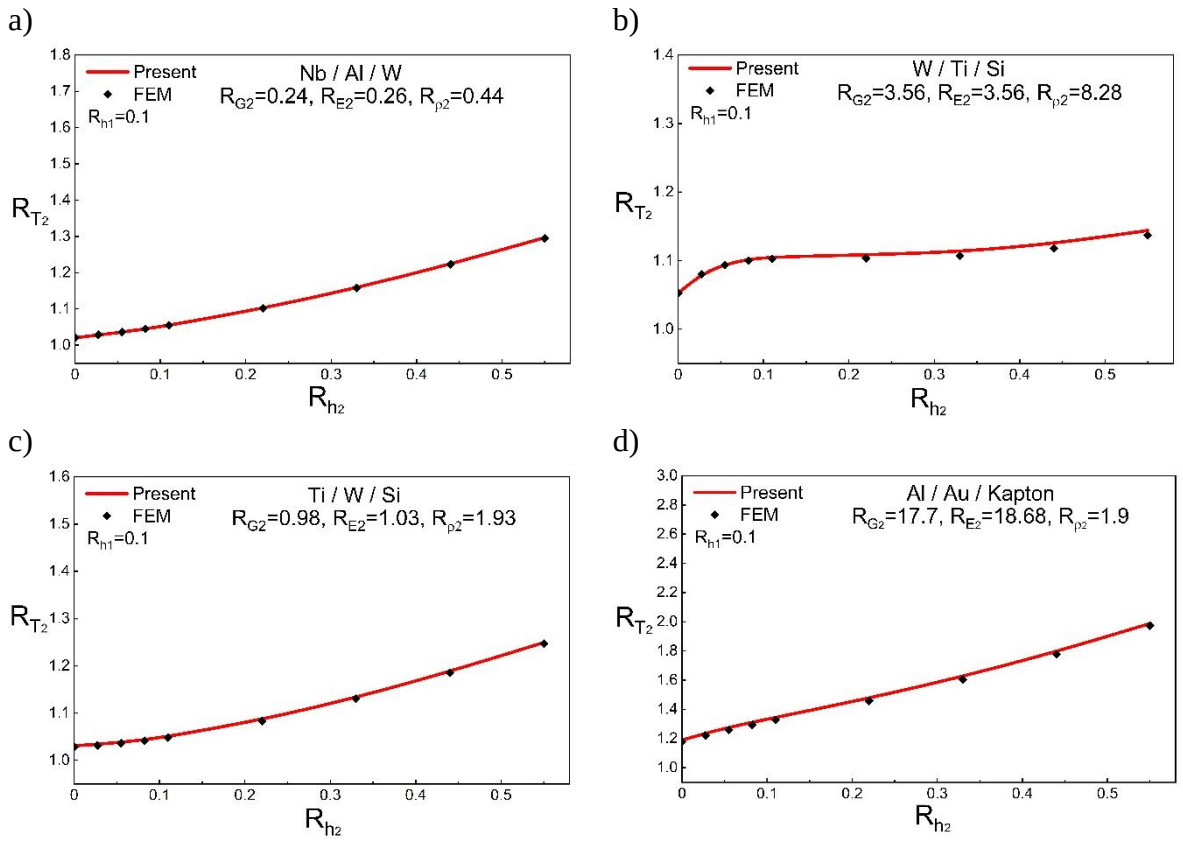

Fig. II.12. Comparison between analytical and numerical models for torsional three-layered beam: a) R_{G2}=0.24, R_{E2}=0.26, $R_{\rho2}$=0.44, b) R_{G2}=3.56, R_{E2}=3.56, $R_{\rho2}$=8.28, c) R_{G2}=0.98, R_{E2}=1.03, $R_{\rho2}$=1.93, and d) R_{G2}=17.7, R_{E2}=18.68, $R_{\rho2}$=1.9.

In this section, the newly developed models were compared to a FEM. An agreement between the FEM and the new models has allowed us to validate them over a wide range of plausible parameters. In the next chapter, these new models will be applied to titanium (Ti) and niobium (Nb) thin films deposited in a multilayer by magnetron sputtering technique.

II.6. Conclusions

This chapter was dedicated on the development of new analytical models for the determination of the elasticity constants of isotropic thin films in a multilayer structure. For the determination of the Young's modulus, the proposed models are based on two different theories (FRCB and CLBT). It was shown that both Extended Pautrot's Model (Ext-PM) and the developed CLBT model (Dev-CLBT) are appropriate to determine the Young's moduli of thin films whatever the coating thickness and the elastic properties of the films and substrate. The Extended Slim model (Ext-Slim) was developed using Hamilton's principle to determine the

shear moduli of thin films in multilayers. The comparison with the finite element model was performed to validate the developed models whatever the ratios R_h, R_E, R_G and R_ρ.

In the next chapter, these new models will be applied to determine the elasticity constants of multilayer coatings by means of the impulse excitation technique. The multilayer structure is composed of titanium and niobium thin films deposited by magnetron sputtering.

Chapter III

Experimental measurements of the elasticity constants of multilayer coatings using Impulse Excitation Technique

III.1. Introduction

After developing analytical models for the determination of the elasticity constants of multilayer coatings, this chapter presents the experimental application of these mechanical models to multilayer coatings deposited by magnetron sputtering. The Ext-PM, Dev-CLBT and Ext-Slim models were applied to determine the Young's and shear moduli of pure titanium, and niobium thin films deposited by DC magnetron sputtering. An uncertainty analysis is performed according to the recommended ISO standard guidelines [JCGM 2008]. The measurement uncertainties are determined in order to quantify the most influencing factors on the global uncertainty of the elasticity constants.

In this chapter, the methodology is developed for evaluating the measurement uncertainties and is applied to determine the Young's and shear moduli of titanium (Ti), and niobium (Nb) films in multilayers deposited by DC magnetron sputtering on different substrates. The morphology and structure of the deposited layers are analyzed. The elastic constants of each layer are discussed with regard to its morphology and structure. A comparison between the reduced modulus determined by IET and NanoIndentation (NI) is performed.

III.2. Experimental applications

III.2.1. Thin-film deposition technique

The deposition technique used during this thesis is magnetron sputtering. It is one of the physical vapor deposition (PVD) techniques, which mainly include thermal evaporation and sputtering in all its forms. The sputtering phenomenon was first observed in 1852 by Grove et al. [Grove 1852] and was proposed by Wright et al. [Wright 1877] for the development of metallic thin films. This method of producing thin films is interesting because it allows all types of materials to be elaborated on any insulating or conductive substrate. It can be used to deposit pure metals as well as metal alloys and ceramics with a single layer or with multilayers. By varying the deposition conditions, materials with various properties can be deposited.

III.2.1.1. Conventional magnetron sputtering

Magnetron sputtering is a deposition technique used at low pressure. Before the deposition phase, the chamber is pumped down with a turbomolecular pump in order to

evacuate any species that can react with the sputtered materials and form undesirable components. The chamber is then filled with inert gas, generally argon (Ar) with a defined flow rate. Using the potential difference created between the cathode (the target) and the anode (the chamber walls plugged to the ground), a partially ionized plasma is formed between the two electrodes. This plasma is composed of ions, electrons and neutral species. Under the effect of a local electric field, the Ar^+ ions created in the discharge are accelerated towards the negatively polarized target to sputter its surface (Fig. III.1). A collision between the Ar^+ ions and the target surface is created. Following this collision, several mechanisms can occur: the sputtering, the adsorption, the nucleation and the diffusion [Pawlowski 2003, Billard 2005]. The sputtering phenomenon occurs when the atoms are expelled from the target surface. These ejected atoms with sufficient energy will eventually collide with the first surface encountered.

The growth of a thin film takes place in several stages [Pawlowski, 2003]: the adsorption stage appears in the first instant of atoms arrival at the substrate surface. Then, particle diffusion within the surface occurs followed by an interaction between the substrate and the deposited particles in order to form stable bonds. These initial stages lead to island nucleation and coalescence. The formation of a continuous film occurs after a sequence of island nucleation and coalescence with volumetric growth, and atoms diffusion inside the film and the substrate [Pawlowski 2003].

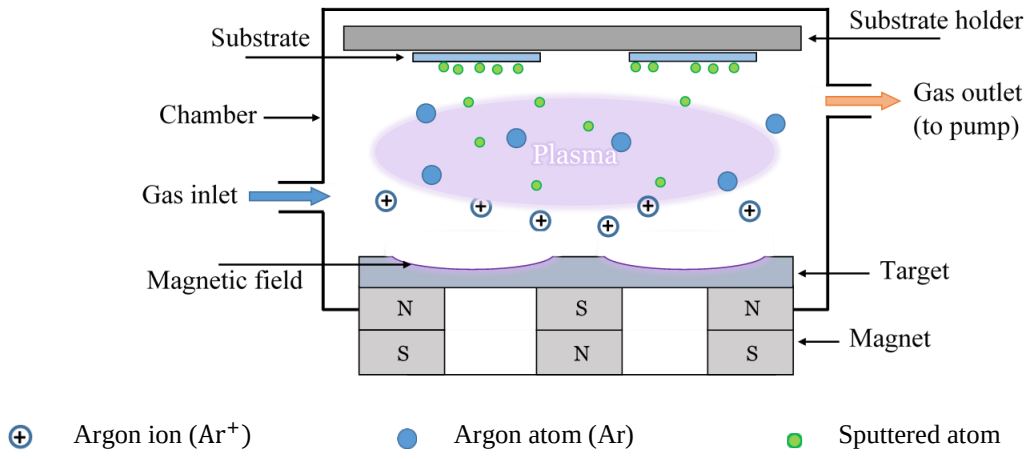

Fig. III.1. Illustration of the magnetron sputtering technique.

The magnetron sputtering can be used to deposit various materials like metals, alloys, dielectric, refractory, or conductive compounds [Nouveau 2001]. It is controlled and adopted for different industrial sectors: mechanical, optical, biomedical and electrical applications. By

changing the deposition conditions, thin films with different microstructural properties can be obtained.

III.2.1.2. Deposition conditions

Titanium (Ti) and niobium (Nb) thin films were deposited at floating temperature, using high purity (99.99%) Ti and Nb targets, on stainless steel AISI316 (sample 1), glass (sample 2) substrates and silicon (Si) wafers by magnetron sputtering in DC mode. The substrates were ultrasonically cleaned in acetone and ethanol for 10 min. Before deposition, they were etched by argon plasma at 0.38 *Pa* and 200 *W* (U_{bias} = -21 *V*) for 30 *min* to remove impurities and surface oxides that could alter the quality of the adhesion of the films. At this phase, the Ti and Nb targets were pre-sputtered for 15 *min*. A DEPHIS4 Physical Vapor Deposition (PVD) machine (Fig. III.2) was used with a 600 *mm* diameter cylindrical deposition chamber of 400 *mm* in height. This was pumped down using a pumping system consisting of a primary pump and a turbomolecular secondary pump to less than 10^{-4} *Pa* before filling it with Ar gas. A constant Ar flow rate of 50 *sccm*[†] led to a constant working pressure of 0.2 *Pa*. The target-substrate distance was kept constant at 10 *cm*. Using a DC-pulsed power supply, the intensity applied to the targets was 3 *A*, 275 *V* discharge voltage (frequency = 50 *kHz*; time off = 4 μs) for the first Ti film and 228 *V* (frequency = 100 *kHz*; time off = 4 μs) for the second Nb film. The substrates were placed on a rotating holder (10 rpm) to ensure a perfect thickness homogeneity of the films. Under these conditions, the deposition of the first (Ti) and second (Nb) films was carried out with a deposition rate of 16.13 *nm/min* and 18.90 *nm/min*, respectively. The stainless steel (AISI316) and glass substrates were used for IET, XRD and NI characterizations, and (100) Si wafers for the Scanning Electron Microscopy (SEM) images.

[†] *Standard Cubic Centimeter per Minute,* cm^3/min

Fig. III.2. PVD machine, DEPHIS4.

III.2.2. Dimensions and Density

The coating has the same length and width as the substrate with different thicknesses. The dimensions of each substrate were measured ten times in ten different locations. The average dimensions and their uncertainties are presented in Table III.1. Samples 1 and 2 correspond to Nb/Ti/AISI316 and Nb/Ti/Glass configurations, respectively. The standard uncertainties on the measured dimensions were evaluated by the type A method by computing the standard deviation [JCGM 2008]. The mass of the substrate was measured using a Sartorius precision balance (0.1 *mg* of precision), and then its density was calculated. The uncertainties on the substrate mass were evaluated following the type B procedure [JCGM 2008]. After deposition, the mass of the composite beam was measured. The bilayer beam corresponds to the Ti film deposited on the substrate. The second film was deposited on the previously coated beam in order to obtain a three-layered beam. The corresponding values are presented in Table III.2. The difference in mass measured before and after each deposited film corresponds to the mass of the film. Its specific mass was estimated by considering the mass and the dimensions of the film.

Table III.1
Average dimensions and measurement uncertainty.

		Length (mm)		Width (mm)		Thickness (µm)	
		L	**u(L)**	**b**	**u(b)**	**h**	**u(h)**
Sample 1	Substrate (AISI316)	69.98	0.027	19.97	$4.7x10^{-3}$	505	2.6
	Film 1 (Ti)	69.98	0.027	19.97	$4.7x10^{-3}$	4.84	0.013
	Film 2 (Nb)	69.98	0.027	19.97	$4.7x10^{-3}$	3.97	0.029
Sample 2	Substrate (Glass)	75.33	0.036	25.38	$9.4x10^{-3}$	1016	8.1
	Film 1 (Ti)	75.33	0.036	25.38	$9.4x10^{-3}$	4.84	0.013
	Film 2 (Nb)	75.33	0.036	25.38	$9.4x10^{-3}$	3.97	0.029

Table III.2
Mass and specific mass with the measurement uncertainty.

		Mass (g)	Specific mass (kg/m^3)	
		m	**ρ**	**u(ρ)**
Sample 1	Substrate (AISI316)	5.561	7879.70	40.75
	Film 1 (Ti)	0.029	4287.47	148.37
	Film 2 (Nb)	0.044	7930.68	189.36
Sample 2	Substrate (Glass)	4.774	2457.70	19.66
	Film 1 (Ti)	0.039	4214.63	108.82
	Film 2 (Nb)	0.063	8300.24	145.12

III.2.3. Impulse Excitation Technique

The theory and principle of the IET were discussed previously. In this section, we focus on presenting the experimental set-up and the handling during a test. In order to stabilize the temperature of the electronic components, the device is turned on for half an hour before starting the experiments. Before starting the test, the sample is placed on a support with negligible interaction (nylon wires placed along the nodal lines of the considered mode) in order to get as close as possible to a free-free (FF) boundary condition (Fig. III.3). These conditions are the simplest to adopt because they represent the configuration with the least interaction between the support system and the sample compared with the other configurations. The sample support used is composed of wires located at the nodal points of the beam where the displacement is equal to zero. The positions of nodal points depend on the harmonic mode used. The support must be used to maintain and isolate the sample from external vibrations without influencing

the desired vibration modes. More explanations concerning the procedure can be found in the literature [Lord 2007, ASTM 2015].

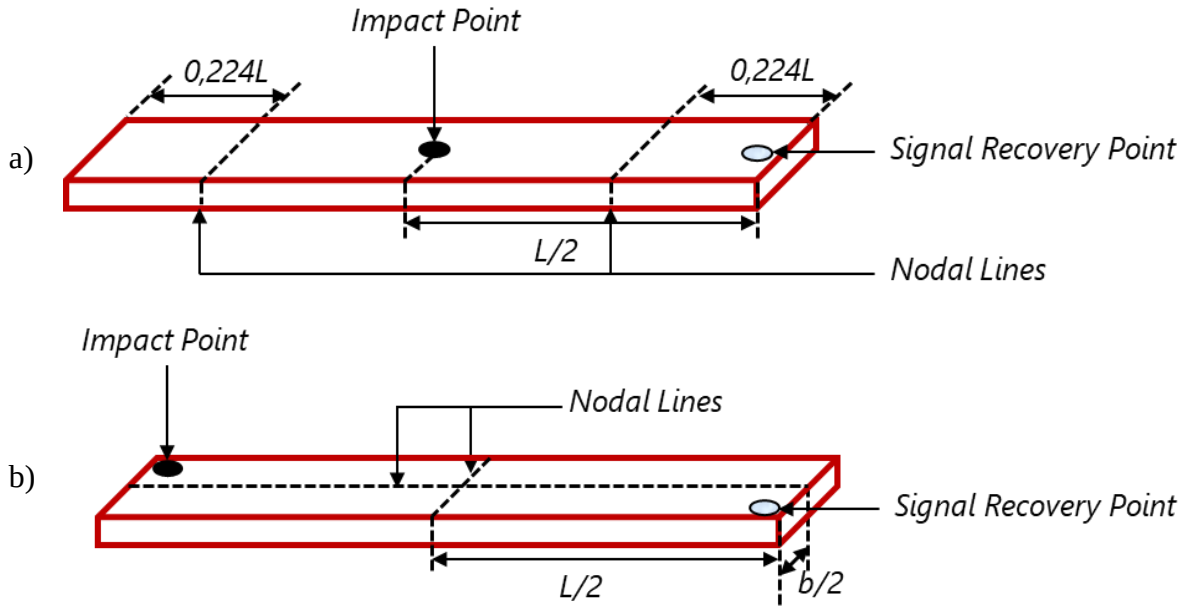

Fig. III.3. Fundamental flexural (a) and torsional (b) configurations applied to the IET.

The resonant frequencies were measured using a professional signal analysis system RFDA (Resonance Frequency and Damping Analysis) built by the company IMCE (Genk, Belgium). The experimental device is equipped with an RFDA transducer, an acoustic microphone with a frequency range up to 100 *kHz*, a universal wire support, an automatic excitation unit and a computer system equipped with RFDA software (Fig. III.4). Using the Fast Fourier Transform (FFT), the amplitudes are represented versus their frequency defining the resonant frequencies of the sample at different vibration modes. More detailed explanations of the procedure can be found in the literature [ASTM 2015]. The measurement reliability can be characterized by its trueness and accuracy, which were investigated in a previous work [Slim 2017a].

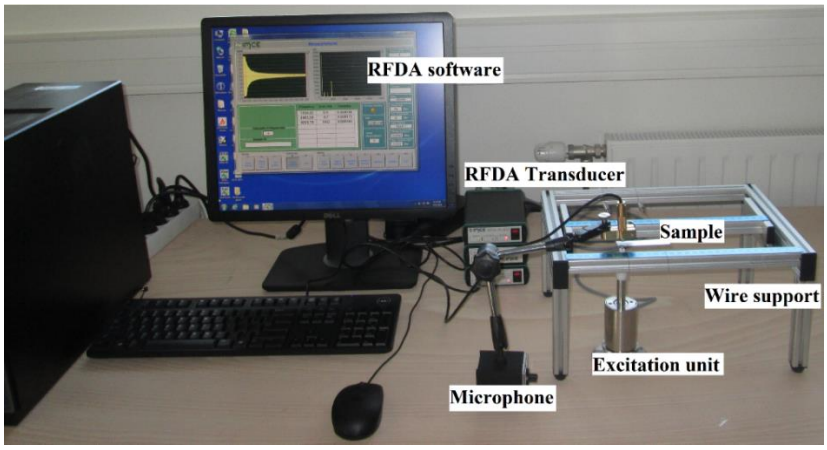

Fig. III.4. Experimental equipment of the IET.

The first four resonant frequencies of substrates (AISI316, Glass), bilayer (Ti/AISI316, Ti/Glass) and three-layer composite beams (Nb/Ti/AISI316, Nb/Ti/Glass) were measured. The vibration measurements were conducted sequentially, i.e., firstly, the resonant frequencies of the substrates were determined; then the titanium film was deposited on each substrate and the resonant frequencies of each bilayer beam were measured again; finally, the third layer (Nb) was deposited and the resonant frequencies of the three-layered beams were measured. As seen from Fig. III.5, the fundamental frequency of the Ti-coated sample is shifted 2.58 *Hz*, and a new additional shift of 0.78 *Hz* can be observed after the elaboration of the Nb second film deposited on the Ti/AISI316 beam. These frequency shifts were used to calculate the substrate and films Young's moduli using the corresponding analytical model.

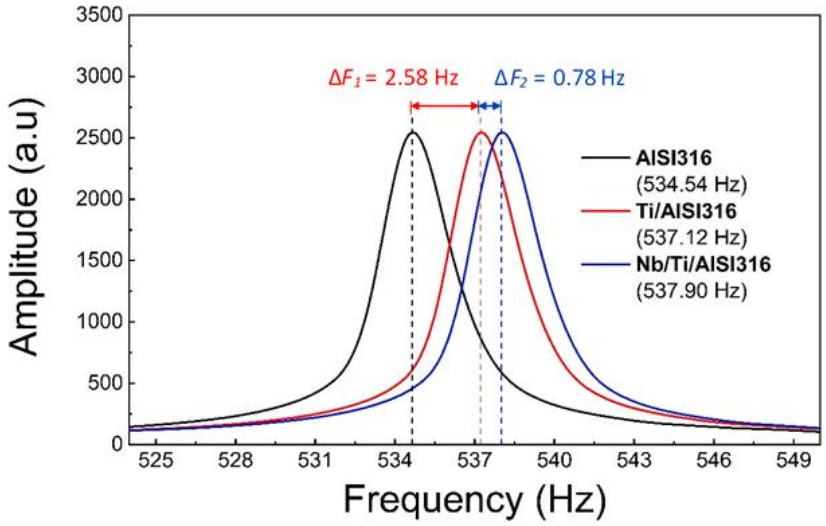

Fig. III.5. The natural frequency of the substrate (AISI 316), one layer coated substrate (Ti/AISI 316) and the multilayer comprising three materials (Nb/Ti/AISI 316).

III.2.4. Nano Indentation

The contact reduced elasticity moduli of the films were also measured by nanoindentation (NI) tests using a TriboIndenter TI 980-Hysitron (Fig. III.6) equipped with a Continuous Stiffness Measurement (CSM) system allowing continuous measurement of the contact stiffness as a function of the penetration depth. For the measurements, a Berkovich diamond tip was used with elasticity constants E_{ind} = 1140 GPa and ν_{ind} = 0.07. Before performing the measurements, the equipment was calibrated using a reference polycarbonate glass specimen. The films reduced moduli were determined by taking the average of ten indents and the uncertainty of measurements was determined from their standard deviation. The tests were carried out under controlled loading. In order to minimize the influence of the substrate or the previous layers, the indenter penetration depth was kept lower than 10% of the coating thickness [Buckle 1960]. The corresponding penetration depth was found to be about 270 *nm* (8 *mN*) for titanium and 300 *nm* (8 *mN*) for niobium. Assuming that the discharge curve is dominated by the elasticity of the material, the contact reduced modulus E_r^c between the material tested and the indenter can be expressed as [Doerner 1986, Oliver 1992, Oliver 2004]:

$$E_c^r = \frac{1}{\beta}\frac{S_c}{2}\sqrt{\frac{\pi}{A_c}} \tag{III.1}$$

Where β is a constant that depends on the geometry of the indenter, which is equal to 1 in the case of axisymmetric geometry of the indenter, S_c is the contact stiffness and A_c is the projected contact area.

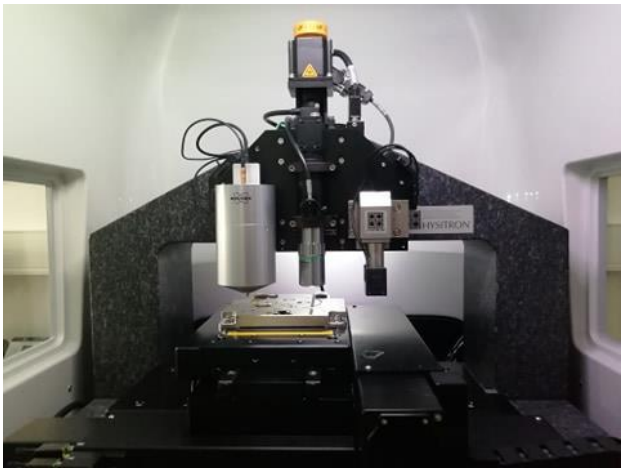

Fig. III.6. TriboIndenter TI 980-Hysitron.

Knowing that the reduced modulus E_c^r depends on the elastic properties of both the specimen and the tip, the Young's modulus of the indented material can be deduced from the following equation [Doerner 1986, Oliver 1992, Oliver 2004]:

$$\frac{1}{E^r} = \frac{1-\nu^2}{E} = \frac{1}{E_c^r} - \frac{1-\nu_{ind}^2}{E_{ind}} \tag{III.2}$$

Where E^r is the reduced modulus of the indented material, E_{ind} is the Young's modulus of the tip and ν and ν_{ind} are the Poisson's ratios of the tested material and the indenter, respectively.

The determination of the reduced modulus of the tested material E^r requires the knowledge of the applied load P, the elastic properties of the tip, the projected contact area A_c and the contact stiffness S_c. The elastic properties of the tip are often known and the applied load is directly measured during the test. The contact stiffness S_c can be determined from the discharge curve or directly during the loading using the CSM feature. The projected contact area A_c can be determined by several approaches. Among the most widespread approaches for the determination of A_c, one can quote the method of Doerner et al. [Doerner 1986], which was then improved by Oliver et al. [Oliver 1992] and the method of Loubet et al. [Loubet 1993, Hochstetter 1999].

Doerner et al. [Doerner 1986] assume that the discharge curve is linear. On the other hand, Oliver et al. [Oliver 1992] have shown by experimentation on different materials, that the discharge curves are rarely linear. They proposed to simulate the discharge curve by a power law as follows [Oliver 1992, Oliver 2004]:

$$P = \alpha(h - h_r)^m \tag{III.3}$$

Where h is the penetration depth, h_r is the residual penetration depth after unloading and α and m are parameters depending on the tested material [Oliver 2004].

From Eq. (III.3), the contact stiffness can be determined from the slope of the unloading curve, which is the derivation of the load P with respect to the penetration depth h:

$$S_c = \frac{dP}{dh} = \alpha m(h - h_r)^{m-1} \tag{III.4}$$

The depth along which the indenter and the specimen are in contact under a load *P* can be determined based on the Sneddon equation [Sneddon 1965, Oliver 1992, Oliver 2004]:

$$h_c = h - \varepsilon \frac{P}{S_c} \tag{III.5}$$

Where ε is a parameter depending on the tip geometry, which is equal to 0.72 in the case of a conical tip. The relation between the contact depth h_c and the projected area A_c was developed by Oliver et al. [Oliver 1992, Oliver 2004]:

$$A_c = C_0 h_c^2 + C_1 h_c + C_2 h_c^{\frac{1}{2}} + \cdots + C_8 h_c^{\frac{1}{128}} \tag{III.6}$$

Where C_0 represents the coefficient relating A_c to h_c in the case of an ideal Berkovich diamond tip. The other coefficients are introduced in order to take into account the imperfection of the tip geometry. They are determined by doing a calibration test on a homogeneous material with known elastic properties, as the polycarbonate glass specimen in this work.

III.2.5. X-ray Diffraction

X-ray Diffraction (XRD) was employed to identify the film crystalline structure using a Bruker D8 Advance diffractometer (Fig. III.7) equipped with a tube delivering CuK_α radiation with a wavelength λ = 0.15418 *nm*. The copper tube was used with point focus mode and the incident beam was shaped by a 1 *mm* collimator and was operated at 40 *kV* and 40 *mA*. Different diffraction patterns were acquired at different inclination angles ψ in order to diffract most of the crystallographic planes. The data were collected with scattering angle 2θ varying between 20° and 150°. Analysis of the diffraction patterns was performed using DIFFRAC.EVA software.

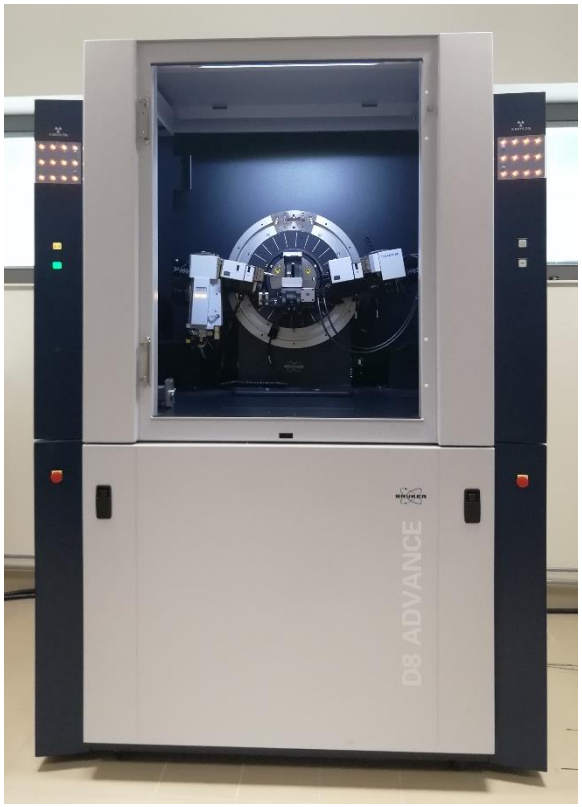

Fig. III.7. X-ray Diffractometer, Bruker D8 Advance.

III.3. Uncertainty analysis

The uncertainty analysis was performed following the ISO standard guidelines: the Guide to the expression of Uncertainty in Measurement (GUM) [JCGM 2008] and the International Vocabulary of Metrology (IVM) [JCGM 2012]. The uncertainty on a quantity x is defined as the standard uncertainty calculated u(x) which is the standard deviation of the distribution of x values. In the present study, the uncertainty analysis is performed to compare the behavior of the different models with regard to their sensitivity to various uncertainty sources. The quantitative values of the uncertainties of different sources related to the frequency measurements were imported from a previous work [Slim 2017a] where the experimental study was performed using the same IET set-up. Thus, other components of the uncertainty are calculated using the uncertainty propagation equation [Bullough 2000].

In this study, the measured quantity is defined as the elasticity constants of the Ti and Nb films. The definitional uncertainty and instrumental measurement uncertainty were neglected in the uncertainty analysis. Moreover, the fluctuations due to the manufacturing process are neglected. Since the elastic behavior for the substrate and the film is assumed to

follow the isotropic Hooke's law, the effects of texture are neglected. The uncertainties coming from the IET measurement system, such as those linked to the window used for computing the FFT and the signal discretization are assumed negligible. To analyze all the sources of uncertainties influencing the elasticity constants measurement using IET, two types of uncertainty components are analyzed: those that appear in the analytical expressions and those that are linked to the instruments and the measurement techniques. The comparison of the uncertainties generated by each of the developed models allows us to judge whether it is preferable to use a model based on the flexural theory rather than the laminated one. A model with better trueness may be less stable than another one and exhibits, in practice, a larger uncertainty.

III.3.1. Frequency uncertainty

A series of experimental measurements was performed to identify and estimate the different sources of uncertainty on the measured frequencies. The sources of uncertainty were determined for the IET [Slim 2017a] and they led to a significant influence on the frequency measurement. Table III.3 presents the uncertainty of the first four resonance frequencies.

Table III.3
Standard uncertainty on the first four resonance frequencies.

Uncertainty (Hz)			
Mode I (Flexural and Torsional)	**Mode II (Flexural)**	**Mode III (Flexural)**	**Mode IV (Flexural)**
0.117	0.147	0.250	0.201

The global uncertainty of the resonant frequencies can be calculated from the following expression [Slim 2017a]:

$$u(f) = \sqrt{u_{pos}^2 + u_{align}^2 + u_{rep}^2 + u_{supp}^2} \quad \text{(III.7)}$$

Where u_{pos}, u_{align}, u_{rep} and u_{supp} are the uncertainties caused by the position of the microphone, the misalignment between the sample nodal lines and the supporting wires, the repeatability and the nature of the support, respectively.

It was found that the measurements are mostly affected by the nature of the support and the misalignment. The support and misalignment uncertainties present the highest contributions. This can be due to the approximate free-free condition [Slim 2017a].

III.3.2. Uncertainty on the substrate and coating elasticity constants

Using the equation of uncertainty propagation, the global uncertainty of the substrate elasticity constants was calculated by developing all the uncertainties that appear in Eqs. (II.5), (II.6) and (II.32). The equation of uncertainty propagation is expressed by assuming that the covariance between the different parameters is null [JCGM 2008]. Using the dimensions uncertainties (Table III.1) and the mass uncertainties (Table III.2) discussed in Section III.2.2, the values of the uncertainty on the substrate specific mass are calculated and also presented in Table III.2. Using the uncertainty of each quantity, the global uncertainty on the substrate elasticity modulus was calculated.

Similarly, the uncertainty of the coatings elasticity constants was calculated using the equation of uncertainty propagation for Ext-PM (Eqs. (II.22)) and (II.66)). The analytical expressions of Dev-CLBT (Eq. (II.85)) and Ext-Slim (Eqs. (II.48) and (II.109)) models present implicit functions. Their corresponding uncertainties cannot be evaluated using the equation of uncertainty propagation. They are calculated using Monte Carlo method by generating a random dispersion on the experimental values.

III.4. Characterizations

III.4.1. Morphology

Using a Scanning Electron Microscope, Hitachi S3500N SEM-FEG operated at 15 *kV*, the thickness of each layer in the film was measured ten times in ten different positions in order to determine the average thicknesses and their uncertainties (Table III.1). Fig. III.8 shows a cross-section SEM image of Nb/Ti/Si multilayer sample. No significant variation appeared in the film thickness. It can be seen that the two films present a porous microstructure with a relatively marked columnar growth. This can be due to the change in energy of incident ions transferred to the adatoms during deposition [Musil 1998, Achache 2016]. The deposition rate can be affected by the pressure and hence the energy of incident ions [Liu 2018, Xu 2019a].

Besides, the absence of bias (samples polarization) can also favor this columnar film growth [Gao 2016, Achache 2016].

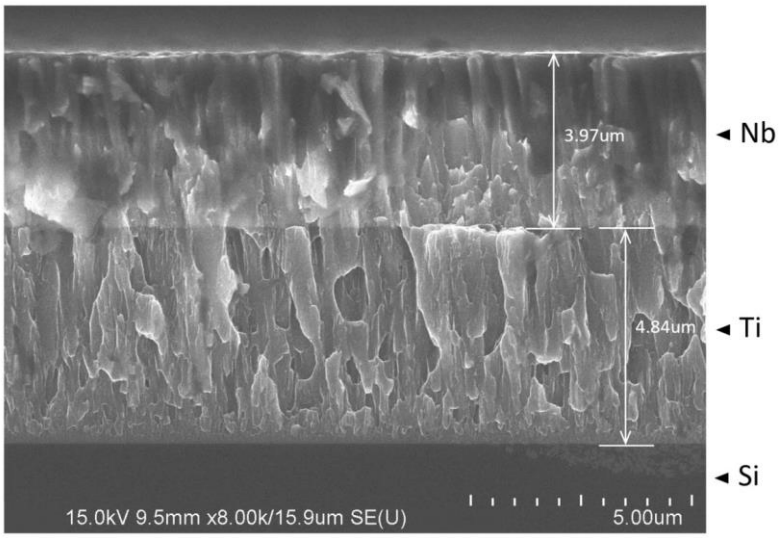

Fig. III.8. Cross-section SEM image of the titanium and niobium films deposited on silicon substrate.

III.4.2. Structural analysis

Fig. III.9 presents the X-ray diffraction patterns of the deposited titanium and niobium films acquired at different inclination angles ψ. The presence of two phases: A very low body-centered cubic (bcc) metastable phase, known as Ti_β (COD CIF file 9012924) and a high hexagonal closed packed (hcp) phase, known as Ti_α (COD CIF file 1532765), can be clearly seen in the structure of the titanium film (Fig. III.9(a)). The formation of the Ti_α stable phase depends on the various sputtering conditions, such as argon pressure, substrate temperature and bias voltage [Naoe 1991, Fréour 2005, Achache 2016, Liu 2018]. The presence of the Ti_β metastable phase in the Ti film could be due to the deposition parameters [Bunshah 1973, Savaloni 2004, Chawla 2008, Chawla 2009, Achache 2016]. Its formation can be favored by the formation of oxide phase due to the presence of trace amounts of water vapor or residual gases during deposition [Vijaya 1996].

Contrariwise, the niobium film structure (Fig. III.9(b)) exhibits a bcc single-phase structure Nb_α (COD CIF file 1539041) similar to several studies on Nb thin films deposited by different out of equilibrium techniques [Goldmann 2003, Okolo 2004, Gontad 2015, Seifried

2018, Xu 2019a]. The Nb films deposited by magnetron sputtering, usually exhibit a polycrystalline bcc structure with preferential (110) orientation [Okolo 2004, Seifried 2018, Xu 2019a]. In the work of Gontad et al. [Gontad 2015], Nb films were grown on Pb disks via pulsed laser deposition. They found that Nb films present only a weak (110) orientation. Noting that from Fig. III.9, some plane families do not diffract with all the inclination angles. This confirms that our films are textured. The texture aspects will be discussed in the next chapters. The penetrations of the CuK_α radiation inside the Ti and Nb films are respectively 4.20 μm and 3.08 μm.

a)

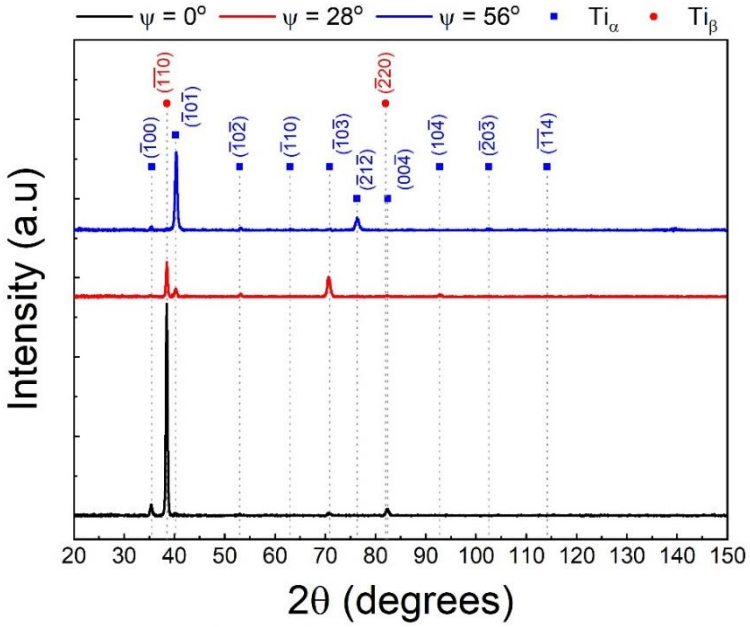

b)

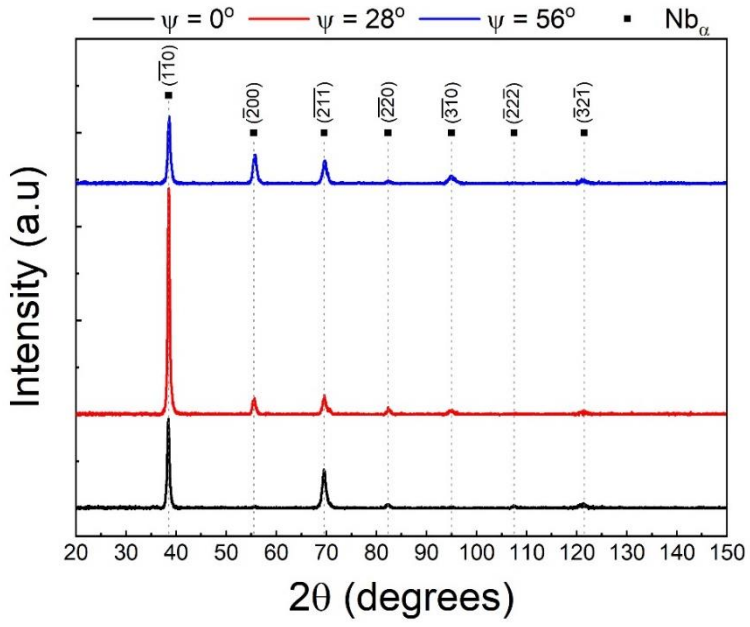

Fig. III.9. X-ray diffraction patterns for different inclination angles: a) titanium film on Si substrate and b) niobium film on Ti-coated Si substrate.

III.4.3. Measurement of the resonance frequencies in a three-layered beam

Table III.4 lists a summary of the measured flexural and torsional resonance frequencies (average value) and the uncertainties for each layered system. The table presents the values measured on two consecutive coatings of Ti and Nb deposited on AISI316 (sample 1) and glass (sample 2) substrates under the same deposition parameters. An increase in flexural and torsional frequencies is observed when each film is added. We can clearly see that the differences ΔF and ΔT in the measured frequencies before and after each deposition, are higher than their corresponding uncertainties, which give us the confidence to use them to determine the elasticity constants of each film. We can see that the contribution (in %) on the measured frequency decreases by taking a higher mode which presents a higher frequency.

Table III.4
Resonance frequencies (F: flexion, T: torsion) of samples measured by IET before and after deposition.

Mode	Sample	Resonance frequency (Hz)			ΔF_1 or ΔT_1 (Hz)	ΔF_2 or ΔT_2 (Hz)	u(F) or u(T)	
		Before deposition	After first deposition	After second deposition			(Hz)	%
I Flexural	1 AISI316	534.54	537.12	537.90	2.58	0.78	0.117	0.02
	2 Glass	980.84	986.93	987.22	6.09	0.29	0.117	0.01
I Torsional	1	1154.26	1160.11	1161.62	5.85	1.51	0.117	0.01
	2	1815.69	1826.31	1827.00	10.62	0.69	0.117	6.4×10^{-3}
II Flexural	1	1481.98	1489.38	1491.70	7.40	2.32	0.147	0.01
	2	2712.05	2728.55	2729.43	16.50	0.88	0.147	5.4×10^{-3}
III Flexural	1	2907.49	2922.14	2925.87	14.65	3.73	0.250	8.6×10^{-3}
	2	5317.45	5351.86	5353.71	34.41	1.85	0.250	4.7×10^{-3}
IV Flexural	1	4807.60	4832.67	4839.57	25.07	6.90	0.201	4.2×10^{-3}
	2	8692.02	8743.18	8745.74	51.16	2.56	0.201	2.3×10^{-3}

III.4.4. Determination of the elasticity constants in a three-layered system

III.4.4.1. Elasticity constants of the substrates

Table III.5 gives the elasticity constants and their uncertainties of stainless steel and glass substrates measured by IET. These constants were calculated using Eq. (II.6) for the fundamental flexural frequency, Eq. (II.5) for the other flexural frequency modes and Eq. (II.42) for the torsional frequency. The Poisson's ratio was calculated by assuming an isotropic elastic behavior of the substrate. The measured elasticity constants of the substrates (Table III.5) are coherent with those reported in the literature for AISI316 [Smithells 1983] and glass substrates [Jämting 1997, Rouxel 2007, Gadaud 2009, Slim 2017b].

Table III.5
Substrate elasticity constants and their uncertainties.

Mode	Sample	IET								
		E_0	$u(E_0)$		G_0	$u(G_0)$		ν_0	$u(\nu_0)$	
		GPa	GPa	%	GPa	GPa	%	-	-	%
I	1 AISI316	200.47	2.33	1.16	80.51	0.93	1.16	0.245	0.020	8.16
	2 Glass	69.90	1.25	1.78	28.79	0.51	1.77	0.214	0.031	14.49
II	1	202.70	2.36	1.16	-	-	-	-	-	-
	2	70.24	1.26	1.79	-	-	-	-	-	-
III	1	203.01	2.36	1.16	-	-	-	-	-	-
	2	70.26	1.26	1.79	-	-	-	-	-	-
IV	1	203.13	2.36	1.16	-	-	-	-	-	-
	2	68.70	1.23	1.79	-	-	-	-	-	-

III.4.4.2. Young's modulus of the coatings

In Table III.6 and Table III.7, the Young's moduli and their uncertainties of the deposited Ti and Nb films were obtained using Pautrot's, Dev-CLBT and Extended Pautrot's (Ext-PM) models. We can notice that the difference between the Young's moduli increases with the frequency mode. The difference between the elasticity moduli determined from the first frequency and the higher frequencies may be due to the shear and inertia effects. They were

taken into account in the frequency equation of the first mode (Eq. (II.6)) using the correction factor, which is not the case in the frequency equation of the other modes (Eq. (II.5)).

Table III.6
Young's modulus of the first Ti film obtained by IET.

Sample	Mode	First film (Ti)					
		Pautrot			Dev-CLBT		
		E_1	$u(E_1)$		E_1	$u(E_1)$	
		GPa	GPa	%	GPa	GPa	%
1 AISI316	I	105.22	4.69	4.46	104.56	4.66	4.46
	II	108.74	2.72	2.50	108.07	2.75	2.54
	III	109.55	2.54	2.32	108.87	2.55	2.34
	IV	112.11	2.06	1.84	111.41	1.98	1.77
2 Glass	I	105.28	2.81	2.67	102.62	2.82	2.75
	II	104.54	2.37	2.27	101.90	2.22	2.18
	III	108.45	2.40	2.21	105.72	2.40	2.27
	IV	100.31	2.18	2.17	97.77	2.17	2.22

The values of Young's moduli of the titanium film presented in Table III.6 varied from 97 *GPa* to 112 *GPa*. The values reported in the literature are highly dispersed: the values found in the present work are consistent with some of them [Chinmulgund 1995, Tsuchiya 2005, Verkhovtsev 2013] and differ from some others [Kim 1997, Cho 1999]. Differences can be explained by the microstructural features, such as phase proportions and the presence of pores [Slim 2019]. It can also be explained by the process itself like in reference [Peraud 1997], where ions are implanted into the crystalline structure during the deposition process.

For the first sample, the uncertainty on the Ti film Young's modulus is in the order of 4.6 *GPa* (4.4 %), 2.7 *GPa* (2.5 %), 2.5 *GPa* (2.3 %) and 2 *GPa* (1.8 %), respectively in mode I, II, III, and IV, approximately for the two models (Table III.6). By moving from the first to the fourth mode, the resonant frequency of the system increases while its contribution to the uncertainty decreases (Table III.4). Therefore, the uncertainty of Ti film Young's modulus decreases at higher modes. The same reasoning is applied to the second sample.

Table III.7
Young's modulus of the second Nb film obtained by IET.

Sample	Mode	Second film (Nb)					
		Ext-PM			Dev-CLBT		
		E_2	$u(E_2)$		E_2	$u(E_2)$	
		GPa	GPa	%	GPa	GPa	%
	I	89.53	8.31	9.28	88.21	7.68	8.71
1	II	92.37	5.3	5.74	91.01	5.42	5.95
AISI316	III	87.74	5.01	5.71	86.45	4.91	5.68
	IV	90.42	4.38	4.84	89.09	4.09	4.59
	I	82.64	5.89	7.13	79.35	5.76	7.26
2	II	83.36	5.3	6.36	80.04	4.96	6.2
Glass	III	83.78	5.37	6.41	80.44	4.9	6.09
	IV	81.11	4.98	6.14	77.89	4.52	5.8

The measured values of the niobium film Young's moduli varied in the range of 77 ~ 92 *GPa* (Table III.7). These values are close to those reported in previous studies for a single layer of niobium characterized by NI [Seifried 2018, Xu 2019a] and they are lower than those given in other studies determined using the Neerfeld-Hill model [Okolo 2004, Czichos 2014] and those of bulk material [Brandes 1992]. This can also be due either to the presence of pores in the film or to the layering of different materials that can toggle the results and the prediction of the Young's modulus of each thin film in a multilayer system.

For a three-layered system, the uncertainty of the Nb film Young's modulus is in the order of 8 *GPa* (9 %), 5.4 *GPa* (5.8 %), 5 *GPa* (5.7 %) and 4 *GPa* (4.8 %) respectively in mode I, II, III, IV with a slight difference between the two models, which was not the case for the bilayer beam. This difference appears starting from the second layer because of the difference in theory and the symmetry assumption of the laminated theory that can relatively affect the results even if it was corrected by the shift of the neutral axis after deposition. The uncertainty of the second film Young's modulus is higher than that of the first film. This can be due to the layering where the cumulating effect of the uncertainties of the two precedent layers (substrate and the first film) contributes to the second film Young's modulus. Since the Nb film has lower elasticity constants and thickness than those of the Ti film, its influence on the resonance frequency is lower.

The Poisson's ratios used in CLBT and Dev-CLBT models for titanium and niobium films were respectively 0.36 [Brandes 1992] and 0.4 [Zhang 2007], which were taken from the literature for bulk material. Fig. III.10 and Fig. III.11 present the frequency ratio as a function of a new ratio expressed as:

$$R_{\nu i} = \frac{\nu_i}{\nu_0} \quad i = 1, \dots, N \tag{III.8}$$

Where index i stands for the number of layers. It can be concluded from these figures that there is no significant influence of the Poisson's ratio on the determination of the Young's modulus in flexural mode. Thus, both models can be used to determine the Young's modulus of each film in a multilayer system considering carefully the different uncertainty sources. The contribution of each uncertainty source on the determination of the film Young's modulus will be described in the next section.

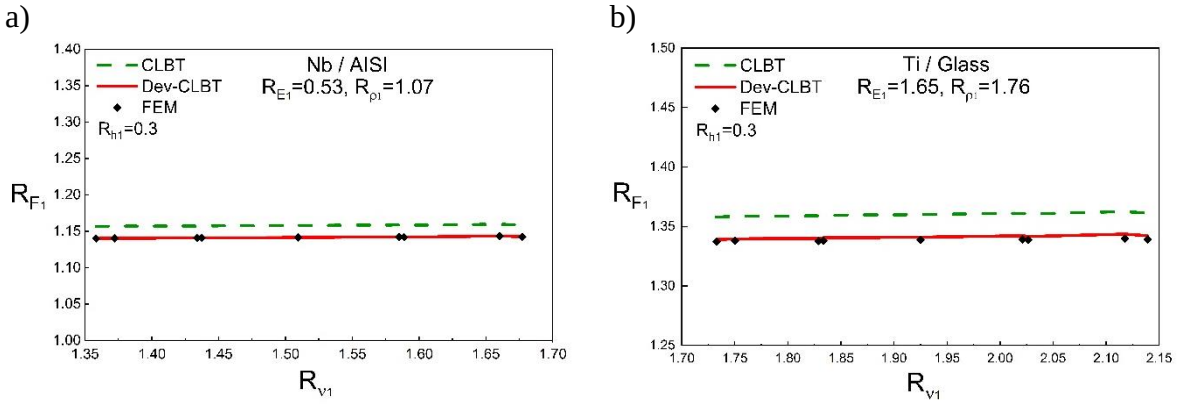

Fig. III.10. Comparison between analytical and numerical models for bilayer isotropic beam (substrate + film) with R_{h1}=0.3 and for different Young's moduli, and density ratios: a) R_{E1}=0.53, $R_{\rho 1}$=1.07, b) R_{E1}=1.65, $R_{\rho 1}$=1.76.

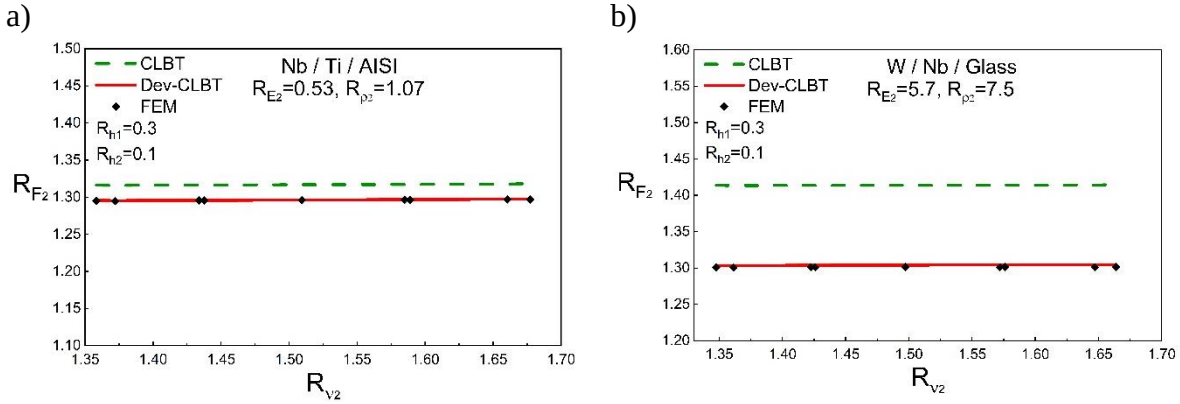

Fig. III.11. Comparison between analytical and numerical models for a multilayer beam comprising three isotropic materials with R_{h1}=0.3, R_{h2}=0.1 and for different Young's moduli and density ratios: a) R_{E2}=0.53, $R_{\rho 2}$=1.07, b) R_{E2}=5.7, $R_{\rho 2}$=7.5.

III.4.4.3. Shear modulus and Poisson's ratio of the coatings

In Table III.8, the shear moduli and their uncertainties of the deposited Ti and Nb films were obtained using Slim's and Extended Slim's (Ext-Slim) models. These values were obtained for the fundamental torsional resonance frequency. From the table, we can conclude that the difference between the shear moduli of the two tested samples measured by IET is due to the measurement uncertainties. All the observed variations between the two samples are lower than the measurement uncertainties. The measured values of the Ti and Nb Young's and shear moduli are lower than the bulk one [Brandes 1992], $E = 120.2\ GPa$, $G = 45.6\ GPa$ for Ti and $E = 104.9\ GPa$, $G = 37.5\ GPa$ for Nb. This can be attributed to the presence of pores in the film owing to our deposition parameters. By assuming the isotropic behavior of the films, the Poisson's ratio of each film was calculated using the corresponding Young's and shear moduli (Table III.9).

A difference between the measured values of the Poisson's ratio and the values found in the literature [Brandes 1992, Donachie 2000, Okolo 2004, Zhang 2007] was observed. This difference is attributed to the measurement uncertainty on the Young's and shear moduli. For the titanium and niobium films, a slight decrease in the Poisson's ratio was observed compared to the corresponding bulk material, respectively 0.361 and 0.397 [Brandes 1992]. The uncertainty of the Poisson's ratio increases for the second film due to the cumulating effect of the uncertainties of the substrate and the Ti film. The difference between the values reported in the literature and the measured values may be due not only to the measurement uncertainty on the Young's and shear moduli but also to the different used elaboration techniques. The same consequence was found in the literature for tungsten films. Faurie et al. [Faurie 2004] have observed a difference between the Poisson's ratios of a tungsten film deposited by Ion Beam Sputtering and bulk tungsten. Slim et al. [Slim 2017b] have found that the difference in tungsten film Poisson's ratios can be due to the difference in the elaboration techniques used.

Table III.8
Shear moduli of the Ti and Nb layers obtained by IET.

Sample	First layer (Ti)			Second layer (Nb)		
	Slim model			Ext-Slim		
	G_1	$u(G_1)$		G_2	$u(G_2)$	
	GPa	GPa	%	GPa	GPa	%
1 (AISI316)	42.84	1.02	2.38	35.17	2.02	5.74
2 (Glass)	42.64	0.87	2.04	32.28	2.09	6.47

Table III.9
Poisson's ratios of the Ti and Nb films obtained by IET.

Sample	Poisson's ratio					
	ν_1	$u(\nu_1)$		ν_2	$u(\nu_2)$	
	-	-	%	-	-	%
1 (AISI316)	0.228	0.062	27.19	0.273	0.139	50.92
2 (Glass)	0.234	0.041	17.52	0.280	0.123	43.93

III.4.4.4. Comparison between Nanoindentation and Impulse Excitation Technique

Since the nanoindentation (NI) technique cannot separate the Young's modulus and the Poisson's ratio, a comparison between the reduced moduli determined by NI and IET was performed. The reduced moduli of the Ti and Nb films measured by the two techniques are presented in Table III.10. From Eq. (III.2), the reduced modulus E^r measured by IET was calculated as a function of the Young's modulus and Poisson's ratio determined by IET. The Young's moduli of the films obtained by NI and their uncertainties can be calculated using the reduced moduli measured by NI (Table III.10) and the Poisson's ratios determined by IET (Table III.9). The corresponding Young's moduli of the films are presented in Table III.11. The difference between the Young's moduli of the Ti and Nb films measured by nanoindentation and IET is lower than the measurement uncertainty. The small variation observed between the values may be due to the difference in the volume analyzed by the two techniques. The Young's modulus measured by NI depends on the moduli parallel and perpendicular to the film surface while the modulus measured by IET is the one parallel to the film surface along the x-axis. This argument is only valid if the films have an anisotropic elastic behavior. This question of anisotropy will be analyzed in detail in Chapter IV. Even if the nanoindentation tests were

carried out at a controlled penetration depth less than 10 % of the film thickness, the results remain influenced by the elastic interaction between the substrate and the film.

Table III.10
The reduced Young's moduli of the Ti and Nb films deposited on glass substrates.

Film	Reduced modulus					
	IET			NI		
	E^r_{IET}	$u(E^r_{IET})$		E^r_{NI}	$u(E^r_{NI})$	
	GPa	GPa	%	GPa	GPa	%
Ti (on Glass)	111.38	3.73	3.35	113.47	3.83	3.38
Nb (on Glass)	89.67	9.26	10.33	94.99	8.25	8.69

Table III.11
The Young's moduli of the Ti and Nb films deposited on glass substrates.

Film	Young's modulus					
	IET			NI		
	E_{IET}	$u(E_{IET})$		E_{NI}	$u(E_{NI})$	
	GPa	GPa	%	GPa	GPa	%
Ti (on Glass)	105.28	2.81	2.67	107.26	2.89	2.70
Nb (on Glass)	82.64	5.89	7.13	87.55	3.87	4.42

III.4.5. Contribution of each uncertainty source on the coating elasticity constants

III.4.5.1. Contribution on the substrate elasticity constants

The measurement uncertainty of the substrate Young's modulus was calculated using the equation of uncertainty propagation applied to Eqs. (II.5) and (II.6) as indicated in the GUM [JCGM 2008] (Section III.3.2). The contribution of each source of error on the substrate Young's modulus uncertainty is presented in Fig. III.12, which corresponds to sample No. 1 (AISI316). The global uncertainty and the various contributions are approximately the same for the first four frequency modes with percentages of approximately 79 % and 20 % respectively, for the substrate thickness and density. Thus, very precise and accurate measurements should be performed on the measurement of the thickness and the density of the substrate. The other quantities can be neglected. The overall uncertainty is around 2.36 *GPa*, which represents 1.16% of the substrate Young's modulus value taken as an example in this study.

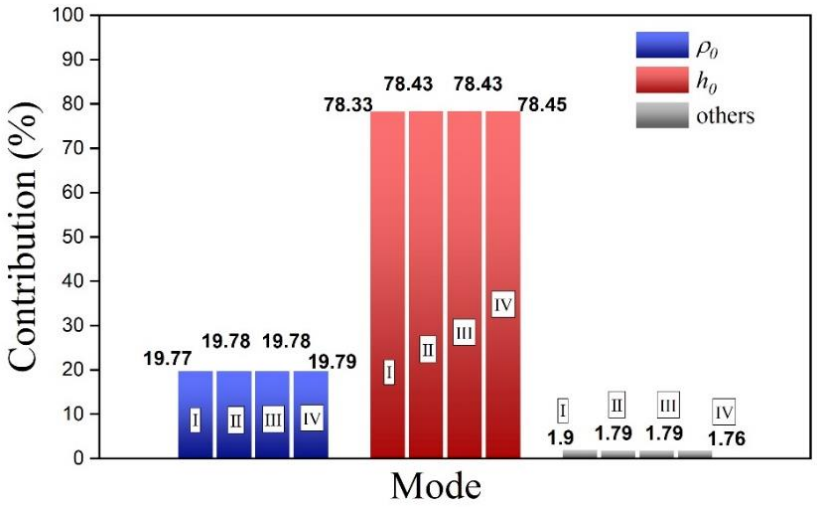

Fig. III.12. Contribution of each error source (in %) on the AISI 316 substrate Young's modulus uncertainty.

Table III.12 presents the contributions of each source of error on the 316 steel substrate shear modulus. By comparing Table III.12 with Fig. III.12, we can see that, for the steel substrate, the most significant sources of uncertainty are the same for both Young's and shear moduli. It is thus recommended to carefully measure the thickness and the density of the substrate by performing more than 10 measurements.

Table III.12
Contribution of each source of error on the uncertainty of the AISI316 substrate shear modulus.

Quantity	Contribution	
	GPa	**%**
L	4.18×10^{-3}	0.45
b	1.58×10^{-3}	0.17
$\boldsymbol{h_0}$	**0.74**	**79.29**
T_0	2.79×10^{-4}	0.03
$\boldsymbol{\rho_0}$	**0.19**	**20.06**
G_0	0.93	100

III.4.5.2. Uncertainty budget for the coating Young's modulus

Fig. III.13 and Fig. III.14 present the contribution of each source on the uncertainty of the Ti and Nb film Young's moduli, respectively. They are calculated using the equation of uncertainty propagation for Pautrot's and Ext-PM models based on the flexural theory. For

Dev-CLBT, the uncertainty was calculated using the Monte Carlo method by generating a random dispersion on the experimental values. As we can notice for both models, the measured density of the film, the substrate Young's modulus, and the two frequencies represent a significant contribution. They are the first to be improved. The contribution of the Ti film Young's modulus was taken into account for the case of the three-layered system. The large contributions of the frequencies are related to the shift in the measured frequency before and after deposition. The contributions can be calculated in *GPa* using the percentage of contributions for each source of uncertainty. In this case, it is also interesting to note that the contributions of different uncertainty sources are in the same order of magnitude for a given mode as for the overall uncertainty generated by the two models.

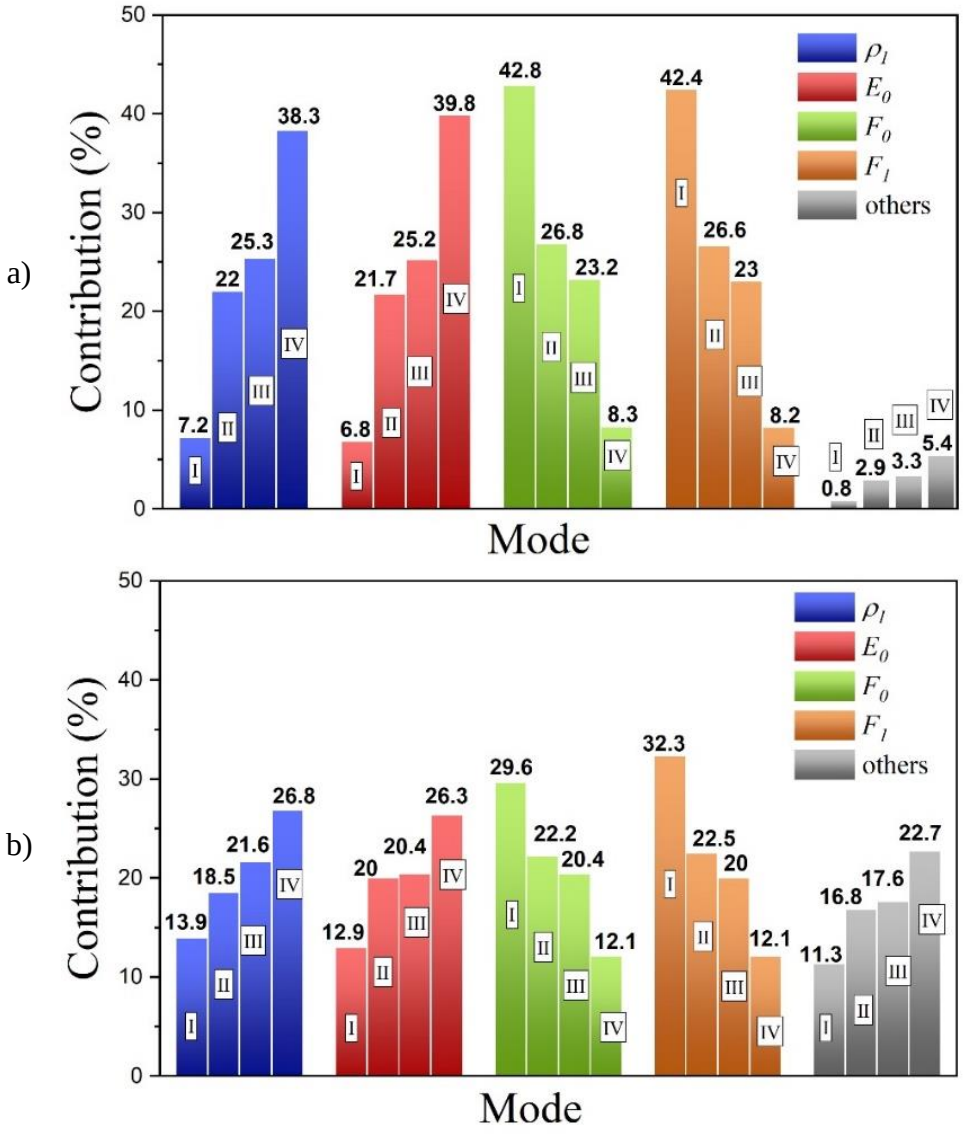

Fig. III.13. Contribution of each uncertainty source (in %) on the first (Ti) film Young's modulus given by: a) Pautrot's model and b) Dev-CLBT model.

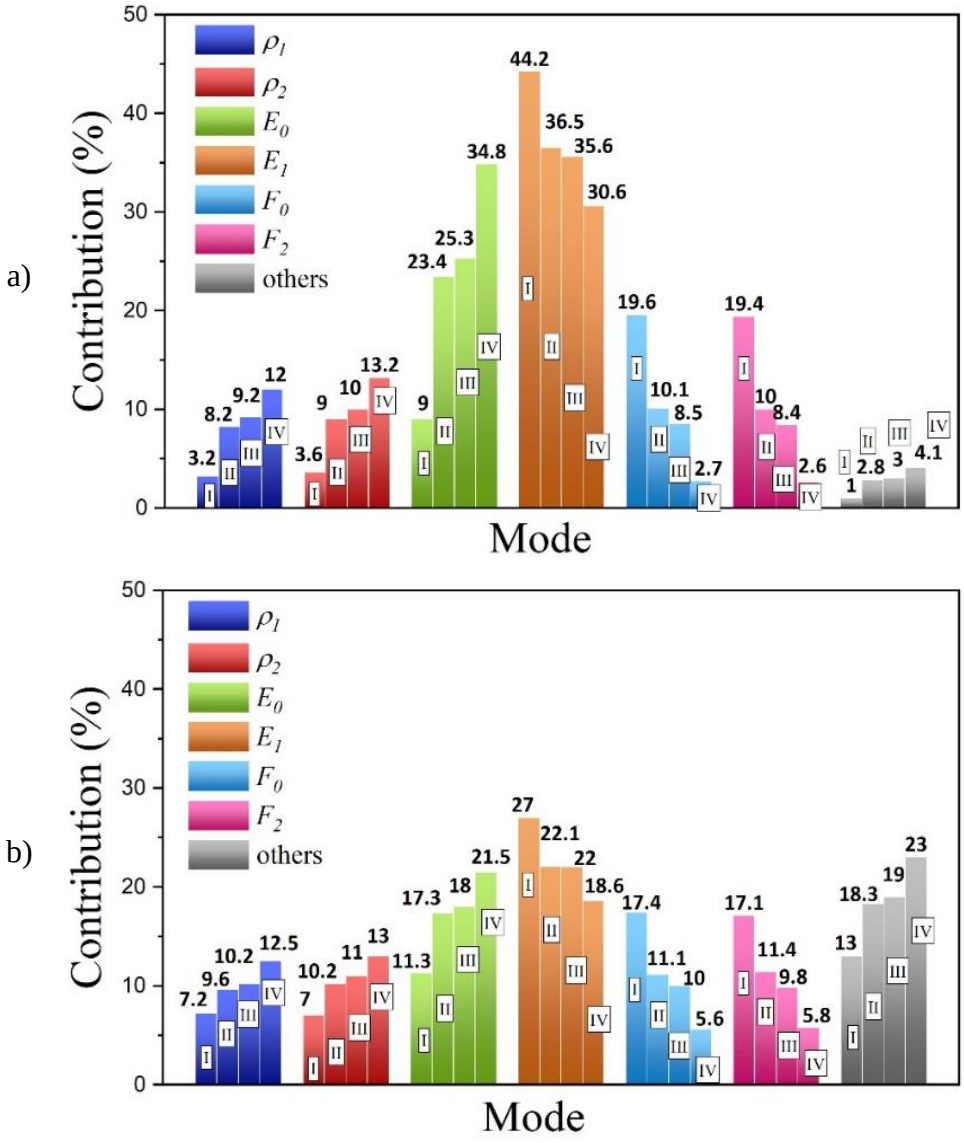

Fig. III.14. Contribution of each uncertainty source (in %) on the second (Nb) film Young's modulus given by: a) Ext-PM and b) Dev-CLBT model.

Furthermore, we can clearly see that, by increasing the mode number, the contribution of the frequency on the film Young's modulus decreases progressively. However, the contribution of the other parameters (E_0, E_1, ρ_1, ρ_2, etc.) increases. Indeed, these parameters are included in the equation of uncertainty propagation for Ext-PM. Especially for a three-layered beam, the first film (Ti) Young's modulus uncertainty presents a significant effect for the determination of the second film (Nb) Young's modulus. It can reach 44 % and 27 % respectively for Ext-PM and Dev-CLBT models. The contribution on the Young's modulus of a thin film becomes higher with the addition of several films. Therefore, this study allows us to conclude that we can use Ext-PM or Dev-CLBT models in all cases for determining the

Young's modulus of each film in the multilayer structure. Their accuracy and uncertainty are similar and better than the other models reported in the literature.

III.4.5.3. Contribution on the coating shear modulus

In the case of film shear modulus, the uncertainties and contributions have been calculated using the Monte Carlo method since Slim and Ext-Slim models present implicit functions. Table III.13 and Table III.14 present the contribution of each source of error on the uncertainty of the shear modulus of the Ti and Nb films respectively. The two tables show that the most influential sources on the measurement of the shear modulus of the films are the film density, the torsional frequencies of the substrate and the composite, and the shear moduli of the precedent layers (substrate and first film). By comparing the two uncertainty analyses on the films Young's and shear moduli, it can be confirmed that the most influential factors on the measurement remain the same with some equivalences. The Young's modulus and the flexural frequencies (in Ext-PM and Dev-CLBT models) correspond to the shear modulus and the torsional frequencies respectively (in Ext-Slim model). These factors have the greatest influence on the measurement of the films elasticity constants.

Table III.13
Contribution of each source of error on the uncertainty of the shear modulus of the Ti film.

Quantity	Contribution	
	GPa	**%**
L	10^{-7}	9.4×10^{-6}
b	10^{-7}	9.5×10^{-6}
h_0	0.02	1.95
h_1	0.04	3.57
ρ_0	4.7×10^{-3}	0.41
$\boldsymbol{\rho_1}$	**0.23**	**22.53**
$\boldsymbol{T_0}$	**0.27**	**26.46**
$\boldsymbol{T_1}$	**0.26**	**25.48**
E_0	10^{-6}	9.6×10^{-5}
E_1	2.96×10^{-7}	2.6×10^{-5}
$\boldsymbol{G_0}$	**0.20**	**19.60**
G_1	1.02	100

Table III.14
Contribution of each source of error on the uncertainty of the shear modulus of the Nb film.

Quantity	Contribution	
	GPa	**%**
L	1.98×10^{-8}	9.8×10^{-7}
b	7.47×10^{-9}	3.7×10^{-7}
h_0	0.03	1.38
h_1	0.03	1.50
h_2	0.02	1.10
ρ_0	0.02	1.22
$\boldsymbol{\rho_1}$	**0.18**	**8.82**
$\boldsymbol{\rho_2}$	**0.20**	**9.73**
$\boldsymbol{T_0}$	**0.23**	**11.37**
$\boldsymbol{T_2}$	**0.24**	**11.65**
E_0	1.7×10^{-8}	8.8×10^{-7}
E_1	2.6×10^{-7}	1.3×10^{-5}
E_2	1.1×10^{-6}	5.4×10^{-5}
$\boldsymbol{G_0}$	**0.42**	**21.03**
$\boldsymbol{G_1}$	**0.65**	**32.20**
G_2	2.02	100

III.5. Conclusions

This chapter was focused on the experimental measurement of the elasticity constants of isotropic thin films in multilayer structure by means of the Impulse Excitation Technique (IET). The mechanical models developed in Chapter II were applied to different coatings. Titanium (4.84 μm) and niobium (3.97 μm) thin films were sputter-deposited on AISI316 steel, glass substrates and silicon wafers. Columnar growth was observed in the films, which gives them a lower density than that of the bulk materials. The structural analysis of the Ti film by X-ray diffraction reveals the presence of two phases: a high stable phase of hexagonal closed packed structure Ti_α and a low metastable phase of body-centered cubic structure Ti_β. The formation of the Ti_β phase can be attributed to the presence of oxygen or carbon in the film.

The Young's and shear moduli of the deposited Ti and Nb films were determined using the developed models and the IET. The Poisson's ratio was determined by assuming that the

elastic behavior of the film is isotropic. A good agreement was found between the obtained moduli and the values reported in the literature. However, some previous studies present values different from the measured ones. This difference might be due to the presence of pores in the two films. However, the presence of the metastable phase Ti_{β} in the titanium film can also alter the elasticity constants of the titanium film. The validation was also performed by comparing the reduced moduli obtained by nanoindentation and IET.

An uncertainty study was carried out according to the recommendations of the ISO standard of the Guide for the expression of Uncertainty of Measurement (GUM). The uncertainty study was applied to titanium and niobium films deposited by magnetron sputtering on the stainless steel substrate (Nb / Ti / AISI316). The measurement uncertainty of the IET represents about 1.1 % for the substrate Young's and shear moduli. The measurement uncertainties on the first and second films Young's moduli were calculated as a function of the frequency mode. By increasing the vibrational mode number, the measurement uncertainty decreases from about 4.4 % to 1.8 % for the first film and from about 9 % to 4.8 % for the second film. The increase of the measurement uncertainties with the addition of another film may be due to the accumulation of uncertainties from the successive films. For the films shear modulus, the measurement uncertainty of the IET represents about 2.38 % and 5.74 % for the Ti and Nb films, respectively. The measured values of the film elasticity constants were lower than the bulk one. This might be due to the presence of pores in the as-deposited films.

In the case of the studied materials, the standard uncertainty on the substrate elasticity constants comes mainly from the uncertainty on its thickness (~79 % of the total uncertainty) and density (~20 % of the total uncertainty). The uncertainty study carried out on the films Young's modulus has shown that the error comes mainly from the measurements of the density of the two coatings, the Young's modulus of the substrate, the Young's modulus of the precedent coating, and the frequency before and after deposition. The same sources of error as for the films Young's modulus were found for the films shear modulus with some equivalences: the flexural frequencies and the Young's moduli were replaced by the torsional frequencies and the shear moduli, respectively.

In this chapter, the macroscopic elasticity constants of titanium film of 4.84 μm thick, consisting of two phases, were determined using IET for a single layer coated beam. Niobium film of 3.97 μm thick was deposited on the bi-coated beam leading to a three-layered beam.

The elasticity constants of the niobium film were determined using the IET, and the methodology proposed for a multilayer structure was approved. In the next chapter, a second step providing the determination of the macroscopic elasticity constants of anisotropic film will be described. The study will be extended to evaluate macroscopically the anisotropic behavior of thin films. Compared to Ext-PM, the Dev-CLBT model can take into account the anisotropy and allow us to develop the vibrational technique (IET) in order to determine the anisotropic moduli of coating in different directions.

Chapter IV

Improvement of the IET to determine the anisotropic elasticity constants of coatings sputter-deposited at oblique incidence

IV.1. Introduction

Thin films, in monolayer or multilayer, often exhibit anisotropy with different properties between the direction perpendicular to the film (z-axis) and the plane of the film (x-y plane). This anisotropy can be attributed to the crystalline texture or the morphology of the grains. In classical PVD/CVD processes, there is generally no (or small) anisotropy in the film plane due to the growth towards the plane normal. The originality of this study is to introduce anisotropy in the plane of the film by tilting substrates. This elastic anisotropy arises inherently owing to the film microstructure developed during deposition. In this context, a new type of coating presenting a broad anisotropy is handled in this chapter wherein the surface anisotropy is utmost. A methodology is developed by improving the IET in order to determine the elasticity constants of a coating having anisotropy in its plane using the IET.

This chapter aims to extend the methodology developed for transversely isotropic coatings to determine their anisotropic constants using the IET. The IET is a reliable technique used for the determination of the film elasticity constants whatever the thickness, the mechanical and the physical properties of the substrate and the film. Firstly, a new model is developed using the Dev-CLBT model (Eq. (II.85)) with anisotropic film. Then, this model is validated by comparison with a Finite Element Model (FEM) taken as a reference. Finally, it is applied to determine the elasticity constants of titanium thin films deposited by magnetron sputtering with GLancing Angle Deposition (GLAD). The morphology and structure of the Ti deposited films are analyzed and the corresponding elasticity constants were correlated to the microstructural properties.

IV.2. Glancing Angle Deposition (GLAD) of thin films

IV.2.1. GLAD technology

Since the appearance of thin-film technology, there has been a growing interest in using the film structure to control its physical properties. Several technological advances have been achieved in terms of surface morphology and film microstructure. Glancing angle deposition technique (GLAD), first reported more than one hundred years ago [Kundt 1886, Kaempf 1905, Bergholm 1913] has been one of the techniques employed to control the structure of thin films. Several studies between the 1950s and 1970s were focused on thin films with tilted columnar

microstructure and the factors controlling its development [König 1950, Knorr 1959, Nieuwenhizen 1966, Dirks 1977]. Kundt et al. [Kundt 1886] recognized that obliquely deposited films exhibit anisotropy in their optical [Holland 1953], electrical [Pugh 1960] and magnetic [Smith 1959] properties. These anisotropic properties were directly associated with the microstructural effect owing to the oblique deposition conditions and were not a side effect of non-uniformity or stress generation in the film. The technique was initially demonstrated in 1995 [Robbie 1995] when the interest in the GLAD process has rapidly grown. Compared with films prepared at normal incidence, the films deposited at oblique incidence exhibit particular properties.

IV.2.1.1. Principle

This technique provides a simple method to design various nanostructured columnar architectures using prevalent processes, such as sputtering or evaporation. The method consists in modifying the substrate inclination to control the ballistic shadowing and nanocrystallized film growth during deposition. The ballistic effect becomes dominant in GLAD extending the total shadow lengths thanks to the oblique deposition geometry. A highly porous film microstructure was developed with directional column growth.

During conventional film deposition, atomic vapor flux strikes and condenses upon a perpendicular substrate with a flat surface (Fig. IV.1(a)) to form a thin film; the deposited film is dense or porous, amorphous or crystalline, depending on the deposition parameters. In GLAD, the substrate is tilted to a glancing angle (Fig. IV.1(b)), thus creating an oblique deposition geometry. The sputtered adatoms arrive at a glancing angle α with respect to the surface normal and then condense on the inclined substrate. They spontaneously form microscopic nuclei (Fig. IV.2(a)). The adatoms are intercepted by growing nanocolumns, which form an angle β with respect to the surface normal. The nuclei grow into columns tilted towards the vapor source due to the ballistic shadowing that prevents incoming vapor from condensing into regions behind the nuclei (Fig. IV.2(b)). These shadowed regions (grey areas) created are thus broadened where no growth occurs.

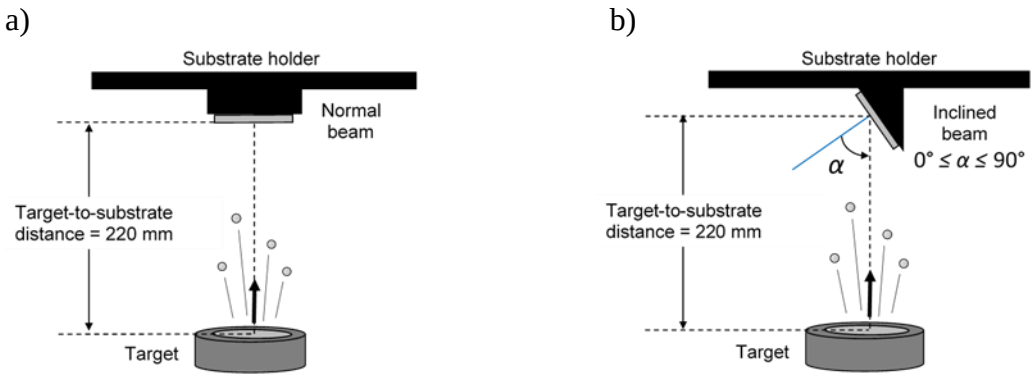

Fig. IV.1. Schematic illustration of PVD configurations in: a) conventional sputtering and b) GLAD sputtering.

The GLAD process can be used under the stationary mode (bottom-up aspect), where columns oriented towards the incoming vapor flux are formed, as discussed before. Along with working pressure, temperature, substrate bias voltage and the deposition rate, an important experimental parameter is used in GLAD to modify the film properties. This parameter is the direction of the incident flux of the deposited species to the substrate surface. It is defined by the angle α formed by the substrate normal and the target normal (Fig. IV.1(b)). The α angle can vary between 0° (normal incidence) and 90° (parallel to the substrate). Furthermore, the GLAD process can be used in dynamic mode (top-down aspect) by employing an additional substrate rotation during glancing deposition. The apparent vapor direction is changed and thus the column growth direction can be manipulated. In this case, more complex film architectures like spiral, zigzag, or nanorods structures can be designed and developed [Hawkeye 2014, Barranco 2016, Dervaux 2017, Antartis 2018].

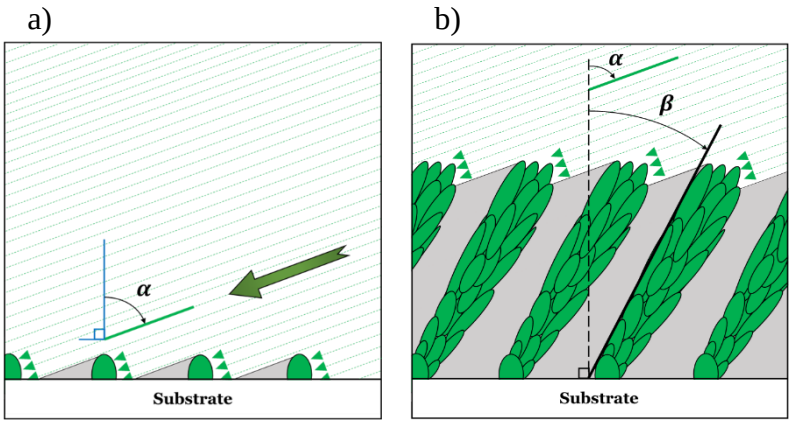

Fig. IV.2. A conceptual view of film growth in the GLAD process.

As the present work is the first to characterize these nanosculptured films with the vibrational technique (IET), the simplest architecture is chosen (i.e. the inclined columns obtained under stationary mode where the substrate position is controlled only by the glancing angle α) among the various GLAD processes.

IV.2.1.2. Controlling the film microstructure

Thanks to their dedicated porosity, texture and anisotropic properties, the GLAD nanostructured thin films were used in many fields. The GLAD coatings are extensively used in optics, thanks to their ability to control the thin film structure on a scale relevant to optical applications [Lakhtakia 2002, Kennedy 2003, Mansour 2010]. Several researchers have elaborated GLAD optical coatings based on controlling the optical anisotropy orientation and thus the refractive index by changing the glancing angle α. Among the optical applications, we cite the birefringent transparent conducting films [Harris 2008], the luminescent devices [Hrudey 2006], the optical filters [Robbie 1997] and the 3D photonic crystals, where the material is precisely structured to form a 3D dielectric crystal lattice [Toader 2001].

Furthermore, GLAD thin films can be applied to sensing applications thanks to their controlled morphology and high porosity. They are used as electrical [Steele 2006], optical [Lakhtakia 2001], gas [Xu 2019b] and mechanical pressure sensors [Kesapragada 2006a]. Many other fields, including catalysis applications [He 2008], energy applications [Bonakdarpour 2008], magnetic materials [Ali 2019], microelectronics [Glassford 1992], neutron phase imaging [Samoto 2019] and nano-mechanical devices [Singh 2004] have used GLAD thin films.

IV.2.2. Mechanical properties of GLAD thin films

The determination of the mechanical properties of these structured thin films was mostly performed by nanoindentation (NI) as a static technique. Among the works in the literature, we can cite those performed on TiO_2-SiO_2 multilayers with different microstructures [Roa 2016], TiO_2 thin films in inclined columns and zigzag multilayers [Jiménez-Piqué 2014, Gaillard 2009], TiAlN tilted columns [Shetty 2011], Cr zigzag multilayers [Lintymer 2005, 2006], and Ti, Cr and SiO thin films as micro springs [Seto 2001]. Gaillard et al [Gaillard 2006] showed that the reduced Young's modulus of Yttria-Stabilized Zirconia (YSZ) thermal barrier coatings are closely related to their columnar microstructure. From these references, the NI technique

simply leads to a global elastic modulus that depends on the elastic moduli in the three directions.

For nanoporous thin films, a new method was developed to determine the indentation modulus using Atomic Force Acoustic Microscopy (AFAM). A recent work [Kopycinska-Müller 2013] has shown a very good agreement between the values of the indentation modulus obtained by the AFAM method and those determined by nanoindentation. Tokas et al. [Tokas 2015] used the AFAM to characterize HfO_2 thin films deposited at glancing angles of 0°, 40°, 57°, 68° and 80°. They found that the indentation modulus increases with a decrease in the glancing angle. More information about the elastic behavior of nanostructured thin films seems inexistent in the literature. Hence, it is important to investigate not only on the elastic properties but also on the plane anisotropy of such films, which are different from conventional films.

In this context, the present chapter aims to propose a new methodology to characterize the elastic anisotropy of thin films deposited with the GLAD technique. This methodology is applied using the impulse excitation technique (IET), which is a dynamic technique, with a newly developed model, based on the laminated beam theory that takes into account the anisotropy of these thin films. The laminated beam theory was previously used to determine the Young's modulus of multilayer thin films as presented in Chapter II.

IV.2.3. Crystallographic orientation

A polycrystalline material is composed of crystallites distributed in the material depending on the elaboration process. The preferential orientation generated during the process can influence the mechanical and physical properties. When depositing a thin film by magnetron sputtering at zero incidences (α = 0°), polycrystalline structure with a preferential orientation can be obtained in zone T or zone 2 (Fig. IV.3) of an extended Structure Zone Model (SZM) [Van der Drift 1967, Thornton 1974]. Different crystallites with random out-of-plane orientation will nucleate. Some crystallites will overgrow the others owing to an anisotropic growth rate that depends on the crystallographic orientation. This phenomenon will evolutionary lead to only one crystallographic out-of-plane orientation with faceted columns. This preferential out-of-plane alignment corresponds either to the geometrically fastest-growing direction in zone T structure or to the plane of the lowest surface energy in zone 2 structure (Fig. IV.3) [Mahieu 2006a].

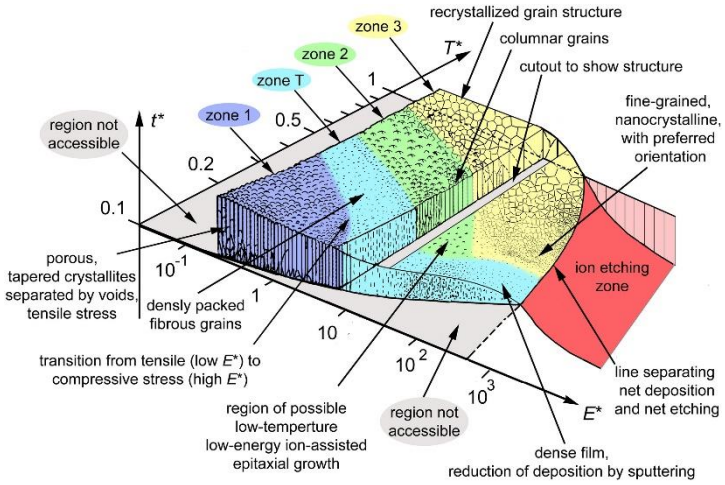

Fig. IV.3. Structure zone diagram applicable to energetic deposition. The reader should avoid reading specific values or predictions since the actual values depend on the material and many other conditions [Anders 2010].

In an oblique deposition, the same phenomenon as that shown for zone T structure at normal deposition appears where the crystallites with the most tilted facets will envelop the other crystallites. The crystallites with the most tilted facets correspond to those having the fastest growing direction perpendicular to the substrate [Mahieu 2006a]. However, no inclination of the columns can develop in zone 2 structure because of the presence of recrystallization and the high surface diffusion, which neglects the shadowing effect and thus the ballistic deposition (β = 0°).

On the other hand, polycrystalline biaxially aligned thin films can be obtained in a glancing deposition. Such thin films have not only a preferential out-of-plane orientation but also an alignment along a direction parallel to the substrate surface known as in-plane alignment. Fig. IV.4 presents the different orientations including the biaxial texture. This texture was already observed on different thin-film material deposited at oblique incidence [Hashimoto 1989, Sato 2001]. The optimization of the degree of out/in-plane alignments leads the film texture to be single-crystalline like. Indeed, several studies on the single-crystalline behavior of Al [Dick 2003], Cu [Kesapragada 2006b], Co [Dick 2000], W_β [Karabacak 2003] and Ti [Liedtke 2018] GLAD thin films, have been performed.

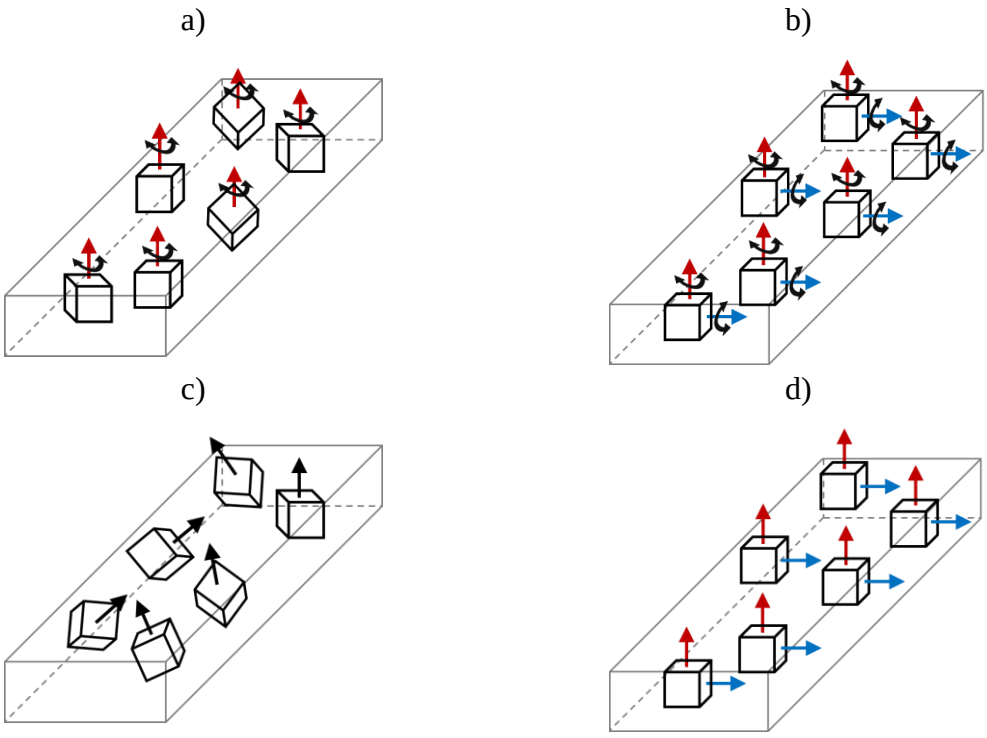

Fig. IV.4. Various texture orientations in crystals: a) fiber texture, b) biaxial texture, c) random orientation and d) single-crystal orientation. The curved double arrows indicate deviations from the preferred directions.

In this work, the crystallographic orientations will be determined from the pole figures plotted using DIFFRAC.TEXTURE software. The pole figures will be represented in stereographic projections. If a lattice has a hexagonal symmetry, the Miller-Bravais [Jackson 1991, Schwarzenbach 2003] indices $(h\ k\ i\ l)$, where $h + k + i = 0$ will be used to define the crystallographic planes of the hexagonal crystal lattice.

IV.3. Measurement methodology of the elastic properties of GLAD films using the IET

The Impulse Excitation Technique (IET) is used to measure the resonance frequencies of a sample impacted by a striker. Flexural, torsional and longitudinal vibration modes can be obtained by vibrating a sample. In the case of thin films, two-steps frequency measurements are performed: for the substrate before deposition, and the whole beam (substrate + film) after deposition. Using a mechanical model that contains the ratio of the two measured frequencies, the density and the dimensions of the substrate and the film, the film elasticity constants can be calculated by an inverse method. The laminated beam theory considers that each layer acts like

a lamina. In our case, it can be applicable for thin films with plane anisotropy under a plane-stress state. This presumption leads to identify the elasticity constants along two perpendicular directions Δ and Π, defined in Fig. IV.5, on the film surface.

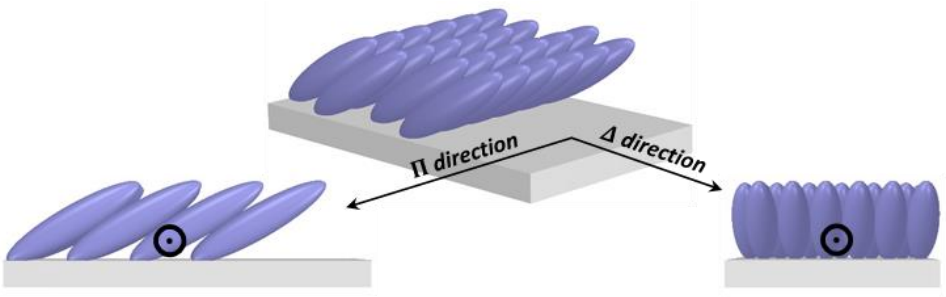

Fig. IV.5. Schematic illustration of the Δ and Π directions.

In the case of anisotropic films, the determination of the elasticity constants along two perpendicular directions seems to be easier by using a plate since it can be easily excited along its two perpendicular directions. This method was used with the IET to determine the anisotropic moduli of a bulk plate [Maletta 2004, Bruno 2006, Gogu 2010, Barkanov 2015]. Contrariwise, the analytical formulations of a plate are rather complex in the case of a bulk plate since they are 2D expressions and require the use of discretization methods and structural optimization with genetic algorithms [Maletta 2004].

In this work, the methodology used consists of depositing different pairs of coatings at an oblique incidence; the x-axis, defined as the longest dimension of the specimen, (resp. y-axis, defined as the transverse dimension) of the first sample coincides with the Δ direction (resp. Π direction). The reciprocal perspective is rather applied for the second sample where the x-axis (resp. y-axis) is parallel to the Π direction (resp. Δ direction), to obtain tilted columns along two different perspectives at a constant glancing angle α (Fig. IV.6). In this way, each pair of beams is vibrated along the x-axis leading to different frequency responses. After that, a simplified 1D model is used for each pair of beams to determine the elastic properties along each direction. This methodology allows us to determine the unknown elasticity constants of the anisotropic film using an analytical model.

a)

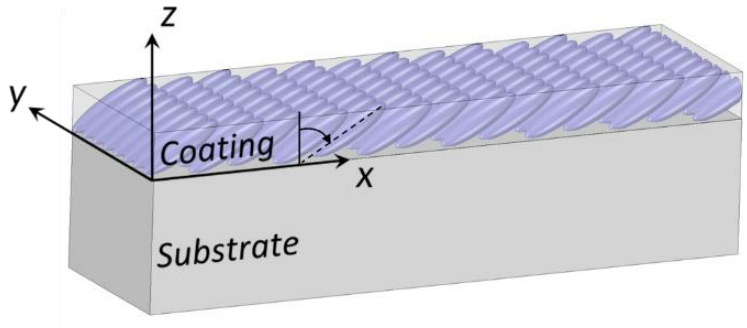

b)

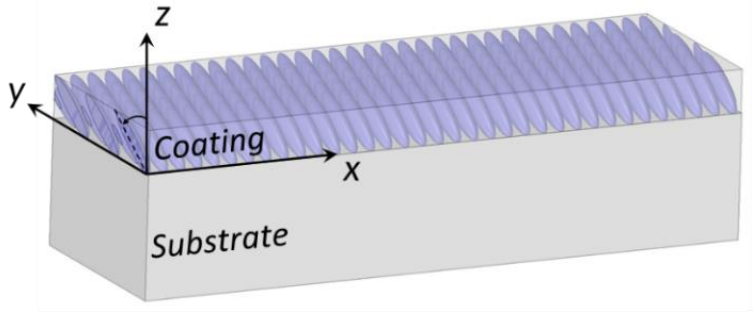

Fig. IV.6. Schematic illustration of the orientation of the columns in a film deposited towards: a) the longitudinal direction (Δ) of the beam and b) the transverse direction (Π) of the beam.

IV.4. Enhanced formulation to determine the elasticity constants of anisotropic coatings

IV.4.1. Homogeneous beam

The flexural and torsional resonance equations of beams were developed to determine the Young's and shear moduli of the isotropic substrate subjected to flexural and torsional vibrations. In the case of a free-free beam with rectangular cross-section, the Young's and shear moduli can be determined from Eqs. (II.6) and (II.32), respectively.

IV.4.2. Developed model for anisotropic coatings

In the literature, two theories were used to develop mechanical models able to determine the Young's modulus of isotropic thin films. The first one is the Flexural Rigidity of a Composite Beam (FRCB), and the second one is the Classical Laminated Beam Theory (CLBT). The difference between the two theories was discussed in Section II.4. Using Eqs. (II.22) and (II.48), the Young's and shear moduli of isotropic thin film can be determined

respectively. The extension of this method to an elastic behavior of anisotropic thin films is presented herein.

For anisotropic film, the Dev-CLBT model (Eq. (II.24)) is extended to consider the corresponding anisotropic properties taking into account the shift of the neutral axis after deposition. For the determination of the shear modulus, Slim's model (Eq. (II.48)) is used based on Hamilton's principle by considering the shift of the neutral axis after deposition.

A simplified 1D model based on the laminated beam theory is developed in this section. It fulfills Kirchhoff hypotheses [Hyer 2009], and it is applicable for thin films with plane anisotropy. Using the plane-stress assumption, three of the six components of stress are generally much smaller than the other three. For a coated substrate, the stresses in the plane of the beam are much higher than the stresses perpendicular to that plane [Hyer 2009]. These negligible components can then be set to zero which simplifies the solution.

From the relation between stresses and strains for the state of plane-stress and taking into account the shift of the neutral axis after deposition, the third-order bending stiffness matrix D_{ij} can be expressed as follows [Hyer 2009]:

$$D_{ij} = \int_{-h_s+e}^{e} \bar{Q}_{ij}^{(s)} z^2 dz + \int_{e}^{e+h_c} \bar{Q}_{ij}^{(c)} z^2 dz \qquad (i,j = 1,2 \; or \; 6) \tag{IV.1}$$

Where:

The indexes s and c refer to the substrate and the coating respectively. $\bar{Q}_{ij}$ are the transformed reduced stiffness elements that are a function of the reduced stiffness elements Q_{ij}. The Q_{ij} elements are a function of the elasticity constants of the corresponding layer. The shift of the neutral axis e, in the case of the two beams, is calculated in unidirectional by taking only the longitudinal component [Gere 2003] of the Young's modulus for each pair of beams, as follows:

$$\begin{pmatrix} e_x \\ e_y \end{pmatrix} = \frac{1}{2} \begin{pmatrix} \dfrac{E_s h_s^2 - E_x h_c^2}{(E_s h_s + E_x h_c)} \\ \dfrac{E_s h_s^2 - E_y h_c^2}{(E_s h_s + E_y h_c)} \end{pmatrix} \tag{IV.2}$$

Working with the x-y axes as principal axes for both substrate and film, the stiffness elements become:

For isotropic substrate [Hyer 2009]:

$$\bar{Q}_{11}^{(s)} = Q_{11}^{(s)} = \bar{Q}_{22}^{(s)} = Q_{22}^{(s)} = \frac{E_s}{1-\nu_s^2} \tag{IV.3}$$

$$\bar{Q}_{12}^{(s)} = Q_{12}^{(s)} = \nu_s\, Q_{11}^{(s)} = \frac{\nu_s E_s}{1-\nu_s^2} \tag{IV.4}$$

$$\bar{Q}_{66}^{(s)} = Q_{66}^{(s)} = G_s = \frac{E_s}{2(1+\nu_s)} \tag{IV.5}$$

For anisotropic film [Hyer 2009]:

$$\begin{pmatrix} \bar{Q}_{11}^{(x)} \\ \bar{Q}_{11}^{(y)} \end{pmatrix} = \begin{pmatrix} Q_{11}^{(x)} \\ Q_{11}^{(y)} \end{pmatrix} = \frac{1}{1-\nu_{yx}\,\nu_{xy}} \begin{pmatrix} E_x \\ E_y \end{pmatrix} \tag{IV.6}$$

$$\begin{pmatrix} \bar{Q}_{22}^{(x)} \\ \bar{Q}_{22}^{(y)} \end{pmatrix} = \begin{pmatrix} Q_{22}^{(x)} \\ Q_{22}^{(y)} \end{pmatrix} = \frac{1}{1-\nu_{yx}\,\nu_{xy}} \begin{pmatrix} E_y \\ E_x \end{pmatrix} \tag{IV.7}$$

$$\begin{pmatrix} \bar{Q}_{12}^{(x)} \\ \bar{Q}_{12}^{(y)} \end{pmatrix} = \begin{pmatrix} Q_{12}^{(x)} \\ Q_{12}^{(y)} \end{pmatrix} = \frac{\nu_{yx}}{1-\nu_{yx}\,\nu_{xy}} \begin{pmatrix} E_x \\ E_y \end{pmatrix} = \frac{\nu_{xy}}{1-\nu_{yx}\,\nu_{xy}} \begin{pmatrix} E_y \\ E_x \end{pmatrix} \tag{IV.8}$$

$$\bar{Q}_{66}^{(x)} = \bar{Q}_{66}^{(y)} = Q_{66}^{(x)} = Q_{66}^{(y)} = G_{xy} \tag{IV.9}$$

Where:

E_x: Young's modulus of the film along the longitudinal direction,

E_y: Young's modulus of the film along the transverse direction,

ν_{xy}: highest Poisson's ratio of the film,

ν_{yx}: lowest Poisson's ratio of the film,

G_{xy}: in-plane shear modulus of the film.

Using the same development as in Section II.4.2 for the isotropic film, the frequency ratio becomes:

$$\begin{pmatrix} R_{F_x} \\ R_{F_y} \end{pmatrix} = \frac{2}{h_s}\sqrt{\frac{3\rho_s}{E_s\,\rho_{eff}}}\begin{pmatrix} \frac{1}{\sqrt{d_{xx}}} \\ \frac{1}{\sqrt{d_{yy}}} \end{pmatrix} \tag{IV.10}$$

Where:

$$\rho_{eff} = \rho_s\, h_s + \rho_c\, h_c \tag{IV.11}$$

$$R_F = \frac{F_t}{F_s} \tag{IV.12}$$

The index t refers to the whole beam,

F_s: first flexural resonance frequency of the naked substrate,

F_t: first flexural resonance frequency of the composite beam (substrate + film),

ρ_{eff}: weighted area density (in kg/m^2),

d_{xx} and d_{yy} represent the (1,1) element of bending matrix $[D]^{-1}$ that can be expressed as:

$$\begin{pmatrix} d_{xx} \\ d_{yy} \end{pmatrix} = \begin{pmatrix} \dfrac{\frac{R_x E_s}{1-\upsilon_s^2} + \frac{H_x\,E_y}{1-\nu_{yx}\nu_{xy}}}{\left[\frac{R_x\,E_s}{1-\upsilon_s^2} + \frac{H_x\,E_x}{1-\nu_{yx}\nu_{xy}}\right]\cdot\left[\frac{R_x\,E_s}{1-\upsilon_s^2} + \frac{H_x\,E_y}{1-\nu_{yx}\nu_{xy}}\right] - \left[\frac{\nu_s\,R_x\,E_s}{1-\upsilon_s^2} + \frac{\nu_{yx}\,H_x\,E_x}{1-\nu_{yx}\nu_{xy}}\right]^2} \\ \dfrac{\frac{R_y\,E_s}{1-\upsilon_s^2} + \frac{H_y\,E_x}{1-\nu_{yx}\nu_{xy}}}{\left[\frac{R_y\,E_s}{1-\upsilon_s^2} + \frac{H_y\,E_y}{1-\nu_{yx}\nu_{xy}}\right]\cdot\left[\frac{R_y\,E_s}{1-\upsilon_s^2} + \frac{H_y\,E_x}{1-\nu_{yx}\nu_{xy}}\right] - \left[\frac{\nu_s\,R_y\,E_s}{1-\upsilon_s^2} + \frac{\nu_{xy}\,H_y\,E_y}{1-\nu_{yx}\nu_{xy}}\right]^2} \end{pmatrix} \tag{IV.13}$$

With:

$$\begin{pmatrix} R_x \\ R_y \end{pmatrix} = \frac{1}{3}\begin{pmatrix} e_x^3 - (-e_x + h_s)^3 \\ e_y^3 - (-e_y + h_s)^3 \end{pmatrix} \tag{IV.14}$$

$$\begin{pmatrix} H_x \\ H_y \end{pmatrix} = \frac{1}{3}\begin{pmatrix} -e_x^3 + (e_x + h_c)^3 \\ -e_y^3 + (e_y + h_c)^3 \end{pmatrix} \tag{IV.15}$$

IV.5. Comparison between the anisotropic model and a finite element model

A 3D finite element model (FEM) was developed using the commercial finite element code ABAQUS [Abaqus 2016] to check the reliability of the developed formulation. A comparison between the developed model and the FEM was performed. The geometrical model is composed of two parts: the substrate and the film. For linear elastic calculations, the 3D stress C3D20 quadratic element was used to mesh the composite beam with free boundary conditions. The same meshing principle as the one used in Section II.5.1, is applied herein. The ABAQUS/Implicit Lanczos eigensolver is used to extract the resonant frequencies of the composite beam. Fig. IV.7 shows the evolution of the frequency ratio R_F as a function of the thickness ratio R_h (Eq. (IV.16)) of the developed and the numerical models for four different anisotropic ratios AR_E (Eq. (IV.17)). The AR_E are chosen to give examples of high and low anisotropy that can correspond to realistic situations.

$$R_h = \frac{h_c}{h_s} \tag{IV.16}$$

$$AR_E = \frac{E_y}{E_x} = \frac{\nu_{yx}}{\nu_{xy}} \tag{IV.17}$$

$$AR_G = \frac{G_{yz}}{G_{xz}} \tag{IV.18}$$

The values of the elasticity constants along the z-axis were assumed equal to those along x or y since there is no influence of the perpendicular direction on the frequency found in the x-y plane. The highest Poisson's ratio of the film ν_{xy} was assumed equal to that for an isotropic material since the Poisson's ratio has a negligible effect on the frequency determined using FEM for isotropic material (Fig. III.10 and Fig. III.11).

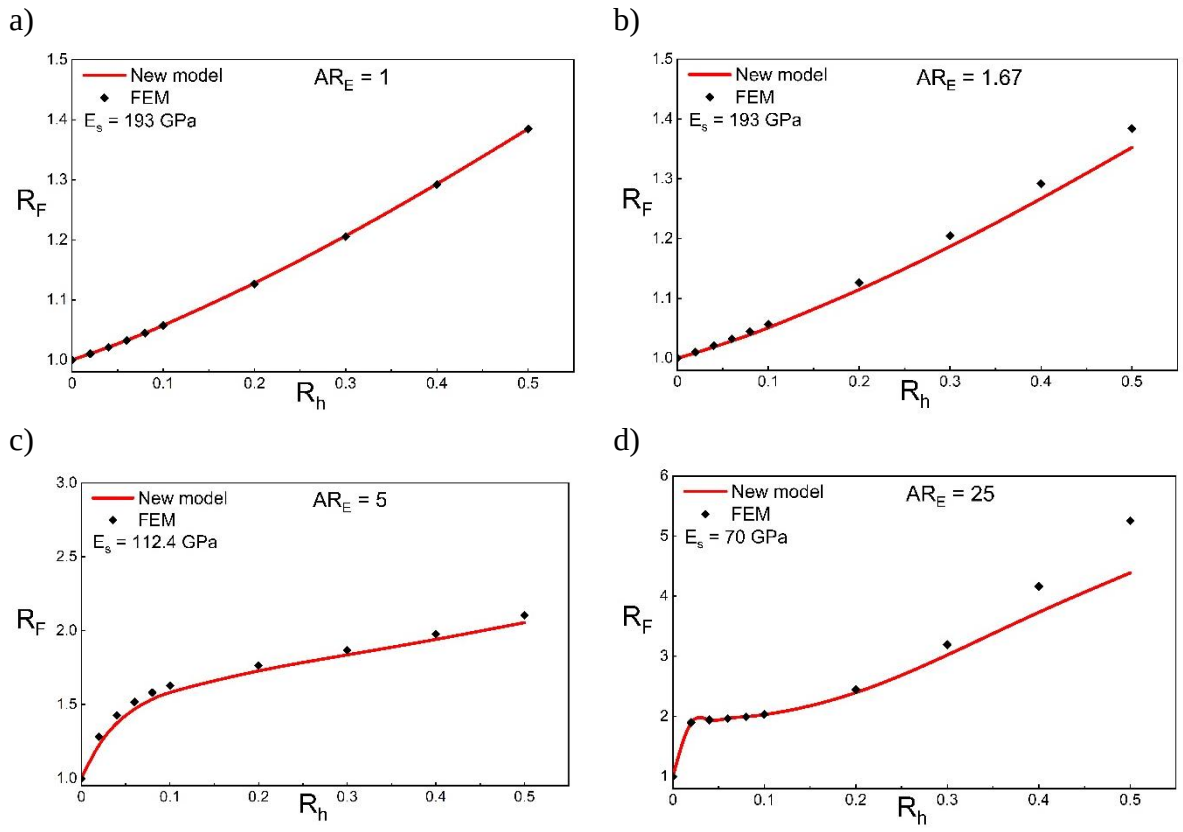

Fig. IV.7. Comparison between the developed analytical model and the numerical model: a) AR_E = 1, b) AR_E = 1.67, c) AR_E = 5 and d) AR_E = 25.

From Fig. IV.7, a good agreement between the developed and the finite element calculations for low thickness ratio R_h can be observed. The difference between the two models increases with R_h and it can be clearly observed in Fig. IV.7(d) where the AR_E is the highest. This could be caused by the plane-stress state assumption on which is based the 1D analytical model while using the 3D FEM that does not make any assumptions. By extracting the stress tensor from the FEM at two different conditions (R_h = 0.1, AR_E = 25) and (R_h = 0.5, AR_E = 25), we found that the two conditions present different stress states and particularly different stresses along the z-axis. With the increase of AR_E, the coupling effect between the directions increases. The developed model neglects the coupling with the third direction (z-axis) that becomes significant owing to the increase in thickness. The difference between the analytical model and the FEM remains approximately constant by increasing the anisotropy ratio at the same substrate and thickness ratio. In the rest of this work, glass substrates were used and the elasticity constants of Ti thin films with R_h < 0.05 were determined using the developed model (Eq. (IV.10)).

IV.6. Experimental procedure and characterization

IV.6.1. Deposition process at oblique incidence

Titanium thin films were deposited on glass substrates and silicon wafers with DC magnetron sputtering technique using a DEPHIS4 Physical vapor deposition (PVD) (Fig. III.2) machine. A high purity (99.99 %) Ti circular target of 200 *mm* diameter was used. The deposition chamber corresponds to a cylinder of 98 liters pumped down with a turbo-molecular pump to less than 10^{-4} *Pa* before filling it with argon. The series was processed at a total working pressure of 0.35 *Pa* (Ar flow rate: 30 *sccm*) with a deposition time of 180 *min*. The intensity applied to the Ti target was 1.5 *A* using a DC-pulsed power supply. The target-to-substrate average distance was 22 *cm* (Fig. IV.1(b)).

Before the deposition process, the substrates were ultrasonically cleaned in acetone and ethanol for 10 *min*. The Ti target was sputter-cleaned for 15 *min* in pure Ar discharge, while a shutter shielded the substrates. Different aluminum holders, inclined with respect to the main plate holder, were fabricated to vary the glancing angle α of the substrates. The holders used carried three orientations α = 0°, 45° and 80° for deposition with respect to the target normal as illustrated in Fig. IV.1. These three orientations were chosen to analyze different critical configurations. The substrates were located on the holder in specific positions in order to minimize self-shadowing [Hawkeye 2014, Barranco 2016]. Fig. IV.8 shows a top view of the Ti target with the position of holders and substrates. Glass substrates were used for the IET and NI characterizations and silicon wafers for the Scanning Electron Microscopy (SEM) images. The dimensions of glass substrates are: length L = 75 *mm*, width b = 25 *mm* and thickness h_s = 1 *mm*.

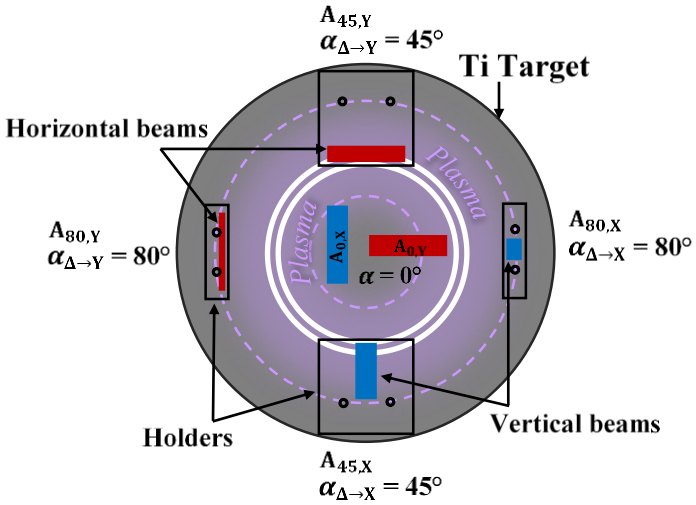

Fig. IV.8. Top-view experimental setup showing the Ti target with a projection of the holders and substrates positions. The samples in red correspond to the horizontal beams. The samples in blue correspond to the vertical beams.

IV.6.2. Morphology

The grain morphology of the deposited titanium films was analyzed using a Hitachi S3500 N SEM-FEG electron microscope. Fig. IV.9(a) shows the cross-sectional SEM images of the Ti films sputter-deposited with respect to the longitudinal direction. The growth morphology of all films exhibits a well-defined columnar growth, as commonly observed for Ti films [Sit 1999, Barranco 2016, Siad 2016, Alvarez 2016, Dervaux 2017, Pedrosa 2017, Sadeghi-khosravieh 2017, Alvarez 2019]. For normal incidence (α = 0°), the resulting structure is only slightly porous since no significant shadowing is achieved and the micro-columns are not separated. As the glancing angle increases, the shadowing effect increases progressively and the structure becomes more porous. With increasing the deposition glancing angle α, the inclination of the columns with respect to the substrate normal increases. The angle between the columns and the substrate normal is defined by β (Fig. IV.9(a)). It is noticeable that the columns boundaries become more distinctive with increasing glancing angle α. In the beginning, a self-shadowing of the initial particles was formed on the substrate surface. These nuclei keep growing to form successive columns separated by voids due to the inclination that favors the shadows.

The surface topography of the films is shown in Fig. IV.9(b). The film surface is considerably influenced by the glancing angle α as mentioned in the literature [Vick 2002, Mahieu 2006a, Barranco 2016, Dervaux 2017, Bouaouina 2018]. At normal incidence (α = 0°), the tops of the columns appear at the film surface with circular facets suggesting a low inter-columnar porosity. As the glancing angle increases, the shadowing effect predominates and the gap between columns significantly increases, providing a higher fraction of inter-columnar porosity. It is necessary to notice that an in-plane anisotropic shadowing is formed, which is the aim of the GLAD technique. Besides, all the columns face the incoming flux, indicated by an arrow. This can be clearly visible with the in-plane arrangement of the columns at α = 80°, for which, the columns are well distributed in the transverse direction of the incident flux [Vick 2002, Lopez-Santos 2016].

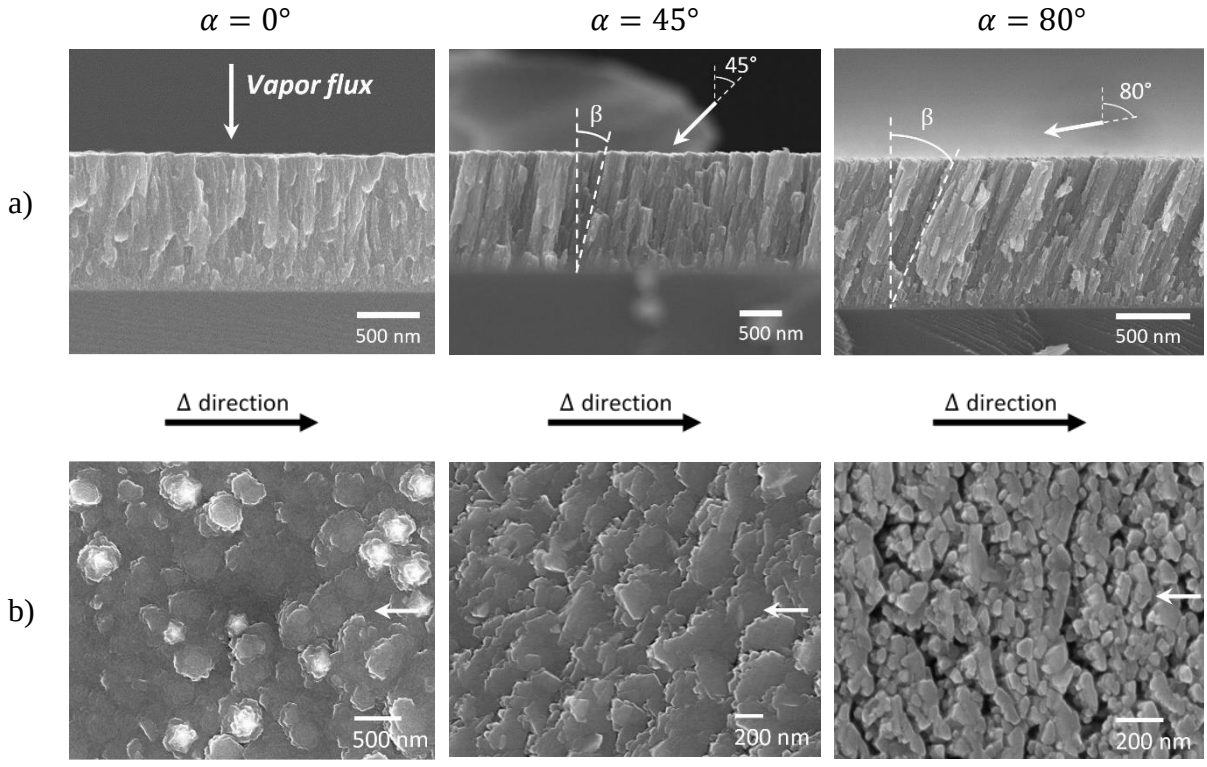

Fig. IV.9. Cross-section (a) and top view (b) SEM images of Ti films grown by glancing angle deposition at various glancing angles α (0°, 45° and 80°).

The column tilt angle β is ordinarily lower than the glancing angle α due to the shadowing effect [Abelmann 1997] and it is measured from the cross-sectional SEM images using ImageJ software [ImageJ 2017], shown in Table IV.1. In order to improve the accuracy of the measured values of β, the average of ten column tilt angle measurements was taken. The

measurement uncertainty of β was estimated from the standard deviation over the ten columns. The experimental β values can be compared with several models proposed in the literature providing different predictive relationships between α and β. One of them is called "tangent rule" (Eq. (IV.19)), which is a semi-empirical formula [Nieuwenhizen 1966, Hawkeye 2014], and it is applicable only for $\alpha < 50°$ since it is not derived from a physical model [Dirks 1977, Hawkeye 2007, Besnard 2010]:

$$\tan \beta_{tan} = \frac{1}{2} \tan \alpha \tag{IV.19}$$

Another relationship was reported to provide a physically based description of the growth mechanism with a geometrical analysis of the inter-columnar geometry. It is called "cosine rule" and was derived by Tait et al. [Tait 1993] as follows:

$$\beta_{cos} = \alpha - \arcsin\left(\frac{1 - \cos \alpha}{2}\right) \tag{IV.20}$$

This is a purely geometrical equation and takes into account the ballistic shadowing growth mechanism without considering the growth kinetics [Hawkeye 2014].

Table IV.1
Microstructural properties of the Ti thin films.

Sample	Deposition Δ direction	Glancing angle	Column tilt angle			Fiber tilt angle		Film thickness	
		α (±2°)	β_{exp} (±3°)	β_{cos} (±2°)	β_{tan} (±2°)	η (°)	u(η) (°)	h_c (µm)	u(h_c) (µm)
$A_{0,X}$	X-axis	0	0	0	0	5.34	0.05	1.101	0.02
$A_{0,Y}$	Y-axis	0	0	0	0	3.97	0.03	1.172	0.02
$A_{45,X}$	X-axis	45	10	31	39	20.62	0.03	1.472	0.011
$A_{45,Y}$	Y-axis	45	8	31	39	26.47	0.04	1.391	0.022
$A_{80,X}$	X-axis	80	23	46	77	45.90	0.03	1.015	0.015
$A_{80,Y}$	Y-axis	80	29	46	77	46.37	0.02	0.914	0.013

For a glancing angle of 45° and 80°, the shadowing effect becomes significant and the columns are tilted approximately by 10° ± 3° and 23° ± 3° respectively as shown in the cross-

sectional SEM images (Fig. IV.9(a)). The values of the experimental column tilt angle are closed to those reported in the literature for Ti films [Siad 2016, Pedrosa 2017, Dervaux 2017, Alvarez 2019]. At low sputtering pressures (0.2 Pa - 0.4 Pa), Pedrosa et al. [Pedrosa 2017] found column tilt angles between 15° and 40° for α = 80°. Alvarez et al. [Alvarez 2019] showed that β varies between 34° and 52° depending on the sputtering power. The column tilt angle depends on different parameters. The difference between the column tilt angles can be attributed to the angular spread of the incoming adatoms owing to the collisional transport process [Mahieu 2006a]. The sputtered particles can collide with the Ar gas atoms during transport from the target to the substrate and hence change its initial direction leading to a spreading of the angular distribution of particles when arriving at the substrate. Alvarez et al. [Alvarez 2014] proposed another phenomenon that can explain the low values of column tilt angle. The phenomenon associates the β angle to the surface trapping probability s_t by a mechanism attributing the low β angle (low shadowing effect) to the increase of s_t [Alvarez 2014].

Compared to the theoretical values of β_{cos} and β_{tan}, the experimental column tilt angle β presents large deviations (Table IV.1). This can be due to the ballistic parameters that affect the column tilt angle like the working pressure [Okamoto 1987, Pedrosa 2017, Dervaux 2017, Bouaouina 2018], the crystalline structure [Siad 2016], the temperature [Sadeghi-Khosravieh 2017], or the geometry of the target [Siad 2016]. Furthermore, Zhu et al. [Zhu 2012] have proved that the column tilt angle β depends on the material type and thus, the two laws (Eqs. (IV.19) and (IV.20)) cannot be general. Furthermore, Siad et al. [Siad 2016] proved that the incidence angle of the incoming particles should be used instead of the substrate angle (α) since it cover the chamber and target geometries (substrate inclination and the particle transport). They also mentioned that the two angles could be merged in some particular conditions, i.e. low pressure or small vapor sources. In this work, the substrate inclination angle is used as glancing angle α, and it was directly measured from the substrate-holder.

The film thickness was measured from the cross-sectional SEM images. Note that the film thickness is defined as the vertical thickness of the film (i.e. measured along the substrate normal), which may be different from the length of a column element depending on the column shape and orientation. From Table IV.1, we can notice that the thicknesses of the Ti films deposited at a constant glancing angle are not equivalent to the same deposition conditions. This can be explained by the different locations of the substrates on the GLAD holder (Fig. IV.8). Several works [Sit 1999, Buzea 2005, Wakefield 2007] have studied the uniformity of

the GLAD films as a function of the substrate position. The same configuration as Fig. IV.8, where the substrates were placed along the longitudinal and the transverse directions, was used. They found that the uniformity of the GLAD films varies with the structure and the glancing angle. For a constant glancing angle, a significant difference between the longitudinal and transverse directions was observed. They also found that an increase in α will lead to larger thickness variations in the longitudinal direction than in the transverse one, which represents the same observation as the Ti films in our case (Table IV.1).

IV.6.3. Crystalline structure and texture evolution of the deposited thin films

In order to characterize the crystalline structure of the Ti films, a Bruker D8 Advance diffractometer equipped with a CuKα tube radiation (λ = 0.15418 *nm*) and operated at 40 *kV* and 40 *mA* was used to acquire X-ray diffraction patterns (XRD) (Fig. III.7). A point focus mode with a 1 *mm* collimator was used for the incident beam. The diffractometric angle 2θ was varied between 30° and 150°. As thin films sputter-deposited by magnetron sputtering had generally non-random crystallographic orientation, an experimental protocol was adopted in order to diffract all the planes families $\{hkil\}$. It consists of diffracting the film along different measurement directions (ϕ,ψ). In order to acquire the sum of the X-ray diffraction patterns as well as pole figures, the azimuthal angle ϕ was varied between 0° and 360°, and the tilt angle ψ was varied between 0° and 70°. The equal-area projection method [Matthies 1992, Kocks 1998] was used to define the measurement increment (step) on the (ϕ,ψ) angles. The resolution was taken equal to 10° for the azimuth and tilt angles.

The XRD patterns of the deposited titanium films are shown in Fig. IV.10, for the three values of the glancing angle α. The identification of the titanium film phases was performed on the sum of the diffraction patterns collected in the range of azimuth and tilt angles mentioned above. It can be clearly seen that all structures exhibit a single hcp (hexagonal closed packed) Ti_α stable phase, compared to the reference powder diffraction data (COD CIF file 1532765). This structure was observed on pure titanium films deposited by different techniques [Savaloni 2004, Chawla 2008, Sadeghi-Khosravieh 2017, Liedtke 2018]. It can be noted that the relative intensity of the (0002) diffracted plane is higher than that of the reference data. As we will see in the texture analysis below, it is due to a $[0002]$ preferential orientation developed in the Ti films.

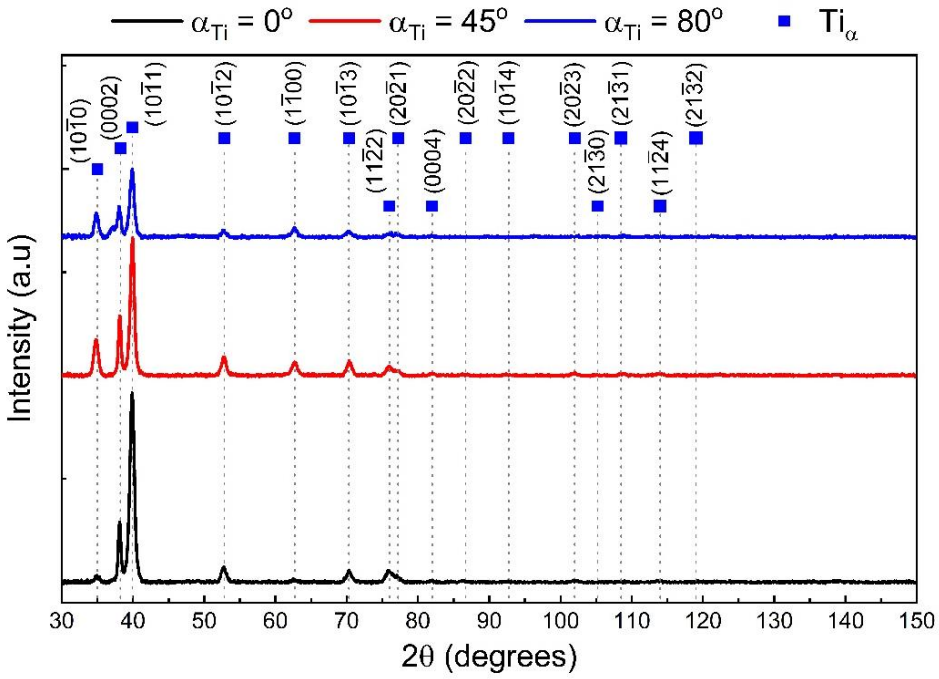

Fig. IV.10. Sum of the X-ray diffraction patterns of titanium films grown for the three values of glancing angle α (0°, 45° and 80°).

Fig. IV.11 shows the experimental pole figures drawn with the DIFFRAC.TEXTURE software and measured for two diffraction peaks that correspond to $\{0002\}$ and $\{10\bar{1}1\}$ planes of the Ti_α phase. In order to perform the texture measurements, the samples were placed on the XRD stage so that the incident flux direction lies with the goniometer azimuthal angle ϕ of 270°. This direction was chosen as a reference for all samples and the black arrows shown in Fig. IV.11, correspond to the incident flux direction. At normal incidence (α = 0°), the pole figure of the $\{0002\}$ plane exhibits a maximum diffracted intensity approximately at the center with a small inclination of 7° $\pm$ 3°. This small deviation of the texture is usual in such sputtering processes and can be due to small angular spread between the substrate normal and the vapor flux direction [Sohn 1994, Slim 2019]. Besides, the $\{10\bar{1}1\}$ pole figure shows a ring around the 7° shifted center with an inclination angle ψ of 61.3° $\pm$ 0.5°, which is coherent with the angle between (0002) and $(10\bar{1}1)$ planes in a hexagonal symmetry. It shows an out-of-plane fiber texture of the film along the $[0002]$ direction that explains the high intensity of the (0002) diffracted plane shown on the XRD pattern. These indications show that the crystalline growth is faster along the c axis of the crystal than along other directions.

The experimental pole figure of the {0002} plane in Fig. IV.11(a) shows that the fiber axis is tilted by 30° ± 3° for α = 45° and 47° ± 3° for α = 80° with respect to the surface normal towards the direction of the incoming vapor flux. During the initial nucleation, each nucleus grows on the substrate, forming crystals with a random orientation before the collision between neighboring crystals. When the diffusion from one crystal to another occurs, the crystal providing the most tilted (variant) facets will predominate [Mahieu 2006a, Sadeghi-Khosravieh 2017, Liedtke 2018]. Then, this prevalent crystal will cover the neighbors allowing an out-of-plane texture of the film with its own preferential orientation. This phenomenon is influenced not only by the geometry of the vapor incident flux but also by the kinetics of crystallite growth. The reader can refer to Section IV.2.3 for more explanation about the formation of the out-of-plane texture.

This tilting of the fiber axis with respect to the film normal was also shown in Ti [Sadeghi-Khosravieh 2017], Cr [Elofsson 2014], Mo [Chen 2012, Liedtke-Grüner 2019], Mg [Tang 2007], HfN [Abadias 2019b], TiN [Bouaouina 2018], AlN [Dellas 2006, Deniz 2007], TiAlN [Shetty 2012] thin films. Despite the presence of a preferential out-of-plane orientation, these studies indicate the presence of in-plane alignment in thin films when tilting the substrate with respect to the material flux i.e. glancing deposition [Hashimoto 1989, Sato 2001, Mahieu 2006a]. The development of the biaxial alignment in thin films is well explained by Mahieu et al. [Mahieu 2006a]. Therefore, the absence of the in-plane orientation is well noticed in the experimental pole figures of the Ti_α phase (Fig. IV.11). This can be due to the deposition parameters that can limit the development of the in-plane orientation [Mahieu 2006a]. Among the parameters that influence the degree of in-plane alignment: the working pressure, the target-to-substrate distance, the glancing angle α, the film thickness h_c, and the degree of unbalancing of the magnetron [Mahieu 2006b, Ghekiere 2006]. Thereby, these parameters can influence the angular spread on the incoming flux and/or the mobility of the adatoms at the surface and thus the resulting in-plane alignment.

The fiber tilt angle η of the Ti grown films of each sample is listed in Table IV.1. It is noticeable from Table IV.1 that the angle calculated using the well-known “cosine rule” is in coherence with the experimental fiber tilt angle η at least in the present case. This is being explained by the physical approach on which is based the “cosine rule” [Tait 1993]. Furthermore, the fiber tilt angle η is not equal to the column tilt angle β as can be seen in Table IV.1, i.e. the crystalline growth direction does not correspond to the column growth direction.

The observations reported in the literature for the hcp crystallites show that the texture formation strongly depends on the material component [Hagemeyer 1993]. For instance, the two axes (column axis and c-axis) are not equal for Ti-hcp films [Sadeghi-Khosravieh 2017, Liedtke 2018] and in contrast, can coincide for Co-hcp in Co-Cr films [Hagemeyer 1993] and Mg-hcp films [Tang 2007]. Fig. IV.12 illustrates the microstructural configuration found in our case.

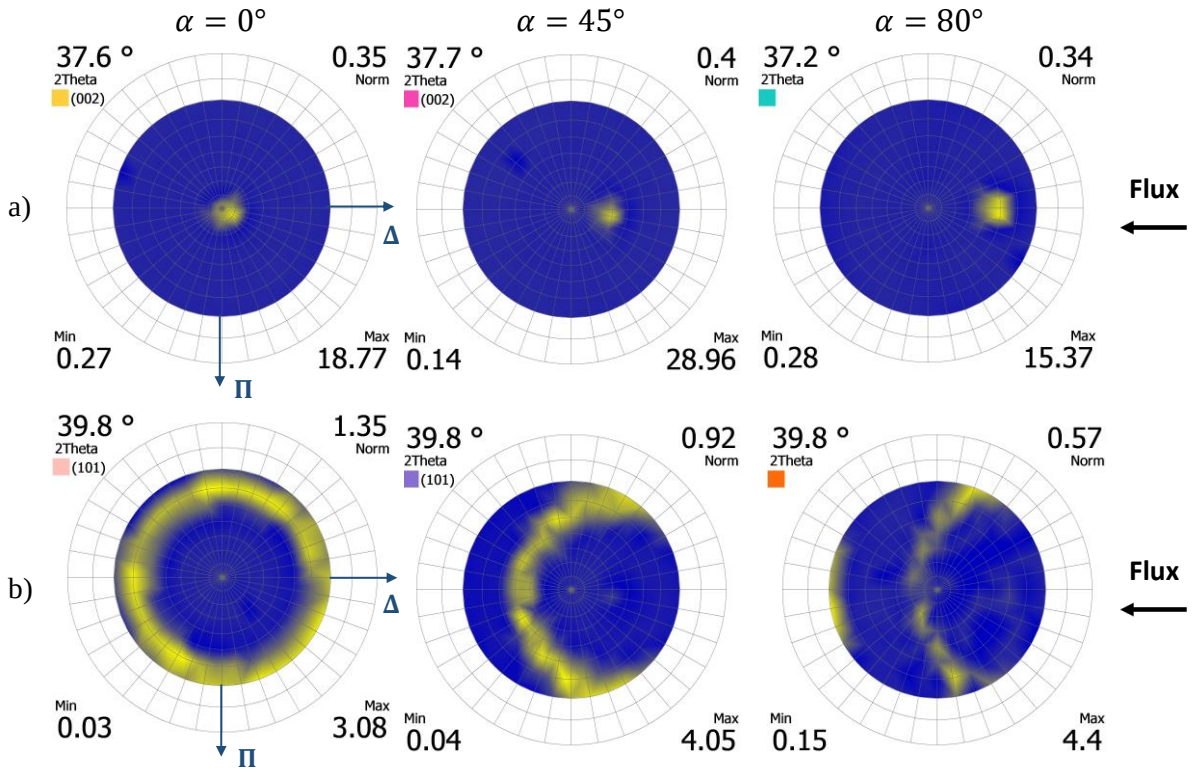

Fig. IV.11. {0002} (a) and $\{10\bar{1}1\}$ (b) experimental pole figures of the Ti_α phase by glancing angle deposition at various glancing angles α (0°, 45° and 80°). The pole figures are represented in stereographic projections and the black arrows at the right of the figures show the vapor flux direction.

The XRD measurements were performed on samples deposited along the longitudinal direction. Very similar XRD patterns and pole figures measurement were also observed on the second sample of each pair of the specimens that are deposited toward the transverse direction i.e. the x-axis of the samples is parallel to the Π direction. These pole figures show the presence of an in-plane anisotropic structure of the film. This requires the use of the developed model (Eq. (IV.10)) in order to determine the elasticity constants of these anisotropic coatings.

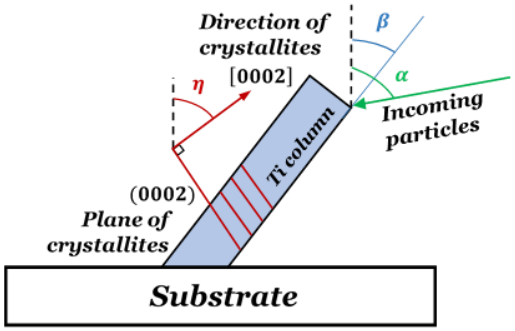

Fig. IV.12. Illustration of an obliquely deposited tilted Ti thin film with columnar growth (column tilt angle β), inclined fiber texture (fiber tilt angle η) and glancing angle α.

IV.7. Determination of the elasticity constants of the titanium anisotropic coatings

IV.7.1. Results

The flexural and torsional resonance frequencies of the samples, measured by the IET before and after deposition, are presented in Table IV.2. The elasticity constants of the glass substrates (assumed isotropic) were determined using Eqs. (II.6) and (II.32), and they are listed in Table IV.3. The uncertainty analysis was performed using the guidelines of the expressions of uncertainty in measurement [JCGM 2008]. It precisely estimates the main sources of uncertainty: thickness and density (Fig. III.12, Table III.12), as detailed in the literature [Slim 2017a]. The main uncertainty values u(x) of the substrate elasticity constants are also listed in Table IV.3. The uncertainties u(x) are the standard uncertainties, i.e. they correspond to one standard deviation.

Table IV.2
Resonance frequencies of glass substrates measured by IET before and after the deposition of the Ti films.

Sample	Flexural resonance frequencies (Hz)		Torsional resonance frequencies (Hz)	
	Before deposition	After deposition	Before deposition	After deposition
$A_{0,X}$	1005.28	1006.19	1860.60	1861.35
$A_{0,Y}$	1006.55	1007.63	1861.55	1862.82
$A_{45,X}$	1018.51	1019.56	1886.91	1888.32
$A_{45,Y}$	1008.74	1009.91	1867.09	1868.02
$A_{80,X}$	1004.35	1003.78	1858.15	1858.61
$A_{80,Y}$	1017.73	1017.76	1884.86	1884.45

Table IV.3
Macroscopic elasticity constants of the glass substrates (assumed to be elastically isotropic).

Sample	E_s (GPa)	u(E_s) (GPa)	G_s (GPa)	u(G_s) (GPa)	ν_s	u(ν_s)
$A_{0,X}$	67.53	0.21	27.381	0.079	0.233	0.005
$A_{0,Y}$	67.92	0.20	27.443	0.078	0.238	0.005
$A_{45,X}$	67.75	0.19	27.397	0.077	0.236	0.005
$A_{45,Y}$	67.53	0.20	27.337	0.077	0.235	0.005
$A_{80,X}$	67.42	0.21	27.262	0.078	0.236	0.005
$A_{80,Y}$	67.79	0.19	27.416	0.076	0.236	0.004
Average	67.66	-	27.373	-	0.236	-
Standard deviation	0.19	-	0.065	-	0.002	-

The Young's moduli E_x and E_y of the titanium films were determined by solving the developed formulation (Eq. (IV.10)) assuming $\nu_{xy} = \nu_{isotropic} = 0.32$ [Leonhardt 2004] and $\nu_{yx} = \nu_{xy}\frac{E_y}{E_x}$ [Hyer 2009]. The shear moduli G_{yz} and G_{xz} of the titanium films were determined using (Eq. (II.48)) with E_x and E_y respectively. The shear moduli were determined by taking the corresponding Young's modulus and using the isotropic model. Using the x and y components, the torsional vibrations are produced in y-z and x-z planes respectively. Table IV.4 and Table IV.5 present the elasticity constants and the anisotropic ratios AR_E (Eq. (IV.17)) and AR_G (Eq. (IV.18)) with their corresponding uncertainty u(x) as a function of the glancing angle α. For the sake of comparison, the Young's moduli of the Ti films were also determined using Eq. (II.22) by assuming the isotropic behavior of the film.

Table IV.4
Macroscopic Young's moduli of the deposited titanium films at various deposition glancing angles.

Sample	E_x (GPa)	$u(E_x)$ (GPa)	E_y (GPa)	$u(E_y)$ (GPa)	AR_E (Eq. (IV.17))	$u(AR_E)$	$E_{isotropic}$ (GPa)	$u(E_{isotropic})$ (GPa)
$A_{0,X}$	88.77	8.72	-	-	0.95	0.13	88.07	5.97
$A_{0,Y}$	-	-	84.71	8.59			85.43	6.05
$A_{45,X}$	82.96	7.39	-	-	0.95	0.15	82.16	4.34
$A_{45,Y}$	-	-	78.42	9.82			79.22	6.18
$A_{80,X}$	31.79	6.40	-	-	1.44	0.46	34.39	3.98
$A_{80,Y}$	-	-	45.86	7.44			43.47	8.87

Table IV.5
Macroscopic shear moduli of the deposited titanium films at various deposition glancing angles.

Sample	G_{yz} (GPa)	$u(G_{yz})$ (GPa)	G_{xz} (GPa)	$u(G_{xz})$ (GPa)	AR_G (Eq. (IV.18))	$u(AR_G)$
$A_{0,X}$	27.92	1.34	-	-	0.96	0.06
$A_{0,Y}$	-	-	29.10	1.38		
$A_{45,X}$	30.20	0.96	-	-	1.26	0.08
$A_{45,Y}$	-	-	23.98	1.34		
$A_{80,X}$	23.52	2.14	-	-	2.26	0.39
$A_{80,Y}$	-	-	13.08	2.02		

IV.7.2. Discussions

The macroscopic elasticity constants of the glass substrates are consistent with the values calculated in Chapter III (Table III.5) and the literature [Rouxel 2007, Gadaud 2009, Slim 2017b]. In this chapter, the average measurements of the thickness and the density were precisely calculated by taking 15 measurements, as they strongly contribute on the measurement of the substrate elasticity constants. Therefore, the uncertainties on the substrate elasticity constants presented in Table IV.3, are found lower than those found in Chapter III (Table III.5).

The values of the titanium film Young's modulus, presented in Table IV.4, varied from 31.79 *GPa* to 88.77 *GPa*. The values published in the literature for Ti thin films are highly

dispersed: the values found in this chapter are consistent with some of them (61 $GPa < E <$113 GPa) [Leonhardt 2004, Tsuchiya 2005] and differ from the values calculated in Chapter III (Table III.6) (97 $GPa < E <$112 GPa) and some others (~115 GPa) [Chinmulgund 1995, Savaloni 2004]. The values of the titanium film shear modulus, presented in Table IV.5, are lower than the values found in Chapter III (~42.64 GPa) and the bulk material (45.6 GPa) [Brandes 1992]. These differences in moduli can be due to the influence of the GLAD process on the elastic properties. However, we can notice that the anisotropic Young's moduli are in good agreement with those calculated by assuming isotropic material of the coating. This can be explained by the negligible effect of the elastic coupling between E_x and E_y, defined in d_{xx} and d_{yy} of Eq. (IV.13).

These results allow us to conclude that the IET leads to a correct value of Young's modulus toward a proper direction i.e. the longitudinal direction even if it is used with the isotropic model instead of the anisotropic one. Upon increasing the glancing angle, the anisotropic ratios AR_E and AR_G increase owing to different factors, among which the non-standard columnar growth and the inclined crystallites toward the vapor flux direction. Another deposition series (samples B) was performed (the details of the microstructural analyses are shown in Chapter V with the same conditions as the present series (samples A) but at 0.42 Pa of working pressure and target-to-substrate distance of 22 cm. The same conclusions can be established to the second deposition series (samples B) and the results of the elasticity constants of samples B will be presented in Chapter V, where they will be used for comparison.

IV.7.3. Effect of film porosity on the elasticity constants

In order to quantify the influence of porosity on the elasticity constants of the Ti film, it is necessary to determine the elasticity constants using a model that takes into account the material porosity. Several models were developed in the literature, based on different assumptions [Schrooten 1999, Vasechko 2016]: the empirical model [Duckworth 1953, Spriggs 1961, Luo 1999] and the one obtained from the first-order Taylor series expansion of different micromechanical models [Nemat-Nasser 1993].

The empirical model is a function of a k constant that is encountered by several disputations and seems dependent on different parameters. Some studies show that this k constant depends on the material type, the elaboration process, the technique of measurement

and the porosity [Spriggs 1961, Luo 1999], and it is thus hardly a constant. Other works used the empirical model with k equal to 7 regardless of material [Anya 1997]. However, the developed relations proposed by Nemat-Nasser et al. [Nemat-Nasser 1993] were inferred from several models with spherical pores. They are independent of experimental factors and are applicable for low volume fraction of pores having a spherical shape, far enough from each other. In the following, Eq. (IV.21) and Eq. (IV.22) [Nemat-Nasser 1993] are used to determine the elasticity constants of the Ti films as follows:

$$E^* \approx E_0(1 - 3p) \tag{IV.21}$$

$$G^* \approx G_0\left(1 - \frac{4p}{1 + \nu_0}\right) \tag{IV.22}$$

Where:

E^*, G^*: Young's and shear moduli of the material with porosity,

E_0, G_0, ν_0: Young's, shear moduli and Poisson's ratio of the material that are free of pores (here we used E_0 = 116 GPa [Leonhardt 2004], ν_0 = 0.32 [Leonhardt 2004], $G_0 = \frac{E_0}{2\,(1+\nu_0)}$),

p: volume fraction of porosity.

The volume fraction of porosity within the Ti films is estimated as follows [Duckworth 1953, Spriggs 1961, Luo 1999, Slim 2019]:

$$p = 1 - \frac{\rho_c}{\rho_0} \tag{IV.23}$$

Where:

ρ_c: film density,

ρ_0: bulk density without pores. For bulk titanium, the bulk density used to calculate the volume fraction is 4500 kg/m^3 [Brandes 1992, Verkhovtsev 2013].

Furthermore, the porosity in the film deposited in GLAD sputtering can be compared to that deposited in conventional sputtering. The relative void fraction, in the former case, is primarily predicted via geometric shadowing analysis of oblique deposition using the following expression [Tait 1993]:

$$p_\alpha = 1 - \frac{2\cos\alpha}{1+\cos\alpha} \tag{IV.24}$$

In this study, the volume fraction of porosity is calculated using Eq. (IV.23) by comparing the film density to the bulk one. The film density was determined by dividing its mass over its volume. The film mass was determined by subtracting the mass of the substrate alone from the mass of the composite beam after deposition. The dimensions were measured taking the average over ten measures in ten different positions. The film thickness was measured from the SEM cross-sectional images.

The porosity assessment was also performed by image analysis using ImageJ software [ImageJ 2017]. Image analysis of SEM top-view images is done by pixel-based measurement, once the microstructure is digitized. The porosity area percentage was estimated by masking the processed SEM microstructure as a binary image (Fig. IV.13) with different thresholding levels. This method was accurately performed on five different SEM images of each glancing angle and the mean value with the uncertainty of the area fraction of porosity were quantified.

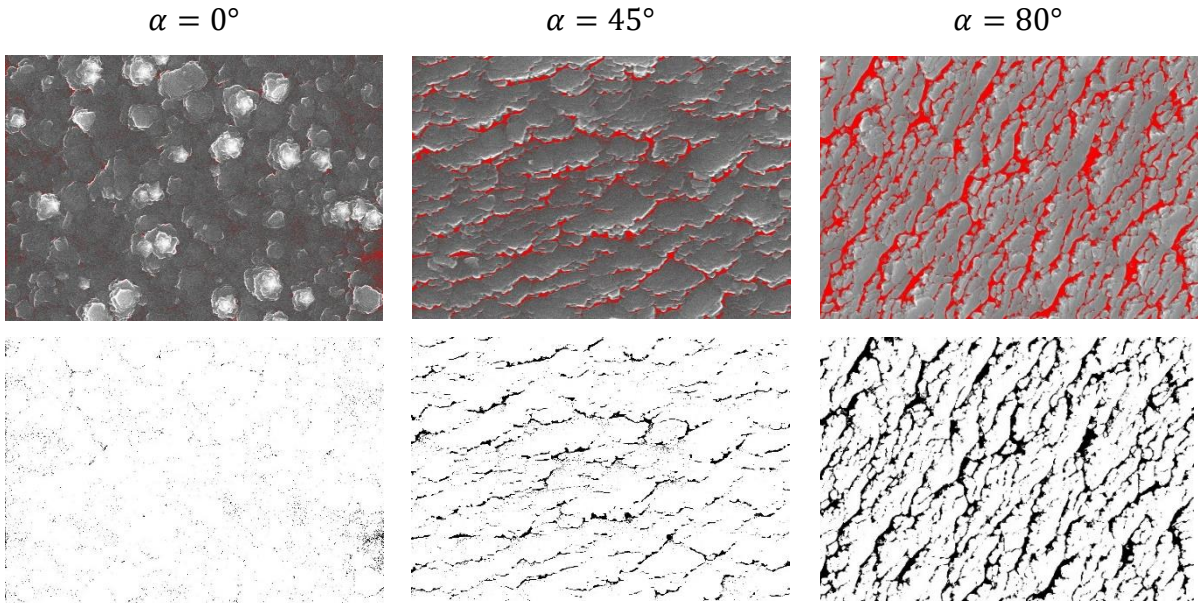

Fig. IV.13. Binary images made by ImageJ software based on SEM top-view images that were used for image analysis at various glancing angles α (0°, 45° and 80°).

Table IV.6 presents the density and the porosity values of the Ti films deposited with the three glancing angles. From either Eq. (IV.23) or image analysis, the results proved that the

porosity percentage within the Ti films increases by increasing the glancing angle. The difference between the values obtained using the two approaches is lower than the measurement uncertainties. The porosity calculated by Eq. (IV.23) was used to determine the elasticity constants of the Ti films. The values of the Young's and shear moduli calculated using respectively Eq. (IV.21) and Eq. (IV.22) and their relative uncertainties are presented in Table IV.7. We can notice that the values of E and G calculated (Table IV.7) are different from the values measured by IET (Table IV.4 and Table IV.5). The difference ($E^* - E^{IET}$) and ($G^* - G^{IET}$) between the elasticity constants measured by IET (Table IV.4 and Table IV.5) and those calculated with porosity (Table IV.7) is presented in Table IV.8. These differences correspond to the contribution of the microstructure. We can notice that the difference is higher than the measurement uncertainties and thus the decrease of the elasticity constants is not only attributed to the presence of pores within the Ti film. Theoretically, this comparison can be used to represent the overall influence of the microstructural properties, as a whole, on the elasticity constants of the films.

Contrariwise, the analytical model proposed by Nemat-Nasser et al. [Nemat-Nasser 1993] presents several assumptions. One of them is that the cavities are simulated as spherical inclusions (isotropic shape) while in GLAD, the cavities should have anisotropic shape. Moreover, the model supposes that the cavities are well separated from each other (without mechanical interaction). However, when the beam is vibrated by the IET, the gap between the column can lead the column to move relative to each other or to bend that would dissipate part of the mechanical energy. Consequently, the influence of the film microstructure needs to be quantified and dissociated in order to determine the contribution of each microstructural parameter (morphology (β), texture (η), etc.) on the elasticity constants of thin films. This aspect will be investigated in the next chapter.

Table IV.6
Density and Porosity values in the Ti films estimated using Eq. (IV.23) and ImageJ with their uncertainties.

Sample	Film density ρ_c (Kg/m^3)	$u(\rho_c)$ (Kg/m^3)	Porosity p (%)		u(p) (%)	
			Eq. (IV.23)	ImageJ	Eq. (IV.23)	ImageJ
$A_{0,X}$	4508.74	94.99	1.98	1.43	2.06	0.10
$A_{0,Y}$	4531.30	90.00	1.49	0.74	1.96	0.39
$A_{45,X}$	4327.57	48.04	5.92	4.71	1.04	0.65
$A_{45,Y}$	4385.55	78.87	4.66	4.23	1.71	1.16
$A_{80,X}$	4213.91	80.77	8.39	10.51	1.76	1.03
$A_{80,Y}$	4171.97	82.40	9.31	10.81	1.79	1.86

Table IV.7
Elasticity constants of the Ti films calculated by taking into account the volume fraction of porosity of Eq. (IV.23).

Sample	Porosity p (%) Eq. (IV.23)	u(p) (%)	E^* (GPa) Eq. (IV.21)	$u(E^*)$ (GPa)	G^* (GPa) Eq. (IV.22)	$u(G^*)$ (GPa)
$A_{0,X}$	1.98	2.06	109.09	7.19	41.30	2.75
$A_{0,Y}$	1.49	1.96	110.80	6.81	41.95	2.61
$A_{45,X}$	5.92	1.04	95.39	3.64	36.05	1.39
$A_{45,Y}$	4.66	1.71	99.78	5.97	37.73	2.29
$A_{80,X}$	8.39	1.76	86.79	6.12	32.76	2.34
$A_{80,Y}$	9.30	1.79	83.62	6.24	31.55	2.39

Table IV.8
Comparison between the macroscopic elasticity constants of the titanium films calculated using Eq. (IV.21) and Eq. (IV.22) and those measured by IET.

Sample	u(E) (GPa)		$[E^* - E^{IET}]$ (GPa)	Relative difference (%)	u(G) (GPa)		$[G^* - G^{IET}]$ (GPa)	Relative difference (%)
	IET	Eq. (IV.21)			IET	Eq. (IV.22)		
$A_{0,X}$	8.72	7.19	20.32	18.6	1.34	2.75	13.38	32.4
$A_{0,Y}$	8.59	6.81	26.09	23.5	1.38	2.61	12.85	30.6
$A_{45,X}$	7.39	3.64	12.43	13.0	0.96	1.39	5.85	16.2
$A_{45,Y}$	9.82	5.97	21.36	21.4	1.34	2.29	13.75	36.4
$A_{80,X}$	6.40	6.12	55.00	63.4	2.14	2.34	9.24	28.2
$A_{80,Y}$	7.44	6.24	37.76	45.2	2.02	2.39	18.47	58.5

IV.8. Hardness and reduced modulus of titanium GLAD films

The hardness and reduced Young's modulus of the Ti films were measured using a TriboIndenter TI 980-Hysitron (Fig. III.6) with Continuous Stiffness Measurement (CSM) option. A Berkovich diamond tip (E_{ind} = 1140 GPa, ν_{ind} = 0.07) was used. Before performing the tests, a calibration procedure was carried out using a polycarbonate glass specimen. The hardness and reduced Young's modulus of the indented material were determined using the Oliver and Pharr method [Oliver 2004]. The hardness was determined from its usual definition [Oliver 2004]:

$$H = \frac{P_{max}}{A_c} \tag{IV.25}$$

Where H is the hardness, P_{max} is the maximum load applied to the indented material and A_c is the projected contact area. The reduced Young's modulus can be deduced from Eq. (III.2) [Oliver 2004].

The film hardness and reduced modulus were determined from the average of ten indents and the measurement uncertainty u(x) was determined from the standard deviation. In order to minimize the effect of the substrate on the film hardness and reduced modulus measurements, the indenter penetration depth was kept lower than 10 % of the film thickness [Buckle 1960] controlled by the indenter penetration load. Fig. IV.14 shows the evolution of hardness H and reduced modulus E^r of the Ti films as a function of the glancing angle α. The measurements were performed on the samples oriented toward x (H_x, E_x^r) and y axes (H_y, E_y^r). We can notice that the hardness as well as the reduced modulus of the Ti film decrease when the glancing angle increases. As discussed in the previous section, this can be due to the increase in porosity with the glancing angle.

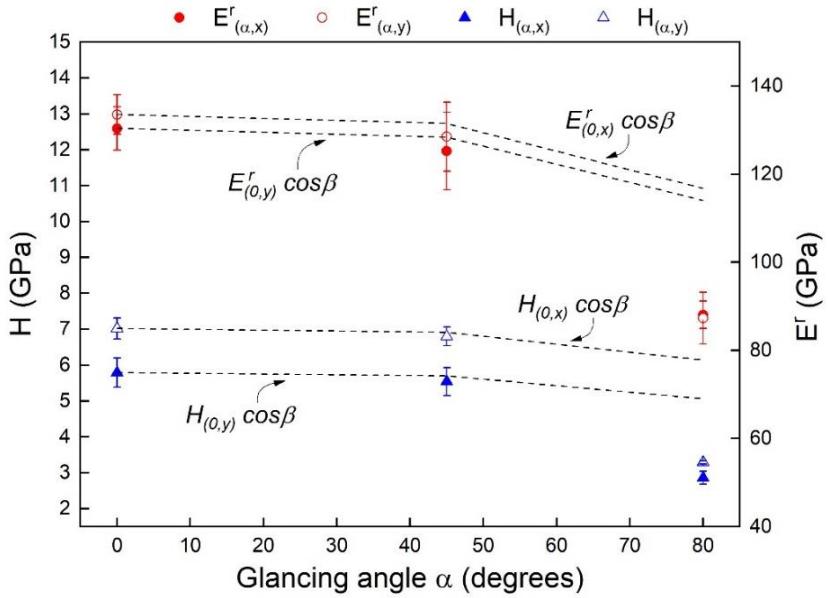

Fig. IV.14. Influence of the deposition glancing angle α on the mean value of the hardness H_c and the reduced modulus E^r of the titanium films measured by nanoindentation.

Furthermore, the values were compared to those of a reference sample deposited at normal geometry (α = 0°). The dashed lines in Fig. IV.14 correspond to the values at zero incidences (H_0, E_0) correlated through the cosine of the column tilt angle β. A good agreement is noticed with the experimental values of the Ti films deposited at α = 0° and 45°. This result allows us to assume that the load applied by the indenter was transmitted through the column axis. At α = 80°, this correlation is no longer valid since the contribution from friction or bending of the column becomes significant. It toggles the results and the prediction of the hardness and the reduced Young's modulus at α > 45°, since the contribution of the frictions and the bending moments of the columns was assumed negligible [Lintymer 2005, Jiménez-Piqué 2014]. From the nanoindentation (Fig. IV.14) and the IET (Table IV.4 and Table IV.5) measurements, we can conclude that the elasticity constants of the Ti anisotropic films depend on many factors (porosity, morphology, texture, etc.). The anisotropic properties of the Ti films are affected by the deposition parameters and notably the glancing angle α.

IV.9. Conclusions

This chapter presents an enhancement in the determination of the macroscopic elasticity constants of thin films with anisotropic behavior. An enhanced formulation was developed allowing the determination of the elasticity constants of a coating by means of the Impulse

Excitation Technique. The model was validated by comparing the results to those obtained from a numerical finite element model.

Titanium thin films were sputter-deposited on inclined glass substrates and Si wafers with three different deposition glancing angles (α = 0°, 45° and 80°). Several substrate-holders were fabricated to obtain the same deposition conditions for all inclined samples. Analyses of morphology, crystalline structure and texture development of Ti thin films deposited at different glancing angles were performed. A porous microstructure with columnar growth was formed. Upon increasing the glancing angle to 45° and 80°, the micro-columns formed were tilted respectively by 10° and 23° toward the vapor flux direction. X-ray diffraction characterization revealed the presence of a single hcp Ti_α phase. Moreover, the film exhibited an out-of-plane $\{0002\}$ fiber texture oriented along the z-axis of the crystallites. The fiber axis was tilted with the c-axis to follow the vapor flux direction. For zero incidence (α = 0°), the $[0002]$ fiber axis was relatively tilted. The fiber tilt angle becomes 21° and 46° at glancing angles of 45° and 80° respectively. The shadowing effect led to the mechanism behind the micro-column tilt angle. The crystallites were kinetically grown to form a preferential orientation related to their evolutionary growth habit.

The anisotropic ratios, $\frac{E_y}{E_x}$ and $\frac{G_{yz}}{G_{xz}}$ increase from 0.95 and 0.96 to 1.44 and 2.26 respectively by increasing the glancing angle from 0° to 80°. The effect of film porosity on the elasticity constants of the Ti film was evaluated. It is noteworthy that the elasticity constants are affected, but not mostly, by the film porosity. The results confirm the influence of other microstructural properties on the elasticity constants of the Ti films. Besides, the hardness and the reduced modulus measured by nanoindentation decreased with increasing the glancing angle. The elastic properties of GLAD films are required in order to use these films at the forefront of engineering and materials science. The macroscopic elasticity constants of anisotropic titanium thin films with a thickness from 1 to 1.5 μm and exhibiting a hcp phase, were determined using the IET. A first step in the methodology has been reached in this chapter. The future improvement of nanostructured thin films requires further study on the determination of their elastic properties taking into account their functional structure, texture development and porosity. In the next chapter, a second step will be tackled, which will require the determination of the macroscopic elasticity constants of the textured Ti films deposited at oblique incidence by taking into account its microstructural properties.

Chapter V

Determination of the elasticity constants of anisotropic coatings by modeling their microstructural properties

V.1. Introduction

The determination of the global behavior of a generally multiphase material, known as macroscopic law behavior, requires knowledge of the behavior of its constituent elements and their arrangement in the material. The physico-chemical properties, the microstructure, the crystallographic texture, the residual stresses and the hardening state of each phase represent complex elements, which are added to the coexistence of the phases within the material, and yield to the analysis and prediction of their complicated behavior.

The objective of this chapter is to present an advanced methodology developed to determine the macroscopic elasticity constants of a thin, textured and porous film. This methodology requires the use of multiscale models that present the macroscopic elastic behavior as a function of the film microstructure. Several studies were performed to determine the macroscopic elasticity constants of anisotropic thin films [Faurie 2010, Hounkpati 2014a, b] (Table I.1). However, to our knowledge, none of these studies were applied to anisotropic films deposited at oblique incidence. Besides, most studies overlook the texture of the film. Thereby, we are mainly interested in the influence of the microstructure (crystallographic and morphological textures) on the elastic properties.

In this chapter, the film microstructure is considered in the multiscale modeling in order to achieve our goal. At first, a brief introduction to the X-ray diffraction (XRD) is presented. Then, we will introduce the different scale transition models used in the literature to link the mesoscopic quantities measured by XRD to the macroscopic ones. Next, the effective rigidity tensor as well as the microscopic strain measured by XRD of a multiphase material are formulated in the framework of the self-consistent model of Kröner-Eshelby (KE) [Eshelby 1957]. This model is used in the present work, to determine the macroscopic elasticity constants of polycrystalline textured titanium films exhibiting a single-phase (Ti_α) and deposited at different glancing angles α.

The influence of the morphological and crystallographic texture on the elastic properties is quantified. The influence of the glancing angle on the microscopic elastic response was also quantified. The residual stress state within the Ti films was determined as a function of the incidence angle. Indeed, the texture of the Ti_α hexagonal phase, the grain shape and the porosity

in the titanium film will be taken into account in the modeling. This work will allow us to have a first set of elasticity constants values of a film deposited at oblique incidence.

V.2. X-Ray Diffraction theory

V.2.1. Principle of diffraction

XRD is an investigative and non-destructive technique that characterizes the crystalline structure of materials. It consists in irradiating a volume of the material with a finely focused mono or polychromatic beam of X-rays having a wavelength closed to the lattice spacing. During the interaction between the incident X-rays beam and the material, intensity peaks appear for specific 2θ diffraction angles (Fig. V.1(a)). A diffraction line appears as a strong peak on the diffraction pattern representing the intensity as a function of the diffraction angle 2θ (Fig. V.1(b)).

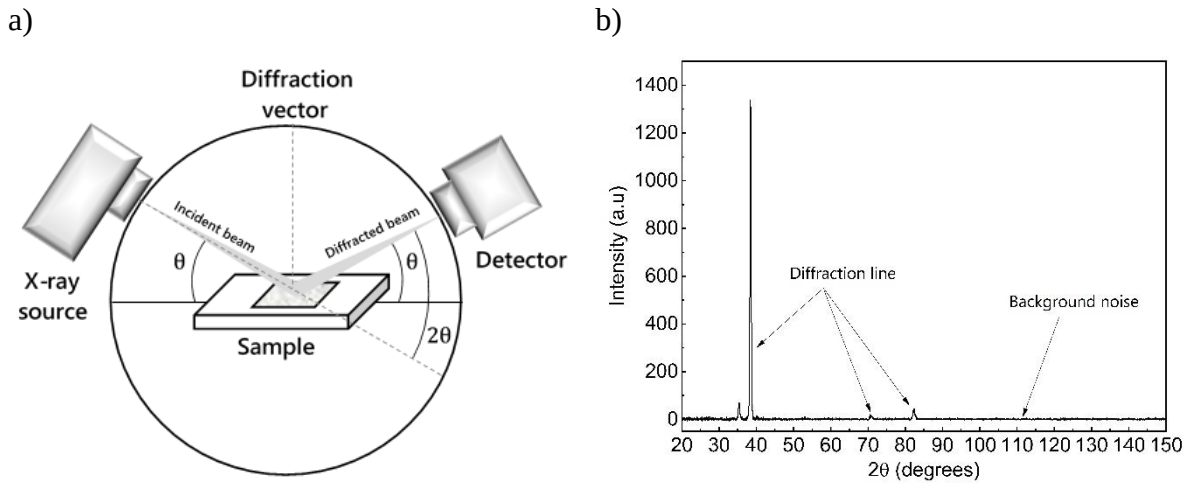

Fig. V.1. a) Schematic illustration of X-ray diffraction, b) diffraction pattern representing the intensity as a function of the diffraction angle, acquired on a titanium film.

The diffraction of an incident beam will not occur unless the Bragg condition is satisfied and the diffraction vector is perpendicular to $(h\ k\ l)$ plane. h, k and l are Miller's indices that specify a diffracted lattice plane family. The diffraction phenomenon allows us to determine the lattice spacing d_{hkl} between two crystallographic planes belonging to the same family of planes $\{h\ k\ l\}$ using the following Bragg's law [Schajer 2013]:

$$2d_{hkl} \sin\theta = n\,\lambda \tag{V.1}$$

Where n is the order of diffraction (usually n = 1), λ is the x-ray wavelength of the radiation used and d_{hkl} is the lattice spacing between planes of given Miller's indices.

The diffraction enables us to reveal the crystalline structure of materials and their crystalline properties, such as the position of atoms inside the unit cell, the defects of the crystal lattice, and the nature of phases embedded in the material and their proportions. From XRD, the preferred orientations (crystallographic textures), the crystallite size and the residual stresses can also be determined.

V.2.2. Principle of strain analysis by X-ray diffraction

XRD is one of the most powerful techniques used for the characterization of the elastic behavior of crystalline materials. The stress state can be determined by using the crystal lattice of the material as a strain gauge. Under the stress effect, a variation in the lattice spacing is generated owing to the deformation of the crystal lattice and thus the diffraction peak is shifted (Fig. V.2). The shift of the diffraction peak is used to measure the elastic strain of the material along the measurement direction.

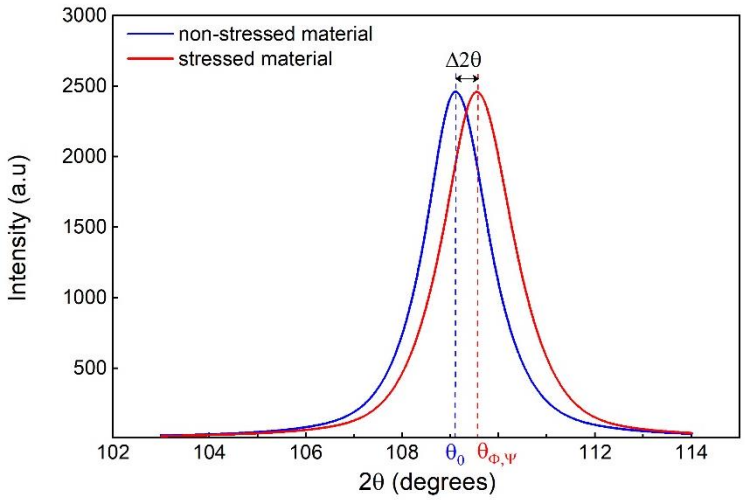

Fig. V.2. Schematic representation of a diffraction peak shifted under the stress effect.

The measurement direction is defined either by the normal to the diffracting plane or by the diffraction vector, which is the bisector of the incident and the diffracted beams (Fig. V.3).

The blue arrows in Fig. V.3 represent the incident and the diffracted beams. The scattering vector $\vec{n}$ defining the measurement direction is expressed in the sample base (S_1, S_2, S_3) using the azimuth angle ϕ and the tilt angle ψ (Fig. V.3) as follows:

$$\vec{n} = \begin{pmatrix} \cos\phi \sin\psi \\ \sin\phi \sin\psi \\ \cos\psi \end{pmatrix} \quad \text{(V.2)}$$

More details on the acquisition geometry of X-ray stress analysis and the diffraction angles can be found in the literature [François 2008].

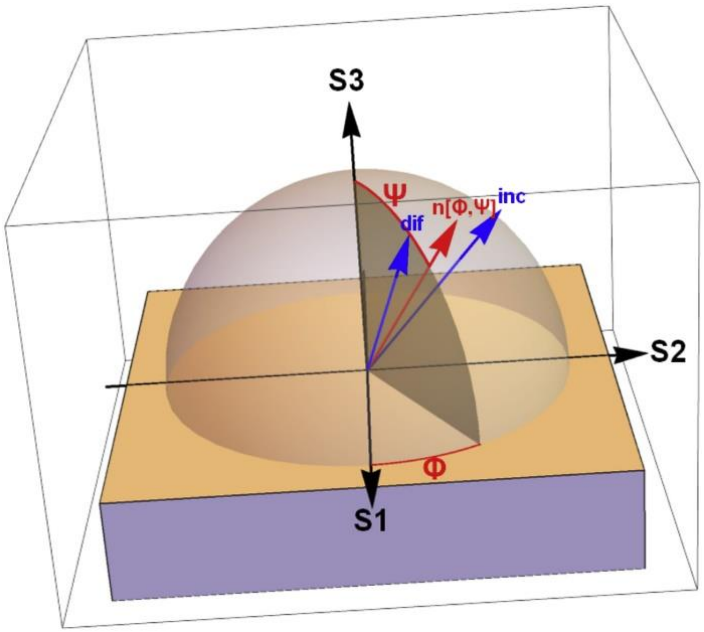

Fig. V.3. Schematic illustration of the azimuth angle ϕ, the tilt angle ψ and the scattering vector $\vec{n}$ in the chi acquisition mode. The blue arrows represent the incident and the diffracted beams [Slim 2019]. S_1 is the Rolling Direction (RD), S_2 is the Transverse Direction (TD) and S_3 is the Normal Direction (ND).

The strain measured by XRD is estimated by different methods, such as conventional, rational and linear methods. Although these methods are mathematically different, they lead to very close strain values. Indeed, the diffraction is only sensitive to elastic strains (small strains) but even with that, uncertainty is still introduced. Qualitative and quantitative evaluations of the trueness of these strain expressions were proposed in the literature [Ferreira 2004]. It was shown from a mechanical point of view that rational strain is the exact strain definition (it is

not based on the approximations). Therefore, the strain measured by XRD is directly linked to the position of the diffraction peak, corresponding to a crystallographic plane $\{h\ k\ l\}$, by the following rational expression [Badawi 1993]:

$$\varepsilon_{\phi,\psi}^{\{hkl\}} = \ln\left(\frac{d_{\phi,\psi}^{\{hkl\}}}{d_0^{\{hkl\}}}\right) = \ln\left(\frac{\sin\theta_0^{\{hkl\}}}{\sin\theta_{\phi,\psi}^{\{hkl\}}}\right) \quad \text{(V.3)}$$

Where $d_0^{\{hkl\}}$ and $\theta_0^{\{hkl\}}$ represent respectively the lattice spacing and the position of the diffraction peak of a non-stressed material and $d_{\phi,\psi}^{\{hkl\}}$ and $\theta_{\phi,\psi}^{\{hkl\}}$ are respectively the lattice spacing and the position of the diffraction peak of a stressed material.

When diffracting a material by X-rays, only a volume portion of the sample is irradiated. It is known as *Representative Volume Element* (RVE), supposed to represent the macroscopic mechanical state. Inside this volume, only a part of the crystallites, whose favorable orientation are diffracted, i.e. they represent 1 to 5 % of RVE. Those are the crystallites in diffraction position, which constitute the so-called *Diffracting Volume* (DV). It is discontinuous (non-convex), and simultaneously varies with the measurement direction. The diffraction techniques allow only the analysis of the periodic domain of the material. However, the periodicity of a crystal is altered by material discontinuities (gaps, grain boundaries, precipitates, etc.) that define the non-defects element volume called *consistent diffraction domains* (Fig. V.4). The size of these domains is smaller than the grain size and thus they form the element volume contributing to the formation of the diffraction peak. Nevertheless, for simplification, we will call the quantities associated with these domains, the second-order quantities. Therefore, the strain measured by XRD corresponds to only one part of the material, so no direct access to the macroscopic mechanical state can be obtained by XRD. In order to determine the macroscopic mechanical state, a relationship between the different scales must be established.

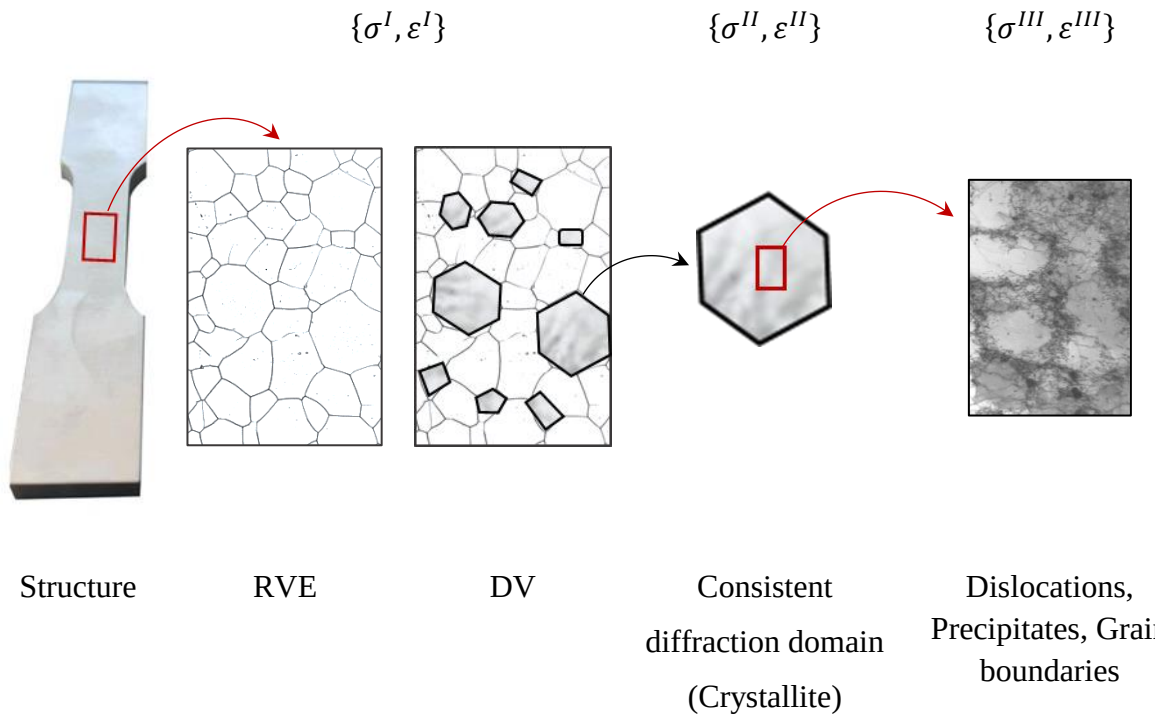

Fig. V.4. The three orders of stresses and strains in the framework of a micromechanical procedure.

V.3. The scale transition approach applied to the elasticity of polycrystals

V.3.1. Observation scales, basic volume of simulations

The modeling of the elastic behavior of the polycrystal is performed by considering it compactly composed of a large number of crystallites. Here, the influence of the grain boundaries is assumed negligible as the volume fraction of the grain boundaries is often low compared to the grain size usually observed in thin films. Each crystallite is also considered as a domain where the mechanical fields are homogeneous and constitute the basic volume taken in simulations. As described in Section V.2.2, the RVE of the simulated material will therefore consist of a sufficient number of these crystallites to ensure good convergence of the simulated results with accuracy. This large number of crystallites allows also defining an average material behavior that is uniform.

The selective nature of the XRD presented in Section V.2 leads to define a classification in three orders of stresses and strains (Fig. V.4) [Macherauch 1973]:

- Order I corresponds to the macroscopic scale, where the mechanical state of the RVE is defined by $\{\sigma^I, \varepsilon^I\}$. At this scale, the stresses σ^I and strains ε^I vary continuously over a very large domain of the material, in the order of a millimeter.
- Order II corresponds to the mesoscopic scale, which is an intermediate scale between the macroscopic and the microscopic scales. The stresses and strains vary continuously over distances in the order of a micrometer. This scale is proportional to the diffracting volume and is relative to the mechanical state $\{\sigma^{II}, \varepsilon^{II}\}$ of the crystallites.
- Order III corresponds to the microscopic scale, where the stresses and strains vary continuously over distances in the order of the inter-atomic distance. The mechanical state at this scale is noted $\{\sigma^{III}, \varepsilon^{III}\}$.

In this work, the macroscopic scale corresponds to the thin film and the mesoscopic scale corresponds to the crystallites.

V.3.2. Description of the crystallographic orientation

A polycrystalline material is constituted of crystallites randomly or preferentially distributed in the material depending on the elaboration process. Their orientations depend on the elaboration process and the treatments that the material undergoes during the various stages of production. The preferential orientation generated during the process can influence the mechanical and physical properties. The reader can refer to Section IV.2.3, for more details about the crystallographic orientation in thin films.

In order to describe the crystallographic orientation, two different coordinate systems are assigned to the crystal and the sample, respectively. Fig. V.5 presents the crystal coordinate system (C_1, C_2, C_3) and the sample coordinate system (S_1, S_2, S_3). The sample vectors S_1 and S_2 are defined in the substrate plane and S_3 is defined in such way that the coordinate system (S_1, S_2, S_3) becomes a direct orthonormal system. The S_1 vector is chosen parallel to the substrate length direction. The crystal axes C_1, C_2 and C_3 are respectively defined by the crystallographic orientations [100], [010] and [001] for materials with cubic symmetry. In the case of materials with hexagonal symmetry, the crystallographic coordinate system is defined by means of an Ortho-Hexagonal (O-H) coordinate system of basic vectors: $(\vec{a} = \vec{a}_1,\ \vec{b} =$

$(\vec{a}_1 + 2\vec{a}_2),\ \vec{c})$, where $\vec{a}_1$, $\vec{a}_2$ and $\vec{c}$ are the basic vectors of the hexagonal system with three axes (Fig. V.6).

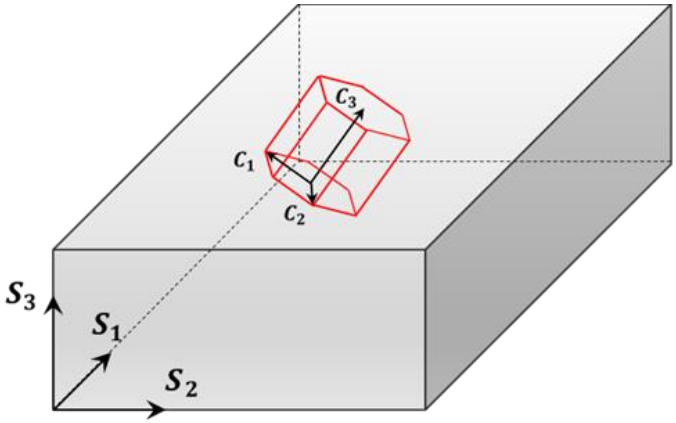

Fig. V.5. Crystal coordinate system (C_1, C_2, C_3) and sample coordinate system (S_1, S_2, S_3).

To describe a crystallographic orientation, it is necessary to link the crystal coordinate system to the sample one. To do this, a matrix allowing the transformation from the crystal to the sample coordinate system is defined. This matrix can be defined in different ways [Hauk 1997, Kocks 1998, Randle 2001].

a) b)

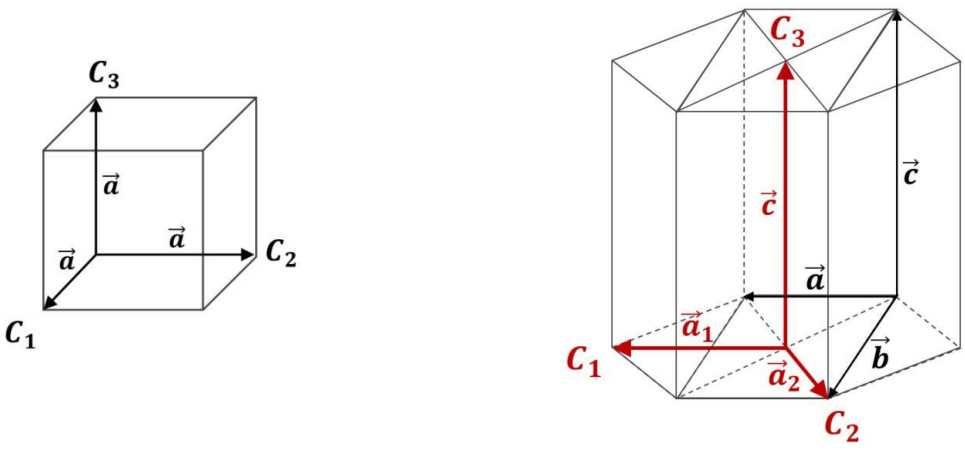

Fig. V.6. Definition of the crystal coordinate system with respect to the crystal lattice: a) cubic and b) hexagonal.

In this work, the relation between the sample system and the crystal system is described through a transformation matrix using the Euler angles according to the Bunge convention $(\varphi_1, \phi, \varphi_2)$ [Bunge 1982]. These Euler angles will be used to describe the orientation (Ω) of

the crystallites. The transformation matrix is defined by three consecutive rotations around the axes of a coordinate system that is parallel initially to the crystal system (C_1, C_2, C_3) and finally to the sample system (S_1, S_2, S_3) with two intermediate orientations:

- First rotation of angle φ_1 around the S_3 axis, where $\varphi_1 \in [0\,;2\pi]$.
- Second rotation of angle ϕ around the new S_1' axis, where $\phi \in [0\,;\pi]$.
- Third rotation of angle φ_2 around the new S_3'' axis, where $\varphi_2 \in [0\,;2\pi]$.

The transformation matrix $g(\varphi_1, \phi, \varphi_2)$ is defined by [Kocks 1998, Hauk 1997]:

$$g(\varphi_1, \phi, \varphi_2) = g_{\varphi_2}.g_{\phi}.g_{\varphi_1} \tag{V.4}$$

With:

$$g_{\varphi_1} = \begin{pmatrix} \cos\varphi_1 & \sin\varphi_1 & 0 \\ -\sin\varphi_1 & \cos\varphi_1 & 0 \\ 0 & 0 & 1 \end{pmatrix}, \quad g_{\phi} = \begin{pmatrix} 1 & 0 & 0 \\ 0 & \cos\phi & \sin\phi \\ 0 & -\sin\phi & \cos\phi \end{pmatrix}, \quad g_{\varphi_2} = \begin{pmatrix} \cos\varphi_2 & \sin\varphi_2 & 0 \\ -\sin\varphi_2 & \cos\varphi_2 & 0 \\ 0 & 0 & 1 \end{pmatrix} \tag{V.5}$$

The expression of g becomes:

$$g = \begin{pmatrix} \cos\varphi_1\cos\varphi_2 - \sin\varphi_1\sin\varphi_2\cos\phi & \sin\varphi_1\cos\varphi_2 + \cos\varphi_1\sin\varphi_2\cos\phi & \sin\varphi_2\sin\phi \\ -\cos\varphi_1\sin\varphi_2 - \sin\varphi_1\cos\varphi_2\cos\phi & -\sin\varphi_1\sin\varphi_2 + \cos\varphi_1\cos\varphi_2\cos\phi & \cos\varphi_2\sin\phi \\ \sin\varphi_1\sin\phi & -\cos\varphi_1\sin\phi & \cos\phi \end{pmatrix} \tag{V.6}$$

With:

$$\begin{pmatrix} Sample \\ system \end{pmatrix}_{(S_1,S_2,S_3)} = g(\varphi_1, \phi, \varphi_2) \begin{pmatrix} crystal \\ system \end{pmatrix}_{(C_1,C_2,C_3)} \tag{V.7}$$

The Bunge angles $(\varphi_1, \phi, \varphi_2)$ used to define the crystallographic orientation of the film $\{h\ k\ l\}\ \langle u\ v\ w\rangle$ relative to the sample coordinate system can be determined from the following relations [Bunge 1982]:

$$\varphi_1 = \sin^{-1}\left[\frac{w}{\sqrt{u^2+v^2+w^2}}\sqrt{\frac{h^2+k^2+l^2}{h^2+k^2}}\right] \quad \text{(V.8)}$$

$$\phi = \cos^{-1}\left[\frac{l}{\sqrt{h^2+k^2+l^2}}\right] \quad \text{(V.9)}$$

$$\varphi_2 = \cos^{-1}\left[\frac{k}{\sqrt{h^2+k^2}}\right] = \sin^{-1}\left[\frac{h}{\sqrt{h^2+k^2}}\right] \quad \text{(V.10)}$$

The transformation matrix that allows writing the sample system tensor in the crystal system is therefore the inverse of the transformation matrix g, i.e. it also represents the transpose of g since this latter is being orthonormal. The rigidity tensor of a crystallite $c(\Omega)$ expressed in the sample coordinate system is then determined, from the rigidity tensor c seen from the crystal system, as follows:

$$c_{ijkl}(\Omega) = g_{im} \cdot g_{jn} \cdot g_{ko} \cdot g_{lp} \cdot c_{mnop} \quad \text{(V.11)}$$

Where Ω represents the crystallographic orientation of the crystallite defined in the sample coordinate system by three Euler angles $\Omega = (\varphi_1, \phi, \varphi_2)$.

V.3.3. Homogenization steps of a heterogeneous material

The mechanical behavior of a heterogeneous material requires the analysis of its microstructure. The homogenization procedure consists in replacing the real heterogeneous material by an equivalent homogeneous material having similar behavior at the macroscopic scale. This procedure presents three main steps [Bornert 2001]: the representation, localization and homogenization steps. We will introduce the laws defining the elastic behavior of the material at each scale. Then, we will present the localization and the concentration laws that ensure the transformation from a mesoscopic scale to a macroscopic scale. The microscopic mechanical states of order III will not be modeled in this work.

V.3.3.1. Macroscopic and mesoscopic elastic behavior: representation step

The macroscopic elastic behavior of the material is described by defining the elastic behavior of the RVE. Using the generalized Hooke's law, the relation between the stress and strain of the RVE at the macroscopic scale is given by the following expressions:

$$\sigma^I = C : \varepsilon^I \tag{V.12}$$

$$\varepsilon^I = S : \sigma^I \tag{V.13}$$

Where the ":" sign represents the double dot tensor product. C and S represent the rigidity and compliance tensors of the polycrystal, respectively. σ^I and ε^I represent the macroscopic stress and strain tensors of the material, respectively. On the mesoscopic scale, Hooke's law is also used to link the stress to the strain of a crystallite of a given phase, according to the following relations:

$$\sigma_\Omega^{II} = c_\Omega^i : \varepsilon_\Omega^{II} \tag{V.14}$$

$$\varepsilon_\Omega^{II} = s_\Omega^i : \sigma_\Omega^{II} \tag{V.15}$$

Where c_Ω^i and s_Ω^i represent the rigidity and compliance tensors of the considered phase i, respectively. σ_Ω^{II} and ε_Ω^{II} represent the mesoscopic stress and strain tensors of the crystallite, respectively. Subscript Ω corresponds to the orientation of the crystallite defined in the sample coordinate system.

V.3.3.2. Mesoscopic to macroscopic scale transition: localization and concentration laws

The transition from a mesoscopic scale to a macroscopic scale is carried out using a relation expressing the proportionality between the local and the macroscopic mechanical states. According to Kröner [Kröner 1958], the mesoscopic stress can be defined by the sum of the macroscopic stress and another term expressing the difference between the mesoscopic and the macroscopic stresses. The corresponding expression is called the concentration equation (Eq. (V.16)). An equivalent relation is also defined for the strain and the corresponding

expression is called the localization equation (Eq. (V.17)). In linear elasticity, these relations are expressed as follows:

$$\sigma_\Omega^{II} = \sigma^I + t_\Omega^i : \sigma^I = \left(I_4 + t_\Omega^i\right) : \sigma^I = B_\Omega^i : \sigma^I \tag{V.16}$$

$$\varepsilon_\Omega^{II} = \varepsilon^I + u_\Omega^i : \varepsilon^I = \left(I_4 + u_\Omega^i\right) : \varepsilon^I = A_\Omega^i : \varepsilon^I \tag{V.17}$$

Where t_Ω^i and u_Ω^i are 4th rank tensors called polarization tensors. A_Ω^i and B_Ω^i are 4th rank tensors called respectively the strain localization tensor and the stress concentration tensor. I_4 is the 4th rank identity tensor. The tensors A_Ω^i and B_Ω^i (and thus u_Ω^i and t_Ω^i) depend on the scale transition model chosen for modeling.

V.3.3.3. Stress-strain consistency: Homogenization step

The homogenization step requires the consistency between the local mechanical state and the macroscopic mechanical state. For this, the macroscopic stress and strain must be necessarily equal to the average of the mesoscopic stress and strain in all the crystallites, respectively. The effective behavior of the heterogeneous material is often formulated using the two Hill's relations on the means of the local mechanical states [Hill 1967]:

$$\sigma^I = \langle \sigma_\Omega^{II} \rangle \tag{V.18}$$

$$\varepsilon^I = \langle \varepsilon_\Omega^{II} \rangle \tag{V.19}$$

Where $\langle \quad \rangle$ defines the average of all the crystallites belonging to the RVE. By substituting Eqs. (V.14) and (V.17) into Eq. (V.18), the following expression can be found:

$$\sigma^I = \langle \sigma_\Omega^{II} \rangle = \langle c_\Omega^i : \varepsilon_\Omega^{II} \rangle = \langle c_\Omega^i : A_\Omega^i \rangle : \varepsilon^I \tag{V.20}$$

By comparing Eq. (V.20) with Eq. (V.12), the effective tensor of the elasticity constants of the polycrystal can be deduced as:

$$C = \langle c_\Omega^i : A_\Omega^i \rangle \tag{V.21}$$

The homogenization problem is thus summarized on the determination of the strain localization tensors whose expression depends on the homogenization model used.

V.4. Scale transition models

For homogenization, several scale transition models can be used for the elasticity. They can be classified into two groups: interaction models in which the grain shape is not defined and interaction models where grain shape is defined through a 4th rank tensor or assumptions on the mechanical state of the material. As examples of the first group are Voigt, Reuss and the Neerfeld-Hill models, which offer analytical expressions to determine approximately the effective mechanical properties of a material. However, as examples of direction-dependent grain-interaction models are the KE self-consistent model, the Mori-Tanaka model, the Vook-Witt and the inverse Vook-Witt models.

V.4.1. Voigt model

The Voigt's model was the first scale transition model developed [Voigt 1910]. It assumes that each crystallite develops the same strain ε_Ω^{II} as the macroscopic material (in the RVE). The strain homogeneity can be expressed as follows:

$$\varepsilon_\Omega^{II} = \varepsilon^I \Longrightarrow A_\Omega = I_4 \tag{V.22}$$

By replacing Eq. (V.22) into Eq. (V.21), we find the effective rigidity tensor C^V of the polycrystal based on the Voigt approximation, as follows:

$$C^V = \langle c_\Omega^i \rangle \tag{V.23}$$

V.4.2. Reuss model

It assumes that each crystallite develops the same stress σ_Ω^{II} as the polycrystal [Reuss 1929]. Stress homogeneity can be expressed as follows:

$$\sigma_\Omega^{II} = \sigma^I \Longrightarrow B_\Omega = I_4 \tag{V.24}$$

By replacing Eqs. (V.15) and (V.24) into Eq. (V.19), the macroscopic rigidity tensor can be expressed as a function of the single-crystal rigidity tensor:

$$\varepsilon^I = \langle \varepsilon_\Omega^{II} \rangle = \langle s_\Omega^i : \sigma_\Omega^{II} \rangle = \langle s_\Omega^i \rangle : \sigma^I \tag{V.25}$$

By analogy with Eq. (V.13), one can write the effective compliance S^R and rigidity C^R tensors within the framework of the Reuss model:

$$S^R = \langle s_\Omega^i \rangle \Longrightarrow C^R = \left[\langle \left[c_\Omega^i \right]^{-1} \rangle \right]^{-1} \tag{V.26}$$

Voigt and Reuss approximations are the first and simplest proposed transition relations. Indeed, they are reduced to a *law of mixture* on the properties of the constituents.

V.4.3. Neerfeld-Hill model

The Voigt and Reuss models are based on the assumptions of a strain field ε_Ω^{II} kinematically admissible and of a stress field σ_Ω^{II} statically admissible, respectively. Therefore, Voigt model satisfies the condition of strain consistency but does not ensure the stress equilibrium. The model neglects all sources of elastic heterogeneity on the mesoscopic strain. However, Reuss model satisfies the stress consistency but does not ensure the strain compatibility. The influence of the elastic heterogeneity on the mesoscopic strain is overestimated in this case. Hill has demonstrated that the Voigt and Reuss models define the upper and lower limits of the polycrystal behavior [Hill 1952] and thus has proposed to calculate the macroscopic rigidity tensor C^H by averaging the rigidity tensors given by Voigt and Reuss models [Neerfeld 1942]:

$$C^H = \frac{1}{2} \left(C^V + C^R \right) \tag{V.27}$$

Hill's model can be adapted to obtain an approximation of the macroscopic rigidity tensor by calculating the arithmetic or the geometric mean of the effective rigidity tensors calculated by Voigt and Reuss models [Hill 1952, Watt 1976]. Even if he does not allow finding the local mechanical states, this model can reproduce accurately the experimental results on a macroscopic scale for polycrystals. It also found that this approach has no clear mechanical meaning and satisfies neither the strain compatibility nor the stress equilibrium.

V.4.4. Kröner-Eshelby self-consistent model

The basic principle of the self-consistent model was proposed by Kröner [Kröner 1958]. It consists of relating the macroscopic mechanical state with the mesoscopic mechanical state using a polarization tensor (Eqs. (V.16) and (V.17)) satisfying both the strain and stress consistencies. In order to determine this polarization tensor, Kröner has used the work done by Eshelby [Eshelby 1957] to solve the inclusion problem immersed in an infinite matrix and subjected to infinite mechanical loading.

The polarization tensor developed by Kröner to determine the effective rigidity tensor from the single-crystal rigidity tensor can be expressed as:

$$u_{\Omega}^{i} = \left[P(C) : \left(c_{\Omega}^{i} - C\right) + I_4\right]^{-1} - I_4 \tag{V.28}$$

The strain localization tensor becomes:

$$A_{\Omega}^{i} = \left[P(C) : \left(c_{\Omega}^{i} - C\right) + I_4\right]^{-1} \tag{V.29}$$

Where $P(C)$ is a non-symmetric 4th order tensor, called Morris tensor [Morris 1970]. It depends on the morphology of the inclusion and the rigidity tensor of the polycrystal. The use of this model implies that the stress/strain field is considered homogeneous in a RVE of the film and a crystallite. This latter was demonstrated by Eshelby in the case of linear elasticity for an ellipsoidal heterogeneity embedded in an infinite matrix [Eshelby 1957]. Assuming that crystallites can be represented by ellipsoids, the components of the Morris tensor $P(C)$ can be expressed as follows [Kocks 1998]:

$$P_{ijkl} = \frac{1}{4\pi}\int_0^{\pi} \sin\theta \, d\theta \int_0^{2\pi} \gamma_{ikjl} \, d\phi \tag{V.30}$$

With:

$$\gamma_{ikjl} = K_{ij}^{-1}(\xi)\, \xi_k\, \xi_l \tag{V.31}$$

$$K_{ip}(\xi) = C_{ijpl}\, \xi_j\, \xi_l \tag{V.32}$$

$$\xi_1 = \frac{\sin\theta\cos\phi}{a_1} \qquad \xi_2 = \frac{\sin\theta\sin\phi}{a_2} \qquad \xi_3 = \frac{\cos\theta}{a_3} \tag{V.33}$$

Where $\theta \in [0\,;\,\pi]$ and $\phi \in [0\,;\,2\pi]$ are spherical coordinates that define the direction of the vector ξ with respect to the principal axes of the ellipsoid, of length $2a_1$, $2a_2$ and $2a_3$ [Kocks 1998]. The morphological texture can be described using the ratios introduced in Eq. (V.33). By substituting Eq. (V.29) into Eq. (V.17), the strain localization equation can be rewritten as follows:

$$\varepsilon_{\Omega}^{II} = \left[P(C) : \left(c_{\Omega}^{i} - C\right) + I_4\right]^{-1} : \varepsilon^{I} \tag{V.34}$$

V.4.4.1. Effective rigidity tensor of the polycrystal for a multiphase material

Based on Hooke's law, the macroscopic elastic behavior of the polycrystal and the mesoscopic elastic behavior of each phase embedded in the film can be defined as:

$$\sigma^{I} = C : \varepsilon^{I} \tag{V.35}$$

$$\sigma_{\Omega}^{i} = c_{\Omega}^{i} : \varepsilon_{\Omega}^{i} \tag{V.36}$$

In order to reduce the indexes in the equations, the mesoscopic strain will be noted ε^{i} instead of ε^{II} in the following, where the index i represents the phase. The average elastic behavior of a multiphase polycrystal is expressed as follows:

$$\sigma^I = \sum_{i=1}^{n} x_i \, \langle \sigma_\Omega^i \rangle_{\Omega \in V_i} \tag{V.37}$$

$$\varepsilon^I = \sum_{i=1}^{n} x_i \, \langle \varepsilon_\Omega^i \rangle_{\Omega \in V_i} \tag{V.38}$$

Where $\langle \quad \rangle_{\Omega \in \mathrm{V}}$ defines the mean over the phase volume. $\langle \sigma_\Omega^i \rangle_{\Omega \in \mathrm{V}_i}$ and $\langle \varepsilon_\Omega^i \rangle_{\Omega \in \mathrm{V}_i}$ represent respectively the average mesoscopic stress and strain on all the orientations over the phase i volume with the corresponding volume fraction x_i.

The strain localization equation of Eq. (V.34) can be rewritten as follows:

$$\varepsilon_\Omega^i = \left[P(C) : \left(c_\Omega^i - C\right) + I_4\right]^{-1} : \varepsilon^I = \left[P(C) : \left(c_\Omega^i - C\right) + I_4\right]^{-1} : C^{-1} : \sigma^I \tag{V.39}$$

From Eqs. (V.37) and (V.39), the macroscopic stress can be written in the following form:

$$\sigma^I = \sum_{i=1}^{n} x_i \, \langle c_\Omega^i : \varepsilon_\Omega^i \rangle_{\Omega \in \mathrm{V}_i} = \sum_{i=1}^{n} \left[x_i \, \langle c_\Omega^i : \left[P(C) : \left(c_\Omega^i - C\right) + I_4\right]^{-1} \rangle_{\Omega \in \mathrm{V}_i} \right] : \varepsilon^I \tag{V.40}$$

Through identification with Eq. (V.35), we can deduce the expression of the effective rigidity tensor C of the polycrystal through an implicit equation, which must be solved by iterations:

$$C = \sum_{i=1}^{n} x_i \, \langle c_\Omega^i : \left[P(C) : \left(c_\Omega^i - C\right) + I_4\right]^{-1} \rangle_{\Omega \in \mathrm{V}_i} \tag{V.41}$$

This expression gives the macroscopic elasticity constants of the film as a function of the Single-Crystal Elasticity Constants (SCECs). The tensor $P(C)$ is function of the crystallite shape and the macroscopic rigidity tensor C. The volume fractions can be calculated from XRD patterns. It can be noted here that tensor C can be anisotropic depending on the shape of the

inclusions and the averaging on the orientations Ω describing the crystallographic texture of the film.

V.4.4.2. Strain obtained by X-ray diffraction for a multiphase material

As described in Section V.2.2, the elastic strain is measured by XRD along the measurement direction defined by the scattering diffraction vector $\vec{n}$ (Eq. (V.3)). The strain of a crystallite belonging to phase i is expressed by Eq. (V.39). Using XRD, a DV is analyzed and the measured strain is the average of all the strains of crystallites belonging to the DV. Thus, the strain measured by XRD can also be obtained by projecting the strain determined using the KE model, in the measurement direction, as follows:

$$\varepsilon_{\phi,\psi}^{\{hkl\}_i} = \ln\left(\frac{\sin\theta_0^{\{hkl\}_i}}{\sin\theta_{\phi,\psi}^{\{hkl\}_i}}\right) = \vec{n}\,.\left[\langle\varepsilon_\Omega^i\rangle_{\Omega\in V_i}\right].\vec{n} \qquad \text{(V.42)}$$

Where $\theta_0^{\{hkl\}_i}$ and $\theta_{\phi,\psi}^{\{hkl\}_i}$ are respectively the position of the diffraction peaks of a non-stressed and a stressed material, ϕ and ψ are the azimuth and tilt angles respectively. By substituting Eq. (V.39) into Eq. (V.42), we obtain the strain measured by XRD as follows:

$$\varepsilon_{\phi,\psi}^{\{hkl\}_i} = \vec{n}\,.\left[\langle\left[P(C):\left(c_\Omega^i - C\right) + I_4\right]^{-1}\rangle_{\Omega\in V_i} : C^{-1} : \sigma^I\right].\vec{n} \qquad \text{(V.43)}$$

V.4.4.3. Limitations of the Kröner-Eshelby self-consistent model

Other direction-dependent grain-interaction models were used to describe the elasticity of materials, such as Vook-Witt and Inverse Vook-Witt [Vook 1965, Witt 1968], Hashin-Shtrikman [Hashin 1962], Mori-Tanaka [Mori 1973] and Normalized self-consistent [Li 1999] models. These models, except for Vook-Witt, were also developed based on the Eshelby inclusion problem and today they are very relevant approaches with an extended predictive nature. Welzel et al. [Welzel 2005, Welzel 2007] have demonstrated that similarities between the Vook-Witt and the Kröner-Eshelby models occur for a polycrystal with extreme flat disc-shaped grains. Such similarities between the inverse Vook-Witt and the Kröner-Eshelby models occur also but much less in the case of extreme needle-like grains. Moreover, the Hashin-Shtrikman and Mori-Tanaka models present similar behavior in the case of linear elasticity.

In this chapter, the elastic behavior of titanium thin films sputter-deposited at oblique incidence is determined. The choice of the micromechanical approach depends on its ability to simulate the strong crystalline and morphological anisotropy developed in this type of film. Voigt, Reuss and Neerfeld-Hill models are not adapted for thin films which generally present grain shape texture (needle-like grains) [Kumar 2006]. At zero incidence, where the growth direction (morphological texture) is normal to the substrate surface, the columnar morphology of the films can induce an elastic anisotropy between the film surface plane and growth direction (morphological texture) [Kumar 2006]. This effect can be studied by taking a mixed Vook-Witt and KE model, as proposed by Baczmanski et al. [Baczmanski 2008]. Furthermore, this effect could be studied using the KE self-consistent model by taking an Eshelby tensor (and therefore a Morris tensor) corresponding to an elongated inclusion (grain) in the growth direction [Nemat-Nasser 1993, Slim 2019].

Therefore, the scale transition models based on the study of Eshelby's unique heterogeneous inclusion are not, by constitution, able to integrate within the same model, the existence of inclusions with different morphologies or inclusions of the same morphology but disoriented with each other. The specific microstructures that can be modeled are therefore limited to polycrystalline assemblies consisting only of spherical or ellipsoidal grain shape preferably oriented in a certain direction of the sample. It was demonstrated by Benveniste et al [Benveniste 1991] that asymmetrical macroscopic rigidity tensor was predicted using the KE self-consistent model in the case of materials comprising more than one or two constituents of different morphologies but having a certain preferential orientation. They have also shown that the KE self-consistent model did not satisfy simultaneously the two relations of Hill on the means of the local mechanical states. Hounkpati et al. [Hounkpati 2015] have noticed that the symmetry of the macroscopic rigidity tensor as well as the model consistency are not verified simultaneously when modeling different morphologies within a RVE. By imposing the symmetry to the rigidity tensor, the self-consistency is lost ($\langle A_\Omega \rangle \neq I_4$, $\langle B_\Omega \rangle \neq I_4$).

To overcome the limits of the KE self-consistent model, the normalized self-consistent model was proposed [Li 1999]. It consists in normalizing the strain localization tensor A_Ω by multiplying it by the inverse of its mean, namely $[\langle A_\Omega \rangle]^{-1}$. The difference between the KE and the normalized self-consistent models, from a physical point of view, lies in the description of the grain. In the case of thin films, the grains are assumed identical and the columns are all oriented toward the incident vapor flux and thus present the same geometrical orientation.

Hence, The KE self-consistent model is the one used in our work. Furthermore, he will allow the quantification of the grains-shape effect on the macroscopic elasticity constants and the elastic behavior of the diffracting volume. Mori-Tanaka model can also be used to determine the elastic behavior of these films.

In most cases, thin films deposited by magnetron sputtering are textured and multiphase. Indeed, the determination of the elasticity constants requires both macroscopic and microscopic measurements. In the case of thin films, it is difficult to make accurate measurements by tensile or resonance ultrasound techniques, which make interesting the methods using the Impulse Excitation Technique (IET), which were developed in the previous chapters. In the following, a methodology for determining the elasticity constants of anisotropic polycrystalline thin films will be presented by modeling the film microstructure. It will be applied to determine the elasticity constants of anisotropic titanium films sputter-deposited using the GLancing Angle Deposition (GLAD) process. The elastic behavior of such polycrystalline films is not known in the literature, which motivates the present study.

V.5. Oblique deposition and characterization

V.5.1. Glancing angle deposition: procedure and conditions

A DEPHIS4 PVD machine (Fig. III.2) was used to deposit titanium thin films at floating temperature, by magnetron sputtering, at oblique incidence on glass, iron and silicon substrates. A high purity (99.99 %) Ti circular target of 200 *mm* diameter was used. The glass substrates were used for NI and XRD measurements, and to determine the elasticity constants of the Ti films by means of the IET. Iron substrates were used to determine the film residual stresses using the curvature method (Stoney's formula). Silicon substrates were used for Scanning Electron Microscope (SEM) imaging. The substrates were ultrasonically cleaned in ethanol and acetone for 10 *min*. Then, they are fixed on the same aluminum holders as those used in Chapter IV, with three different inclinations α = 0°, 45° and 80° for deposition with respect to the target normal (Fig. IV.1). The target-to-substrate distance was set at 22 *cm*. The deposition chamber was first pumped down with a turbo-molecular pump to less than 10^{-4} *Pa*. Before the deposition process, the titanium target was sputter-cleaned for 20 *min* in pure argon discharge (Ar flow rate: 50 *sccm*) to remove impurities and surface contamination. The deposition process was carried out under a low pressure of 0.42 *Pa* with an argon flow rate of 40 *sccm*. The electrical

current intensity applied to the Ti target was 1.5 *A* using a DC-pulsed power supply for 240 *min* of deposition. The dimensions, mass and density of the glass substrates and Ti films are presented in Table V.1 and Table V.2. As for the case of series A, one pair of samples B were used for each glancing angle configuration, one along the longitudinal direction and the other one along the transverse direction.

Table V.1
Average dimensions and measurement uncertainties of the samples of series B.

Sample	Length (mm)		Width (mm)		Thickness			
					Substrate (mm)		Film (µm)	
	L	u(L)	b	u(b)	h_s	$u(h_s)$	h_c	$u(h_c)$
$B_{0,X}$	75.41	0.01	25.31	0.01	1.003	0.001	1.461	0.032
$B_{0,Y}$	75.48	0.05	25.35	0.03	0.975	0.001	1.380	0.032
$B_{45,X}$	75.36	0.01	25.35	0.01	1.016	0.002	2.063	0.067
$B_{45,Y}$	75.49	0.01	25.38	0.02	0.986	0.001	1.592	0.056
$B_{80,X}$	75.36	0.02	25.38	0.01	1.039	0.002	1.997	0.057
$B_{80,Y}$	75.43	0.04	25.4	0.01	0.969	0.002	1.187	0.059

Table V.2
Mass and density with the measurement uncertainties of the samples of series B.

Sample	Mass ($\pm 10^{-4}$ g)		Density (kg/m^3)			
	Substrate	Film	Substrate		Film	
			ρ_s	$u(\rho_s)$	ρ_c	$u(\rho_c)$
$B_{0,X}$	4.7178	0.0119	2464.44	2.66	4267.52	100.13
$B_{0,Y}$	4.5745	0.0111	2452.05	4.17	4203.72	104.73
$B_{45,X}$	4.7641	0.0155	2454.53	4.94	3932.91	130.24
$B_{45,Y}$	4.6217	0.0124	2446.49	3.16	4065.35	146.75
$B_{80,X}$	4.8741	0.0129	2452.71	4.86	3377.37	99.91
$B_{80,Y}$	4.5663	0.0081	2459.59	5.33	3561.69	182.43

V.5.2. Morphology

The grain morphology of the deposited titanium films was analyzed using a Hitachi S3500 N SEM-FEG electron microscope. Fig. V.7(a) and (b) show respectively the fractured cross-section and film surface (top-view) SEM images of the Ti films.

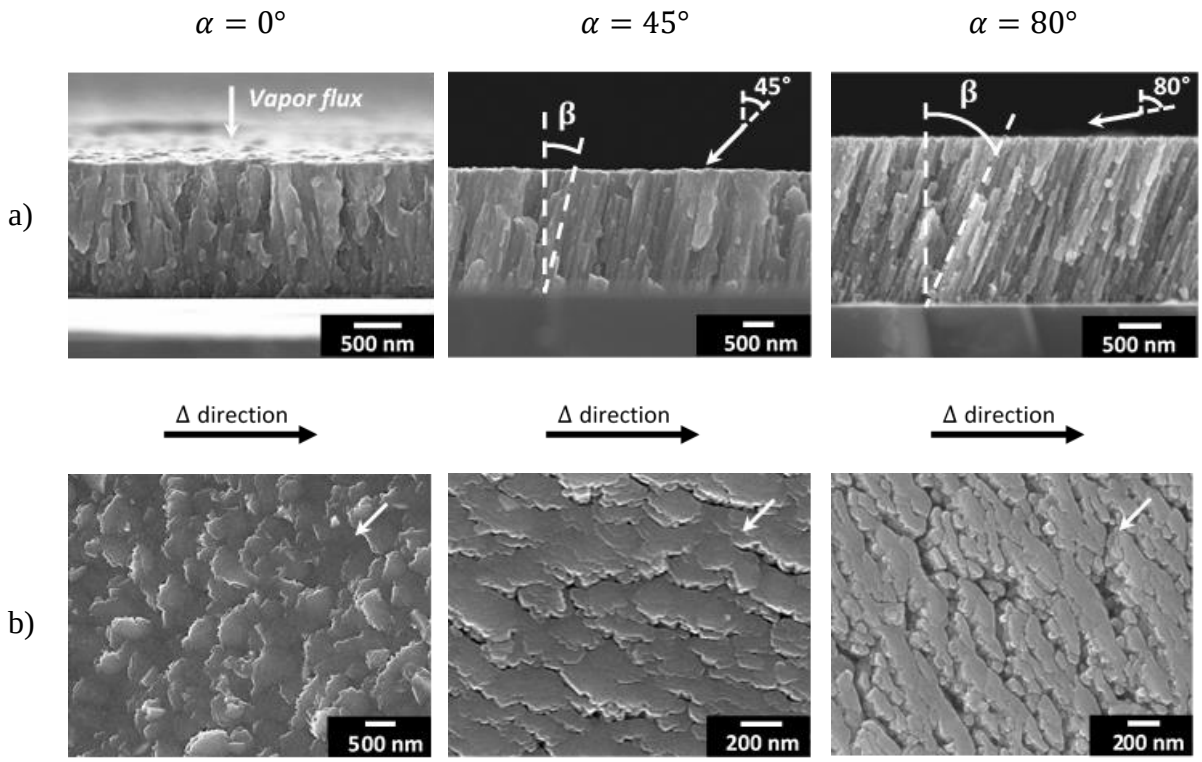

Fig. V.7. Cross-section (a) and top view (b) SEM images of Ti films grown by glancing angle deposition at various glancing angles α (0°, 45° and 80°).

It can be seen that the films exhibit a columnar growth, as commonly observed in Fig. IV.9. For zero incidence (α = 0°), the obtained structure is only slightly porous since no significant shadowing is performed and the micro-columns are not separated. As the glancing angle increases, the shadowing effect increases progressively and the structure becomes more porous. With increasing the deposition glancing angle α, the column tilt angle β increases. The film surface is considerably influenced by the glancing angle α. At zero incidence, the tops of the columns appear at the film surface with low inter-columnar porosity. For α > 0°, the in-plane anisotropic shadowing is formed owing to the oblique configuration and the gap between columns significantly increases. The column tilt angle β is ordinarily lower than the glancing angle α due to the shadowing effect [Abelmann 1997]. The shadowing effect on film growth at oblique deposition was explained in Section IV.6.2. The microstructural properties of the Ti films are presented in Table V.3.

Table V.3
Microstructural properties of the Ti thin films of series B.

Sample	Deposition Δ direction	Glancing angle α (±2°)	Column tilt angle β (±3°)	Fiber tilt angle η	u(η)
$B_{0,X}$	X-axis	0	0	14.79	0.07
$B_{0,Y}$	Y-axis	0	0	15.06	0.07
$B_{45,X}$	X-axis	45	5	27.75	0.04
$B_{45,Y}$	Y-axis	45	4	26.66	0.05
$B_{80,X}$	X-axis	80	21	42.95	0.04
$B_{80,Y}$	Y-axis	80	21	42.05	0.09

The columnar aspect leads to a low density of the film compared to the bulk material. The film porosity was determined from densities using Eq. (IV.23). The film density was calculated using its dimensions and mass. The density of the bulk titanium used in the calculation is 4500 kg/m^3. The obtained values for the porosity of samples B are presented in Table V.8. As we can see from Fig. V.7(a), the films are made up of needle-like grains (morphological texture), which is susceptible to induce an elastic anisotropy even in the absence of crystallographic texture [Koch 2004, Kumar 2006, Slim 2019]. The morphological texture was taken into account in the mechanical modeling. The columnar shape of the grains was introduced in the KE simulation using the ratios (Morris tensor) presented in Eq. (V.33). The grains were considered as ellipsoidal inclusions with a radius in the direction perpendicular to the film surface six times larger than the radii in the two other directions (Fig. V.8).

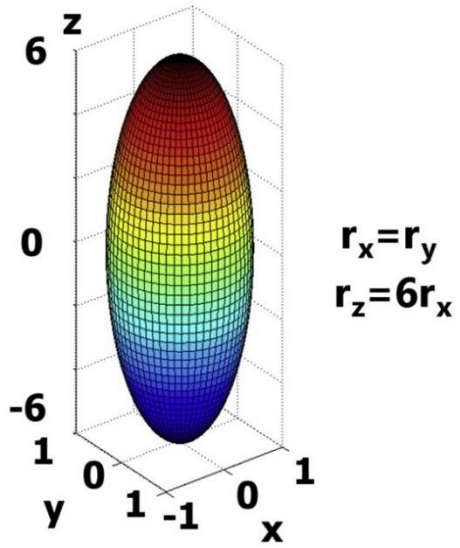

Fig. V.8. Ellipsoidal grain (needle-like grain) [Slim 2019].

The ellipsoidal grains are expressed in the sample coordinate system by replacing g_ϕ in Eq. (V.5) with g_β. The grain orientation used according to Bunge convention is then $\Omega \equiv (\varphi_1 = 0°,\ \phi = \beta,\ \varphi_2 = 0°)$ for the samples horizontally deposited ($B_{0,Y}$, $B_{45,Y}$, $B_{80,Y}$) and $(\varphi_1 = 90°,\ \phi = \beta,\ \varphi_2 = 0°)$ for those vertically deposited ($B_{0,X}$, $B_{45,X}$, $B_{80,X}$).

V.5.3. Crystalline structure and texture of the deposited titanium films

Thin films deposited by magnetron sputtering have generally a non-random crystallographic orientation. The film crystalline structure and texture were investigated by XRD using the Bruker D8 Advance diffractometer machine (Fig. III.7). The experimental protocol adopted is presented in Section IV.6.3.

V.5.3.1. Structural analysis

The identification of the titanium film phases was performed on the sum of the diffraction patterns collected using the experimental procedure introduced above. Fig. V.9 shows the sum of all the patterns for all the azimuth/tilt angles used. These diffraction patterns reveal the presence of single hexagonal closed packed (hcp) (P63/mmc) Ti_α phase for all samples in the investigated 2θ range. The structure of this phase can be obtained in the Crystallography Open Database (COD: http://www.crystallography.net) as ID entry 1532765. Fig. V.10 shows the intensity profile of the main (0002) peak of Ti_α at different glancing angles α. It can be noticed that a monotonic intensity variation of the (0002) XRD line is found with increasing α. The intensity is maximum for the Ti film deposited at $\alpha = 0°$. This change of intensity is accompanied by a reduction of the (0002) XRD line broadening from $\Gamma_{0,X} = \Gamma_{0,Y} = 0.45° \pm 0.01°$ (at $\alpha = 0°$) to slightly $\Gamma_{45,X} = \Gamma_{45,Y} = 0.48° \pm 0.01°$ (at $\alpha = 45°$) and to $\Gamma_{80,X} = \Gamma_{80,Y} = 0.55° \pm 0.02°$ (at $\alpha = 80°$). The symbol " Γ " represents the full-width at half maximum of the (0002) peak.

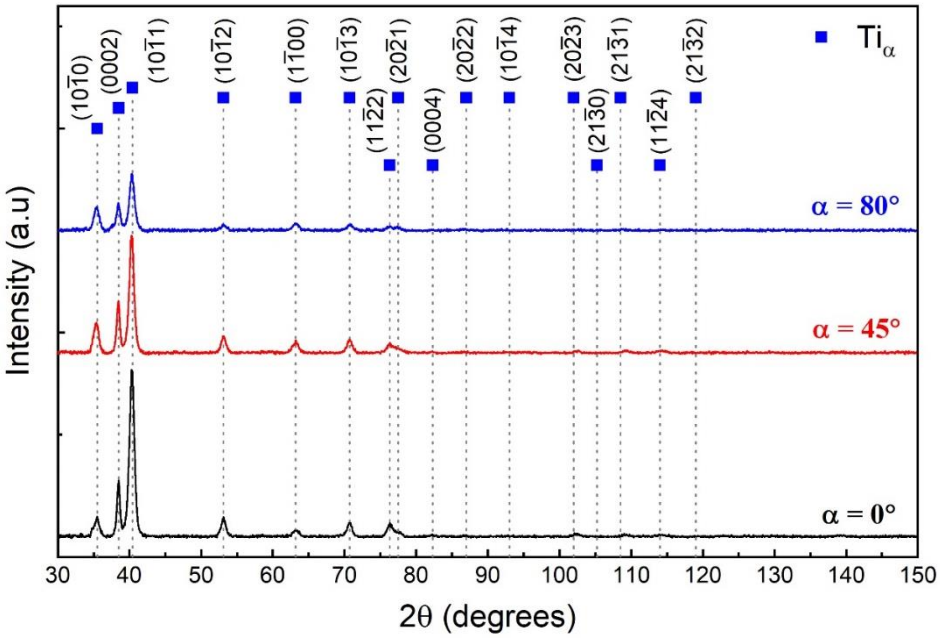

Fig. V.9. Sum of the XRD patterns of titanium films grown at the three values of glancing angle α (0°, 45° and 80°) for the samples of series B.

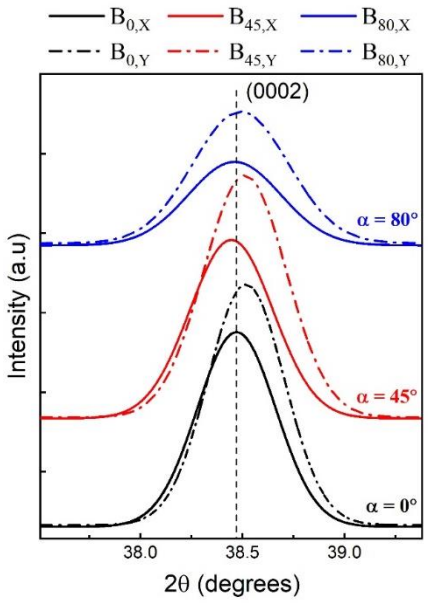

Fig. V.10. Intensity profile around the (0002) peak of Ti_α at the three values of glancing angle α (0°, 45° and 80°).

V.5.3.2. Texture

Fig. V.11 and Fig. V.12 show the experimental and recalculated pole figures of the Ti_α phase plotted using the DIFFRAC.TEXTURE software. The recalculated poles figures were

calculated using the Harmonic method. The texture measurements were carried out on the coated glass samples placed on the XRD stage so that the incident flux direction lies with the goniometer azimuthal angle ϕ = 90°. It can be seen that the texture of the Ti_α phase can be described reasonably well by an ideal $\{0002\}$ fiber, i.e. [0002] axis perpendicular to the film surface. The fiber texture formation was discussed in Sections IV.2.3 and IV.6.3. We can notice that the measured intensities spread by about 10° in tilt and 35° in azimuth around the ideal fiber. Furthermore, we can notably observe in Fig. V.11 with $\alpha = 0°$ that the pole is slightly shifted towards Δ direction. The angular spread and the fiber shift are usual in such sputtering processes and can be due to small angular spread between the substrate normal and the vapor flux direction [Sohn 1994, Slim 2019]. For α = 45° and 80°, the fiber axis is tilted towards the direction of the incoming vapor flux. This tilting of the fiber axis with respect to the film normal is defined by a fiber tilt angle η. Two rings were found at ~ 61° and ~ 82° of inclination in the $\{10\bar{1}1\}_\alpha$ pole figures of Fig. V.12.

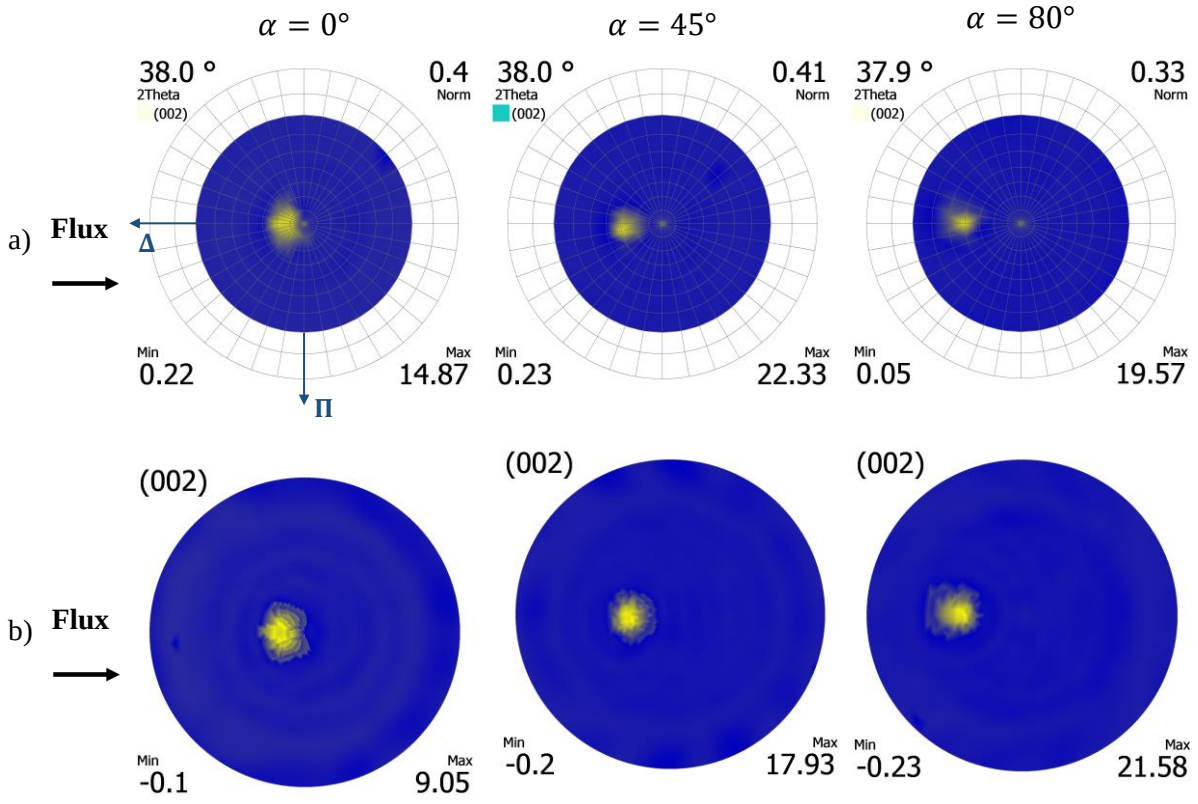

Fig. V.11. $\{0002\}_\alpha$ (a) experimental and (b) recalculated pole figures of the Ti_α phase of films deposited at various glancing angles α (0°, 45° and 80°). The pole figures are represented in stereographic projections and the black arrows at the left of the figures show the vapor flux direction.

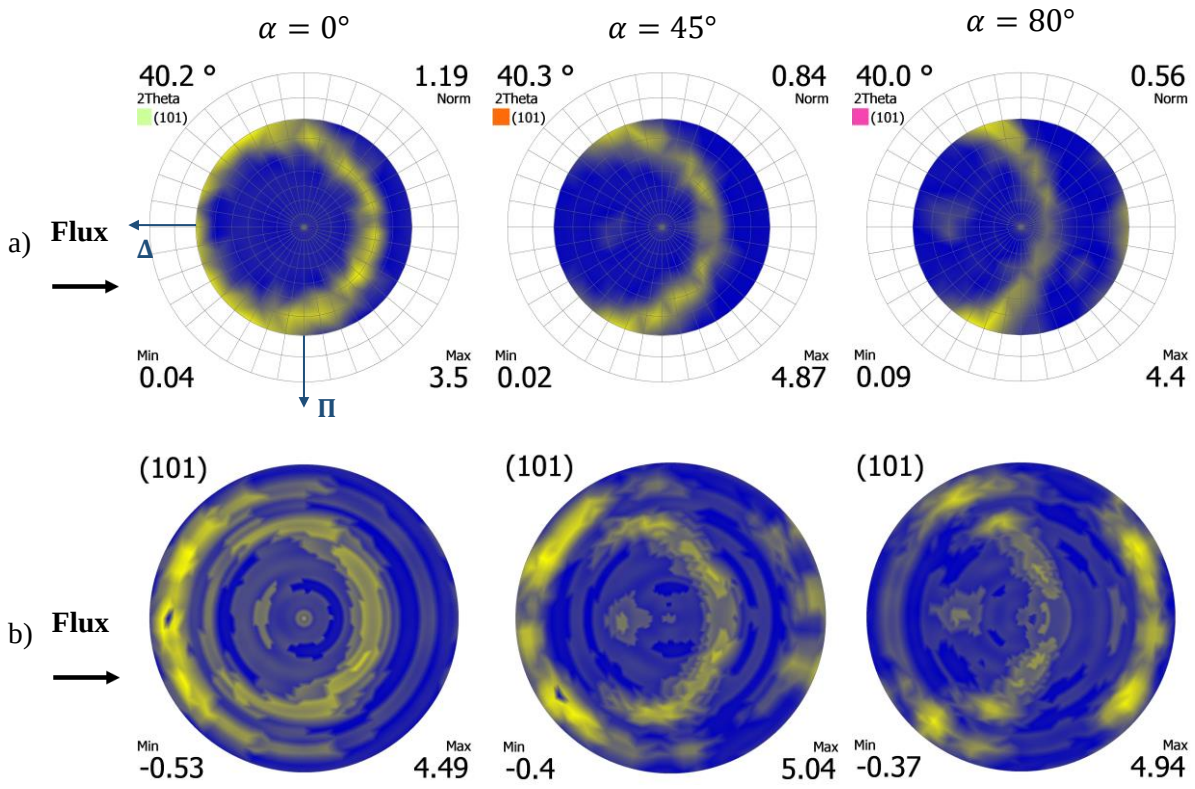

Fig. V.12. $\{10\bar{1}1\}_\alpha$ (a) experimental and (b) recalculated pole figures of the Ti_α phase of films deposited at various glancing angles α (0°, 45° and 80°). The pole figures are represented in stereographic projections and the black arrows at the left of the figures show the vapor flux direction.

Therefore, measuring only in $\theta - 2\theta$ scans (2θ mode) for GLAD films can lead to wrong interpretation of the preferred orientation. In order to determine the values of the fiber tilt angle η at different glancing angles α, the samples were diffracted in ψ mode. Fig. V.13 shows the $\{0002\}_\alpha$ intensity profile taken along the ψ direction at $\phi = 0°$ for vertically deposited samples ($B_{0,X}$, $B_{45,X}$, $B_{80,X}$) and at $\phi = 90°$ for horizontally deposited samples ($B_{0,Y}$, $B_{45,Y}$, $B_{80,Y}$). By fitting the XRD experimental data using a pseudo-Voigt function, the fiber tilt angles with the measurement uncertainties were determined (Table V.3).

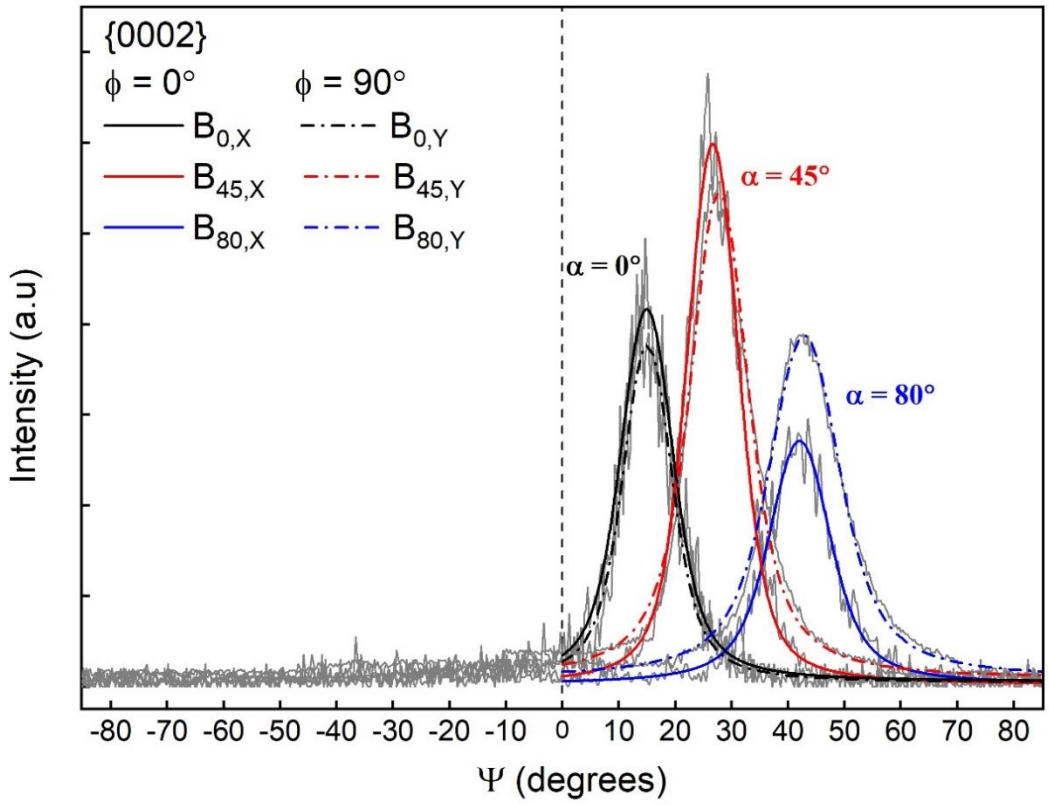

Fig. V.13. $\{0002\}_\alpha$ XRD intensity profile along the ψ axis at $\phi = 0°/90°$ for Ti films deposited at different glancing angles α (0°, 45° and 80°). The grey lines correspond to experimental acquisitions.

The films deposited on the steel substrates (AISI316) have the same texture as those deposited on the glass substrates. This allows concluding that, in our case, the texture is more managed by the growth of the film rather than an epitaxy on the substrate. The XRD measurements presented herein were for samples deposited horizontally (mentioned as Y index). Very similar XRD patterns and pole figures measurements were also observed on the second sample of each pair of the samples that were deposited toward the transverse direction, i.e. the X-axis of the samples is parallel to the Δ direction.

Eqs. (V.8), (V.9) and (V.10) can be used to determine the angles, which define an ideal orientation. In our case, the Ti films develop a polycrystalline growth with fiber-texture type, which is not perfect and obviously does not represent an ideal orientation. The experimental data were compared to theoretical values calculated using the "Groupes ponctuels" Crystallography software [Rousseau 2018]. The $\{0002\}$ and $\{10\bar{1}1\}$ ideal orientations of the Ti_α phase are presented in Fig. V.14.

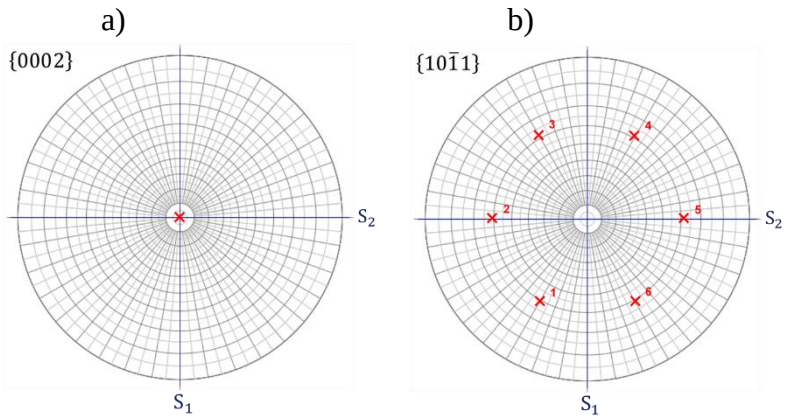

Fig. V.14. $\{0002\}_\alpha$ (a) and $\{10\bar{1}1\}_\alpha$ (b) simulated pole figures of the Ti_α phase with ideal orientation. The pole figures are represented in stereographic projections. The Red Crosses represent the poles of the northern hemisphere.

In order to simulate the pole figures of the Ti_α phase at different glancing angles α, the new position of the intensity poles of the $\{0002\}_\alpha$ and $\{10\bar{1}1\}_\alpha$ family of planes, tilted owing to the oblique configuration, should be identified. To do that, the following equation was solved:

$$\vec{V}_{\phi_i,\psi_i} = \begin{pmatrix} \cos\phi_i \sin\psi_i \\ \sin\phi_i \sin\psi_i \\ \cos\psi_i \end{pmatrix} = [g(\varphi_1, \eta, \varphi_2)]^T \begin{pmatrix} \cos\phi \sin\psi \\ \sin\phi \sin\psi \\ \cos\psi \end{pmatrix} \quad \text{(V.44)}$$

Where (ϕ_i, ψ_i) and (ϕ, ψ) are respectively the new and reference positions of the intensity pole i.

The new poles positions were calculated from Eq. (V.44) and the simulated pole figures of the $\{0002\}_\alpha$ and $\{10\bar{1}1\}_\alpha$ family of planes at the three glancing angles α are presented in Fig. V.15.

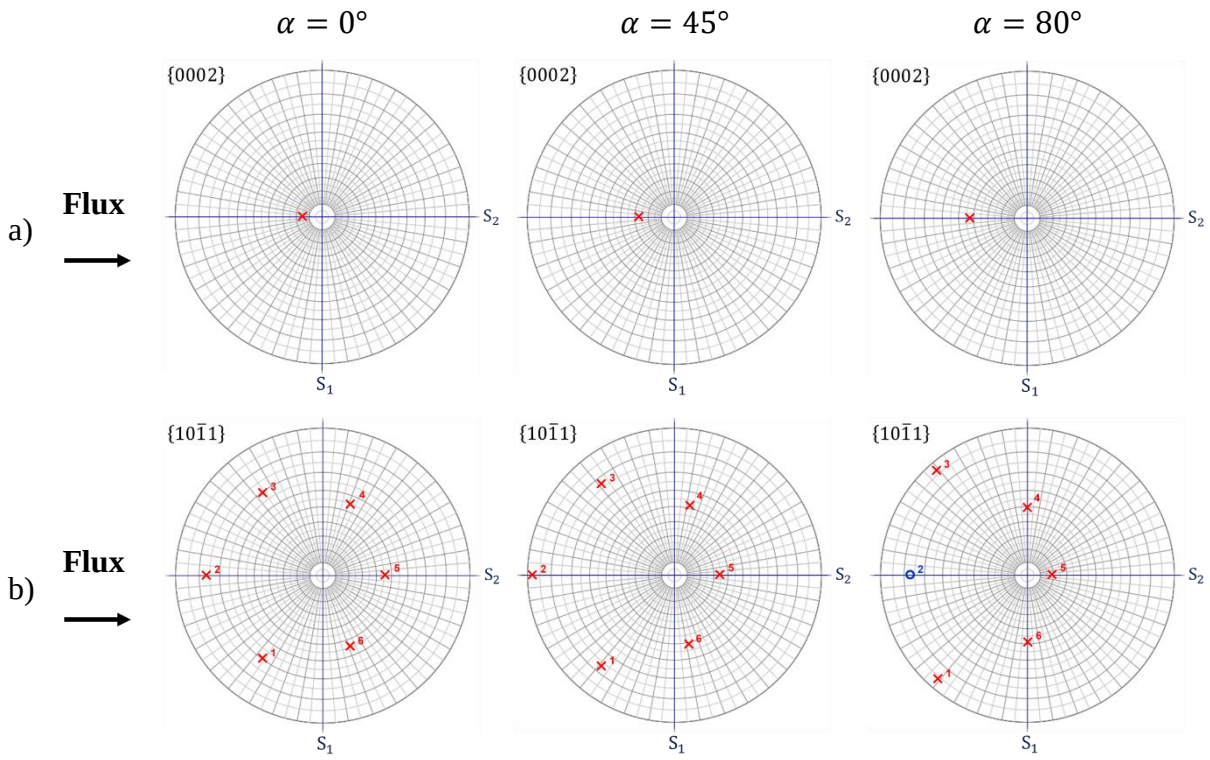

Fig. V.15. $\{0002\}_{\alpha}$ (a) and $\{10\bar{1}1\}_{\alpha}$ (b) simulated pole figures of the Ti_{α} phase with an ideal orientation at different glancing angles α (0°, 45° and 80°). The pole figures are represented in stereographic projections. The Red Crosses represent the poles of the northern hemisphere. The blue circle represents the poles of the southern hemisphere. The black arrows at the left of the figures show the vapor flux direction.

The relation between the sample system and the crystal system is described through the transformation matrix (Eq. (V.6)) using the Euler angles according to the Bunge convention [Bunge 1982]. The orientation of each crystallite is defined as $\Omega \equiv (\varphi_1,\ \phi,\ \varphi_2)$. In the mechanical modeling, the angular spread of the texture around the ideal components is neglected. By comparing the simulated pole figures (Fig. V.15) with the experimental pole figures of Ti_{α} phase (Fig. V.11 and Fig. V.12), we can notice that the intensity poles are approximately located at the same positions. So we can conclude that the texture of Ti_{α} phase can be described using the following Euler angles, according to the Bunge convention: $\Omega \equiv (\varphi_1 = 0°,\ \phi = \eta,\ 0 \leq \varphi_2 \leq 360°)$ for the samples horizontally deposited ($B_{0,Y}$, $B_{45,Y}$, $B_{80,Y}$) and $(\varphi_1 = 90°,\ \phi = \eta,\ 0 \leq \varphi_2 \leq 360°)$ for those vertically deposited ($B_{0,X}$, $B_{45,X}$, $B_{80,X}$).

V.6. Application of the self-consistent model to polycrystalline titanium thin films sputter-deposited at oblique incidence

V.6.1. Determination of the macroscopic elasticity constants of the titanium films using the Impulse Excitation Technique

The torsional and flexural resonance frequencies of the glass substrates before and after deposition are given in Table V.4. The macroscopic elasticity constants of the glass substrates, and their uncertainties, are presented in Table V.5. Table V.6 and Table V.7 present the macroscopic elasticity constants of the titanium thin films deposited on the glass substrates and their uncertainties. The elasticity constants and their uncertainties were calculated using the methodology presented in Section IV.3. The dimensions and masses of the substrates and films are presented respectively in Table V.1 and Table V.2.

Table V.4
Resonance frequencies of glass substrates measured by IET before and after deposition of the Ti films.

Sample	Flexural resonance frequencies (Hz)		Torsional resonance frequencies (Hz)	
	Before deposition	After deposition	Before deposition	After deposition
$B_{0,X}$	966.334	968.105	1792.796	1795.170
$B_{0,Y}$	936.110	937.745	1739.270	1741.480
$B_{45,X}$	975.923	977.284	1810.487	1812.940
$B_{45,Y}$	946.571	948.199	1757.214	1759.310
$B_{80,X}$	1000.010	999.504	1852.695	1852.360
$B_{80,Y}$	936.616	937.193	1734.936	1735.380

Table V.5
Macroscopic elasticity constants of the glass substrates (assumed to be elastically isotropic).

Sample	E_s (GPa)	$u(E_s)$ (GPa)	G_s (GPa)	$u(G_s)$ (GPa)	ν_s	$u(\nu_s)$
$B_{0,X}$	70.31	0.21	28.341	0.084	0.240	0.005
$B_{0,Y}$	69.73	0.26	28.200	0.090	0.236	0.006
$B_{45,X}$	69.42	0.41	28.112	0.164	0.235	0.010
$B_{45,Y}$	69.38	0.22	28.078	0.086	0.236	0.005
$B_{80,X}$	69.45	0.21	28.131	0.081	0.234	0.005
$B_{80,Y}$	70.71	0.44	28.559	0.175	0.238	0.010

Table V.6
Macroscopic Young's moduli of the titanium films deposited at various deposition glancing angles.

Sample	E_x (GPa)	$u(E_x)$ (GPa)	E_y (GPa)	$u(E_y)$ (GPa)	AR_E	$u(AR_E)$	$E_{isotropic}$ (GPa)	$u(E_{isotropic})$ (GPa)
$B_{0,X}$	99.56	7.85	-	-	0.96	0.11	98.88	5.34
$B_{0,Y}$	-	-	95.82	8.66			96.47	5.88
$B_{45,X}$	62.83	6.69	-	-	1.46	0.19	68.23	3.95
$B_{45,Y}$	-	-	92.05	7.83			87.08	5.48
$B_{80,X}$	15.63	8.22	-	-	4.18	2.27	19.44	3.89
$B_{80,Y}$	-	-	65.34	9.26			57.32	6.87

Table V.7
Macroscopic shear moduli of the titanium films deposited at various deposition glancing angles.

Sample	G_{yz} (GPa)	$u(G_{yz})$ (GPa)	G_{xz} (GPa)	$u(G_{xz})$ (GPa)	AR_G	$u(AR_G)$
$B_{0,X}$	33.83	1.46	-	-	0.98	0.06
$B_{0,Y}$	-	-	33.27	1.52		
$B_{45,X}$	27.75	1.27	-	-	1.07	0.07
$B_{45,Y}$	-	-	29.65	1.55		
$B_{80,X}$	11.24	0.98	-	-	1.59	0.21
$B_{80,Y}$	-	-	17.89	1.76		

Young's and shear moduli measured with IET (Table V.6 and Table V.7) are significantly lower than those of the bulk material (~ 120.2 *GPa* and ~ 45.6 *GPa* respectively) [Brandes 1992, Donachie 2000], even for the film deposited with normal incidence. This may be due to the high porosity present in the film. The density and porosity calculated using Eq. (IV.23), are presented in Table V.8. The density of bulk titanium used in the calculation of porosity is ρ = 4500 kg/m^3 [Brandes 1992, Verkhovtsev 2013]. The density of the film was calculated using the mass and dimensions of the film (Table V.1 and Table V.2).

The porosity assessment was also performed by image analysis using ImageJ software [ImageJ 2017]. Image analysis of SEM top-view images was done as described in Section IV.7.3. This method was carefully performed on five different SEM images of each film and the mean value with the uncertainty of the area fraction of porosity were quantified. The results

of the image analysis are also presented in Table V.8. We can notice, from either Eq. (IV.23) or image analysis, that the porosity within the Ti films increases by increasing the glancing angle. The difference between the values obtained using the two approaches is lower than the measurement uncertainties.

Table V.8
Density and Porosity in the Ti films estimated using Eq. (IV.23) and ImageJ with their uncertainties.

Sample	Film density ρ_c (Kg/m^3)	$u(\rho_c)$ (Kg/m^3)	Porosity p (%)		u(p) (%)	
			Eq. (IV.23)	ImageJ	Eq. (IV.23)	ImageJ
$B_{0,X}$	4267.52	100.13	5.17	4.62	2.23	0.51
$B_{0,Y}$	4203.72	104.73	6.58	5.83	2.33	0.78
$B_{45,X}$	3932.91	130.24	12.60	11.21	2.90	0.94
$B_{45,Y}$	4065.35	146.75	9.66	7.54	3.26	1.31
$B_{80,X}$	3377.37	99.91	24.95	26.81	2.22	1.12
$B_{80,Y}$	3561.69	182.43	20.85	22.21	4.05	1.08

Nemat-Nasser et al. [Nemat-Nasser 1993] have shown that with a first-order Taylor series development on different micromechanical models, the same relations for spherical pores, were obtained whatever the model. Young's and shear moduli calculated using Eqs. (IV.21) and (IV.22) with their uncertainties are presented in Table V.9. The Young's modulus and Poisson's ratio of the compact material are respectively 116 *GPa* and 0.32 [Leonhardt 2004]. The shear modulus is calculated from the Young's modulus and Poisson's ratio, assuming an isotropic behavior.

Table V.9
Elasticity constants of the Ti films calculated by taking into account the volume fraction of porosity of Eq. (IV.23) and the values of the compact material (without porosity).

Sample	Porosity p (%) Eq. (IV.23)	u(p) (%)	E^* (GPa) Eq. (IV.21)	$u(E^*)$ (GPa)	G^* (GPa) Eq. (IV.22)	$u(G^*)$ (GPa)
$B_{0,X}$	5.17	2.23	98.02	7.75	37.06	2.96
$B_{0,Y}$	6.58	2.33	93.09	8.10	35.17	3.09
$B_{45,X}$	12.60	2.90	72.14	10.08	27.16	3.86
$B_{45,Y}$	9.66	3.26	82.39	11.35	31.08	4.34
$B_{80,X}$	24.95	2.22	29.18	7.73	10.72	2.96
$B_{80,Y}$	20.85	4.05	43.44	14.11	16.18	5.40

The comparison between the elasticity constants measured by IET and those calculated with porosity are presented in Table V.10. The difference corresponds to the contribution of the microstructure. We can notice that the influence of the microstructure on the measured Young's moduli becomes significant at 45° and 80° of incidence, where this influence is higher than the measurement uncertainty. Therefore, the decrease in Young's modulus of the deposited titanium film cannot be due only to the presence of pores within the film. The influence of the microstructure on the measured shear modulus remains approximately constant.

Theoretically, this comparison can be used to represent the overall influence of the microstructural properties, as a whole, on the elasticity constants of such type of films. Nevertheless, their influence needs to be quantified and dissociated in order to determine the contribution of each microstructural parameter (morphology (β), texture (η), etc.) on the elasticity constants of thin films. This effect will be investigated in the next sections.

Table V.10
Comparison between the macroscopic elasticity constants of the titanium films calculated using Eq. (IV.21) and Eq. (IV.22) and those measured by IET.

Sample	$[\mathbf{E}^{\mathbf{IET}} - \mathbf{E}^{*}]$ (GPa)	u(E) (GPa)	Relative difference (%)	$[\mathbf{G}^{\mathbf{IET}} - \mathbf{G}^{*}]$ (GPa)	u(G) (GPa)	Relative difference (%)
$B_{0,X}$	1.54	7.85	1.6	3.23	1.46	8.7
$B_{0,Y}$	2.73	8.66	2.9	1.90	1.52	5.4
$B_{45,X}$	9.31	6.69	12.9	0.59	1.27	2.2
$B_{45,Y}$	9.66	7.83	11.7	1.43	1.55	4.6
$B_{80,X}$	13.55	8.22	46.4	0.52	0.98	4.9
$B_{80,Y}$	21.9	9.26	50.4	1.71	1.76	10.6

V.6.2. The macroscopic elasticity constants of the titanium films recalculated using the self-consistent model

The macroscopic elasticity constants were recalculated using the microscopic approach. The KE self-consistent model was used to determine the effective rigidity tensor C by taking into account the microstructure of the Ti film. Since the analytical expression of the effective stiffness tensor of the polycrystal calculated with the KE model cannot be determined

analytically, the calculation of the macroscopic elasticity constants of the Ti films was done by numerical iterations. The SCECs of the Ti_α phase and its Zener anisotropy ratio A^α [Zener 1948, François 2009] used in the calculation are the average of data found in the literature (Table V.11). Zener anisotropy ratio A allows us to quantify the anisotropy of a crystal. For hexagonal crystal, A is defined by [Kocks 1998]:

$$A = \frac{c_{11} + c_{12} - c_{33}}{c_{13}} \tag{V.45}$$

The crystalline orientation Ω of the films was taken into account using the Euler angles (Bunge convention) determined in Section V.5.3.2. Kelvin's notation was used for the index contraction [Kelvin 1856, Mehrabadi 1990]. The porosity (Table V.8) was taken into account in the calculation as a second phase and supposing its rigidity tensor equal to zero. Thus, Eq. (V.41) is rewritten as follows:

$$C = \left[V_\alpha \langle c_\Omega^\alpha : [P(C) : (c_\Omega^\alpha - C) + I_4]^{-1} \rangle_{\Omega \in V_\alpha} + V_p \, c_\Omega^p : \left[P(C) : \left(c_\Omega^p - C\right) + I_4\right]\right. \tag{V.46}$$

Where V_α and V_p represent the volume fractions of the α phase and the porosity. With zero rigidity of porosity, the second term on the right hand side of Eq. (V.46) will disappear and the volume fraction of the α phase becomes equal to $\left(1 - V_p\right)$. Therefore, no particular shape was attributed to the porosity.

Table V.11
SCECs of the Ti_α in GPa (Voigt's notation).

Material	c_{11}^α	c_{12}^α	c_{13}^α	c_{33}^α	c_{44}^α	A^α	Reference
Ti_α	162.4	92	69	180.7	46.7	1.068	[Simmons 1971]
Ti_α	162	91	69	181	46.7	1.043	[Chung 1967]
Ti_α	160	90	66	181	46.5	1.045	[Brandes 1992]
Average	161.47	91	68	180.9	46.63	1.052	
Standard deviation	1.28	1	1.73	0.17	0.11	0.014	

The simulation was achieved using the KE model with 5000 crystallites. This choice of 5000 number of diffracting crystallites is sufficient to ensure convergence for the planes with

low multiplicity. Using the SCECs of the Ti_{α} phase found previously (Table V.11) and assuming that the Ti_{α} phase exhibits an ideal fiber texture, the macroscopic rigidity tensor of the effective material was calculated. The components of the elasticity tensor were presented in Table V.12 for the Ti films at different configurations.

Table V.12
The components of the macroscopic rigidity tensor of the Ti films calculated using the KE model and using the average crystal values of Table V.11 in GPa (Kelvin's notation).

Sample	$\mathbf{C_{11}}$	$\mathbf{C_{22}}$	$\mathbf{C_{33}}$	$\mathbf{C_{12}}$	$\mathbf{C_{13}}$	$\mathbf{C_{23}}$	$\mathbf{C_{44}}$	$\mathbf{C_{55}}$	$\mathbf{C_{66}}$
$B_{0,X}$	130.7	131.1	162.5	68.3	55.4	55.5	84.1	84.1	62.6
$B_{0,Y}$	123.1	123.4	158.3	63.2	51.9	52.1	81.6	81.5	60.1
$B_{45,X}$	94.1	94.4	135.9	43.3	40.7	40.8	70.5	70.2	50.7
$B_{45,Y}$	108.1	108.7	144.6	52.0	46.9	47.1	75.7	75.5	56.4
$B_{80,X}$	47.8	49.8	91.9	18.0	21.1	22.5	49.8	45.6	30.8
$B_{80,Y}$	62.3	76.4	100.9	28.1	27.2	30.7	55.0	49.9	41.6

The effective rigidity tensors (in *GPa*) are slightly anisotropic in the film plane, with different properties between direction 3 (perpendicular to the film plane) and the other two directions for the three different glancing angles. At α = 0° and 45°, transversely isotropic films were obtained with axis 3 perpendicular to the film surface ($C_{11} \approx C_{22}$, $C_{13} \approx C_{23}$ and $C_{44} \approx C_{55}$). It is noted that (C_{11} and C_{22}), (C_{13} and C_{23}) and (C_{44} and C_{55}) become slightly different at α = 80°. The corresponding elasticity constants in the different directions are shown in Table V.13. The uncertainties presented in Table V.14 were calculated using the Monte Carlo method: knowing the distribution (standard uncertainty) of the input data, the distribution of the macroscopic elasticity constants can be computed by generating random sets of synthetic data centered on the values of the SCECs found in the literature.

Table V.13
The macroscopic elasticity constants of the Ti films calculated using KE model in GPa.

Sample	E_x	E_y	E_z	ν_{xy}	ν_{xz}	ν_{yz}	G_{xy}	G_{xz}	G_{yz}
$B_{0,X}$	90.1	90.4	131.6	0.44	0.19	0.19	31.3	42.0	42.0
$B_{0,Y}$	86.1	86.3	129.3	0.43	0.19	0.19	30.0	40.8	40.8
$B_{45,X}$	70.1	70.3	111.8	0.38	0.19	0.19	25.4	35.1	35.2
$B_{45,Y}$	78.4	78.8	117.0	0.39	0.20	0.20	28.2	37.8	37.9
$B_{80,X}$	38.7	39.7	75.6	0.29	0.16	0.16	15.1	22.2	23.4
$B_{80,Y}$	48.9	59.3	81.6	0.30	0.19	0.19	20.6	24.6	26.3

Table V.14
The measurement uncertainty on the macroscopic elasticity constants of the Ti films calculated using the KE model in GPa.

Sample	$u(E_x)$	$u(E_y)$	$u(E_z)$	$u(\nu_{xy})$	$u(\nu_{xz})$	$u(\nu_{yz})$	$u(G_{xy})$	$u(G_{xz})$	$u(G_{yz})$
$B_{0,X}$	13.7	13.7	4.8	0.07	0.02	0.02	4.4	1.8	2.2
$B_{0,Y}$	14.4	13.8	2.3	0.09	0.03	0.03	4.8	1.5	1.5
$B_{45,X}$	9.8	8.7	2.3	0.09	0.03	0.02	6.0	3.1	3.2
$B_{45,Y}$	12.2	14.3	2.3	0.09	0.03	0.03	5.9	2.5	2.2
$B_{80,X}$	6.3	8.6	12.0	0.16	0.08	0.07	5.2	4.6	5.2
$B_{80,Y}$	6.4	12.5	11.5	0.11	0.05	0.04	6.9	5.1	4.3

It can be observed from Table V.13 that the films exhibit a transversely isotropic behavior with weak anisotropy in the plane of the film surface at α = 80°. The difference between E_x and E_y can be attributed to the calculation uncertainty. The elasticity constants measured by IET and the recalculated elasticity constants are presented in Table V.15. The measured Young's moduli E_x and E_y obtained for α = 0° and 45° are different from those recalculated. The difference can be attributed to the measurements or the KE calculations uncertainties, which are in the same order. However, for α = 80°, we can see that the difference between the measured and recalculated Young's modulus in the x-direction E_x is higher than the measurements or calculations uncertainties. The value measured by IET is lower than the value obtained by the calculation. This can be attributed to the effect of the modulus in the z-direction on the one in the x-direction, that becomes significant at α = 80° and which is not considered in the analytical model (Eq. (IV.13)). Unlike the Young's moduli, the shear moduli

G_{yz} and G_{xz} measured by IET are lower than those calculated using KE model. This difference can be attributed to the isotropic assumption on which is based the analytical model used for shear modulus determination (Eq. (II.48)). On the other hand, the difference between the measured and calculated elasticity constants can be attributed to the inability of the KE model to model the microstructures presenting high porosity ($p \geq 12\%$). In order to verify the trueness of this presumption, a prediction of the Ti films of series A will be provided and discussed subsequently.

Table V.15
Comparison between the macroscopic elasticity constants of the titanium films calculated with the KE model and those measured by IET in GPa.

Sample		E_x	$u(E_x)$	E_y	$u(E_y)$	G_{yz}	$u(G_{yz})$	G_{xz}	$u(G_{xz})$
$B_{0,X}$	IET	99.56	7.85	-	-	33.83	1.46	-	-
	KE model	90.14	13.66	90.35	13.67	42.03	2.24	42.03	1.75
	Difference	9.42		-		8.20		-	
$B_{0,Y}$	IET	-	-	95.82	8.66	-	-	33.27	1.52
	KE model	86.06	14.44	86.25	13.83	40.80	1.50	40.75	1.49
	Difference	-		9.57		-		7.48	
$B_{45,X}$	IET	62.83	6.69	-	-	27.75	1.27	-	-
	KE model	70.12	9.82	70.31	8.73	35.21	3.23	35.09	3.12
	Difference	7.29		-		7.46		-	
$B_{45,Y}$	IET	-	-	92.05	7.83	-	-	29.65	1.55
	KE model	78.39	12.15	78.81	14.26	37.85	2.23	37.76	2.45
	Difference	-		13.24		-		8.11	
$B_{80,X}$	IET	15.63	8.22	-	-	11.24	0.98	-	-
	KE model	38.68	6.33	39.68	8.63	23.44	5.15	22.19	4.56
	Difference	23.05		-		12.20		-	
$B_{80,Y}$	IET	-	-	65.34	9.26	-	-	17.89	1.76
	KE model	48.93	6.39	59.26	12.51	26.27	4.34	24.63	5.14
	Difference	-		6.08		-		6.74	

V.6.3. Influence of the microstructural properties on the macroscopic behavior

The influences of the porosity, the crystallographic and morphological textures on the elasticity constants were taken into account in the calculation of the rigidity tensor of the film.

However, it can be interesting to study the relative influence of these factors on the elasticity constants of the film. It is indeed easy to imagine that a very small tilt angle of the columns would lead to very poor sensitivity. To quantify this effect, the factors were varied one by one with the help of the KE model. A reference configuration was chosen (no texture, no porosity, spherical inclusions) and the various factors were introduced one by one with respect to this reference. The results are presented in Table V.16 and shown in Fig. V.16. The vertical samples ($B_{0,X}$, $B_{45,X}$, $B_{80,X}$) were chosen to study the effect on the elasticity constants E_x, G_{yz} with their uncertainty u(E_x), u(G_{yz}), while the horizontal samples ($B_{0,Y}$, $B_{45,Y}$, $B_{80,Y}$) were chosen to study the effect on the modulus E_y, G_{xz} with their uncertainty u(E_y), u(G_{xz}).

Table V.16
Effect of the porosity, the morphological and crystallographic textures on the Young's and shear moduli in GPa.

Elasticity constants	**Reference configuration**	**Texture of Ti_α phase**			**Porosity**			**Elongated and tilted grains**			**Uncertainty of measurements performed by IET**		
		0°	45°	80°	0°	45°	80°	0°	45°	80°	0°	45°	80°
E_x		+9	+7	+4	+12	+22	+58	+0.1	+0.3	+0.19	7.9	6.7	8.2
E_y	114.60	+9	+8	+4	+15	+22	+48	+0.4	+0.2	+0.04	8.7	7.8	9.3
E_z		-25	-16	-5	+15	+22	+48	-0.18	-0.3	-0.37		-	
G_{yz}		-3	-3	-2	+4	+8	+21	≈ 0	-0.1	≈ 0	1.5	1.3	1.0
G_{xz}	43.35	-3	-3	-2	+6	+8	+18	-0.2	-0.2	-0.1	1.5	1.6	1.8
G_{xy}		+7	+6	+3	+5	+8	+18	+0.2	+0.2	+0.2		-	

It can be observed from Table V.16 or Fig. V.16 that the porosity has a dominant effect on the Young's and shear moduli, while the morphological texture has a negligible effect for all films deposited at three glancing angles. We can also notice that the texture has a negligible effect (less than uncertainty) on Young's moduli determined in the three directions for α = 80°. However, for α = 0° and 45°, its effect is superior to the uncertainty. However, the effect of the texture on the shear moduli is higher than the measurement uncertainty for all films deposited at three glancing angles.

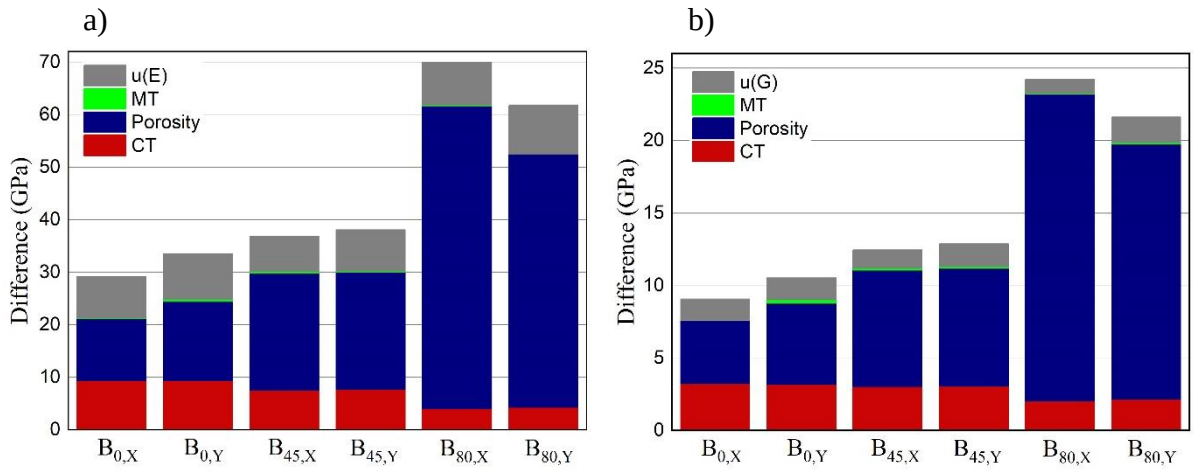

Fig. V.16. Effect of the porosity, the morphological and crystallographic textures on: a) Young's moduli and b) shear moduli, (MT): Morphological texture, (CT): Crystallographic texture.

The results of a comparison between non-textured and textured thin films are presented in Table V.17. It can be noticed that the effect of non-tilted fiber (η = 0°) is higher than the measurement uncertainty. Then, by tilting the fiber texture, the effects of the texture and the tilted fiber compensate each other and thus the combined effect becomes negligible compared to the measurement uncertainty. It can also be noticed that no plane anisotropy is induced due to the texture of Ti_{α} phase. It might be possible to obtain a difference in Young's moduli in the x and y directions for textures different from the fiber texture found in this study. Furthermore, the porosity, the morphological and crystallographic textures do not have a significant effect on the Poisson's ratios in the different directions. In conclusion, the porosity has the strongest effect on the Young's and shear moduli of the Ti film.

Table V.17
Effect of the texture of the Ti_α phase in GPa.

Sample		E_x	E_y	E_z	G_{xy}	G_{xz}	G_{yz}
	No texture	114.6	114.6	114.6	43.4	43.4	43.4
	Fiber (η = 0°)	104.4	104.4	114.3	35.2	46.6	46.6
	Difference	10.2	10.2	0.3	8.2	-3.2	-3.2
$B_{0,X}$	Tilted fiber (η = 14.79°)	105.2	105.2	139.7	35.9	46.7	46.7
	Difference	9.4	9.4	-25.1	7.5	-3.3	-3.3
$B_{0,Y}$	Tilted fiber (η = 15.06°)	105.2	105.2	139.6	35.9	46.7	46.7
	Difference	9.4	9.4	-25	7.5	-3.3	-3.3
$B_{45,X}$	Tilted fiber (η = 27.75°)	107.2	107.1	130.5	37.5	46.6	46.5
	Difference	7.4	7.5	-15.9	5.9	-3.2	-3.1
$B_{45,Y}$	Tilted fiber (η = 26.66°)	106.9	106.9	131.4	37.4	46.5	46.6
	Difference	7.7	7.7	-16.8	6.0	-3.1	-3.2
$B_{80,X}$	Tilted fiber (η = 42.95°)	110.7	110.6	119.1	40.5	45.6	45.5
	Difference	3.9	4.0	-4.5	2.9	-2.2	-2.1
$B_{80,Y}$	Tilted fiber (η = 42.05°)	110.4	110.3	119.7	40.3	45.7	45.6
	Difference	4.2	4.3	-5.1	3.1	-2.3	-2.2

V.6.4. Influence of the microstructural properties on the elastic behavior of the diffracting volume

As can be seen from Table V.18, the effect of the morphological texture on the macroscopic elasticity constants is not very pronounced. However, several studies [Hendrix 1998, Koch 2004, Slim 2019] showed that the grain shape texture has a more pronounced effect on the microscopic elastic response than on the macroscopic elastic response. The influence of the microstructural properties on the behavior of the diffraction volume is evaluated by analyzing the microscopic elastic response of the Ti_α phase presented in Eq. (V.43). To do this, we suppose that the composite (substrate + film) of thickness *h* is subjected to a biaxial stress state determined by bending under applied strain. Assuming a null curvature radius on the transverse direction (ε_{yy} = 0) and a planar stress state (σ_{zz} = 0), the macroscopic stress and strain tensors can be expressed as a function of a curvature radius *R* on the longitudinal direction (x-direction) as follows:

$$\varepsilon^I = \frac{h}{2R}\begin{pmatrix} 1 & 0 & 0 \\ 0 & 0 & 0 \\ 0 & 0 & -\frac{C_{13}}{C_{33}} \end{pmatrix} \tag{V.47}$$

$$\sigma^I = \frac{h}{2R}\begin{pmatrix} C_{11} - \frac{C_{13}^2}{C_{33}} & 0 & 0 \\ 0 & C_{12} - \frac{C_{13}\,C_{23}}{C_{33}} & 0 \\ 0 & 0 & 0 \end{pmatrix} \tag{V.48}$$

Since the initial residual stress state is not known yet, the variation of strains between an initial (R_0 = 790 *mm*) and a loaded stress (R = 530 *mm*, 400 *mm*, 330 *mm*, 210 *mm*, 150 *mm* and 120 *mm*) is considered in the following expression:

$$\Delta\varepsilon_{\phi,\psi}^{\{hkl\}_\alpha} = \left[\varepsilon_{\phi,\psi}^{\{hkl\}_\alpha}\right]_R - \left[\varepsilon_{\phi,\psi}^{\{hkl\}_\alpha}\right]_{R_0=790mm} \tag{V.49}$$

This expression is applicable for a purely elastic behavior where the initial residual stress state remains constant and thus the stress-free lattice parameters are not necessarily required. The microscopic strain was calculated on three different plane families, $\{11\bar{2}4\}_\alpha$, $\{20\bar{2}3\}_\alpha$ and $\{21\bar{3}1\}_\alpha$. Fig. V.17 shows the $\{11\bar{2}4\}_\alpha$, $\{20\bar{2}3\}_\alpha$ and $\{21\bar{3}1\}_\alpha$ recalculated pole figures of the Ti_α phase at different glancing angles.

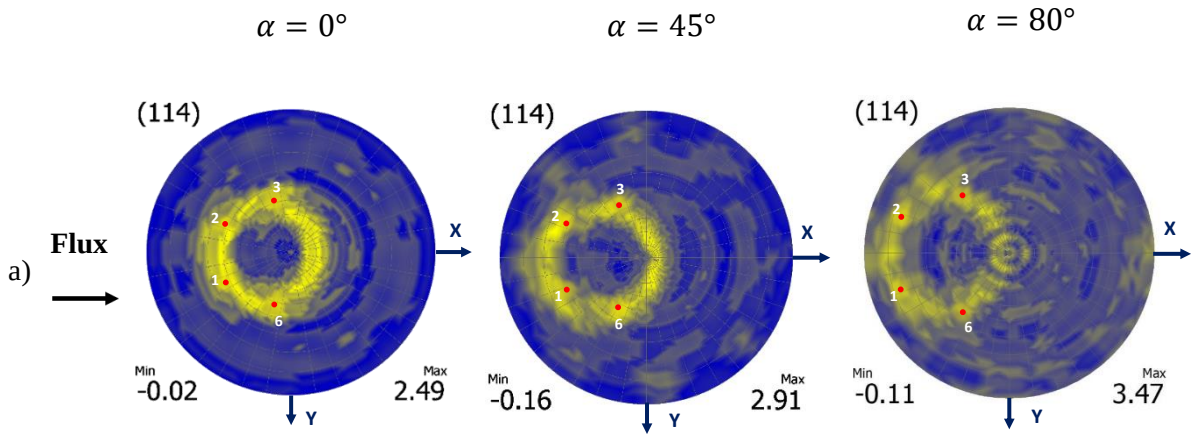

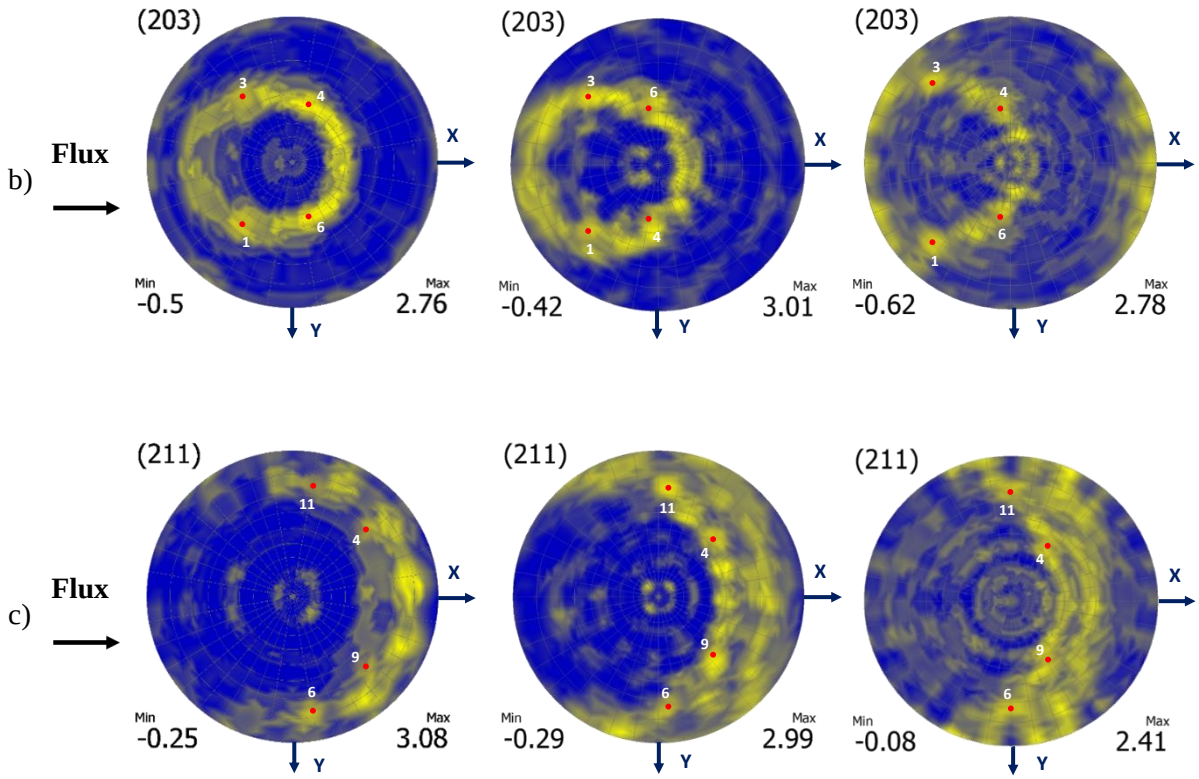

Fig. V.17. a) $\{11\bar{2}4\}_\alpha$, b) $\{20\bar{2}3\}_\alpha$ and c) $\{21\bar{3}1\}_\alpha$ recalculated pole figures of the Ti_α phase of films deposited at various glancing angles α (0°, 45° and 80°). The red dots represent the poles of the ideal orientations. The pole figures are represented in stereographic projections. The black arrows "Flux" at the left of the figures show the vapor flux direction.

In order to determine the microscopic strains at different glancing angles, the new positions of the intensity poles of the $\{11\bar{2}4\}_\alpha$, $\{20\bar{2}3\}_\alpha$ and $\{21\bar{3}1\}_\alpha$ family of planes, tilted owing to the oblique configuration were calculated using Eq. (V.44). The corresponding (ϕ,ψ) angles of the intensity poles are presented in Appendix A. The (ϕ,ψ) angles vary from glancing angle to another due to different tilts of the [0002] fiber texture. The theoretical pole figures of the $\{11\bar{2}4\}_\alpha$, $\{20\bar{2}3\}_\alpha$ and $\{21\bar{3}1\}_\alpha$ family of planes at the three glancing angles α are also presented in Fig. V.17. Among the calculated intensity poles presented in Table A.1, Table A.2, and Table A.3, only four poles of each plane family were taken into account in the microscopic calculation. The microscopic strains were calculated on the poles indicated by red dots in Fig. V.17.

Fig. V.18 shows the linear relationship between the strain variation and the inverse of the curvature radius at the three glancing angles. It can be noticed that the microscopic strain varies depending on the crystallographic plane $\{h\ k\ l\}$, the measurement direction and the glancing angle.

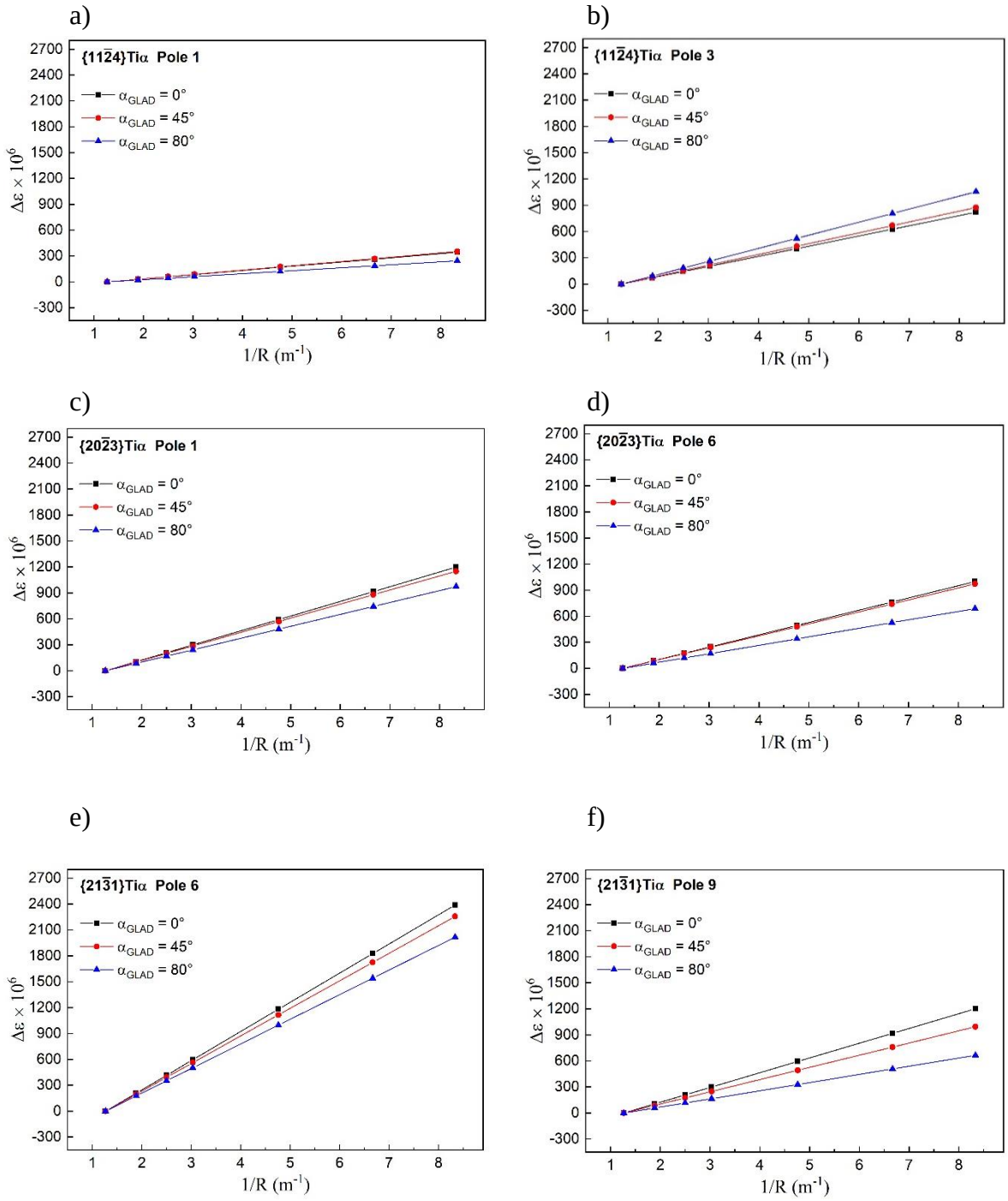

Fig. V.18. Strain variation as a function of the inverse of the curvature radius calculated using the KE model at various glancing angles α (0°, 45° and 80°).

A comparison of the elastic response of a textured film, a porous film, a grain shape textured film and an isotropic film (no morphological and crystallographic texture, no porosity) was done. The results of three different poles are presented in Fig. V.19. The strain variations of all the intensity poles determined from the KE model are presented in Appendix A.

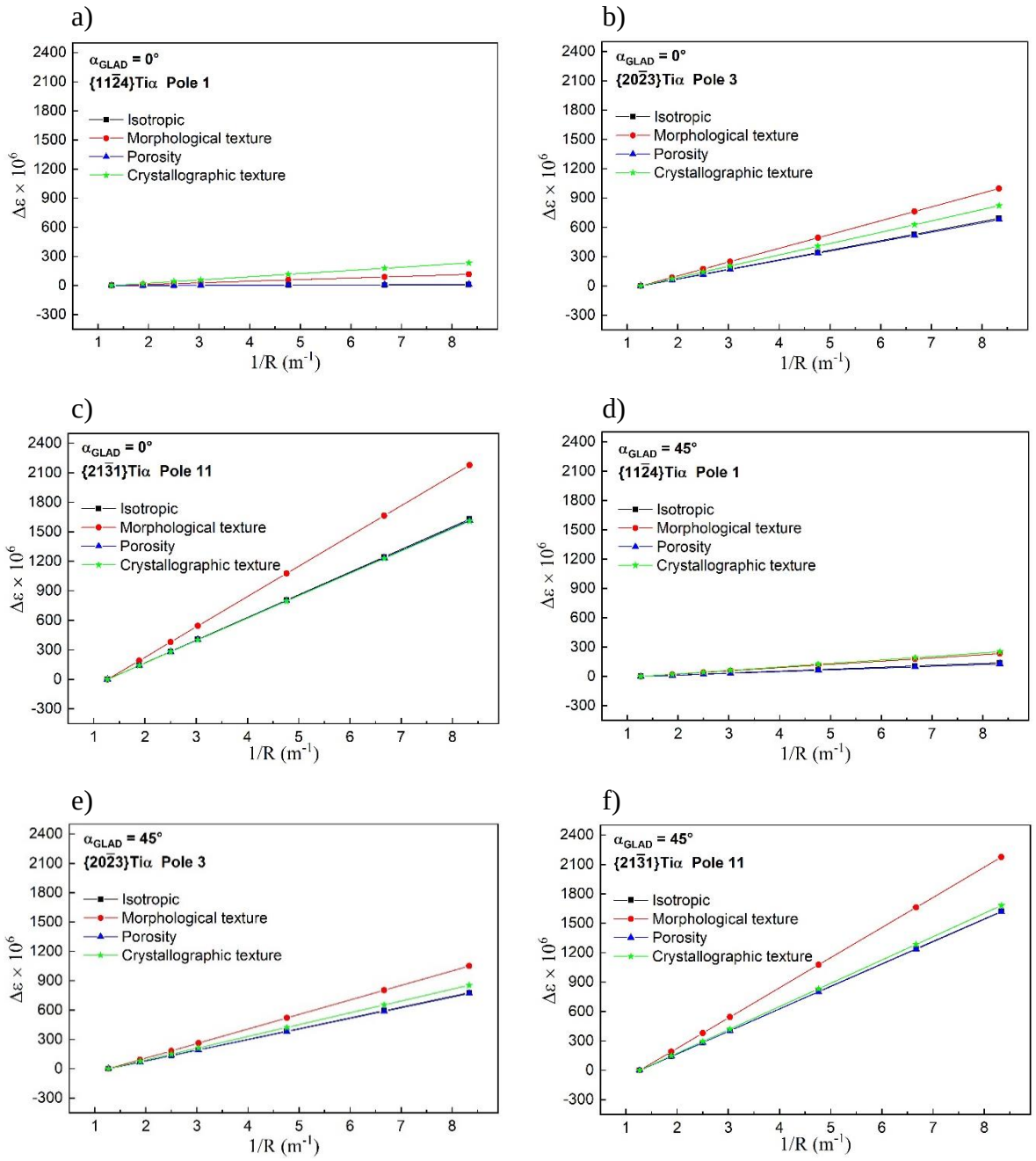

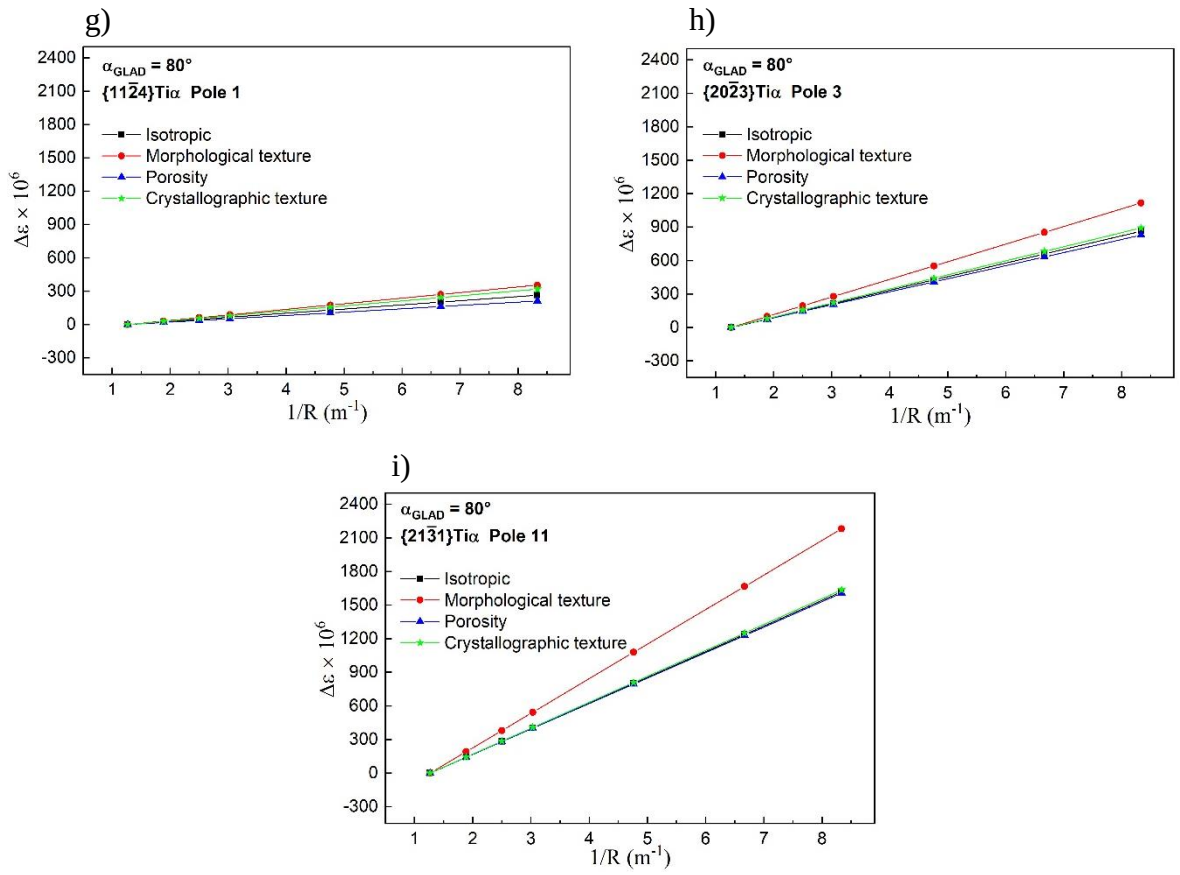

Fig. V.19. Effects of the porosity, the crystallographic, and the morphological textures on the elastic behavior of the diffracting volume. The strain variation was calculated using the KE model at various glancing angles α (0°, 45° and 80°).

It can be noticed from Fig. V.19 and the figures presented in Appendix A, that the effect of the morphological texture is more pronounced on the elastic behavior of the diffracting volume than on the elastic behavior of the film itself, as mentioned in the literature [Hendrix 1998, Koch 2004, Slim 2019]. The effects of the morphological and crystallographic textures are more or less pronounced depending on the crystallographic plane $\{h\ k\ l\}$, the measurement direction and the glancing angle. For instance, we can notice from the intensity pole 1 of the $\{11\bar{2}4\}_{\alpha}$ family of planes that the effect of the crystallographic texture predominates at α = 0°. However, at α = 80° of the same intensity pole, the microscopic behavior is influenced by the morphological texture. The porosity effect on the elastic behavior of the diffracting volume is less important than the effects of the grain shape and the crystallographic texture.

V.6.5. Prediction of the elasticity constants of titanium thin films presented in chapter IV

The experimental protocol and conditions adopted to characterize the films are the same as those presented in Section V.5.3. Using the single-crystal elasticity constants of the Ti_{α} phase (Table V.11) and assuming that the phase exhibits an ideal fiber texture, the elasticity constants in the different directions were calculated and presented in Table V.18. Their corresponding uncertainties, presented in Table V.19, were calculated using Monte Carlo method. The simulation was also carried out on 5000 crystallites by taking into account the microstructure of the films determined in Chapter IV. It can be noticed that all the films exhibit a transversely isotropic behavior with the absence of any plane anisotropy. These results can confirm the discussion and conclusion extracted from the results of Ti films of series B. The difference between the elasticity constants of the films presented in this chapter and those presented in Chapter IV can be attributed to the difference in the microstructure (porosity, morphology and texture).

Table V.18
The macroscopic elasticity constants of the Ti films of series A (presented in Chapter IV) calculated using KE model in GPa.

Sample	E_x	E_y	E_z	ν_{xy}	ν_{xz}	ν_{yz}	G_{xy}	G_{xz}	G_{yz}
$A_{0,X}$	98.9	98.8	140.5	0.47	0.19	0.19	33.6	44.9	44.9
$A_{0,Y}$	100.1	100.1	141.5	0.47	0.19	0.19	34.0	45.3	45.3
$A_{45,X}$	88.8	88.9	126.3	0.42	0.20	0.20	31.2	41.2	41.3
$A_{45,Y}$	93.2	93.4	124.4	0.41	0.22	0.22	33.0	42.3	42.3
$A_{80,X}$	86.5	88.0	103.0	0.33	0.26	0.27	32.7	37.2	38.0
$A_{80,Y}$	83.7	88.5	98.9	0.32	0.26	0.27	32.4	35.7	37.1

Table V.19
The measurement uncertainty on the macroscopic elasticity constants of the Ti films of series A calculated using KE model in GPa.

Sample	$u(E_x)$	$u(E_y)$	$u(E_z)$	$u(\nu_{xy})$	$u(\nu_{xz})$	$u(\nu_{yz})$	$u(G_{xy})$	$u(G_{xz})$	$u(G_{yz})$
$A_{0,X}$	13.8	13.8	4.8	0.06	0.02	0.02	4.4	1.8	2.2
$A_{0,Y}$	14.8	16.2	2.3	0.07	0.03	0.02	4.8	1.5	1.5
$A_{45,X}$	10.4	9.1	2.2	0.07	0.03	0.02	6.0	3.1	3.2
$A_{45,Y}$	12.5	15.4	2.3	0.07	0.03	0.02	5.9	2.5	2.2
$A_{80,X}$	7.4	9.0	12.0	0.07	0.06	0.05	5.2	4.6	5.2
$A_{80,Y}$	7.2	12.6	11.7	0.08	0.05	0.04	6.9	5.1	4.3

In order to verify the results of the elasticity constants calculated using the KE model, they were compared with those measured experimentally. The comparison was presented in Table V.20. As expected, the difference in Young's modulus between the two approaches is lower than the measurements or calculations uncertainties at α = 0° and 45°. It becomes higher than the uncertainties at α = 80°, while the film porosity remains lower than 10 % (Table IV.6). The two samples $A_{80,X}$ and $A_{80,Y}$ present low porosity (p = 8.39% and 9.30% respect.) compared with those of samples $B_{45,X}$, $B_{45,Y}$, $B_{80,X}$ and $B_{80,Y}$. However, their fiber tilt angles (η = 45.9° for $A_{80,X}$ and 46.4° for $A_{80,Y}$. (Table IV.1) are higher than those of series B. This indicates that the accuracy of the KE model does not depend on the porosity presented in the material but on a combined effect (porosity + texture).

It can be concluded that the elastic behavior of the GLAD films is not well described by the KE model. The KE model may not be well adapted to high porous materials, where significant pores interaction can probably be achieved. Although the porosity is described as an additional phase with zero rigidity, its shape (geometry) cannot be modeled with the KE model. However, this can be a preliminary study presenting the elastic behavior of such films. In order to study the validity range of the KE model, a comparison with other scale transition models is necessarily required.

Table V.20
Comparison between the macroscopic elasticity constants of the Ti films of series A calculated using the KE model and those measured by IET in GPa.

Sample		E_x	$u(E_x)$	E_y	$u(E_y)$	G_{yz}	$u(G_{yz})$	G_{xz}	$u(G_{xz})$
$A_{0,X}$	IET	88.77	8.72	-	-	27.92	1.34	-	-
	KE model	98.88	13.82	98.76	13.84	44.86	2.24	44.88	1.75
	Difference	10.11		-		16.94		-	
$A_{0,Y}$	IET	-	-	84.71	8.59	-	-	29.10	1.38
	KE model	100.14	14.83	100.13	16.18	45.30	1.50	45.30	1.49
	Difference	-		15.42		-		16.20	
$A_{45,X}$	IET	82.96	7.39	-	-	30.20	0.96	-	-
	KE model	88.76	10.35	88.93	9.10	41.29	3.23	41.29	3.12
	Difference	5.80		-		11.09		-	
$A_{45,Y}$	IET	-	-	78.42	9.82	-	-	23.98	1.34
	KE model	93.22	12.51	93.38	15.39	42.32	2.23	42.28	2.45
	Difference	-		14.96		-		18.30	
$A_{80,X}$	IET	31.79	6.40	-	-	29.52	2.14	-	-
	KE model	86.45	7.42	87.96	8.97	38.01	5.15	37.16	4.56
	Difference	54.66		-		8.49		-	
$A_{80,Y}$	IET	-	-	45.86	7.44	-	-	13.08	2.02
	KE model	83.66	7.24	88.49	12.57	37.11	4.34	35.69	5.14
	Difference	-		42.63		-		22.61	

A comparison between the nanoindentation (NI) experimental results and the calculated results was performed. Delafargue et al. [Delafargue 2004] have proposed explicit relations used to recalculate the reduced modulus of transversely isotropic and general orthotropic materials using the macroscopic rigidity tensor of the effective material. The reduced modulus measured by NI was compared to the recalculated reduced modulus. In the case of an orthotropic material indented in the x_3 direction, perpendicular to the sample surface, the reduced modulus can be recalculated as follows:

$$M_3 = \sqrt{M_{31}M_{32}} \tag{V.50}$$

With:

$$M_{31} = 2\sqrt{\frac{C_{31}^2 - C_{13}^2}{C_{11}}\left(\frac{1}{\frac{1}{2}C_{55}} + \frac{2}{C_{31} + C_{13}}\right)^{-1}} \quad \text{(V.51)}$$

$$M_{32} = 2\sqrt{\frac{C_{32}^2 - C_{23}^2}{C_{22}}\left(\frac{1}{\frac{1}{2}C_{44}} + \frac{2}{C_{32} + C_{23}}\right)^{-1}} \quad \text{(V.52)}$$

$$C_{31} = \sqrt{C_{11}C_{33}} \quad \text{(V.53)}$$

$$C_{32} = \sqrt{C_{22}C_{33}} \quad \text{(V.54)}$$

Table V.21 shows the recalculated and measured reduced moduli of the Ti films and their uncertainties. By comparing the recalculated reduced modulus and the reduced modulus obtained by NI on the Ti films of series A presented in Fig. IV.14, we can notice a difference at α = 0° and 45° that can be attributed to the measurements and calculations uncertainties. For α = 80°, the difference is higher than the measurements and calculations uncertainties. As expected, this is influenced by coupled effects: high porosity and high fiber tilt angle and thus the KE model cannot accurately model such microstructure. It can also be noted that this difference can be due to the contribution of the substrate or the influence of the porosity and the morphological and crystallographic textures on the film when performing NI. The agreement between the results of NI and KE at α = 0° and 45° confirms the absence of anisotropy in the film plane, and thus the difference between the directions x and y found at α = 45° using the IET is rather due to the porosity.

Table V.21
Recalculated and measured reduced modulus of the Ti films of series A with their uncertainties in GPa.

Sample	Reduced modulus		Uncertainty	
	Nanoindentation	**Recalculated**	**Nanoindentation**	**Recalculated**
$A_{0,X}$	130.41	137.77	4.93	2.96
$A_{0,Y}$	133.56	139.06	4.48	1.76
$A_{45,X}$	125.25	124.81	3.81	2.67
$A_{45,Y}$	128.53	126.22	4.84	2.17
$A_{80,X}$	88.07	109.63	3.11	6.97
$A_{80,Y}$	87.30	105.90	5.90	7.07

V.7. Residual stress analysis

V.7.1. Residual stresses: definition and origin

Most of the materials are not perfectly homogeneous in reality and present heterogeneities (defects), such as porosity or inclusions and grain boundaries. Discontinuities exist also at the microscopic scale inside a grain: dislocations, precipitates [Chomel 2000]. The residual stresses are therefore the static stresses existing in a material with the absence of any external loading and being in mechanical equilibrium. They result from incompatible or stress-free strains created by a process [Hauk 1997]. We can highlight residual stresses generated thanks to thermal or plastic sources. Further, they can appear due to volume changes induced by phase transformations or due to strain ensuring the continuity of the material exhibiting point defects (interstitial or substitutional atom, gap) and linear (dislocations) or 2D (grain and interphase boundaries) defects.

The residual stresses can also be linked to different out-of-equilibrium processes used for material production. In the case of thin films with columnar growth obtained by magnetron sputtering, these intrinsic stresses can be generated due to attractive forces at the columns boundary. The intrinsic stresses can be modified subsequently by applying external stresses or finishing treatments.

V.7.2. Determination of the residual stresses and the strain/stress-free diffraction angle

V.7.2.1. Curvature method

Residual stresses in thin films can be measured using the curvature method [Stoney 1909]. The method is based on measuring the curvature of the substrate before and after deposition. The residual stresses σ_R^I are determined using the following Stoney's formula [Stoney 1909]:

$$\sigma_R^I = \frac{h_s^2}{6\,h_c}\frac{E_s}{(1-\upsilon_s)}\left(\frac{1}{R_2}-\frac{1}{R_1}\right) \quad \text{(V.55)}$$

Where E_s and υ_s are respectively the Young's modulus and Poisson's ratio of the substrate, h_s and h_c are respectively the thickness of the substrate and the film and R_1 and R_2 are respectively the curvature measured on the substrate before and after deposition. The curvatures of the substrate before and after deposition were measured using an Altisurf 500 profilometer. The residual stresses σ_R^I measured using the curvature method are presented in Table V.22.

Table V.22
The residual stresses in the Ti films determined using the curvature method.

Sample	E_s	υ_s	h_s	h_c	R_1	R_2	σ_R^I	$u(\sigma_R^I)$
	(GPa)		(mm)	(µm)	(mm)	(mm)	(MPa)	(MPa)
$B_{0,Y}$	200	0.291	0.2	1.380	9004	4404	158.08	4.19
$B_{45,Y}$	200	0.291	0.2	1.592	8491	4512	122.69	5.44
$B_{80,Y}$	200	0.291	0.2	1.187	6139	4771	73.99	3.99

One can mention that Stoney's formula is only valid for macroscopically isotropic materials. Indeed, the anisotropy found for the Ti films is between the z-direction and the x-y plane and thus it does not influence the formula. As the thickness of the films is higher than 1 μm (the minimal value), the stress measurements will be less influenced by the thickness variation [Detor 2009]. It can be noticed that the residual stress of the Ti film under normal deposition (α = 0°) conditions is tensile. It is consistent with some results found in the literature

(50 *MPa* [Fang 2000], 200 *MPa* [Siad 2016]). With the change of glancing angle, the absolute value of the stress suddenly drop for α > 45° to reach a low value at α = 80°.

V.7.2.2. Crystallite group method

Among the techniques for determining residual stresses in crystalline materials, XRD has attracted special attention because it allows a non-destructive and quantitative evaluation of surface stresses. This technique allows us also to obtain complex information on the mechanical state of material precisely of its diffracting volume, intermediate between the macroscopic and mesoscopic scales (Fig. V.4). Using XRD, the stress state can be determined in the closest volume to the film surface.

The residual stress state of the examined samples can be determined by means of the Crystallite Group Method (CGM) using different $\{h\,k\,l\}$ reflections from the diffraction patterns [Noyan 1987, Zaouali 1991, Hauk 1997, Kurz 2014]. As seen previously, the macroscopic elastic behavior of the Ti films can be supposed transversely isotropic (C_{11} = C_{22}, C_{13} = C_{23} and C_{44} = C_{55}). The isotropy in the film plane was also tested by evaluating the microscopic strain measured at different ϕ angles and constant ψ angle. It can be seen that the difference between the measured strains presented in Table V.23 at different ϕ values is attributed to the measurement uncertainty. Furthermore, no shear stress was considered in the residual stress state as no obvious dependence of the measured strain was obtained at positive and negative ψ values. In addition, the components of stress along the z-direction can be considered null, as the film is thin. From these elements, the residual stress state in the films deposited by magnetron sputtering can be considered as follows:

$$\sigma_{xx} = \sigma_{yy} \;\; ; \; \sigma_{xy} \approx 0 \;\; ; \;\; \sigma_{iz} \approx 0 \qquad \text{(V.56)}$$

Using at least two independent measurement directions, the residual stress state $\sigma_R^{\{hkl\}_i}$ as well as the position of the diffraction peaks of a non-stressed material (reference diffraction angle) $\theta_0^{\{hkl\}_i}$ can be determined using the following expression:

$$\varepsilon_{\phi,\psi}^{\{hkl\}_i} = \ln\left(\frac{\sin\theta_0^{\{hkl\}}}{\sin\theta_{\phi,\psi}^{\{hkl\}}}\right) = \vec{n}\,.\left[\langle\left[P(C):\left(c_\Omega^i - C\right) + I_4\right]^{-1}\rangle_{\Omega\in V_i} : C^{-1} : \sigma_R^i\right].\vec{n} \qquad \text{(V.57)}$$

Table V.23
The microscopic strain measured at different plane families and measurement directions.

Sample	$\{11\bar{2}4\}_\alpha$				$\{20\bar{2}3\}_\alpha$			
	ψ (°)	**ϕ (°)**	$\boldsymbol{\varepsilon_{\phi,\psi}^{hkl}}$ **(× 10⁶)**	$\boldsymbol{u(\varepsilon_{\phi,\psi}^{hkl})}$ **(× 10⁶)**	**ψ (°)**	**ϕ (°)**	$\boldsymbol{\varepsilon_{\phi,\psi}^{hkl}}$ **(× 10⁶)**	$\boldsymbol{u(\varepsilon_{\phi,\psi}^{hkl})}$ **(× 10⁶)**
$B_{0,Y}$	40.86	18.13	831.63	265.45	44.59	197.33	2384.93	340.17
		161.87	780.88	256.56		342.67	2375.76	318.71
$B_{45,Y}$	45.57	29.48	939.14	247.12	42.30	5.26	1106.56	325.14
		150.52	976.61	247.27		174.74	1202.39	341.12
$B_{80,Y}$	54.44	40.16	982.32	247.08	43.16	168.45	740.75	325.39
		139.84	1019.78	247.23		11.55	836.62	341.36

The residual stress and the reference diffraction angle were determined on two different plane families, $\{11\bar{2}4\}_\alpha$ and $\{20\bar{2}3\}_\alpha$ using the SCECs of the Ti_α (Table V.11) and the calculated rigidity tensors (Table V.12). The experiments achieved on the $\{21\bar{3}1\}_\alpha$ family of planes were not used because of their diffraction peaks not well defined (Fig. V.17(c)). The results were presented in Table V.24. The strain measurements using the CGM were performed at specific (ϕ,ψ) angles corresponding to intensity poles of the theoretical pole figures (Fig. V.17) as the deposited Ti films had a tilted fiber texture.

Table V.24
The reference diffraction positions and the residual stresses in the Ti films determined using the crystallite group method.

Sample	$\{11\bar{2}4\}_\alpha$			$\{20\bar{2}3\}_\alpha$		
	$\boldsymbol{\theta_0^{hkl}}$ **(°)**	$\boldsymbol{\sigma_R^\alpha}$ **(MPa)**	$\boldsymbol{u(\sigma_R^\alpha)}$ **(MPa)**	$\boldsymbol{\theta_0^{hkl}}$ **(°)**	$\boldsymbol{\sigma_R^\alpha}$ **(MPa)**	$\boldsymbol{u(\sigma_R^\alpha)}$ **(MPa)**
$B_{0,Y}$	57.20°	122.09	35.60	51.22°	157.78	23.71
$B_{45,Y}$	57.03°	103.36	19.82	51.15°	146.70	24.08
$B_{80,Y}$	57.04°	41.54	6.06	51.12°	54.29	6.80

Knowing the residual stress in the Ti_α phase and the phase proportion, the macroscopic residual stress σ_R^I in the film can be determined using Eq. (V.37) ($\sigma_R^I = x_\alpha \sigma_R^\alpha$). The mean of

the stresses measured on the two planes $\{11\bar{2}4\}_\alpha$ and $\{20\bar{2}3\}_\alpha$ were used in the calculations. The phase proportion was taken equal to $(1-p)$. Table V.25 shows a comparison between the residual stresses determined using the curvature and the crystallite group methods. It can be noticed that, except for the films at α = 80°, the difference between the residual stresses determined using the two methods is attributed to the measurements or the calculations uncertainties. At 80° of inclination, no consistency between the residual stress measured using the curvature method and the one calculated using the KE model (CGM) was present. From the residual stress analysis, this is related to incorrect values of XEC calculated using the KE model and hence the same conclusion as above can be extracted.

Table V.25
Comparison between the residual stresses determined using the curvature and the crystallite group methods.

Sample	Method	σ_R^I (MPa)	u(σ_R^I) (MPa)
$B_{0,X}$	Curvature	158.08	4.19
	CGM	139.94	29.66
	Difference	18.14	
$B_{45,X}$	Curvature	122.69	5.44
	CGM	125.03	21.95
	Difference	2.34	
$B_{80,X}$	Curvature	73.99	3.99
	CGM	47.92	6.43
	Difference	26.07	

The decrease of the stress level with the increase of the glancing angle is explained by the increase of porosity, i.e. voids between the columns [Stoney 1909, Hawkeye 2014]. Indeed the density of the films decreases with the increase of the glancing angle [Tait 1990, Jensen 2004]. Generally, the stress state depends on adatoms mobility and thus on the energy of the incoming particles. Since all the films were deposited in only one deposition process, the energy distribution is the same for each sample. In this case, the stress state is only influenced by the particle transport conditions: the geometry of the target, the position of the samples on the holder relative to the center of the target, the self-shadowing effect and the shape of the racetracks [Siad 2016]. The drop of the tensile stress at α = 80° can be explained by two combined phenomena: the decrease of the particles energy at the grain level and the increase of the intercolumnar voids due to self-shadowing at the column level. The increase of the

intercolumnar voids leads to the relaxation of the film stress while suggesting that the stress state remains almost constant inside a polycrystalline column.

V.8. Conclusions

After determining the elasticity constants of titanium films in the previous chapter using the IET, this chapter has described this determination by taking into account the film microstructure. The objective was focused on modeling the microstructure of titanium films using the self-consistent KE model.

Single-phase (Ti_α) titanium films were deposited by DC magnetron sputtering at different glancing angles. The microstructural properties of the films were determined using the XRD and the SEM. Their Young's and shear moduli were measured by IET. The porosity in the films was taken into account in the mechanical model supposing its rigidity tensor equal to zero. It was quantified by image analysis using the ImageJ software and by comparing each film density to the density of its bulk material. It was determined from the experimental pole figures plotted using the data collected by XRD. The morphological texture was taken into account through the Morris tensor. The anisotropic KE model was used to simulate the macroscopic and microscopic elastic behavior of the deposited titanium films. The SCECs of the Ti_α phase, used as entry data, were the average of data found in the literature.

From the determined elasticity constants, we can conclude that the elastic behavior of the titanium films is transversely isotropic at any glancing angle. The elasticity constants of the titanium films calculated using the KE model are in good agreement with those measured by IET, except for the films deposited at α = 80°. It can be concluded that the KE model is not able to simulate films presenting high porosity. The analysis of uncertainty sources on the macroscopic rigidity tensors comes mainly from the uncertainties of the experimental quantities and the SCECs found in the literature. The uncertainties in the experimental quantities should be improved in further studies.

To check the accuracy of the model, the elasticity constants of the titanium films of series A measured by IET in Chapter IV were predicted. These films present microstructures different from the ones deposited in this chapter. The same conclusions as those found for series B were predicted. Using different simulations, we were able to show the effects of the porosity, the crystallographic texture and the grain-shape texture on the macroscopic elasticity constants

of the films. A significant effect of the porosity with a decrease in Young's and shear moduli was observed. The higher porosity contribution has a primordial role in the determination of the elasticity constants using the KE model. The effects of the porosity, the crystallographic texture and the grain-shape texture on the microscopic behavior of the films were studied. A significant effect of the crystallographic and morphological textures was observed. The domination of one factor over the other was noticed depending on the crystallographic plane, the measurement direction and the glancing angle. The porosity effect on the elastic behavior of the diffracting volume is less important than the effects of the grain shape and the crystallographic texture.

The trueness of the KE model was also evaluated by comparing the reduced modulus measured by nanoindentation with the reduced modulus calculated through explicit relations function of the components of the effective rigidity tensor. The residual stresses within the film and the Ti_{α} phase were determined using the curvature method and the crystallite group method used in the strain measurements by XRD. In addition, improving the quality of XRD strain measurements is essential to ensure better quality results. Other analyses of the microscopic elastic behavior of asymmetrical textured Ti films will be evaluated under applied loading. This analysis allows us to study the validity range of the KE model by comparing the experimental and recalculated microscopic strains. In order to model more precisely the microstructure of GLAD films, other scale transition models will be used in future works. In addition, improving the quality of strain measurements by XRD is essential to ensure more accuracy in the results.

General conclusions and future works

The objective of this thesis is to develop a methodology for measuring the macroscopic elasticity constants of polycrystalline, porous and textured coatings. The approach presented in this work was proceeded using experimental and theoretical tools. The experimental tools used during this thesis are the Impulse Excitation Technique (IET) to measure the macroscopic elasticity constants of the film and the X-Ray Diffraction (XRD) to determine the microstructural properties of the film and to characterize the microscopic behavior of the phases. The micromechanical models were used as theoretical tools to simulate the macroscopic and microscopic elastic behavior of the films.

We started with a macroscopic characterization of the elastic behavior of multilayers by assuming that their properties are isotropic. Different analytical models (Ext-PM, Dev-CLBT and Ext-Slim) that allow us to determine the elasticity constants of coatings were developed. These developed models were compared with a finite element model taken as a reference. We have shown that the Ext-PM, Dev-CLBT and Ext-Slim models are reliable in determining the elasticity constants of multilayers. This is due to the shift of the neutral axis taken by these models after each deposition.

The new models were applied to titanium and niobium films deposited in multilayers on stainless steel and glass substrates. The elasticity constants of each film were determined using the impulse excitation technique. The study of the uncertainties on the measurements of Young's and shear moduli was carried out in Chapter III. The study has shown that the uncertainty on the measurements of the substrate Young's and shear moduli is mainly due to the film thickness and density. While in the case of Young's modulus of the titanium film, the measured density of the film, the substrate Young’s modulus and the two frequencies represent a significant contribution. By depositing a second film of niobium, the contribution of the Ti film Young’s modulus was added to the factors in the case of the three-layered system. As the number of vibration modes increases, the contribution of frequency on the films Young's modulus decreases, while that of the density and Young's modulus of the substrate and the previous films increases.

By evaluating the measurement uncertainties of the shear modulus, the most influential sources on the measurement of the film shear modulus are the density of the film, the torsional frequencies of the substrate and the composite and the shear moduli of the previous layers (substrate and titanium first film). By comparing the two uncertainty analyses on the films Young's and shear moduli, it can be confirmed that the most influential factors on the measurement remain the same with some equivalences. The Young's modulus and the flexural frequencies (in Ext-PM and Dev-CLBT) correspond to the shear modulus and the torsional frequencies respectively (in Ext-Slim). These factors have the highest influence on the measurement of the film elasticity constants.

A new model for determining the elasticity constants of thin films sputter-deposited at oblique incidence was developed through the application of the Classical Laminate Beam Theory (CLBT). This new model takes into account the shift of the neutral axis after deposition and the anisotropy in the film plane. The model was validated by comparing it with a finite element model taken as a reference. Titanium thin films were deposited by magnetron sputtering at different glancing angles (α = 0°, 45° and 80°), its Young's moduli were determined using the new model and the IET and its shear moduli using Slim's model with the corresponding Young's modulus. By increasing the glancing angle, a decrease in the Young's and shear moduli of the titanium film compared to that of the bulk material was observed. The growth morphology of all films exhibits a well-defined columnar growth inclined by an angle β with respect to the surface normal for glancing angle different than zero. The structural analysis of the films shows the presence of a single hcp (hexagonal closed acked) Ti_{α} stable phase for the three glancing angles. The texture of this phase represents a fiber with {0002} axis tilted by an angle η with respect to the surface normal. According to calculations made with the Nemat-Nasser model, the decrease in Young's modulus cannot be attributed solely to the decrease in the density of the film (related to porosity) compared to the density of the bulk material.

The macroscopic elasticity constants were recalculated using a micromechanical model. In this work, we used the Kröner-Eshelby (KE) model. The texture of the titanium films was determined from the pole figures. The fiber tilt angle η was measured by X-ray diffraction. The columns tilt angle β was measured on the images observed by scanning electron microscopy. The porosity in the film was measured by image analysis and by comparing the density of the film and the bulk material with no pores. Using the self-consistent model, we formulated the

effective rigidity tensor of porous and single-phase (Ti_α) films with tilted columns and fibers. Then, the macroscopic elasticity constants of the titanium films were determined by taking into account the microstructural properties (porosity, crystallographic and morphological textures) of each film. According to the calculation, it was found that the films exhibit a transversely isotropic behavior weakly anisotropic in the film plane at $\alpha = 80°$. The differences between the Young's and shear moduli measured by the IET and recalculated by the self-consistent model were attributed to the measurement and calculation uncertainties for films deposited at 0° and 45° of inclination. On the other hand, for $\alpha = 80°$, we noticed that this difference is greater than the uncertainties. This may be due to the inability of the self-consistent model to model the microstructures presenting high porosity ($p > 12\%$). The macroscopic elasticity constants of the titanium films presented in Chapter IV were recalculated and the same conclusion was found. We have shown that the porosity in the film has a dominant effect on the Young's and shear moduli. The effect of morphological or/and crystallographic textures on the microscopic behavior becomes dominant. The influence of the glancing angle on the microscopic elastic behavior was also demonstrated and quantified. This work allowed us to have a first set of elasticity constants values of a film deposited at oblique incidence.

Another comparison can be proposed to evaluate the results calculated using the KE model. It consists in measuring the microscopic strain by XRD under applied loading. The loading can be performed in bending using different bending templates with different curvature radii as those used in Section V.6.4. By comparing the experimental strains at different families of planes, measurement directions and glancing angles to the corresponding strains calculated in Section V.6.4, one can realize if the elastic behavior of the Ti films is well described by the KE model or not.

In this work, the elastic behavior of GLAD films is not well described by the KE model. The KE model may not be well adapted to highly porous materials, where significant pores interaction can probably be achieved. The macroscopic elastic anisotropy can be studied using other scale transition models like the Mori-Tanaka model that could more precisely simulate the microstructure of GLAD films.

In order to determine the macroscopic elasticity constants of titanium films, we used the Single-Crystal Elasticity Constants (SCECs) of the Ti_α phase from the literature. However, it may be possible that the behavior of our Ti_α phase is different from that found in the literature. The determination of the rigidity tensor of this phase will allow us to compare the coefficients

c_{ij}^{α} calculated with those existing in the literature and not to impose a set of values that may not correspond to our case. For this, it will be necessary to carry out strain measurements on the diffraction peaks of the Ti_{α} phase under applied loading.

The Crystallite Group Method (CGM) was used in the self-consistent model and the strain measurements by X-ray diffraction. The crystallographic texture of the films was taken into account by idealizing the crystallographic orientations of the Ti_{α} phase. However, the texture of the films can be described more precisely using the orientation distribution functions.

References

[Abadias 2019a] G. Abadias, J.J. Colin, D. Tingaud, P. Djemia, L. Belliard, C. Tromas, Elastic properties of α- and β-tantalum thin films, Thin Solid Films, 688 (2019) 137403.

[Abadias 2019b] G. Abadias, F. Anğay, R. Mareus and C. Mastail, Texture and stress evolution in HfN films sputter-deposited at oblique angles, Coatings 9 (2019) 712.

[Abadias 2020] G. Abadias, C-H Li, L. Belliard, Q.M. Hu, N. Greneche, P. Djemia, Large influence of vacancies on the elastic constants of cubic epitaxial tantalum nitride layers grown by reactive magnetron sputtering, Acta Materialia, 184 (2020) 254–266.

[Abaqus 2016] Abaqus Analysis User's Manual (6.13).

[Abegunde 2020] O.O. Abegunde, E.T. Akinlabi, O.P. Oladijo, Influence of sputtering parameters on the structural and mechanical properties of TiC thin film coating, Applied Surface Science, 520 (2020) 146323.

[Abelmann 1997] L. Abelmann, C. Lodder, Oblique evaporation and surface diffusion, Thin Solid Films, 305 (1997) 1–21.

[Achache 2016] S. Achache, S. Lamri, A. Alhussein, A. Billard, M. François, F. Sanchette, Gum Metal thin films obtained by magnetron sputtering of a Ti-Nb-Zr-Ta target, Materials Science and Engineering A, 673 (2016) 492-502.

[Ait-Djafer 2015] A.Z. Ait-Djafer, N. Saoula, H. Aknouche, B. Guedouar, N. Madaoui, Deposition and characterization of titanium aluminum nitride coatings prepared by RF magnetron sputtering, Applied Surface Science 350 (2015) 6-9.

[Alfano 2007] M. Alfano, L. Pagnotta, A non-destructive technique for the elastic characterization of thin isotropic plates, NDT&E International, 40 (2007) 112–120.

[Ali 2019] Z. Ali, D. Basaula, W. Zhou, J. Brock, M. Khan, K. F. Eid, Controlling the charge transport mode in permalloy films using oblique angle deposition, Journal of Magnetism and Magnetic Materials, 484 (2019) 430–436.

[Alvarez 2014] R. Alvarez, C. Lopez-Santos, J. Parra-Barranco, V. Rico, A. Barranco, J. Cotrino, A. R. Gonzalez-Elipe, A. Palmero, Nanocolumnar growth of thin films deposited at oblique angles: Beyond the tangent rule, Journal of Vacuum Science and Technology B 32 (2014) 041802.

[Alvarez 2016] R. Alvarez, J. M. Garcia-Martin, A. Garcia-Valenzuela, M. Macias-Montero, F. J. Ferrer, J. Santiso, V. Rico, J. Cotrino, A. R. Gonzalez-Elipe, A. Palmero, Nanostructured Ti thin films by magnetron sputtering at oblique angles, J. Phys. D: Appl. Phys. 49 (2016) 045303.

[Alvarez 2019] R. Alvarez, A. Garcia-Valenzuela, V. Rico, J. M. Garcia-Martin, J. Cotrino, A. R. Gonzalez-Elipe, A. Palmero, Kinetic energy-induced growth regimes of

nanocolumnar Ti thin films deposited by evaporation and magnetron sputtering, Nanotechnology 30 (2019) 475603.

[Anders 2010] A. Anders, A structure zone diagram including plasma-based deposition and ion etching, Thin Solid Films 518 (15) (2010) 4087-4090.

[Antartis 2018] D. A. Antartis, R. N. Mott, I. Chasiotis, Silicon nanosprings fabricated by glancing angle deposition for ultra-compliant films and interfaces, Mater. Des. 144 (2018) 182–191.

[Anya 1997] C. C. Anya, S. C. Roberts, Pressureless sintering and elastic constants of $Al2O3-SiC$ nanocomposites, Journal of the European Ceramic Society, 17 (1997) 565-573.

[Apreutesei 2017] M. Apreutesei, P. Djemia, L. Belliard, G. Abadias, C. Esnouf, A. Billard, P. Steyer, Structural-elastic relationships of Zr-TL (TL ¼ Cu, Co, Ni) thin films metallic glasses, Journal of Alloys and Compounds, 707 (2017) 126-131.

[ASTM 2015] ASTM, E1876-15, Standard Test Method for Dynamic Young's Modulus, Shear Modulus and Poisson's Ratio by Impulse Excitation of Vibration, (2015).

[Atri 1999] R.R. Atri, K.S. Ravichandran, S.K. Jha, Elastic properties of in-situ processed Ti–TiB composites measured by impulse excitation of vibration, Materials Science and Engineering A, 271 (1999) 150–159.

[Baczmanski 2003] A. Baczmanski, C. Braham, W. Seiler, Microstresses in textured polycrystals studied by the multireflection diffraction method and self-consistent model, Philosophical Magazine (Taylor and Francis) 83 (2003) 3225-3246.

[Baczmanski 2008] A. Baczmanski, P. Lipinski, A. Tidu, K. Wierzbanowski, B. Pathiraj, Quantitative estimation of incompatibility stresses and elastic energy stored in ferritic steel, Journal of applied crystallography 41 (2008) 854-867.

[Badawi 1993] K.F. Badawi, C. Kahloun, J. Grilhé, Formalisme rationnel de la méthode de détermination des contraintes résiduelles par diffraction des rayons X: application aux couches minces, Journal de Physique III, EDP Sciences 3 (1993) 1183-1188.

[Bao 2018] W. Bao, J. Xue, J.X. Liu, X. Wang, Y. Gu, F. Xu, G.J. Zhang, Coating SiC on Zircaloy-4 by magnetron sputtering at room temperature, Journal of Alloys and Compounds, 730 (2018) 81-87.

[Barkanov 2015] E. Barkanov, M. Wesolowski, W. Hufenbach, M. Dannemann, An effectiveness improvement of the inverse technique based on vibration tests, Computers and Structures 146 (2015) 152–162.

[Barral 1987] M. Barral, J.L. Lebrun, J.M. Sprauel, G. Maeder, X-ray macrostress determination on textured material: use of the ODF for calculating the X-ray compliances, Metallurgical Transactions A, 18A (1987) 1229-1238.

[Barranco 2016] A. Barranco, A. Borras, A. R. Gonzalez-Elipe, A. Palmero, Perspectives on oblique angle deposition of thin films: from fundamentals to devices, Prog. Mater. Sci. 76 (2016) 59–153.

[Bellan 2004] C. Bellan, J. Dhers, Evaluation of Young modulus of CVD coatings by different techniques, Thin Solid Films 469–470 (2004) 214– 220.

[Benveniste 1991] Y. Benveniste, G.J. Dvorak and T. Chen, On diagonal and elastic symmetry of the approximate effective stiffness tensor of heterogeneous media, Journal of the Mechanics and Physics of Solids 39 (1991) 927–946.

[Berdichevsky 2009] V.L. Berdichevsky: Variational principles of continuum mechanics, Interaction of Mechanics and Mathematics, Springer-Verlag Berlin Heidelberg (2009).

[Bergholm 1913] C. Bergholm, Über doppelbrechung in kathoden zerstäubten metallsuchten, Ann Phys 348 (1913) 1–23.

[Berry 1975] B.S. Berry, W.C. Pritchet, Vibrating reed internal friction apparatus for films and foils, IBM J. Res. Dev. 19 (1975) 334–343.

[Besnard 2010] A. Besnard, N. Martin, C. Millot, J. Gavoille, R. Salut, Effect of sputtering pressure on some properties of chromium thin films obliquely deposited, IOP Conf. Ser. Mater. Sci. Eng. 12 (2010) 012015.

[Billard 2005] A. Billard, F. Perry, Pulvérisation cathodique Magnétron, Techniques de l'ingénieur, M1654 (2005).

[Bonakdarpour 2008] A. Bonakdarpour, M. D. Fleischauer, M. J. Brett, J. R. Dahn, Columnar support structures for oxygen reduction electrocatalysts prepared by glancing angle deposition, Appl. Catal. A: Gen 349 (2008) 110–115.

[Bornert 2001] M. Bornert, T. Bretheau and P. Gilormini, Homogénéisation en mécanique des matériaux 2 : Comportements non linéaires et problèmes ouverts, Hermes Science, Paris (2001).

[Bouaouina 2018] B. Bouaouina, C. Mastail, A. Besnard, R. Mareus, F. Nita, A. Miche, G. Abadias, Nanocolumnar TiN thin film growth by oblique angle sputter-deposition: experiments vs. simulations, Mater. Des. 160 (2018) 338–349.

[Bramowicz 2016] M. Bramowicz, L. Braic, F.A. Azem, S. Kulesza, I. Birlik, A. Vladescu, Mechanical properties and fractal analysis of the surface texture of sputtered hydroxyapatite coatings, Applied Surface Science, 379 (2016) 338–346.

[Brandes 1992] E.A. Brandes and G.B. Brook, Smithells Metals Reference Book (7th edition), Butterworth-Heinemann, Oxford (1992).

[Bruno 2006] L. Bruno, G. Felice, L. Pagnotta, A. Poggialini, A mixed numerical-experimental methodology for determining the elastic constants of orthotropic materials, Proc. of SPIE, 6341 (2006) 63410J 1–6.

[Buckle 1960] H. Buckle, L'essai de microdureté et ses applications, Publications Scientifiques et Techniques du Ministère de l'Air, ISSN 0370-1999, 1960.

[Bullough 2000] C.K. Bullough, The determination of uncertainties in Dynamic Young's Modulus, Standards Measurement and Testing Project No. SMT4-CT97-2165 (2000).

[Bunge 1982] H.J. Bunge, Texture analysis in materials science, Butterworths, London (1982).

[Bunshah 1973] R.F. Bunshah, R.S. Juntz, Influence of condensation temperature on microstructure and tensile properties of titanium sheet produced by high-rate physical vapor deposition process, Metall. Trans. 4 (1973) 21–26.

[Buzea 2005] C. Buzea, K. Kaminska, G. Beydaghyan, T. Brown, C. Elliott, C. Dean, K. Robbie, Thickness and density evaluation for nanostructured thin films by glancing angle deposition, Journal of Vacuum Science and Technology B, 23 (2005) 2545–2552.

[Chaabani 2017] A. Chaabani, A. Njeh, W. Donner, A. Klein, M.H. Ben Ghozlen, Elasticity study of textured barium strontium titanate thin films by X-ray diffraction and laser acoustic waves, Japanese Journal of Applied Physics, 56 (2017) 055501.

[Chapelon 2006] L.L. Chapelon, J. Vitiello, D. Neira, J. Torres, J.C. Royer, D. Barbier, F. Naudin, G. Tas, P. Mukundhan and J. Clerico, Measuring the Young's modulus of ultralow-k materials with the nondestructive picosecond ultrasonic method, Microelectronic Engineering, 83 (2006) 2346–2350.

[Chawla 2008] V. Chawla, R. Jayaganthan, A.K. Chawla, Ramesh Chandra, Morphological study of magnetron sputtered Ti thin films on silicon substrate, Materials Chemistry and Physics 111 (2008) 414–418.

[Chawla 2009] V. Chawla, R. Jayaganthan, A.K. Chawla, R. Chandra, Microstructural characterizations of magnetron sputtered Ti films on glass substrate, Journal of Materials Processing Technology, 209 (2009) 3444–3451.

[Chen 2005] S. Chen, L. Liu, T. Wang, Investigation of the mechanical properties of thin films by nanoindentation, considering the effects of thickness and different coating–substrate combinations, Surface and Coatings Technology, 191 (2005) 25–32.

[Chen 2009] X. Chen, B.L. Kirsch, R. Senter, S.H. Tolbert, V. Gupta, Tensile testing of thin films supported on compliant substrates, Mechanics of Materials, 41 (2009) 839–848.

[Chen 2012] L. Chen, T.-M. Lu, G.-C. Wang, Incident flux angle induced crystal texture transformation in nanostructured molybdenum films, J. Appl. Phys. 112 (2012) 024303.

[Chinmulgund 1995] M. Chinmulgund, R.B. Inturi, J.A. Barnard, Effect of Ar gas pressure on growth, structure, and mechanical properties of sputtered Ti, Al, TiAl, and Ti3Al films, Thin Solid Films 270 (1995) 260–263.

[Cho 1999] K.H. Cho, Y. Kim, Elastic modulus measurement of multilayer metallic thin films, Journal of Materials Research 14 (1999) 1996–2001.

[Chomel 2000] P. Chomel, Comportement thermomécanique des alliages métalliques. Techniques de l'ingénieur, BM5012 (2000).

[Choudhary 2015] R.K. Choudhary, S.C. Mishra, P. Mishra, P.K. Limaye, K. Singh, Mechanical and tribological properties of crystalline aluminum nitride coatings deposited on stainless steel by magnetron sputtering, Journal of Nuclear Materials, 466 (2015) 69–79.

[Chung 1967] D.H. Chung and W.R. Buessem, The elastic anisotropy of crystals, Journal of applied physics 38 (1967) 2010-2012.

[Cianci 2007] E. Cianci, A. Coppa, V. Foglietti, Young's modulus and residual stress of DF PECVD silicon nitride for MEMS free-standing membranes, Microelectronic Engineering, 84 (2007) 1296–1299.

[Colin 2017] J.J. Colin, G. Abadias, A. Michel, C. Jaouen, On the origin of the metastable β-Ta phase stabilization in tantalum sputtered thin films, Acta Materialia, 126 (2017) 481–493.

[Colombi 2013] P. Colombi, P. Bergese, E. Bontempi, L. Borgese, S. Federici, S.S. Keller, A. Boisen, L.E. Depero, Sensitive determination of the Young's modulus of thin films by polymeric microcantilevers, Measurement Science and Technology, 24 (2013) 125603.

[Czichos 2014] H. Czichos, B. Skrotzki, F.G. Simon, Das Ingenieurwissen: Werkstoffe, Springer Vieweg, Berlin, Heidelberg, 2014.

[Delafargue 2004] A. Delafargue, F.J. Ulm, Explicit approximations of the indentation modulus of elastically orthotropic solids for conical indenters, International Journal of Solids and Structures 41 (2004) 7351-7360.

[Dellas 2006] N. S. Dellas, J. M. E. Harper, Effect of deposition angle on fiber axis tilt in sputtered aluminum nitride and pure metal films, Thin Solid Films 515 (2006) 1647–1650.

[Deng 2005] X. Deng, N. Chawla, K.K. Chawla, M. Koopman, J.P. Chu, Mechanical behavior of multilayered nanoscale metal–ceramic composites, Adv. Eng. Mater. 7 (2005) 1099.

[Deniz 2007] D. Deniz, J. M. E. Harper, J. W. Hoehn, F. Chen, Tilted fiber texture in aluminum nitride thin films, J. Vac. Sci. Technol. A 25 (2007) 1214–1218.

[Dervaux 2017] J. Dervaux, P. A. Cormier, P. Moskovkin, O. Douheret, S. Konstantinidis, R. Lazzaroni, S. Lucas, R. Snyders, Synthesis of nanostructured Ti thin films by combining glancing angle deposition and magnetron sputtering: a joint experimental and modeling study, Thin Solid Films 636 (2017) 644–657.

[Detor 2009] A.J. Detor, A.M. Hodge, E. Chason, Y. Wang, H. Xu, M. Conyers, A. Nikroo, A. Hamza, Stress and microstructure evolution in thick sputtered films, Acta Mater 57 (2009) 2055-2065.

[Dick 2000] B. Dick, M. J. Brett, T. J. Smy, M. R. Freeman, M. Malac, R. F. Egerton, Periodic magnetic microstructures by glancing angle deposition, Journal of Vacuum Science and Technology A 18 (2000) 1838-1844.

[Dick 2003] B. Dick, M. Brett, T. Smy, Investigation of substrate rotation at glancing incidence on thin-film morphology, Journal of Vacuum Science and Technology B, 21 (2003) 2569–2575.

[Dirks 1977] A. G. Dirks, H. J. Leamy, Columnar microstructure in vapor-deposited thin films, Thin Solid Films, 47 (1977) 219–233.

[Djaziri 2014] S. Djaziri, P.O. Renault, E. Le Bouhris, P. Goudeau, D. Faurie, G. Geandier, C. Mocuta, D. Thiaudière, Comparative study of the mechanical properties of nanostructured thin films on stretchable substrates, Journal of Applied Physics, 116 (2014) 093504.

[Doerner 1986] M.F. Doerner, W.D. Nix, A method for interpreting the data from depth-sensing indentation instruments, J. Mater. Res. 1 (4) (1986) 601–609.

[Donachie 2000] Matthew J. Donachie, Titanium: A Technical Guide, Second Edition, ASM International, Materials Park, Ohio, USA, ISBN: 0-87170-686-5 (2000).

[Dong 2013] J. Dong, P. Du, X. Zhang, Characterization of the Young's modulus and residual stresses for a sputtered silicon oxynitride film using micro-structures, Thin Solid Films, 545 (2013) 414–418.

[Duckworth 1953] W. Duckworth, Discussion on compression strength of porous sintered Al2O3 and ZrO2, Journal of the American Ceramic Society, 36 (2) (1953) 68.

[Efstathiou 2010] C. Efstathiou, D.E. Boyce, J.S. Park, U. Lienert, P.R. Dawson, M.P. Miller, A method of measuring single-crystal elastic moduli using high-energy X-ray diffraction and a crystal-based finite element model, Acta Materialia, 58 (2010) 5806–5819.

[Elofsson 2014] V. Elofsson, M. Saraiva, R. D. Boyd, K. Sarakinos, Double in-plane alignment in biaxially textured thin films, Applied Physics Letters, 105 (2014) 233113.

[Escobar 2015] D. Escobar, R. Ospina, A.G. Gómez, E. Restrepo-Parra, Microstructure, residual stress and hardness study of nanocrystalline titanium–zirconium nitride thin films, Ceramics International, 41 (2015) 947–952.

[Eshelby 1957] J.D. Eshelby, The determination of the elastic field of an ellipsoidal inclusion, and related problems, Proceedings of the Royal Society A, 241 (1957) 376–396.

[Etienne 2004] S. Etienne, Z. Ayadi, M. Nivoit, and J. Montagnon: Elastic modulus determination of a thin layer, Materials Science and Engineering A, 370 (2004) 181–185.

[Fang 2000] W. Fang, C.Y. Lo, On the thermal expansion coefficients of thin films, Sens. Actuators Phys. 84 (2000) 310-314.

[Faurie 2004] D. Faurie, P.O. Renault, E. Le Bouhris, P. Villain, Ph. Goudeau, F. Badawi, Measurement of thin film elastic constants by X-ray diffraction, Thin Solid Films, 469-470 (2004) 201-205.

[Faurie 2005] D. Faurie, P.O. Renault, E. Le Bouhris, P. Goudeau, Determination of elastic constants of fiber-textured gold film by combining synchrotron X-ray diffraction and in situ tensile testing, Journal of Applied Physics, 98 (2005) 093511.

[Faurie 2010] D. Faurie, P. Djemia, E. Le Bouhris, P.O. Renault, Y. Roussigné, S.M. Chérif, R. Brenner, O. Castelnau, G. Patriarche, Ph Goudeau, Elastic anisotropy of polycrystalline Au films: modeling and respective contributions of X-ray diffraction, nanoindentation and Brillouin light scattering, Acta Mater. 58 (2010) 4998-5007.

[Feng 1998] L. Feng, J. Tang, J.S. Zabinski, Tribological properties of magnetron-sputtered TiC coatings, Materials Science and Engineering A, 257 (1998) 240–249.

[Ferreira 2004] C. Ferreira, Contribution à l'étude métrologique de l'analyse des contraintes par diffraction des rayons X : dispersions, erreurs, incertitudes. Thèse de Doctorat de l'Université de Nantes (2004).

[François 2008] M. François, Unified description for the geometry of X-ray stress analysis: proposal for a consistent approach, Journal of Applied Crystallography 41 (2008) 44-55.

[François 2009] D. François, A. Pineau, A. Zaoui, Comportement mécanique des matériaux : Elasticité et plasticité, Lavoisier, Hermès, Paris (2009).

[Fréour 2005] S. Fréour, D. Gloaguen, M. François, A. Perronnet, R. Guillén, Determination of single-crystal elasticity constants in a cubic phase within a multiphase alloy: X-ray diffraction measurements and inverse-scale transition modelling, Journal of Applied Crystallography, 38 (2005) 30–37.

[Gadaud 2004] P. Gadaud, S. Pautrot, Application of the dynamical flexural resonance technique to industrial materials characterization, Materials Science and Engineering A, 370 (2004) 422–426.

[Gadaud 2009] P. Gadaud, X. Milhet, S. Pautrot, Bulk and coated materials shear modulus determination by means of torsional resonant method, Materials Science and Engineering A, 521-522 (2009) 303–306.

[Gaillard 2006] Y. Gaillard, E. Jimenez-Pique, M. Anglada, Scale dependence of the Young's modulus measured by nanoindentation in columnar YSZ EB-PVD thermal barriers coatings, Philosophical Magazine, 86 (2006) 33-35, 5441-5451.

[Gaillard 2009] Y. Gaillard, V. J. Rico, E. Jiménez-Piqué, A. R. González-Elipe, Nanoindentation of TiO_2 thin films with different microstructures, J. Phys. D: Appl. Phys. 42 (2009) 145305.

[Gamboa 2016] F. Gamboa, A. Lopez, F. Avilés, J.E. Corona, A.I. Oliva, A vibrating reed apparatus to measure the natural frequency of multilayered thin films, Meas. Sci. Techno. 27 (2016) 045002.

[Gamonpilas 2004] C. Gamonpilas, E.P. Busso, On the effect of substrate properties on the indentation behaviour of coated systems, Materials Science and Engineering A, 380 (2004) 52–61.

[Gao 2016] L. Gao, S. Jiang, R. Li, Effect of sputtering pressure on structure and dielectric properties of bismuth magnesium niobate thin films prepared by RF magnetron sputtering, Thin Solid Films 603 (2016) 391-394.

[Geandier 2010] G. Geandier, P.O. Renault, E. Le Bourhis, P. Goudeau, D. Faurie, C. Le Bourlot, P. Djémia, O. Castelnau, S.M. Chérif, Elastic-strain distribution in metallic film-polymer substrate composites, Applied Physics Letters, 96 (2010) 041905.

[Géradin 1994] M. Géradin, D. Rixen, Mechanical vibrations, Wiley-Masson (1994).

[Gere 2003] J. Gere, Mechanics of Materials, Cengage Learning (2003).

[Gerthoffer 2017] A. Gerthoffer, C. Poulain, F. Roux, F. Emieux, L. Grenet, S. Perraud, CIGS solar cells on ultra-thin glass substrates: Determination of mechanical properties by nanoindentation and application to bending-induced strain calculation, Solar Energy Materials and Solar Cells, 166 (2017) 254–261.

[Ghekiere 2006] P. Ghekiere, S. Mahieu, R. De Gryse, D. Depla, Structure evolution of the biaxial alignment in sputter-deposited MgO and Cr, Thin Solid Films 515 (2006) 485–488.

[Girault 2013] B. Girault, D. Eyidi, P. Goudeau, T. Sauvage, P. Guerin, E. Le Bouhris, P.O. Renault, Controlled nanostructuration of polycrystalline tungsten thin films, Journal of Applied Physics, 113 (2013) 174310.

[Glassford 1992] K. M. Glassford, J. R. Chelikowsky, Structural and electronic properties of titanium dioxide, Phys. Rev. B. 46 (1992) 1284-1298.

[Gnäupel-Herold 1998] T. Gnäupel-Herold, P.C. Brand, H.J. Prask, Calculation of single-crystal elastic constants for cubic crystal symmetry from powder diffraction data, Journal of Applied Crystallography, 31 (1998) 929–935.

[Gnäupel-Herold 2012] T. Gnaüpel-Herold, A.A. Creuziger, M. Iadicola, A model for calculating diffraction elastic constants, Journal of Applied Crystallography 45 (2012) 197-206.

[Gogu 2010] C. Gogu, R. Haftka, R. Le Riche, J. Molimard, Effect of approximation fidelity on vibration-based elastic constants identification, Structural and Multidisciplinary Optimization, 42 (2010) 293–304.

[Goldmann 2003] A. Goldmann, 2.11.7 Nb (Niobium) (Z=41), in: A. Goldmann (Ed.), Noble Metals, Noble Metal Halides and Nonmagnetic Transition Metals, Springer-Verlag, Berlin, Heidelberg (2003) 196-204.

[Gong 2014] M.F. Gong, S.R. Qiao, F. Mei, Determining Young's modulus and Poisson's ratio of thin hard films, Surface Engineering, 30 (8) (2014) 589–593.

[Gontad 2015] F. Gontad, A. Lorusso, M. Panareo, A.G. Monteduro, G. Maruccio, E. Broitman, A. Perrone, Nanomechanical and electrical properties of Nb thin films deposited on Pb substrates by pulsed laser deposition as a new concept photocathode for superconductor cavities, Nucl. Instrum. Methods Phys. Res., Sect. A 804 (2015) 132–136.

[Grieseler 2016] R. Grieseler, F. Theska, T. Stürzel, B. Hähnlein, M. Stubenrauch, M. Hopfeld, T. Kups, J. Pezoldt, P. Schaaf, Elastic properties of nanolaminar Cr_2AlC films and beams determined by in-situ scanning electron microscope bending tests, Thin Solid Films, 604 (2016) 85–89.

[Grove 1852] W.R. Grove, On the electro-chemical polarity of gases, Philosophical Transactions of the Royal Society, 142 (1852) 87-101.

[Grüter 2010] R.R. Grüter, Z. Khan, R. Paxman, J.W. Ndieyira, B. Dueck, B.A. Bircher, J.L. Yang, U. Drechsler, M. Despont, R.A. McKendry and B.W. Hoogenboom, Disentangling mechanical and mass effects on nanomechanical resonators, Applied Physics Letters, 96 (2010) 023113.

[Hagemeyer 1993] A. Hagemeyer, H. J. Richter, H. Hibst, V. Maier, L. Marosi, Crystallographic texture and morphology of obliquely deposited Co–Cr magnetic thin films on flexible polymeric substrates, Thin Solid Films, 230 (1993) 199–202.

[Hanada 1989] T. Hanada, Y. Bessyo, N. Soga, Elastic constants of amorphous thin films in the systems SiO_2–Al_2O_3 and $AlPO_4$–Al_2O_3, J. Non-Cryst. Solids 113 (1989) 213.

[Harris 2008] K. D. Harris, A. C. van Popta, J. C. Sit, D. J. Broer, M. J. Brett, A birefringent and transparent electrical conductor. Adv Funct Mater 18 (2008) 2147–2153.

[Hashimoto 1989] T. Hashimoto, K. Okamoto, K. Hara, M. Kamiya, H. Fujiwara, Alignment of columnar grains in obliquely deposited aluminum films, Thin Solid Films, 182 (1989) 197.

[Hashin 1962] Z. Hashin, S. Shtrikman, A variational approach to the theory of the elastic behavior of polycrystals, Journal of the Mechanics and Physics of Solids, 10 (4) (1962) 343–352.

[Hauert 2009] A. Hauert, A. Rossoll, A. Mortensen, Young's modulus of ceramic particle reinforced aluminum: Measurement by the Impulse Excitation Technique and confrontation with analytical models, Composites: Part A, 40 (2009) 524–529.

[Hauk 1997] V. Hauk, Structural and residual stress analysis by nondestructive methods, Elsevier Science B.V., Amsterdam, (1997).

[Hawkeye 2007] M. M. Hawkeye, M. J. Brett, Glancing angle deposition: fabrication, properties and applications of micro- and nanostructured thin films, J. Vac. Sci. Technol. A 25 (2007) 1317-1335.

[Hawkeye 2014] M.M. Hawkeye, M.T. Taschuk, M.J. Brett, Glancing angle deposition of thin films: Engineering the nanoscale, John Wiley & Sons (2014).

[Hayakawa 1985] M. Hayakawa, S. Imai, M. Oka, Determination of single-crystal elastic constants from a cubic polycrystalline aggregate, Journal of applied crystallography, 18 (1985) 513–518.

[He 2008] Y. P. He, Z. Y. Zhang, Y. P. Zhao, Optical and photocatalytic properties of oblique angle deposited nanorod array, J. Vac. Sci. Technol. B 26 (2008) 1350–1358.

[He 2016] W. He, P. Goudeau, E. Le Bourhis, P.O Renault, J.C. Dupré, P. Doumalin, S. Wang, Study on young's modulus of thin films on kapton by microtensile testing combined with dual DIC system, Surface and Coatings Technology, 308 (2016) 273–279.

[Heinen 1995] D. Heinen, H.G. Bohn, and W. Schilling, On the mechanical strength of freestanding and substrate bonded Al thin films, Journal of Applied Physics, 77 (1995) 3742.

[Hendrix 1998] B.C. Hendrix, L.G. Yu, Self-consistent elastic properties for transversely isotropic polycrystals, Acta Materialia, 46(1) (1998) 127–135.

[Hill 1952] R. Hill, The elastic behaviour of a crystalline aggregate, Proceedings of the Physical Society, Section A, 65(5) (1952) 349–353.

[Hill 1967] R. Hill, The essential structure of constitutive laws for metals composites and polycrystals, Journal of the mechanics and physics of solids 15 (1967) 79-95.

[Hochstetter 1999] G. Hochstetter, A. Jimenez, J.-L. Loubet, Strain-rate effects on hardness of glassy polymers in the nanoscale range, Comparison between quasi-static and continuous stiffness measurements, Journal of Macromolecular Science, Part B: Physics, 38 (5), 681 (1999).

[Holland 1953] L. Holland, The effect of vapor incidence on the structure of evaporated aluminum films, Journal of the Optical Society of America, 43 (1953) 376-380.

[Hollman 1997] P. Hollman, M. Larsson, P. Hedenqvist, S. Hogmark, Tensile testing as a method for determining the Young's modulus of thin hard coating, Surface and Coatings Technology, 90 (1997) 234–238.

[Hounkpati 2014a] V. Hounkpati, S. Fréour, D. Gloaguen, V. Legrand, Influence of morphologic texture on stress analysis by X-ray and neutron diffraction in single-phase metallic materials, Journal of Materials Science, 49 (2014) 7049–7065.

[Hounkpati 2014b] V. Hounkpati, S. Fréour, D. Gloaguen, V. Legrand, Accounting for a distribution of morphologies and orientations on stresses analysis by X-ray and neutron diffraction: Normalized Self-Consistent modeling, Advanced Materials Research, 996 (2014) 82–87.

[Hounkpati 2015] V. Hounkpati, Analyse multiéchelle du comportement mécanique des matériaux métalliques biphasés, Thèse de doctorat de l'ECN, Nantes, (2015).

[Howard 1999] C.J. Howard, E.H. Kisi, Measurement of single-crystal elastic constants by neutron diffraction from polycrystals, Journal of Applied Crystallography, 32 (1999) 624–633.

[Hoy-Benítez 2012] J.A. Hoy Benítez, F. Avilés, F. Gamboa, R. Peón-Escalante, A.I. Oliva, Vibration modeling and testing of bilayer beams for determination of film elastic modulus, Meas. Sci. Technol. 23 (2012) 045605

[Hrudey 2006] P. C. P. Hrudey, K. L. Westra, M. J. Brett, Highly ordered organic Alq3 chiral luminescent thin films fabricated by glancing-angle deposition, Adv Mater 18 (2006) 224–228.

[Huang 2000] H. Huang, F. Spaepen, Tensile testing of free-standing Cu, Ag and Al thin films and Ag/Cu multilayers, Acta Materialia, 48 (2000) 3261–3269.

[Huang 2013] H.S. Huang, H.J. Pei, Y.C. Chang, C.J. Lee, J.C. Huang, Tensile behaviors of amorphous-ZrCu/nanocrystalline-Cu multilayered thin film on polyimide substrate. Thin Solid Films, 529 (2013) 177–180.

[Hurley 2001] D.C. Hurley, V.K. Tewary, A.J. Richards, Surface acoustic wave methods to determine the anisotropic elastic properties of thin films, Measurement Science and Technology, 12 (2001) 1486–1494.

[Hyer 2009] M.W. Hyer, Stress Analysis of Fiber-Reinforced Composite Materials, first ed. DEStech publications Inc., Lancaster (2009).

[Ilic 2010] B. Ilic, S. Krylov, H.G. Craighead, Young's modulus and density measurements of thin atomic layer deposited films using resonant nanomechanics, Journal of Applied Physics, 108 (2010) 044317.

[ImageJ 2017] W. S. Rasband, ImageJ, U. S. National Institutes of Health, Bethesda, Maryland, USA, 2017 (http://imagej.nih.gov/ij/, n.d. http://imagej.nih.gov/ij/).

[Isselé 2012] H. Isselé, D. Mercier, G. Parry, R. Estevez, L. Vignoud, C. Olagnon, Determination of the Young's modulus of a TiN thin film by nanoindentation: analytical models and FEM simulation, e-Journal of Surface Science and Nanotechnology, 10 (2012) 624–629.

[Jackson 1991] A. G. Jackson, Handbook of Crystallography For Electron Microscopists and Others, Library of Congress Cataloging-in-Publication Data (1991) Springer-Verlag New York Inc.

[Jämting 1997] A. Jämting, J. Bell, M. Swain, N. Schwarzer, Investigation of the elastic modulus of thin films using simple biaxial bending techniques, Thin Solid Films 308 (1997) 304–309.

[Javed 2010] A. Javed, J.B. Sun, An investigation of structural phase transformation and electrical resistivity in Ta films, Applied Surface Science, 257 (2010) 1211–1215.

[JCGM 2008] JCGM 100: Evaluation of measurement data - Guide to the expression of uncertainty in measurement (2008) (https://www.bipm.org/en/about-us/).

[JCGM 2012] JCGM 200: International vocabulary of metrology - Basic and general concepts and associated terms (IVM) (2012) (https://www.bipm.org/en/about-us/).

[Jensen 2004] M.O. Jensen, M.J. Brett, Porosity engineering in glancing angle deposition thin films, Appl. Phys. A 80 (2004) 763-768.

[Jiménez-Piqué 2014] E. Jiménez-Piqué, L. González-García, V. J. Rico, A. R. González-Elipe, Nanoindentation of nanocolumnar TiO_2 thin films with single and stacked zig-zag layers, Thin Solid Films 550 (2014) 444–449.

[Kaempf 1905] K. Kaempf, Grösse und ursache der doppelbrechung in kundtschenspiegeln und erzeugung von doppelbrechung in metallspiegelndurch zug, Ann Phys 321 (1905) 308–33.

[Kaman 2014] J. Kaman, Young's Modulus and Energy Dissipation Determination Methods by AFM, with Particular Reference to a Chalcogenide Thin Film, Periodica Polytechnica Electrical Engineering and Computer Science, 59 (1) (2015) 18–25.

[Karabacak 2003] T. Karabacak, A. Mallikarjunan, J. P. Singh, D. Ye, G. C. Wang, T. M. Lu, β-phase tungsten nanorod formation by oblique-angle sputter deposition, Appl. Phys. Lett. 83 (2003) 3096.

[Kelvin 1856] W.T.L. Kelvin, Elements of a mathematical theory of elasticity, Philosophical Transactions Royal Society, 146 (1856) 481–498.

[Kennedy 2003] S. R. Kennedy, M. J. Brett, Porous broadband antireflection coating by glancing angle deposition, Appl. Opt. 42 (2003) 4573–4579.

[Kesapragada 2006a] S. V. Kesapragada, P. Victor, O. Nalamasu, D. Gall, Nanospring pressure sensors grown by glancing angle deposition, Nano Letters, 6 (4) (2006) 854–857.

[Kesapragada 2006b] S.V. Kesapragada, D. Gall, Anisotropic broadening of Cu nanorods during glancing angle deposition, Appl. Phys. Lett. 89 (2006) 203121.

[Kim 1997] Y. Kim, Elastic modulus measurement of thin film using a dynamic method, Journal of Electronic Materials, 26 (1997) 1002–1008.

[Kim 2009] T-S. Kim, D. Chumakov, E. Zschech, and R.H. Dauskardt, Tailoring UV cure depth profiles for optimal mechanical properties of organosilicate thin films, Applied Physics Letters, 95 (2009) 071902.

[Knorr 1959] T. G. Knorr, R. W. Hoffman, Dependence of geometric magnetic anisotropy in thin iron films, Phys. Rev. 113 (1959) 1039-1046.

[Koch 2004] N. Koch, U. Welzel, H. Wern, E.J. Mittemeijer, Mechanical elastic constants and diffraction stress factors of macroscopically elastically anisotropic polycrystals: the effect of grain-shape (morphological) texture, Phil. Mag. 84 (33) (2004) 3547-3570.

[Kocks 1998] U. F. Kocks, C. N. Tome, H. R. Wenk, Texture and anisotropy: Preferred orientations in polycrystals and their effect on materials properties, Cambridge University Press (1998).

[König 1950] H. König, G. Helwig, Über die struktur schrägaufgedampfter schichten und ihr einfluß auf die entwicklung submikroskopischer oberflächen rauhigkeiten, Optik 6 (1950) 111–24.

[Kopycinska-Müller 2013]

M. Kopycinska-Müller, K. B. Yeap, S. Mahajan, B. Köhler, N. Kuzeyeva, T. Müller, E. Zschech, K. J. Wolter, Mechanical characterization of nanoporous materials by use of atomic force acoustic microscopy methods, Nanotechnology 24 (2013) 355703.

[Kraft 1998] O. Kraft, R. Schwaiger, W.D. Nix, Measurement of mechanical properties in small dimensions by microbeam deflection, Materials Research Society Symposium-Proceedings, 518 (1998) 39–44.

[Kröner 1958] V.E. Kröner, Berechnunug der elastischen Konstanten des Vielkristalls aus den Konstanten des Einkristalls, Zeitschrift für Physik, 151 (1958) 504–518.

[Kumar 2006] A. Kumar, U. Welzel, E.J. Mittemeijer, Direction-dependent grain interaction in nickel and copper thin films, analysed by X-ray diffraction, Acta Mater. 54 (2006) 1419-1430.

[Kundt 1886] A. Kundt, Ueber die electromagnetische drehung der polarisationsebene des lichtes im eisen, Annalen der Physik 263 (1886) 191–202.

[Kurz 2014] S.J.B. Kurz, U. Welzel, E. Bischoff, E.J. Mittemeijer, Diffraction stress analysis of highly planar-faulted, macroscopically elastically anisotropic thin films and application to tensilely loaded nanocrystalline Ni and Ni(W), J. Appl. Crystallogr. 47 (2014) 291-302.

[Lakhtakia 2001] A. Lakhtakia, W. McCall, J. A. Sherwin, Q. Wu, I. J. Hodgkinson, Sculptured-thin-film spectral holes for optical sensing of fluids, Opt. Commun. 194 (2001) 33–46.

[Lakhtakia 2002] A. Lakhtakia, Sculptured thin films: accomplishments and emerging uses, Mater. Sci. Eng. C 19 (2002) 427-434.

[Laroze 1974] S. Laroze, Théorie des poutres, Masson (1974).

[Ledbetter 1988] H.M. Ledbetter, S.A. Kim, Low temperature elastic constants of deformed polycrystalline copper, Materials Science and Engineering A, 101 (1988) 87–92.

[Leisure 1997] R.G. Leisure, F.A. Willis, Resonant ultrasound spectroscopy, Journal of Physics Condensed Matter 9 (1997) 6001–6029.

[Leonhardt 2004] M. Leonhardt, D. Schneider, J. Kaspar, S. Schenk, Characterizing the porosity in thin titanium films by laser-acoustics, Surface & Coatings Technology 185 (2004) 292-302.

[Li 1999] J.Y. Li, On micromechanics approximation for the effective thermoelastic moduli of multi-phase composite materials, Mechanics of Materials, 31 (1999) 149–159.

[Liedtke 2018] S. Liedtke, C. Grüner, J. W. Gerlach, A. Lotnyk, B. Rauschenbach, Crystalline Ti-nanostructures prepared by oblique angle deposition at room temperature, Journal of Vacuum Science and Technology B, Nanotechnology and Microelectronics: Materials, Processing, Measurement, and Phenomena 36 (2018) 031804.

[Liedtke-Grüner 2019] S. Liedtke-Grüner, C. Grüner, A. Lotnyk, J. W. Gerlach, M. Mensing, P. Schumacher, B. Rauschenbach, Crystallinity and texture of molybdenum thin films obliquely deposited at room temperature, Thin Solid Films 685 (2019) 8–16.

[Lima 2005] R.S. Lima, S.E. Kruger, G. Lamouche, B.R. Marple, Elastic Modulus Measurements via Laser-Ultrasonic and Knoop Indentation Techniques in Thermally Sprayed Coatings, Journal of Thermal Spray Technology, 14 (1) 2005 52–60.

[Lintymer 2005] J. Lintymer, N. Martin, J.-M. Chappé, P. Delobelle, J. Takadoum, Nanoindentation of chromium zigzag thin films sputter deposited, Surface & Coatings Technology 200 (2005) 269– 272.

[Lintymer 2006] J. Lintymer, N. Martin, J.-M. Chappé, J. Takadoum, P. Delobelle, Modeling of Young's modulus, hardness and stiffness of chromium zigzag multilayers sputter deposited, Thin Solid Films 503 (2006) 177 – 189.

[Liu 2008] Y. Liu, T. Nakamura, Anelastic Behavior of Plasma-Sprayed Zirconia Coatings, Journal of the American Ceramic Society, 91 (12) (2008) 4036–4043.

[Liu 2016] G. Liu, Y. Yang, B. Huang, X. Luo, S. Ouyang, G. Zhao, N. Jin, P. Li, Effects of substrate temperature on the structure, residual stress and nanohardness of Ti6Al4V films prepared by magnetron sputtering, Applied Surface Science, 370 (2016) 53–58.

[Liu 2018] G. Liu, Y. Yang, N. Jin, X. Luo, B. Huang, P. Li, Z. Kou, The structural characterizations of Ti-17 alloy films prepared by magnetron sputtering, Applied Surface Science, 427 (2018) 774–781.

[López-Puerto 2014] A. López-Puerto, F. Avilés, F. Gamboa, A.I. Oliva, A vibrational approach to determine the elastic modulus of individual thin films in multilayers, Thin Solid Films, 565 (2014) 228–236.

[Lopez-Santos 2016] C. Lopez-Santos, R. Alvarez, A. Garcia-Valenzuela, V. Rico, M. Loeffler, A. R. Gonzalez-Elipe, A. Palmero, Nanocolumnar association and domain formation in porous thin films grown by evaporation at oblique angles, Nanotechnology 27 (2016) 395702.

[Lord 2007] J. D. Lord, R. Morrell, Measurement Good Practice Guide No. 98, Elastic Modulus Measurement, National Physical Laboratory, Hampton Road, Teddington, Middlesex, United Kingdom, 2007.

[Loubet 1993] J.-L. Loubet, M. Bauer, A. Tonck, S. Bec, B. Gauthier-Manuel, Nano-indentation with a surface force apparatus, NATO Advanced study institute Series E. M. Natasi, p. 429-447 (1993).

[Lugscheider 2001] E. Lugscheider, K. Bobzin, S. Barwulf, A. Etzkorn, Mechanical properties of EB-PVD-thermal barrier coatings by nanoindentation, Surface and Coatings Technology, 138 (2001) 9–13.

[Luo 1999] J. Luo, R. Stevens, Porosity-dependence of elastic moduli and hardness of 3Y-TZP ceramics, Ceramics International 25 (1999) 281-286.

[Ma 2012] S. Ma, H. Huang, M. Lu, and M. Veidt, A simple resonant method that can simultaneously measure elastic modulus and density of thin films, Surface and Coatings Technology, 209 (2012) 208–211.

[Macherauch 1973] E. Macherauch, H. Wohlfahrt and U. Wolfstief, Zur zweckmässigen Definition von Eigenspannungen. Härterei-Technische Mitteilungen 28 (1973) 201-211.

[Mahieu 2006a] S. Mahieu, P. Ghekiere, D. Depla, R. De Gryse, Biaxial alignment in sputter deposited thin films, Thin Solid Films 515 (2006) 1229–1249.

[Mahieu 2006b] S. Mahieu, PhD Thesis, Biaxial alignment in sputter deposited thin films, University of Ghent, Belgium, 2006.

[Maletta 2004] C. Maletta, L. Pagnotta, On the determination of mechanical properties of composite laminates using genetic algorithms, International Journal of Mechanics and Materials in Design, 1 (2004) 199–211.

[Mansour 2010] M. Mansour, A. S. Keita, B. Gallas, J. Rivory, A. Besnard, N. Martin, Optical anisotropy of tilted columns thin films of chromium deposited at oblique incidence, Optical Materials 32 (2010) 1146–1153.

[Martins 2009] P. Martins, C. Malhaire, S. Brida, D. Barbier, On the determination of Poisson's ratio of stressed monolayer and bilayer submicron thick films, Microsystem Technologies, 15 (2009) 1343–1348.

[Martinschitz 2006] K. J. Martinschitz, E. Eiper, S. Massl, H. Köstenbauer, R. Daniel, G. Fontalvo, C. Mitterer, J. Keckes, Rapid determination of stress factors and absolute residual stresses in thin films, Journal of Applied Crystallography 39 (2006) 777-783.

[Martinschitz 2009] K.J. Martinschitz, R. Daniel, C. Mitterer, J. Keckes, Elastic constants of fiber textured thin films determined by X-ray diffraction, Journal of Applied Crystallography, 42 (2009) 416–428.

[Massabò 2017] R. Massabò, Cut-off frequencies and correction factors of equivalent single layer theories, Procedia Engineering, 199 (2017) 1466-1471.

[Matthies 1992] S. Matthies, H. R. Wenk, Optimization of texture measurements by pole figure coverage with hexagonal grids, Physica Status Solidi (a) 133 (1992) 253-257.

[Mazot 1998] P. Mazot, S. Pautrot, Détermination du module d'Young de dépôts par flexion dynamique: Application aux systèmes bicouche et tricouche, Ann. Chim. Sci. Mater. 23 (1998) 821–827.

[Mehrabadi 1990] M.M. Mehrabadi, S.C. Cowin, Eigentensors of linear anisotropic elastic materials, Quarterly Journal of Mechanics and Applied Mathematics, 43 (1990) 15–41.

[Mendels 2005] D.A. Mendels , N.M.P. Evanno, A. Cuenat, Determination of the elastic properties of multilayered foils by the four-point micro-bending test, Philosophical Magazine, 85 (16) (2005) 1765–1782.

[Migliori 2005] A. Migliori, J.D. Maynard, Implementation of a modern resonant ultrasound spectroscopy system for the measurement of the elastic moduli of small solid specimens, Review of Scientific Instruments, 76 (2005) 121301.

[Mogilnikov 2002] K.P. Mogilnikov and M.R. Baklanov, Determination of Young's Modulus of Porous Low-k Films by Ellipsometric Porosimetry, Electrochemical and Solid State Letters, 5 (12) (2002) 29–31.

[Mori 1973] T. Mori, K. Tanaka, Average stress in matrix and average elastic energy of materials with misfitting inclusions, Acta Metallurgica, 21 (1973) 571–574.

[Morris 1970] P.R. Morris, Elastic constants of polycrystals, International Journal of Engineering Science 8 (1970) 49-61.

[Musil 1998] J. Musil, Recent advances in magnetron sputtering technology, Surf. Coat. Technol. 100 (1998) 280–286.

[Nagakubo 2020] A. Nagakubo, H.T. Lee, H. Ogi, T. Moriyama, and T. Ono, Elastic constants of beta tungsten thin films studied by picosecond ultrasonics and density functional theory, Applied Physics Letters, 116 (2020) 021901.

[Naoe 1991] M. Naoe, S. Ono, T. Hirata, Crystal orientation in titanium thin films deposited by the sputtering method without plasma damage, Mater. Sci. Eng. A 134 (1991) 1292-1295.

[Neerfeld 1942] H. Neerfeld, Zur Spannungsberechnung aus röntgenographischen Dehnungsmessungen, Mitteilungen aus dem Kaiser-Wilhelm-Institut für Eisenforschung zu Düsseldorf, 24 (1942) 61–70.

[Nemat-Nasser 1993] S. Nemat-Nasser, M. Hori, Micromechanics: Overall properties of heterogeneous materials, Elsevier Science Publishers B. V, North-Holland-Amsterdam (1993).

[Nieuwenhizen 1966] J. M. Nieuwenhizen, H. B. Haanstra, Microfractography of thin films, Philips Tech. Rev. 27 (1966) 87-91.

[Nieves 2003] F.J. Nieves, F. Gascón, A. Bayón, Measurement of the dynamic elastic constants of short isotropic cylinders, Journal of Sound and Vibration, 265 (2003) 917–933.

[Nouveau 2001] C. Nouveau, Etude de revêtements durs ($CrxNy$) obtenus par méthodes P.V.D : relation et caractérisations. Application à l'usinage du bois, Thèse de doctorat de l'ENSAM, Cluny, (2001).

[Noyan 1987] I.C. Noyan, J.B. Cohen, Residual Stress Measurement by Diffraction and Interpretation; Springer: New York, NY, USA (1987).

[Okamoto 1987] K. Okamoto, T. Hashimoto, K. Hara, M. Kamiya, and H. Fujiwara, Columnar structure and texture of iron films prepared at various evaporation rates, Thin Solid Films 147 (1987) 299-311.

[Okolo 2004] B. Okolo, P. Lamparter, U. Welzel, E.J. Mittemeijer, Stress, texture, and microstructure in niobium thin films sputter deposited onto amorphous substrates, J. Appl. Phys. 95 (2004) 466–476.

[Oliver 1992] W.C. Oliver, G.M. Pharr, An improved technique for determining hardness and elastic modulus using load and displacement sensing indentation experiments, Journal of Materials Research 7 (6) (1992).

[Oliver 2004] W.C. Oliver, G.M. Pharr, Measurement of hardness and elastic modulus by instrumented indentation: advances in understanding and refinements to methodology, Journal of Materials Research 19 (1) (2004).

[Pagnotta 2009] L. Pagnotta, G. Stigliano, Elastic characterization of isotropic plates of any shape via dynamic tests: Practical aspects and experimental applications, Mechanics Research Communications, 36 (2009) 154–161.

[Pandure 2014] P.S. Pandure, V.K.S. Jatti, T.P. Singh, Finite Element Simulation of Nano-indentation of DLC Coated HSS Substrate, Procedia Materials Science, 6 (2014) 1619–1624.

[Parthasarathi 1995] S. Parthasarathi, B.R. Tittmann, K. Sampath, and E.J. Onesto, Ultrasonic characterization of elastic anisotropy in plasma-sprayed alumina coatings, Journal of Thermal Spray Technology, 4 (4) (1995) 367–373.

[Patel 2014] D.K. Patel, H.F. Al-Harbi, S.R. Kalidindi, Extracting single-crystal elastic constants from polycrystalline samples using spherical nanoindentation and orientation measurements, Acta Materialia, 79 (2014) 108–116.

[Patel 2018] M. Patel, M.P.S. Kiran, S. Kumari, V. Singh, S. Singh, V.V.B. Prasad, Effect of oxidation and residual stress on mechanical properties of SiC seal coated C/SiC composite, Ceramics International, 44 (2018) 1633–1640.

[Pawlowski 2003] L. Pawlowski, Dépôts physiques : Techniques, microstructure et propriétés, Presses polytechniques et universitaires normandes, (2003).

[Pedrosa 2017] P. Pedrosa, A. Ferreira, J. M. Cote, N. Martina, M. Arab Pour Yazdi, A. Billard, S. Lanceros-Mendez, F. Vaz, Influence of the sputtering pressure on the morphological features and electrical resistivity anisotropy of nanostructured titanium films, Applied Surface Science, 420 (2017) 681-690.

[Peraud 1997] S. Peraud, S. Pautrot, P. Villechaise, P. Mazot, and J. Mendez, Determination of Young's modulus by a resonant technique applied to two dynamically ion mixed thin films, Thin Solid Films, 292 (1997) 55–60.

[Pfeiler 2007] M. Pfeiler, K. Kutschej, M. Penoy, C. Michotte, C. Mitterer, M. Kathrein, The influence of bias voltage on structure and mechanical/tribological properties of arc evaporated Ti–Al–V–N coatings, Surface and Coatings Technology, 202 (2007) 1050–1054.

[Pugh 1960] E. W. Pugh, E. L. Boyd, J. F. Fredman, Angle-of-incidence anisotropy in evaporated nickel-iron films, IBM Journal of Research and Development, 4 (1960) 163-172.

[Rao 2006] S.S. Rao, Vibration of Continuous Systems, John Wiley & Sons, Inc. (2006) 713–720.

[Rabe 2006] U. Rabe, Atomic force acoustic microscopy, Applied Scanning Probe Methods II, NanoScience and Technology, B Bhushan and H Fuchs (eds), Springer, Berlin, Heidelberg, (2006) 37–90.

[Radovic 2004] M. Radovic, E. Lara-Curzio, L. Riester, Comparison of different experimental techniques for determination of elastic properties of solids, Materials Science and Engineering A, 368 (2004) 56-70.

[Raj 2009] S.V. Raj, R. Pawlik, W. Loewenthal, Young's moduli of cold and vacuum plasma sprayed metallic coatings, Materials Science and Engineering A, 513-514 (2009) 59-63.

[Randle 2001] V. Randle, O. Engler, Introduction to texture analysis-Macrostress, microtexture and orientation mapping, Gordon and Breach Science Publishers (2001).

[Read 2001] D.T. Read, Y.W. Cheng, R.R. Keller, J.D. McCloskey, Tensile properties of free-standing aluminum thin films, Scripta Materalia, 45 (2001) 583-589.

[Renault 2003] P.O. Renault, E. Le Bouhris, P. Villain, P. Goudeau, K.F. Badawi, D. Faurie, Measurement of the elastic constants of textured anisotropic thin films from X-ray diffraction data, Applied Physics Letters, 83 (3) (2003) 472-475.

[Reuss 1929] A. Reuss, Berechnung der Fliessgrenze von Mischkristallen auf Grund der Plastizitätsbedingung für Einkristalle, ZAMM – Journal of Applied Mathematics and Mechanics / Zeitschrift für Angewandte Mathematik und Mechanik 9(1) (1929) 49-58.

[Roa 2016] J. J. Roa, V. Rico, M. Oliva-Ramírez, A. R. González-Elipe, E. Jiménez-Piqué, Nanoindentation and scratch resistance of multilayered TiO_2-SiO_2 coatings with different nanocolumnar structures deposited by PV-OAD, J. Phys. D: Appl. Phys. 49 (2016) 135104.

[Robbie 1995] K. Robbie, L. J. Friedrich, S. K. Dew, T. Smy, M. J. Brett, Fabrication of thin films with highly porous microstructures, Journal of Vacuum Science and Technology A 13 (1995) 1032.

[Robbie 1997] K. Robbie, M. J. Brett, Sculptured thin films and glancing angle deposition: growth mechanics and applications, Journal of Vacuum Science and Technology A 15 (1997) 1460–1465.

[Romero 2003] J. Romero, A. Lousa, E. Martinez, J. Esteve, Nanometric chromium/chromium carbide multilayers for tribological applications, Surf. Coat. Technol. 163–164 (2003) 392.

[Rousseau 2010] J.J. Rousseau, Physique et simulations numériques, Université du Maine, Le Mans (2010).

[Rouxel 2007] T. Rouxel, Elastic properties and short- to medium-range order in glasses, Journal of the American Ceramic Society 90 (2007) 3019-3039.

[Rouzaud 1995] A. Rouzaud, E. Barbier, J. Ernoult, E. Quesnel, A method for elastic modulus measurements of magnetron sputtered thin films dedicated to mechanical applications, Thin Solid Films, 270 (1995) 270-274.

[Sadeghi-Khosravieh 2017]

S. Sadeghi-Khosravieh, K. Robbie, Morphology and crystal texture in tilted columnar micro-structured titanium thin film coatings, Thin Solid Films 627 (2017) 69-76.

[Saha 2002] R. Saha, W.D. Nix, Effects of the substrate on the determination of thin film mechanical properties by nanoindentation, Acta Materialia, 50 (2002) 23–38.

[Samoto 2019] T. Samoto, H. Takano, A. Momose, Gadolinium oblique evaporation approach to make large scale neutron absorption gratings for phase imaging, Jpn. J. Appl. Phys. 58 (2019) SDDF12 1-6.

[Sanchette 1999] F. Sanchette, S. Sanchette, A. Billard, J. Lepage, M. Nivoit, C. Frantz, Détermination par une méthode vibratoire du module d'Young de revêtement Al-MT-(N) (MT = Cr, Ti) déposés sur des substrats en acier pulvérisation cathodique magnétron, Revue de Métallurgie Paris 96 (2) (1999) 259–267.

[Sato 2001] Y. Sato, K. Matsuo, Y. Takahashi, K. Muranaka, K. Fujino, S. Hahakura, K. Ohmatsu, H. Takei, IEEE Trans. Appl. Supercond. 11 (2001) 3365.

[Savaloni 2004] H. Savaloni, A. Taherizadeh, A. Zendehnam, Residual stress and structural characteristics in Ti and Cu sputtered films on glass substrates at different substrate temperatures and film thickness. Phys. B: Condens. Mat. 349 (2004) 44–55.

[Schajer 2013] G.S. Schajer, Practical residual stress measurement methods. John Wiley & Sons. (2013).

[Schalko 2011] J. Schalko, R. Beigelbeck, M. Stifter, M. Schneider, A. Bittner, U. Schmid, Improved load-deflection method for the extraction of elastomechanical properties of circularly shaped thin-film diaphragms, Proc. SPIE 8066, Smart Sensors, Actuators, and MEMS V, (2011) 80661J.

[Schneider 1997] D. Schneider, T. Schwarz, H.J. Scheibe, M. Panzner, Non-destructive evaluation of diamond and diamond-like carbon films by laser induced surface acoustic waves, Thin Solid Films, 295 (1997) 107-116.

[Schrooten 1999] J. Schrooten, G. Roebben, J.A. Helsen, Young's modulus of bioactive glass coated oral implants: porosity corrected bulk modulus versus resonance frequency analysis, Scripta Materialia, 41 (10) (1999) 1047-1053.

[Schwarzenbach 2003] D. Schwarzenbach, Note on Bravais–Miller indices, J. Appl. Cryst. 36 (2003) 1270-1271.

[Sedlak 2005] P. Sedlak, H. Seiner, M. Landa, V. Novak, P. Sittner, L. Manosa, Elastic constants of bcc austenite and 2H orthorombic martensite in CuAlNi shape memory alloy, Acta Materialia, 53 (2005) 3643e3661.

[Sedmák 2013] P. Sedmák, H. Seiner, P. Sedlák, M. Landa, R. Mušálek, J. Matějíček, Application of resonant ultrasound spectroscopy to determine elastic constants of plasma-sprayed coatings with high internal friction, Surface and Coatings Technology, 232 (2013) 747-757.

[Seifried 2018] F. Seifried, H. Leiste, R. Schwaiger, S. Ulrich, H.J. Seifert, M. Stueber, Structure, morphology and selected mechanical properties of magnetron sputtered (Mo, Ta, Nb) thin films on NiTi shape memory alloys, Surface and Coatings Technology, 347 (2018) 379–389.

[Seto 2001] M.W. Seto, B. Dick, M.J. Brett, Microsprings and microcantilevers: studies of mechanical response, J. Micromech. Microeng. 11 (2001) 582–588.

[Shaochen 2018] L. Shaochen, Z. Jian, Z. Ruihua, F. Shangchao, Y. Daqin, Effects of sputtering pressure on microstructure and mechanical properties of ZrN films deposited by magnetron sputtering, Materials Research Bulletin, 105 (2018) 231–236.

[Sharma 2016] A. Sharma, S. Mohan, S. Suwas, The effect of the deposition rate on the crystallographic texture, microstructure evolution and magnetic properties in sputter deposited Ni-Mn-Ga thin films, Thin Solid Films, 616 (2016) 530-542.

[Sharpe 1997] W.N. Sharpe, Jr., Bin Yuan, R.L. Edwards, A New Technique for Measuring the Mechanical Properties of Thin Films, Journal of Microelectromechanical Systems, 6 (3) (1997) 193-199.

[Shen 2000] Y.G. Shen, Y.W. Mai, Q.C. Zhang, D.R. McKenzie, W.D. McFall, W.E. McBride, Residual stress, microstructure and structure of tungsten thin films deposited by magnetron sputtering, Journal of Applied Physics, 87 (1) (2000) 177.

[Shetty 2011] A.R. Shetty, A. Karimi, M. Cantoni, Effect of deposition angle on the structure and properties of pulsed-DC magnetron sputtered TiAlN thin films, Thin Solid Films 519 (2011) 4262–4270.

[Shetty 2012] A. R. Shetty, A. Karimi, Texture mechanisms and microstructure of biaxial thin films grown by oblique angle deposition, Phys Status Solidi B 249 (2012) 1531–1540.

[Siad 2016] A. Siad, A. Besnard, C. Nouveau, P. Jacquet, Critical angles in DC magnetron glad thin films, Vacuum 131 (2016) 305–311.

[Simmons 1971] G. Simmons and H. Wang, Single crystal elastic constants and calculated aggregate properties, The MIT Press (1971).

[Singh 1998] A.K. Singh, H.K. Mao, J. Shu, R.J. Hemley, Estimation of single-crystal elastic moduli from polycrystalline x-ray diffraction at high pressure: application to FeO and Iron, Physical Review Letters 80 (10) (1998) 2157-2160.

[Singh 2004] J. P. Singh, D. L. Liu, D. X. Ye, R. C. Picu, T. M. Lu, G. C. Wang, Metal-coated Si springs: Nanoelectromechanical actuators, Applied Physics Letters 84 (2004) 3657.

[Sit 1999] J.C. Sit, D. Vick, K. Robbie, M. J. Brett, Thin film microstructure control using glancing angle deposition by sputtering, J. Mater. Res. 14 (1999) 1197-1199.

[Slim 2017a] M.F. Slim, A. Alhussein, A. Billard, F. Sanchette, M. François, On the determination of Young's modulus of thin film with Impulse Excitation Technique, Journal of Materials Research, 32 (2017) 497-511.

[Slim 2017b] M.F. Slim, A. Alhussein, F. Sanchette, B. Guelorget, M. François, An enhanced formulation to determine Young's and shear modulus of thin films by means of Impulse Excitation Technique, Thin Solid Films, 631 (2017) 172-179.

[Slim 2018] M.F. Slim, Caractérisation multiéchelle de l'élasticité de films minces – méthode vibratoire et diffraction des rayons X, Thèse de doctorat de l'UTT, Nogent, (2018).

[Slim 2019] M.F. Slim, A. Alhussein, E. Zgheib, M. François, Determination of single-crystal elasticity constants of the beta phase in a multiphase tungsten thin film using impulse excitation technique, X-ray diffraction and micro-mechanical modeling, Acta Materialia, 175 (2019) 348-360.

[Smith 1959] D.O. Smith, Anisotropy in Permalloy Films, Journal of Applied Physics, 30 (1959) S264-S265.

[Sneddon 1965] I.N. Sneddon, The relation between load and penetration in the axisymmetric Boussinesq problem for a punch of arbitrary profile, Int. J. Eng. Sci. 3 (1) (1965) 47–57.

[Sohn 1994] Y.H. Sohn, R.R. Biederman, R.D. Sisson JR., Microstructural development in physical vapour-deposited partially stabilized zirconia thermal barrier coatings, Thin Solid Films 250 (1994) 1-7.

[Spinner 1961] S. Spinner, W.E. Tefft, A method for determining mechanical resonance frequencies and for calculating elastic moduli from these frequencies, Procedings, ASTM (1961) 1221–1238.

[Spriggs 1961] R. M. Spriggs, Expression for Effect of Porosity on Elastic Modulus of Polycrystalline Refractory Materials, Particularly Aluminum Oxide, Journal of The American Ceramic Society-Discussions and Notes, 1961, 628-629.

[Stachiv 2014] I. Stachiv, D. Vokoun, and Y-R. Jeng, Measurement of Young's modulus and volumetric mass density/thickness of ultrathin films utilizing resonant based mass sensors, Applied Physics Letters, 104 (2014) 083102.

[Stan 2009] G. Stan, S.W. King, R.F. Cock, Elastic modulus of low-k dielectric thin films measured by load-dependent contact-resonance atomic force microscopy, Journal of Materials Research, 24 (9) (2009) 2960-2964.

[Steele 2006] J. J. Steele, A. C. van Popta, M. M. Hawkeye, J. C. Sit, M. J. Brett, Nanostructured gradient index optical filter for high-speed humidity sensing, Sens Actuat B – Chem 120 (2006) 213–219.

[Stoney 1909] G.G. Stoney, The tension of metallic films deposited by electrolysis, Proceedings of the Royal Society of London. Series A 82 (553) (1909) 172-175.

[Sungwoo 2005] S. Cho, J.F. Cardenas-Garcia, I. Chasiotis, Measurement of nanodisplacements and elastic properties of MEMS via the microscopic hole method, Sensors and Actuators A, 120 (2005) 163-171.

[Tait 1990] R.N. Tait, T. Smy, M.J. Brett, A ballistic deposition model for films evaporated over topography, Thin Solid Films 187 (1990) 375-384.

[Tait 1993] R. N. Tait, T. Smy, M. J. Brett, Modelling and characterization of columnar growth in evaporated films, Thin Solid Films, 226 (1993) 196–201.

[Talling 2008] R.J. Talling, R.J. Dashwood, M. Jackson, S. Kuramoto, D. Dye, Determination of (C11 - C12) in Ti-36Nb-2Ta-3Zr-0.3O (wt. %) (Gum metal), Scripta Mater. 59 (2008) 669-672.

[Tan 2010] Y. Tan, A. Shyam, W.B. Choi, E. Lara-Curzio, S. Sampath, Anisotropic elastic properties of thermal spray coatings determined via resonant ultrasound spectroscopy, Acta Materialia, 58 (2010) 5305-5315.

[Tanaka 1996] K. Tanaka, M. Koiwa, Single-crystal elastic constants of intermetallic compounds, Intermetallics, 4 (1996) S29-S39.

[Tane 2013] M. Tane, Y. Nagai, H. Kimizuka, K. Hahihara, Y. Kawamura, Elastic properties of an Mg-Zn-Y alloy single crystal with a long-period stacking-ordered structure, Acta Materialia, 61 (2013) 6338-6351.

[Tane 2017] M. Tane, K. Yamori, T. Sekino, T. Mayama, Impact of grain shape on the micromechanics-based extraction of single-crystalline elastic constants from polycrystalline samples with crystallographic texture, Acta Materialia, 122 (2017) 239-251.

[Tang 2007] F. Tang, G.-C. Wang, T.-M. Lu, In situ reflection high energy electron diffraction surface pole figure study of biaxial texture evolution in anisotropic Mg nanoblades during shadowing growth, J. Appl. Phys. 102 (2007) 014306.

[Thomasovà 2015] M. Thomasovà, P. Sedlàk, H. Seiner, M. Janovskà, M. Kabla, D. Shilo, M. Landab, Young's moduli of sputter-deposited NiTi films determined by resonant ultrasound spectroscopy: Austenite, R-phase, and martensite, Scripta Materialia, 101 (2015) 24–27.

[Thornton 1974] J. A. Thornton, Influence of apparatus geometry and deposition conditions on structure and topography of thick sputtered coatings, J. Vac. Sci. Technol. 11 (1974) 666–670.

[Timoshenko 1951] S. Timoshenko, J.N. Goodier, Theory of Elasticity, MacGraw-Hill, 1951.

[Toader 2001] O. Toader, S. John, Proposed square spiral microfabrication architecture for large three-dimensional photonic band gap crystals, Science 292 (2001) 1133-1135.

[Tokas 2015] R. B. Tokas, S. Jena, P. Sarkar, S. R. Polaki, S. Thakur, S. Basu, N. K. Sahoo, Oblique angle deposition of HfO_2 thin films: quantitative assessment of indentation modulus and microstructural properties, Mater. Res. Express 2 (2015) 035010.

[Tsakalakos 1981] T. Tsakalakos, The bulge test: A comparison of theory and experiment for isotropic and anisotropic films, Thin Solid Films, 75 (1981) 293-305.

[Tsuchiya 2005] T. Tsuchiya, M. Hirata, N. Chiba, Young's modulus, fracture strain, and tensile strength of sputtered titanium thin films, Thin Solid Films 484 (2005) 245–250.

[Van der Drift 1967] A. Van der Drift, Evolutionary selection, a principle governing growth orientation in vapour-deposited layers, Philips Res Pep 22 (1967) 267–288.

[Vannucci 2018] P. Vannucci, Anisotropic elasticity, Lecture Notes in Applied and Computational Mechanics, Springer, 85 (2018).

[Vasechko 2016] V. Vasechko, G. Pecanac, B. Kuhn, J. Malzbender, Mechanical properties of porous ITM alloy, International Journal of Hydrogen Energy, 41 (2016) 562-569.

[Verkhovtsev 2013] A. V. Verkhovtsev, A. V. Yakubovich, G. B. Sushko, M. Hanauske, A. V. Solov'yov, Molecular dynamics simulations of the nanoindentation process of titanium crystal, Computational Materials Science, 76 (2013) 20–26.

[Vick 2002] D. Vick, T. Smy, M. J. Brett, Growth behavior of evaporated porous thin films, J. Mater. Res. 17 (2002) 2904.

[Vijaya 1996] H.S. Vijaya, G.K. Muralidhar, G.N. Subbanna, G. Mohan Rao, S. Mohan, Characterization of titanium thin films prepared by bias assisted magnetron sputtering, Metall. Mater. Trans. 27B (1996) 1057-1060.

[Vlassak 1992] J.J. Vlassak, W.D. Nix, A new bulge test technique for the determination of Young's modulus and Poisson's ratio of thin films, Journal of Materials Research, 7 (1992) 3242-3249.

[Voigt 1910] W. Voigt, Lehrbucht der KristallPhysik, Berlin, Teubner (1910).

[Vook 1965] R.W. Vook, F. Witt, Thermally induced strains in evaporated films, Journal of Applied Physics, 36 (7) (1965) 2169-2171.

[Wakefield 2007] N. G. Wakefield , A. L. Elias , M. J. Brett , J. C. Sit, D. J. Broer, Alignment of Liquid Crystals Infiltrated into Porous Thin Films with Tailored Nanostructures Grown by Glancing Angle Deposition, Molecular Crystals and Liquid Crystals, 475 (1) (2007) 85-96.

[Walter 2015] Eric Walter, Méthodes numériques et optimisation, un guide du consommateur, 2015.

[Watt 1976] J.P. Watt, The elastic properties of composite materials, Reviews of Geophysics and Space Physics 14 (1976) 541-563.

[Welzel 2003] U. Welzel, M. Leoni, E.J. Mittemeijer, The determination of stresses in thin films; modeling elastic grain interaction, Philosophical Magazine, 83 (5) (2003) 603-630.

[Welzel 2005] U. Welzel, S. Fréour, E.J. Mittemeijer, Direction-dependent elastic grain-interaction models e a comparative study, Phil. Mag. 85 (21) (2005) 2391-2414.

[Welzel 2007] U. Welzel, S. Fréour, Extension of the Vook-Witt and inverse Vook-Witt elastic grain-interaction models to general loading states, Phil. Mag. 87 (26) (2007) 3921-3943.

[Whiting 1995] R. Whiting, M.A. Angadi, S. Tripathi, Evaluation of elastic moduli in thin-film substrate systems by the two-layer vibrating reed method, Mater. Sci. Eng. B 30 (1995) 35.

[Williams 1992] E.W. Williams, Magnetic thin films and multilayers in data storage applications, Mater. Des. 13 (1992) 115.

[Witt 1968] F. Witt, R.W. Vook, Thermally induced strains in cubic metal films, Journal of Applied Physics, 39 (1968) 2773-2776.

[Wright 1877] A.W. Wright, On the Production of transparent Metallic Films by Electrical Discharge in Exhausted Tubes, American Journal of Science and Arts, 13 (1877) 49-55.

[Xu 2019a] Z. Xu, L. Yate, Y. Qiu, W. Aperador, E. Coy, B. Jiang, S. Moya, G. Wang, H. Pan, Potential of niobium-based thin films as a protective and osteogenic

coating for dental implants: The role of the nonmetal elements, Materials Science and Engineering C 96 (2019) 166–175.

[Xu 2019b] X. Xu, M. Arab Pour Yazdi, J. B. Sanchez, A. Billard, F. Bergera, N. Martin, Reactive co-sputtering of tungsten oxide thin films by glancing angle deposition for gas sensors, Materials Today: Proceedings 6 (2019) 314–318.

[Ying 2010] X.N. Ying, L. Zhang, Y.H. Yuan, The mechanical spectra of deposited materials by a composite reed vibration method, Physica B 405 (2010) 2039.

[Zaouali 1991] M. Zaouali, J.L. Lebrun, X-ray diffraction determination of texture and internal stresses in magnetron PVD molybdenum thin films, Surf. Coating. Technol. 50 (1991) 5-10.

[Zener 1948] C. Zener, Elasticity and Anelasticity of Metals, University of Chicago Press (1948).

[Zhang 2007] J.-M. Zhang, Y. Zhang, K.-W. Xu, V. Ji, Young's modulus surface and Poisson's ratio curve for cubic metals, J. Phys. Chem. Solids 68 (2007) 503-510.

[Zhang 2013] L. Zhang, H. Yang, X. Pang, K. Gao, A.A. Volinsky, Microstructure, residual stress, and fracture of sputtered TiN films, Surface and Coatings Technology, 224 (2013) 120-125.

[Zhang 2017] S. Zhang, Z. Wang, P. Guo, P. Ke, M. Odén, A. Wang, Temperature induced super hard CrB_2 coatings with preferred (001) orientation deposited by DC magnetron sputtering technique, Surface and Coatings Technology, 322 (2017) 134-140.

[Zhao 2011] X. Zhao, Z. Xie, P. Munroe, Nanoindentation of hard multilayer coatings: Finite element modeling, Materials Science and Engineering A, 528 (2011) 1111–1116.

[Zhu 2012] Y. Zhu, H. Jiao, Rugate filter with multi-channel grown by glancing angle deposition, Optik 123 (2012) 1501–1503.

[Ziegele 1997] H. Ziegele, H.J. Scheibe, B. Schultrich, DLC and metallic nanometer multilayers deposited by laser arc discharge, Surf. Coat. Technol. 97 (1997) 385.

Appendix A

Table A.1
The theoretical position of the intensity poles of the $\{11\bar{2}4\}_{\alpha}$ family of planes, tilted owing to the oblique configuration, and calculated using Eq. (V.44).

Intensity pole	Normal configuration		GLAD					
			α = 0°		α = 45°		α = 80°	
	ψ (°)	ϕ (°)	ψ (°)	ϕ (°)	ψ (°)	ϕ (°)	ψ (°)	ϕ (°)
4	38.44	240	26.33	-134.45	19.69	22.66	19.57	158.12
5		300		-45.51		157.34		21.88
6	38.44	0	40.86	18.13	45.57	29.48	54.44	40.16
3		180		161.87		150.52		139.84
1	38.44	60	51.94	66.75	62.71	69.53	77.23	71.41
2		120		113.25		110.47		108.59

Table A.2
The theoretical position of the intensity poles of the $\{20\bar{2}3\}_\alpha$ family of planes, tilted owing to the oblique configuration, and calculated using Eq. (V.44).

Intensity pole	Normal configuration		GLAD					
			α = 0°		α = 45°		α = 80°	
	ψ (°)	ϕ (°)	ψ (°)	ϕ (°)	ψ (°)	ϕ (°)	ψ (°)	ϕ (°)
5	50.70	270	35.64	270	24.05	270	8.65	270
4	50.70	210	44.59	-162.67	42.30	5.26	43.16	168.45
6		330		-17.33		174.74		11.55
1	50.70	30	59.26	38.77	66.89	43.23	77.81	46.72
3		150		141.23		136.77		133.28
2	50.70	90	65.76	90	77.36	90	92.75	90

Table A.3
The theoretical position of the intensity poles of the $\{21\bar{3}1\}_{\alpha}$ family of planes, tilted owing to the oblique configuration, and calculated using Eq. (V.44).

Intensity pole	Normal configuration		GLAD					
			α = 0°		α = 45°		α = 80°	
	ψ (°)	ϕ (°)	ψ (°)	ϕ (°)	ψ (°)	ϕ (°)	ψ (°)	ϕ (°)
10	78.36	-109.11	64.20	-110.86	53.45	-113.52	39.67	-120.15
5		-70.89		-69.14		-66.48		-59.85
4	78.36	-130.89	67.22	-134.06	59.17	-138.27	49.78	-147.11
9		-49.11		-45.94		-41.70		-32.89
11	78.36	-169.11	75.94	-172.52	74.73	-175.55	74.11	-179.87
6		-10.89		-7.48		-4.45		359.87
8	78.36	10.89	81.56	13.51	84.42	14.90	88.52	15.82
3		169.11		166.49		165.10		164.18
1	78.36	49.11	89.86	50.12	98.73	49.56	110.25	46.89
12		130.89		129.88		130.44		133.11
7	78.36	70.89	92.62	71.28	103.58	70.74	118.04	68.70
2		109.11		108.72		109.26		111.30

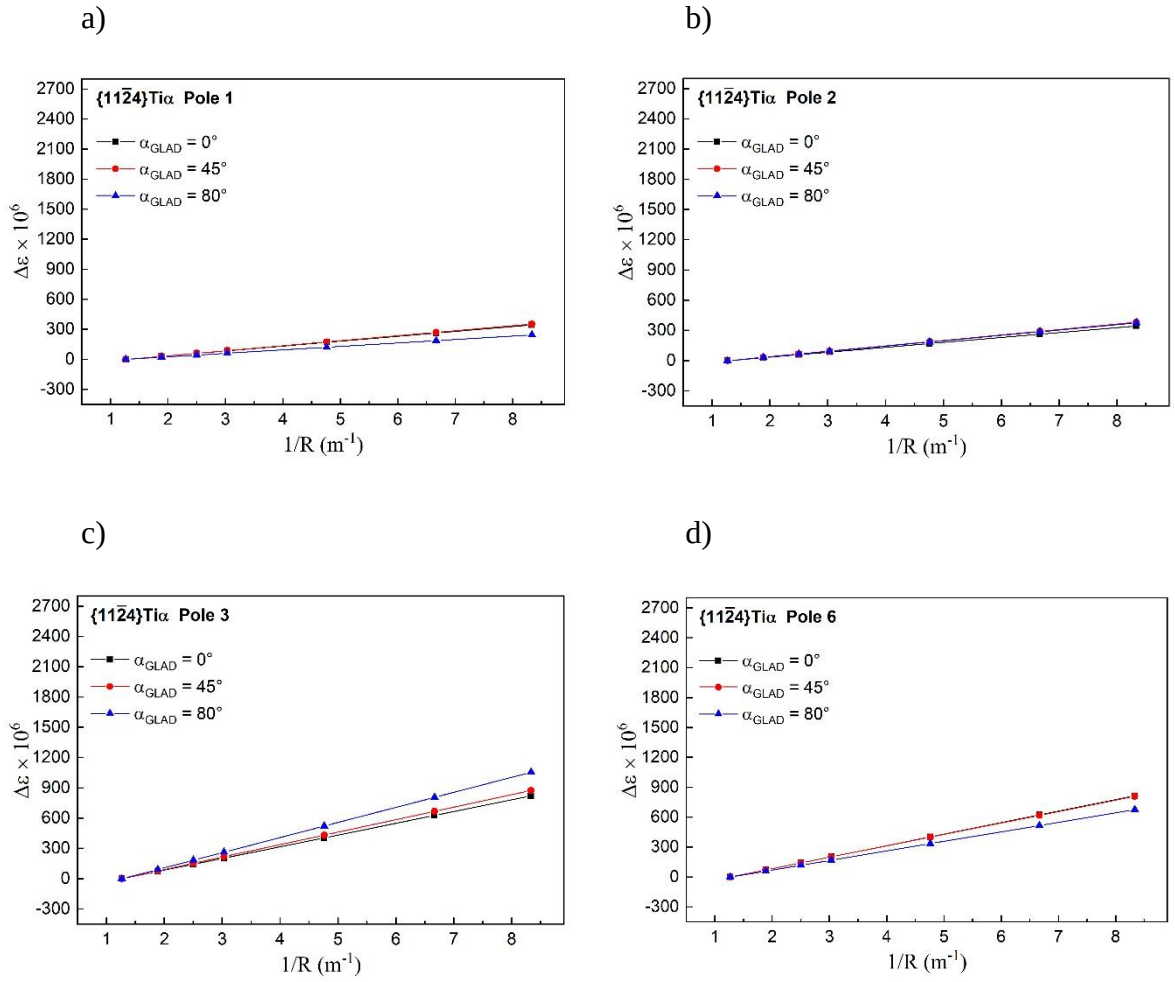

Fig. A.1. Strain variation of the $\{11\bar{2}4\}_{\alpha}$ family of planes as a function of the inverse of the curvature radius calculated using the KE model at various glancing angles α (0°, 45° and 80°).

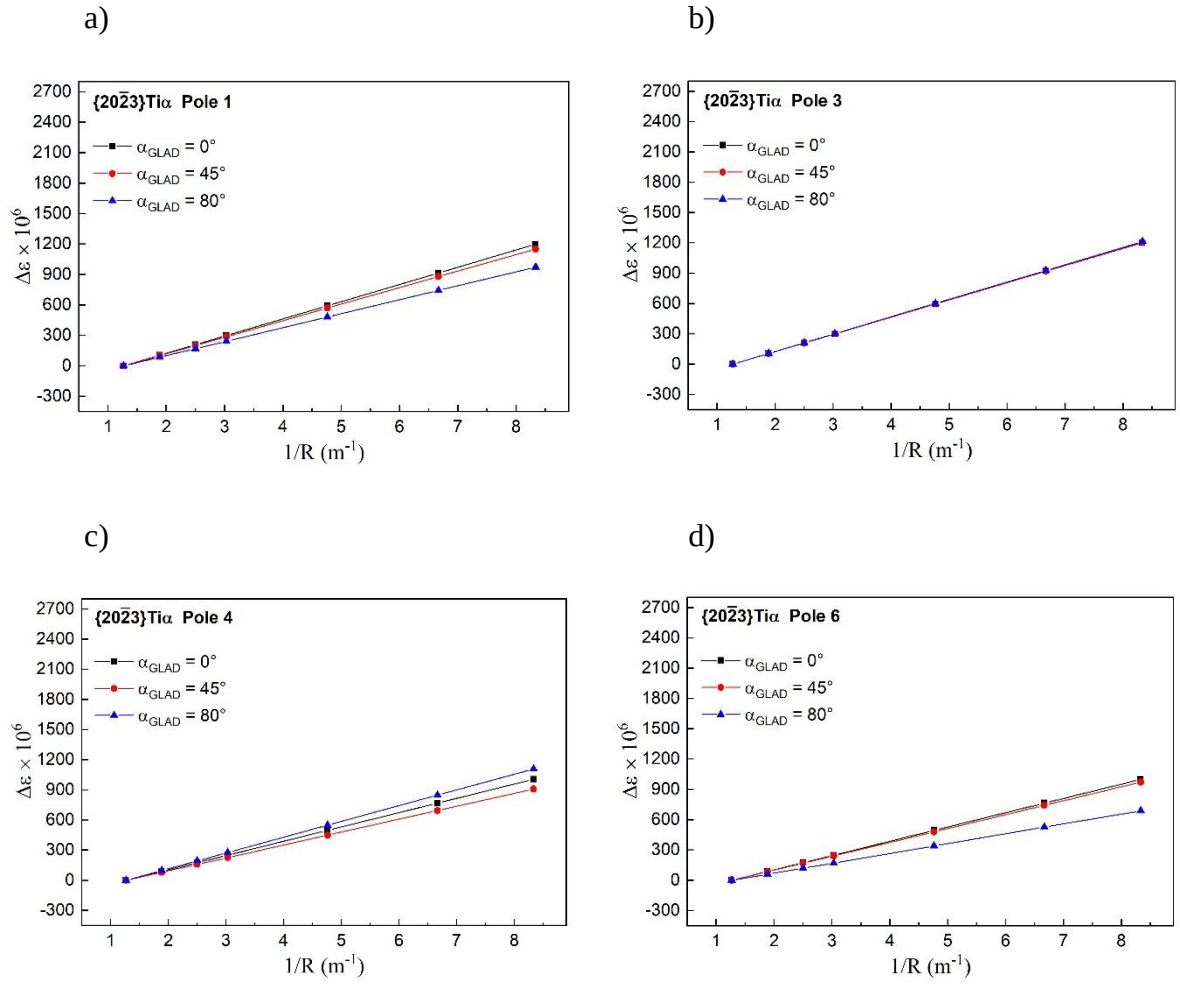

Fig. A.2. Strain variation of the $\{20\bar{2}3\}_{\alpha}$ family of planes as a function of the inverse of the curvature radius calculated using the KE model at various glancing angles α (0°, 45° and 80°).

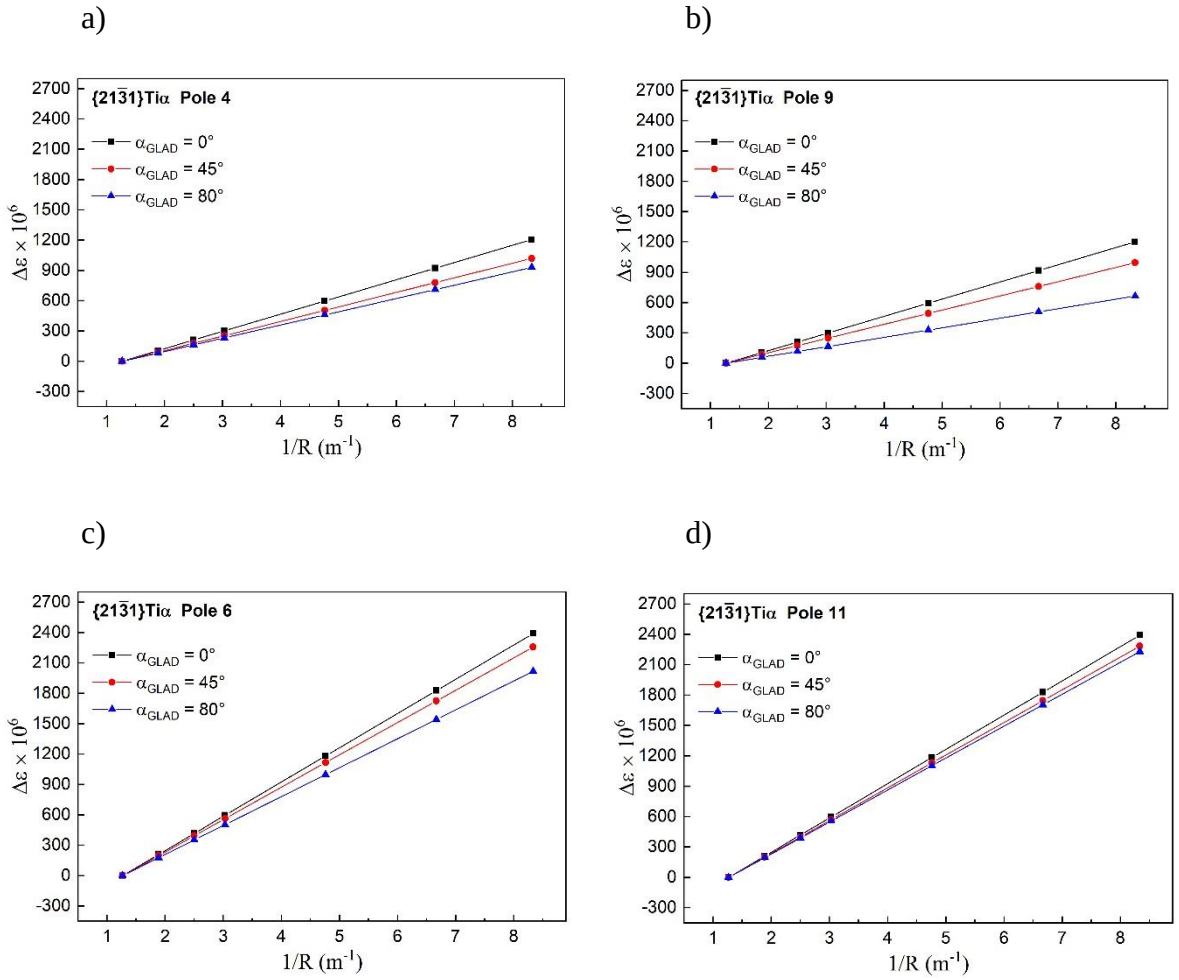

Fig. A.3. Strain variation of the $\{21\bar{3}1\}_{\alpha}$ family of planes as a function of the inverse of the curvature radius calculated using the KE model at various glancing angles α (0°, 45° and 80°).

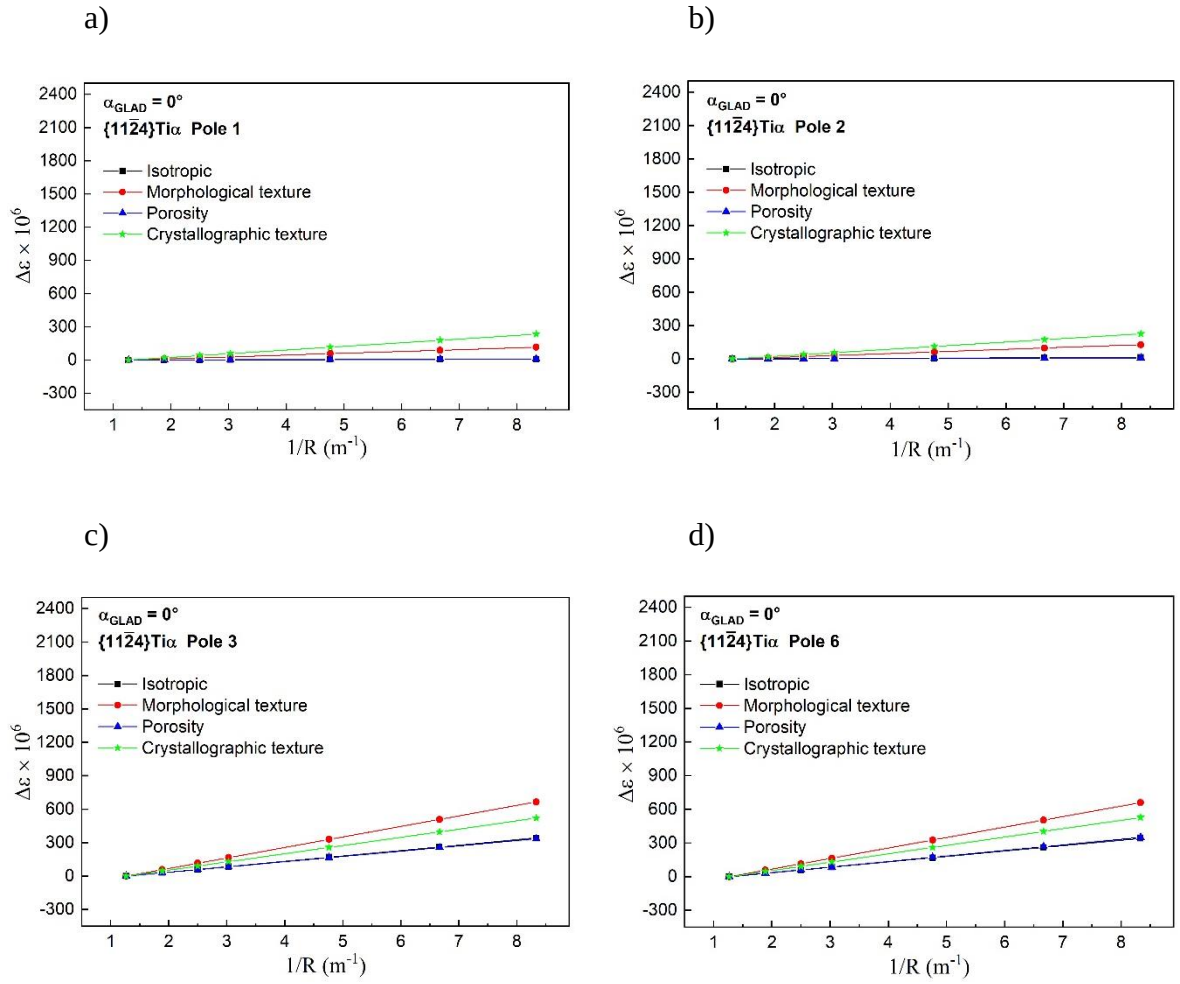

Fig. A.4. Effects of the porosity, the crystallographic, and the morphological textures on the elastic behavior of the diffracting volume of the $\{11\bar{2}4\}_{\alpha}$ family of planes. The strain variation was calculated using the KE model at α = 0°.

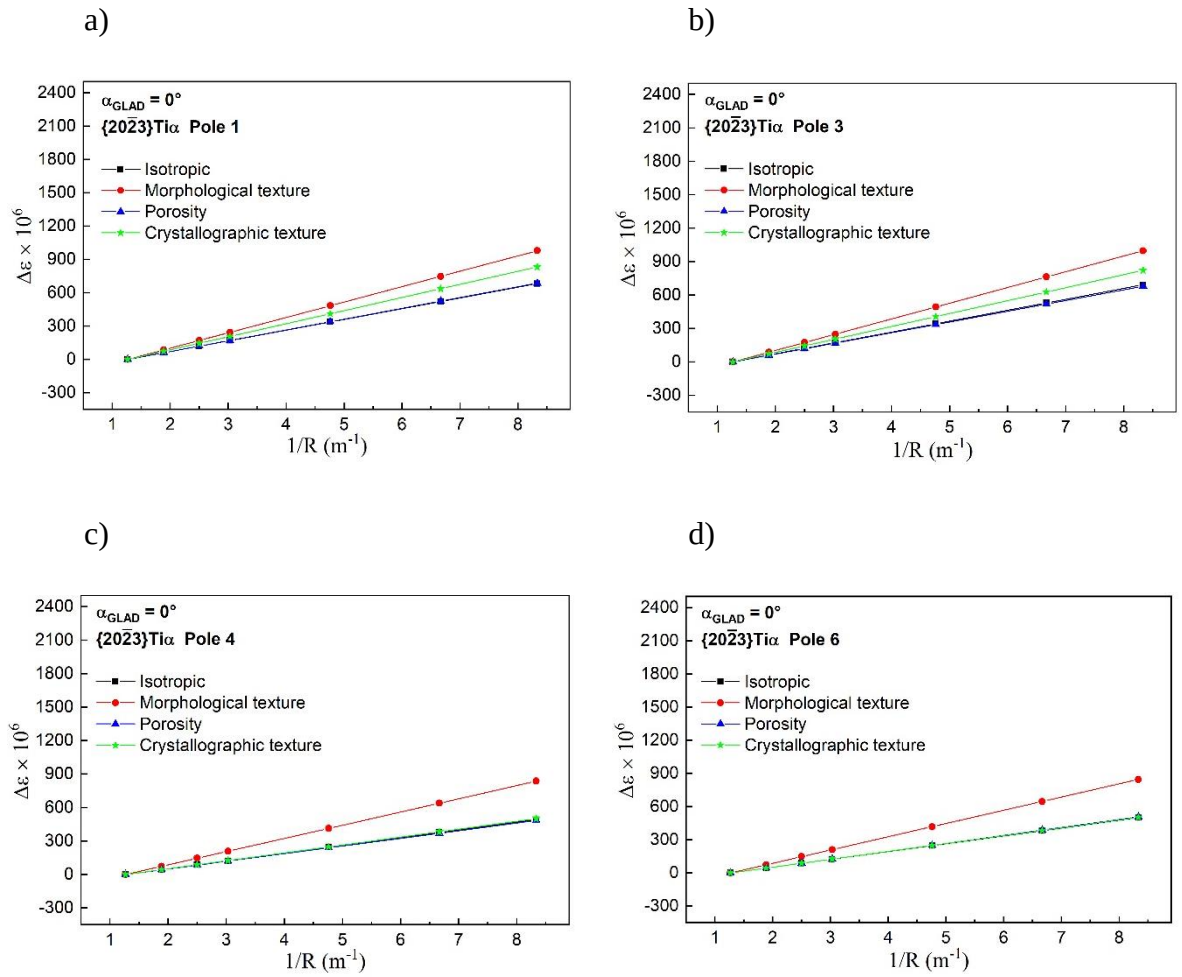

Fig. A.5. Effects of the porosity, the crystallographic, and the morphological textures on the elastic behavior of the diffracting volume of the $\{20\bar{2}3\}_\alpha$ family of planes. The strain variation was calculated using the KE model at α = 0°.

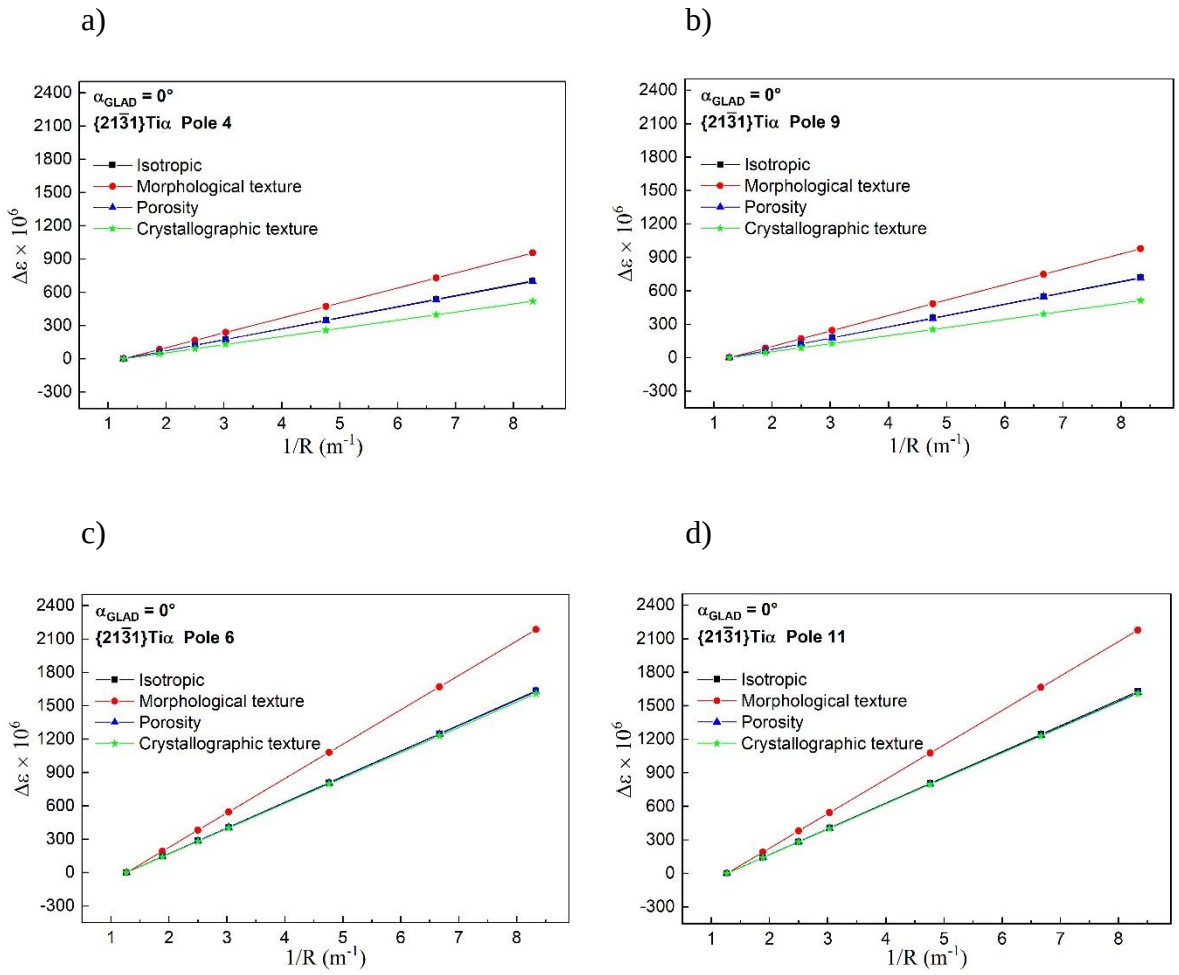

Fig. A.6. Effects of the porosity, the crystallographic, and the morphological textures on the elastic behavior of the diffracting volume of the $\{21\bar{3}1\}_{\alpha}$ family of planes. The strain variation was calculated using the KE model at α = 0°.

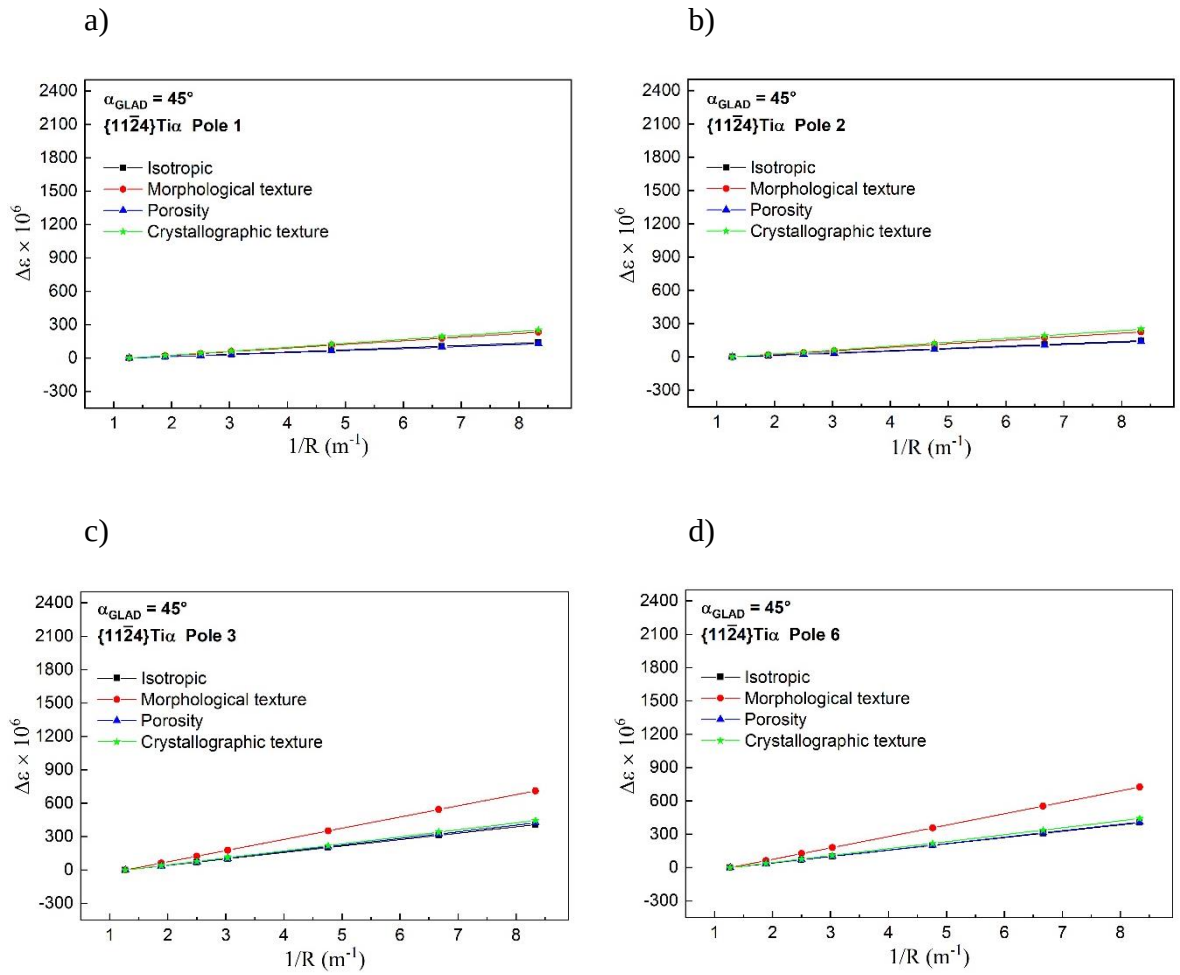

Fig. A.7. Effects of the porosity, the crystallographic, and the morphological textures on the elastic behavior of the diffracting volume of the $\{11\bar{2}4\}_\alpha$ family of planes. The strain variation was calculated using the KE model at α = 45°.

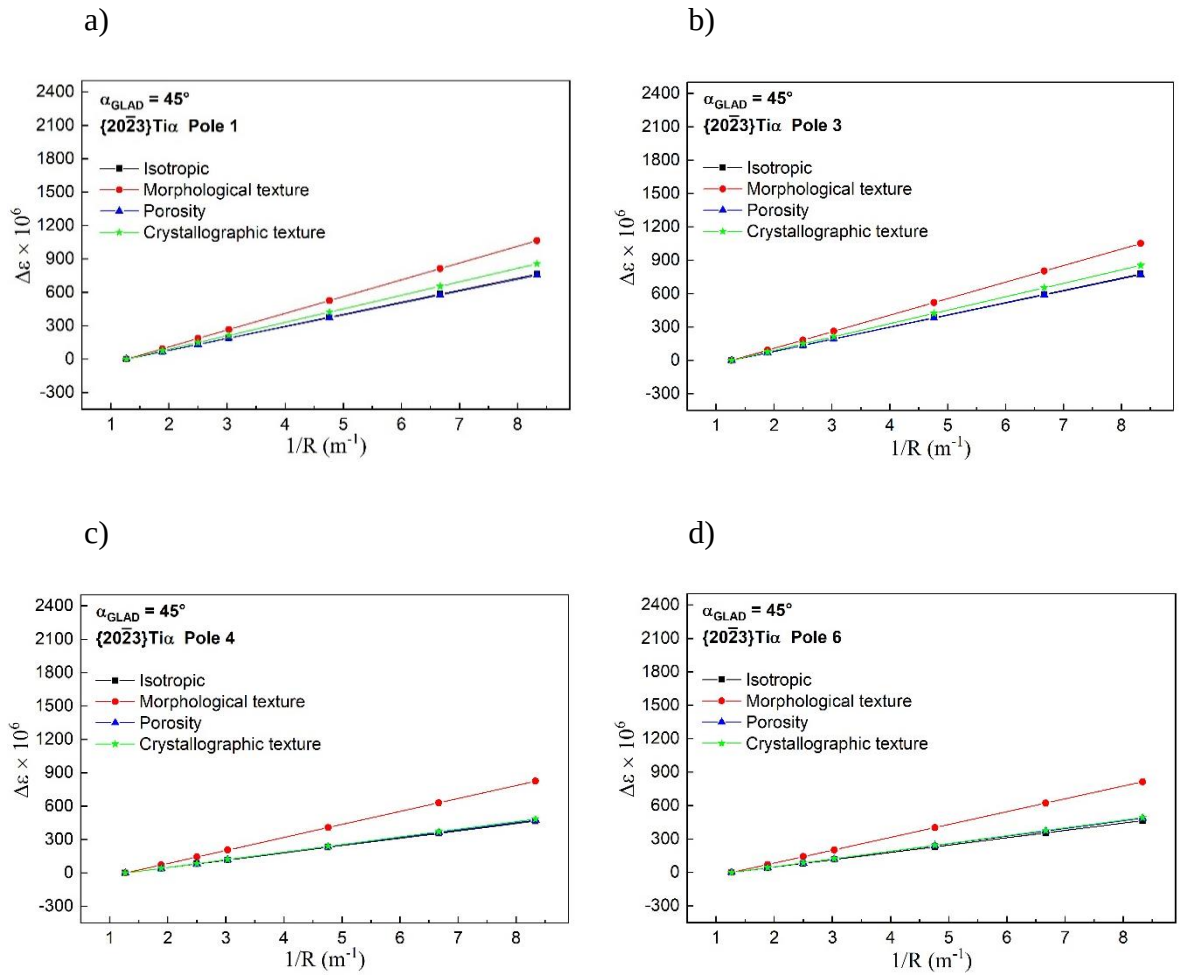

Fig. A.8. Effects of the porosity, the crystallographic, and the morphological textures on the elastic behavior of the diffracting volume of the $\{20\bar{2}3\}_{\alpha}$ family of planes. The strain variation was calculated using the KE model at α = 45°.

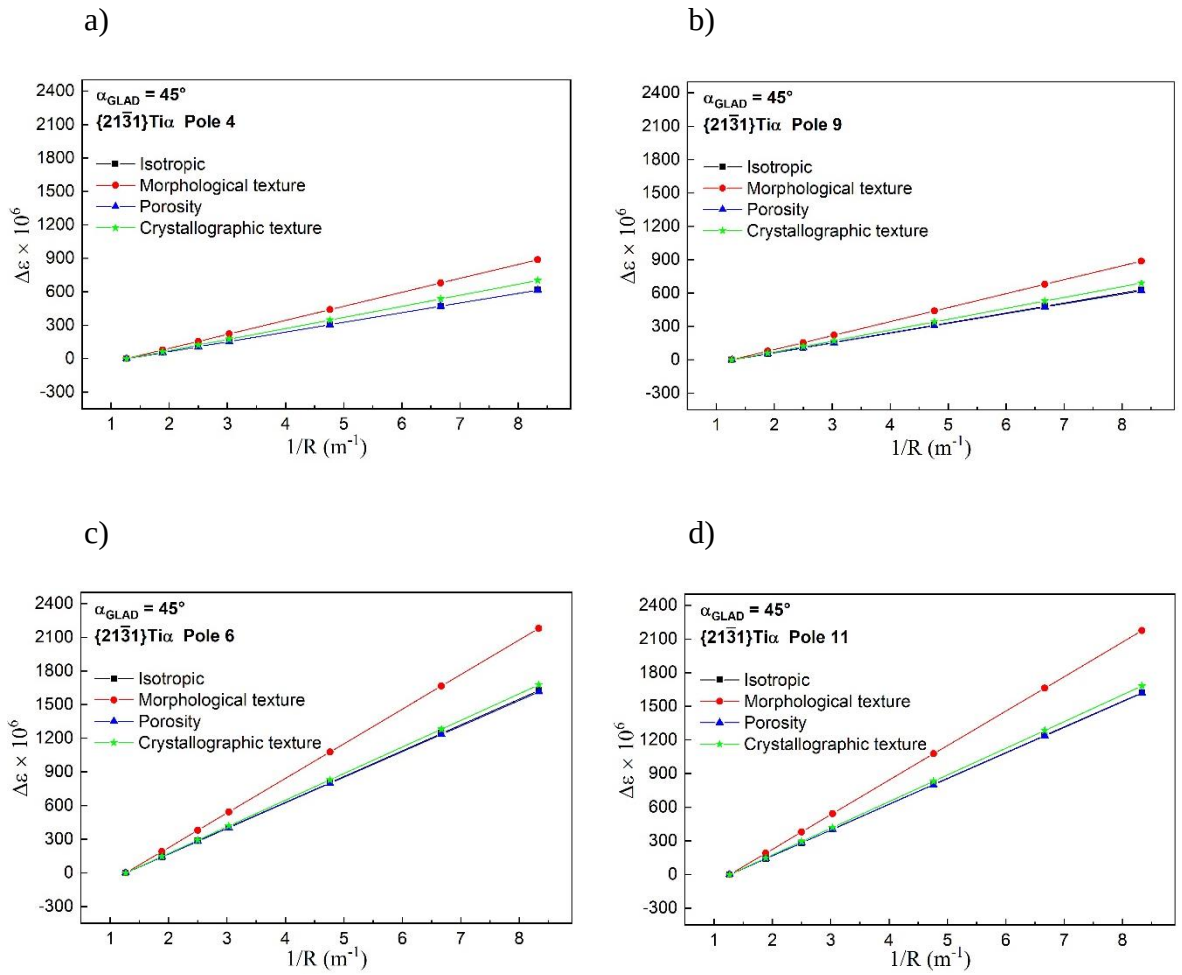

Fig. A.9. Effects of the porosity, the crystallographic, and the morphological textures on the elastic behavior of the diffracting volume of the $\{21\bar{3}1\}_{\alpha}$ family of planes. The strain variation was calculated using the KE model at α = 45°.

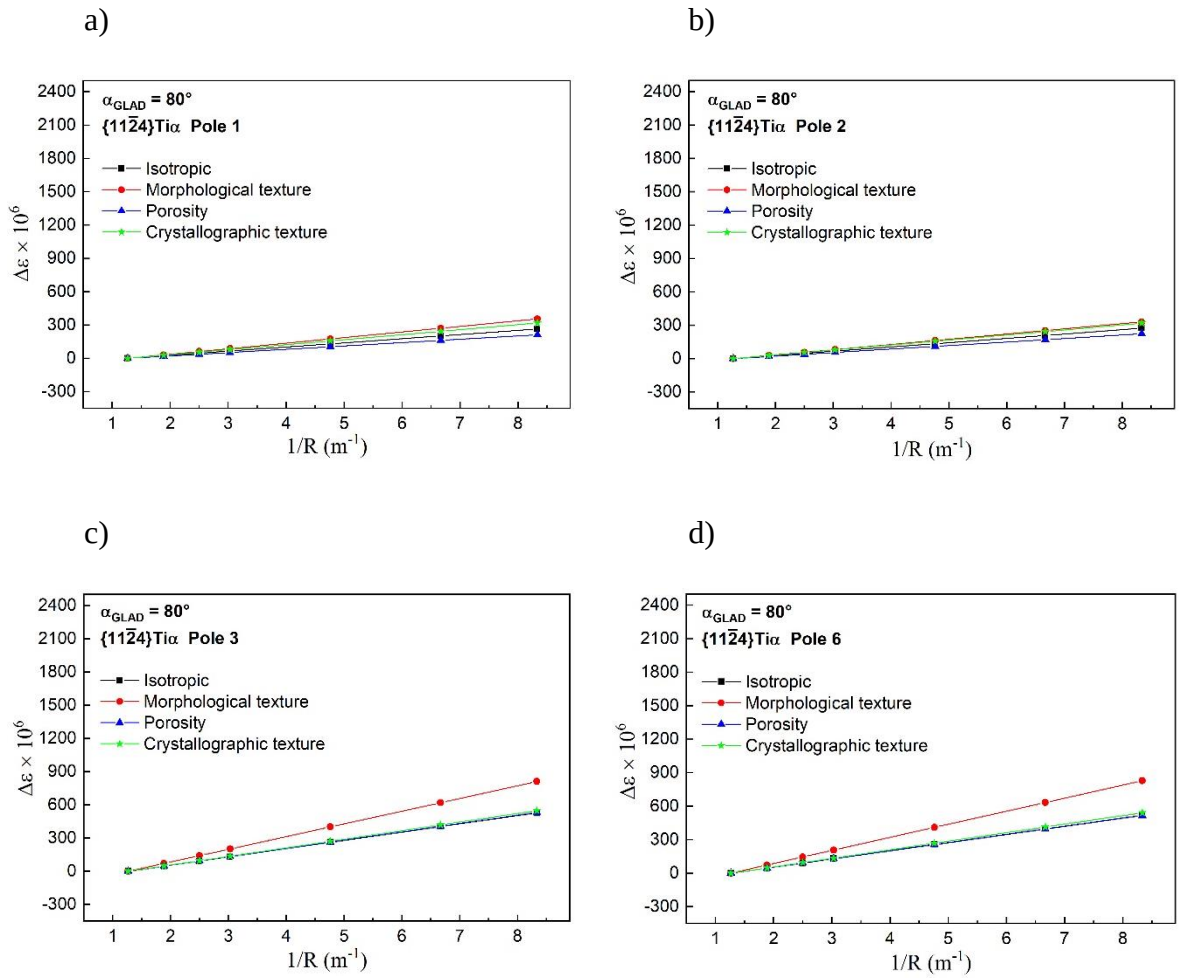

Fig. A.10. Effects of the porosity, the crystallographic, and the morphological textures on the elastic behavior of the diffracting volume of the $\{11\bar{2}4\}_\alpha$ family of planes. The strain variation was calculated using the KE model at α = 80°.

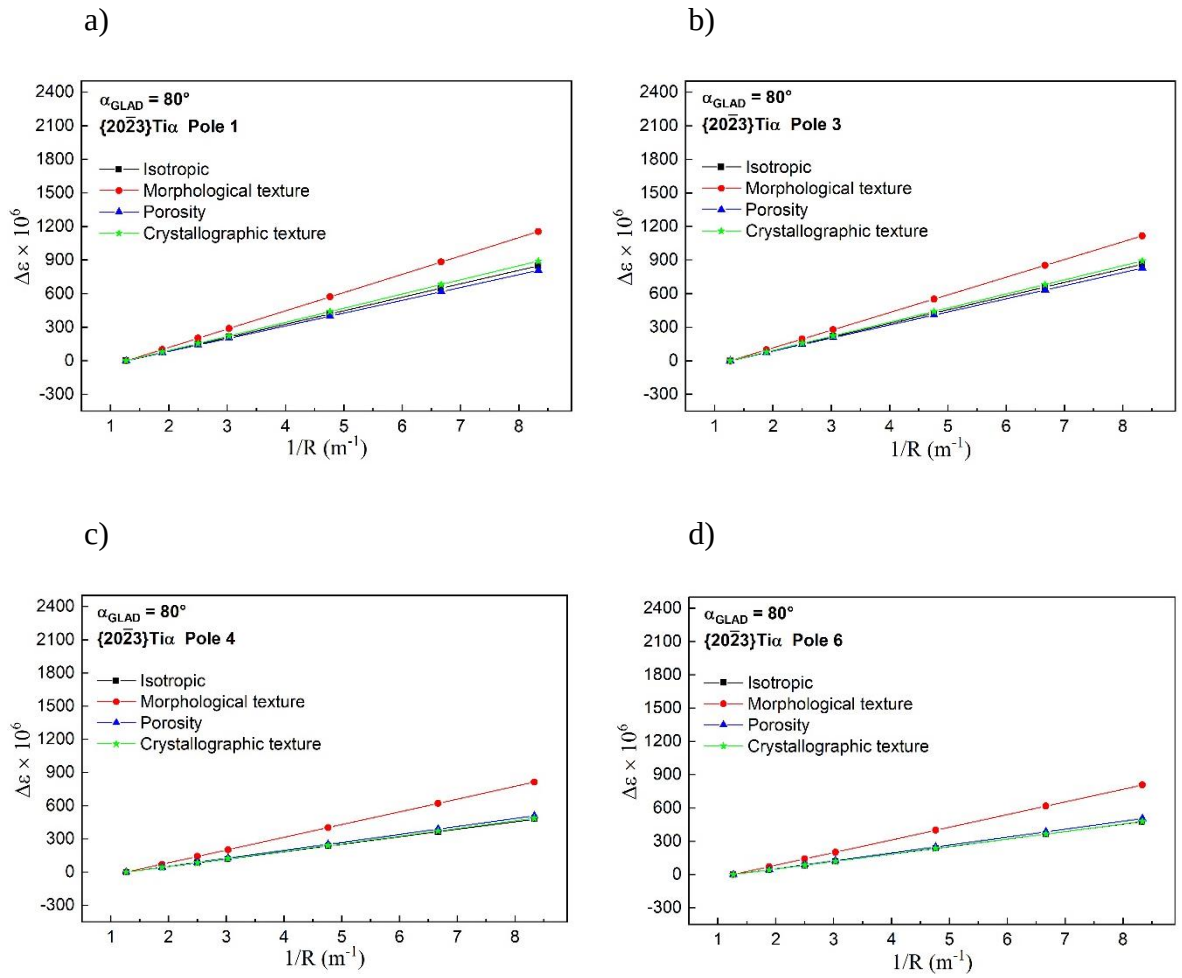

Fig. A.11. Effects of the porosity, the crystallographic, and the morphological textures on the elastic behavior of the diffracting volume of the $\{20\bar{2}3\}_\alpha$ family of planes. The strain variation was calculated using the KE model at α = 80°.

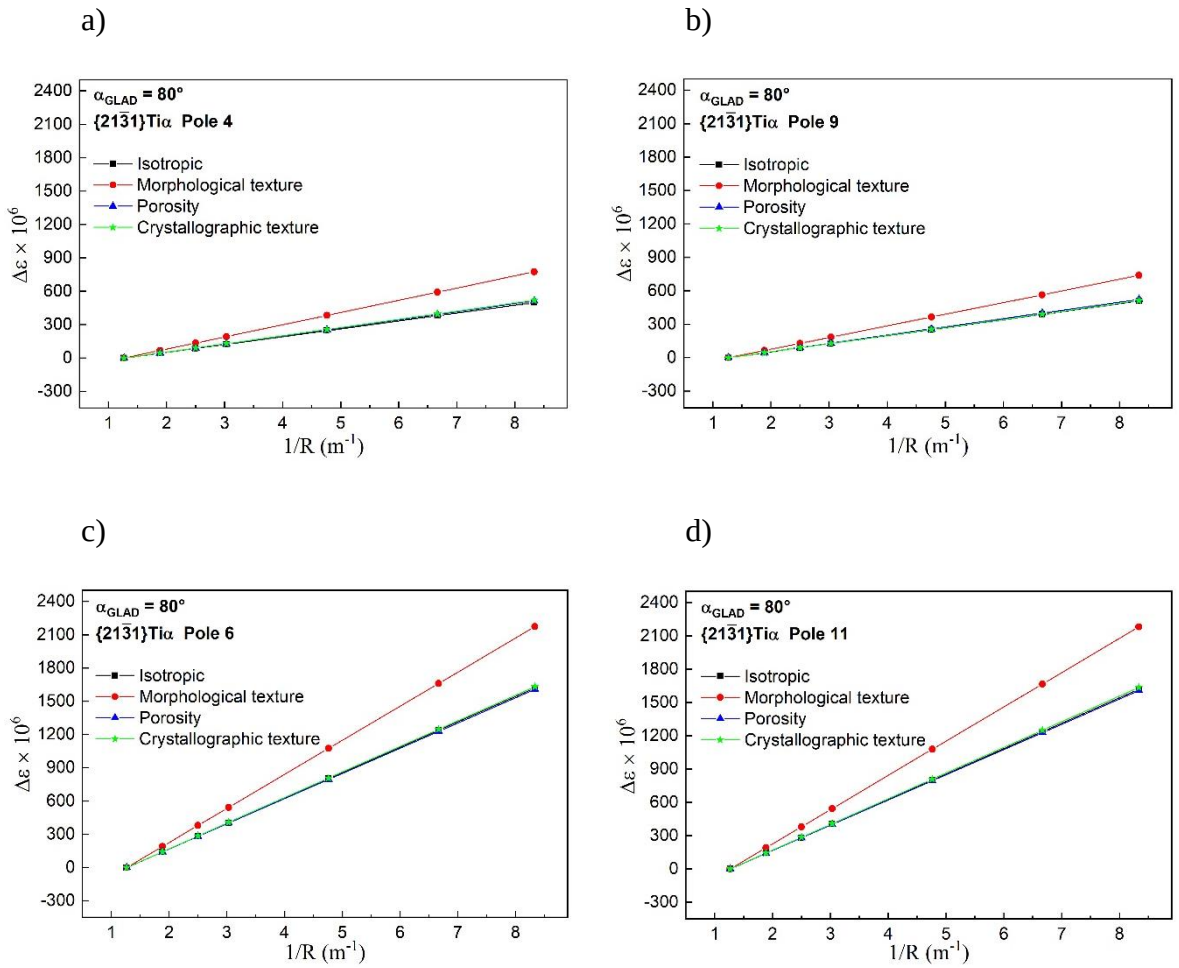

Fig. A.12. Effects of the porosity, the crystallographic, and the morphological textures on the elastic behavior of the diffracting volume of the $\{21\bar{3}1\}_{\alpha}$ family of planes. The strain variation was calculated using the KE model at α = 80°.

Appendix B Résumé en Français

Modélisation et caractérisation multiéchelle du comportement élastique des couches minces anisotropes

Introduction générale

Dans de nombreuses applications industrielles, des nouveaux matériaux sous forme de revêtements ont été développés pour faire face aux différentes contraintes technologiques et économiques imposées dans la société industrielle. Aujourd'hui, les revêtements sont largement utilisés dans des domaines aussi divers que la mécanique, l'électronique, l'optique, les industries chimique et aéronautique, etc. Un revêtement joue un rôle d'une couche protective dans le but de protéger, par exemple, une pièce et d'améliorer sa tenue en service. L'épaisseur de ces couches varie de quelques nanomètres à quelques centaines de micromètres. De plus, un revêtement peut être constituer d'une seule couche ou de multicouches en fonction des applications exigées. Les revêtements peuvent être élaborés par différentes techniques parmi lesquelles nous citons à titre d'exemple : dépôts physiques en phase vapeur (PVD), dépôts chimiques en phase vapeur (CVD) et la projection thermique. Dans cette thèse, nous nous intéresserons en particulier aux couches minces élaborées par pulvérisation cathodique magnétron (l'une des techniques PVD).

D'un point de vue général, une couche mince élaborée par pulvérisation cathodique magnétron est multiphasée, texturée, poreuse et présente des grains sous forme de colonnes [Liu 2018, Slim 2019]. De plus, les propriétés microstructurales (la structure, la texture, la morphologie et la porosité) dépendent des paramètres d'élaboration [Ait-Djafer 2015, Zhang 2017]. Cependant, ces propriétés microstructurales peuvent influencer les propriétés physiques et mécaniques de la couche. Ce qui provoque un comportement anisotrope à la couche. Afin d'assurer la bonne tenue en service des pièces mécaniques, il est indispensable de contrôler les propriétés des composants revêtus. En effet, nous nous intéresserons en particulier aux propriétés élastiques des couches minces élaborées par pulvérisation cathodique magnétron.

La prédiction du comportement élastique des composants revêtus nécessite une connaissance parfaite des constantes d'élasticité de la couche qui dépendent de ses propriétés microstructurales. L'identification des constantes d'élasticité est importante dans le domaine de l'ingénierie où le choix du matériau repose sur la détermination de ses constantes d'élasticité. Etant donné que les couches minces déposées par pulvérisation cathodique magnétron sont souvent anisotropes, la connaissance des constantes d'élasticité anisotropes est nécessaire pour la prédiction du comportement élastique du matériau. Les constantes d'élasticité permettent également de prédire le niveau de contraintes résiduelles issues du procédé d'élaboration.

Cette thèse a pour objectif de déterminer les constantes d'élasticité macroscopiques des couches minces anisotropes. Nous proposerons des méthodologies qui permettent de déterminer les constantes d'élasticité des couches minces ayant un comportement élastique anisotrope. Deux différentes approches seront utilisées dans ce travail. Une approche macroscopique consiste à déterminer les constantes d'élasticité d'un film par mesures vibratoires à l'aide de la technique d'excitation impulsionnelle. Une approche microscopique consiste à déterminer les constantes d'élasticité d'un film en prenant en compte ses propriétés microstructurales (porosité, texture morphologique et texture cristallographique). La texture cristallographique

sera obtenue par diffraction des rayons X. La porosité sera mesurée par analyse d'images. La texture morphologique sera observée par un microscope électronique à balayage.

Ce manuscrit s'articule donc autour de cinq chapitres.

Le premier chapitre présentera des généralités sur l'élasticité et son intérêt pour l'ingénierie. Les tenseurs de souplesse et de rigidité de matériaux généralement anisotropes et de certains autres avec des symétries particulières seront illustrés. La détermination des constantes d'élasticité à partir des tenseurs de rigidité sera également présentée. Ensuite, nous introduirons plusieurs techniques de caractérisation utilisées pour déterminer les constantes d'élasticité des couches minces tout en énumérant les différents problèmes rencontrés. La technique d'excitation impulsionnelle sera choisie parmi les différentes techniques pour mesurer les constantes d'élasticité macroscopiques de nos couches. À l'aide d'une synthèse bibliographique nous montrerons que les couches minces élaborées par pulvérisation cathodique magnétron sont souvent poreuses, polycristallines, texturées, multiphasées et leur comportement élastique dépend des paramètres du procédé au travers de la microstructure. Donc une caractérisation des constantes d'élasticité des couches minces, en tenant compte de leurs microstructures, est nécessaire. Afin de caractériser l'anisotropie des couches minces, deux approches seront développées au cours de ce travail. La technique d'excitation impulsionnelle et la diffraction des rayons X seront utilisées pour les caractérisations élastiques macroscopiques et microscopiques, respectivement.

Le deuxième chapitre sera dédié au développement des nouveaux modèles pour déterminer le module d'Young et le module de cisaillement des multicouches supposant isotropes quelles que soient l'épaisseur et les propriétés mécaniques et physiques du substrat et des couches. Ces modèles seront validés par comparaison avec un modèle éléments finis pris comme une référence.

Dans le troisième chapitre, les modèles mécaniques développés seront appliqués à des multicouches de titane et de niobium. Les constantes d'élasticité de chaque couche, supposée isotrope, seront déterminées par la technique d'excitation impulsionnelle. Ensuite, une comparaison entre les modules réduits déterminés par la technique d'excitation impulsionnelle et par nanoindentation sera faite.

Le quatrième chapitre est composé de deux parties. La première partie sera consacrée au développement d'un modèle pour déterminer les constantes d'élasticité d'un dépôt anisotrope. Le domaine de validité du modèle développé sera déterminé en comparant ses résultats à ceux d'un modèle éléments finis pris comme une référence. La deuxième partie portera sur la caractérisation élastique macroscopique des films de titane anisotropes, élaborés par pulvérisation cathodique magnétron à incidence oblique. Les constantes d'élasticité de chaque couche déposée seront corrélées avec la morphologie, la structure, la texture et l'angle d'incidence de chaque couche. Ce chapitre permet d'établir une première méthodologie de caractérisation élastique macroscopique d'un film mince anisotrope.

Enfin, le cinquième chapitre portera sur la deuxième méthodologie de caractérisation des films anisotropes. Nous commencerons par une brève introduction sur la diffraction des rayons X. Puis nous formulerons le tenseur de rigidité effectif et la déformation microscopique mesurée par diffraction des rayons X dans le cadre du modèle micromécanique de Kröner-Eshelby [Eshelby 1957]. Ensuite, à l'aide des propriétés microstructurales obtenues par diffraction des rayons X et du modèle autocohérent, les constantes d'élasticité macroscopiques des couches de titane déposées à incidence oblique (couches poreuses, texturées et monophasées) seront déterminées. Ceci nous permettra d'avoir un premier jeu de valeurs des constantes d'élasticité macroscopiques des couches déposées à incidence oblique car ces dernières ne sont pas été déterminées dans la littérature. Enfin, nous étudierons l'effet de la porosité et de la texture morphologique et cristallographique sur les constantes d'élasticité macroscopiques et sur le comportement microscopique des dépôts de titane.

Chapitre I Introduction à l'élasticité des couches minces

Le comportement élastique d'un matériau quelconque est défini par un tenseur de souplesse S_{ijkl} ou un tenseur de rigidité C_{ijkl}, qui relie l'état des contraintes à celui des déformations élastiques. Ce sont des tenseurs de quatrième ordre, ils contiennent 81 composantes dans une base orthonormée (x_1, x_2, x_3) [Vannucci 2018]. Selon la loi de Hooke, les relations linéaires entre la contrainte σ et la déformation ε s'écrivent sous une forme tensorielle comme suit [Vannucci 2018] :

$$\sigma_{ij} = C_{ijkl}\,\varepsilon_{ij} \tag{I.1}$$

$$\varepsilon_{ij} = S_{ijkl}\,\sigma_{ij} \tag{I.2}$$

Avec i, j, k et $l \in \{1, 2, 3\}$.

Du fait de la symétrie des tenseurs des contraintes et des déformations, les tenseurs de rigidité et de souplesse peuvent être réarrangées en un tenseur d'ordre 2 à 6×6 composantes. Les équations (I.1) et (I.2) s'écrivent sous forme non contractée selon la convention de Kelvin comme suit [Kelvin 1856] :

$$\begin{Bmatrix} \sigma_{11} \\ \sigma_{22} \\ \sigma_{33} \\ \sqrt{2}\sigma_{23} \\ \sqrt{2}\sigma_{31} \\ \sqrt{2}\sigma_{12} \end{Bmatrix} = \begin{bmatrix} C_{1111} & C_{1122} & C_{1133} & \sqrt{2}C_{1123} & \sqrt{2}C_{1131} & \sqrt{2}C_{1112} \\ C_{2211} & C_{2222} & C_{2233} & \sqrt{2}C_{2223} & \sqrt{2}C_{2231} & \sqrt{2}C_{2212} \\ C_{3311} & C_{3322} & C_{3333} & \sqrt{2}C_{3323} & \sqrt{2}C_{3331} & \sqrt{2}C_{3312} \\ \sqrt{2}C_{2311} & \sqrt{2}C_{2322} & \sqrt{2}C_{2333} & 2C_{2323} & 2C_{2331} & 2C_{2312} \\ \sqrt{2}C_{3111} & \sqrt{2}C_{3122} & \sqrt{2}C_{3133} & 2C_{3123} & 2C_{3131} & 2C_{3112} \\ \sqrt{2}C_{1211} & \sqrt{2}C_{1222} & \sqrt{2}C_{1233} & 2C_{1223} & 2C_{1231} & 2C_{1212} \end{bmatrix} \begin{Bmatrix} \varepsilon_{11} \\ \varepsilon_{22} \\ \varepsilon_{33} \\ \sqrt{2}\varepsilon_{23} \\ \sqrt{2}\varepsilon_{31} \\ \sqrt{2}\varepsilon_{12} \end{Bmatrix} \tag{I.3}$$

$$\begin{Bmatrix} \varepsilon_{11} \\ \varepsilon_{22} \\ \varepsilon_{33} \\ \sqrt{2}\varepsilon_{23} \\ \sqrt{2}\varepsilon_{31} \\ \sqrt{2}\varepsilon_{12} \end{Bmatrix} = \begin{bmatrix} S_{1111} & S_{1122} & S_{1133} & \sqrt{2}S_{1123} & \sqrt{2}S_{1131} & \sqrt{2}S_{1112} \\ S_{2211} & S_{2222} & S_{2233} & \sqrt{2}S_{2223} & \sqrt{2}S_{2231} & \sqrt{2}S_{2212} \\ S_{3311} & S_{3322} & S_{3333} & \sqrt{2}S_{3323} & \sqrt{2}S_{3331} & \sqrt{2}S_{3312} \\ \sqrt{2}S_{2311} & \sqrt{2}S_{2322} & \sqrt{2}S_{2333} & 2S_{2323} & 2S_{2331} & 2S_{2312} \\ \sqrt{2}S_{3111} & \sqrt{2}S_{3122} & \sqrt{2}S_{3133} & 2S_{3123} & 2S_{3131} & 2S_{3112} \\ \sqrt{2}S_{1211} & \sqrt{2}S_{1222} & \sqrt{2}S_{1233} & 2S_{1223} & 2S_{1231} & 2S_{1212} \end{bmatrix} \begin{Bmatrix} \sigma_{11} \\ \sigma_{22} \\ \sigma_{33} \\ \sqrt{2}\sigma_{23} \\ \sqrt{2}\sigma_{31} \\ \sqrt{2}\sigma_{12} \end{Bmatrix} \quad \text{(I.4)}$$

Les équations (I.3) et (I.4) peuvent s'écrire avec contraction d'indice sous la forme suivante :

$$\begin{Bmatrix} \sigma_1 \\ \sigma_2 \\ \sigma_3 \\ \sigma_4 \\ \sigma_5 \\ \sigma_6 \end{Bmatrix} = \begin{bmatrix} C_{11}C_{12}C_{13}C_{14}C_{15}C_{16} \\ C_{21}C_{22}C_{23}C_{24}C_{25}C_{26} \\ C_{31}C_{32}C_{33}C_{34}C_{35}C_{36} \\ C_{41}C_{42}C_{43}C_{44}C_{45}C_{46} \\ C_{51}C_{52}C_{53}C_{54}C_{55}C_{56} \\ C_{61}C_{62}C_{63}C_{64}C_{65}C_{66} \end{bmatrix} \begin{Bmatrix} \varepsilon_1 \\ \varepsilon_2 \\ \varepsilon_3 \\ \varepsilon_4 \\ \varepsilon_5 \\ \varepsilon_6 \end{Bmatrix} \quad \text{(I.5)}$$

$$\begin{Bmatrix} \varepsilon_1 \\ \varepsilon_2 \\ \varepsilon_3 \\ \varepsilon_4 \\ \varepsilon_5 \\ \varepsilon_6 \end{Bmatrix} = \begin{bmatrix} S_{11}S_{12}S_{13}S_{14}S_{15}S_{16} \\ S_{21}S_{22}S_{23}S_{24}S_{25}S_{26} \\ S_{31}S_{32}S_{33}S_{34}S_{35}S_{36} \\ S_{41}S_{42}S_{43}S_{44}S_{45}S_{46} \\ S_{51}S_{52}S_{53}S_{54}S_{55}S_{56} \\ S_{61}S_{62}S_{63}S_{64}S_{65}S_{66} \end{bmatrix} \begin{Bmatrix} \sigma_1 \\ \sigma_2 \\ \sigma_3 \\ \sigma_4 \\ \sigma_5 \\ \sigma_6 \end{Bmatrix} \quad \text{(I.6)}$$

Un matériau anisotrope élastiquement est un matériau qui présente des propriétés élastiques différentes selon les directions (monocristal, polycristal à morphologie orientée, texture, multiphase, composite, bois, multicouches, etc.). Grâce aux symétries des tenseurs de contraintes et de déformations, le nombre de composantes des tenseurs de rigidité et de souplesse passe de 36 à 21 composantes indépendantes. Ce matériau présente une anisotropie quelconque (symétrie triclinique) et son tenseur de rigidité peut s'écrire comme suit :

$$[C] = \begin{bmatrix} C_{11}\ C_{12}\ C_{13}C_{14}C_{15}C_{16} \\ C_{22}\ C_{23}C_{24}C_{25}C_{26} \\ C_{33}C_{34}C_{35}C_{36} \\ C_{44}C_{45}C_{46} \\ sym \quad C_{55}C_{56} \\ C_{66} \end{bmatrix} \quad \text{(I.7)}$$

Grâce à d'autres symétries matérielles, ces 21 composantes peuvent se réduire jusqu'à deux composantes dans le cas d'un matériau isotrope.

Les constantes d'élasticité sont nécessaires pour prédire le comportement élastique d'un matériau sous différents types de sollicitations. Plusieurs modèles analytiques et numériques ont été développés, en utilisant les propriétés élastiques d'un matériau, afin de concevoir des

structures, de prédire la durée de vie de leurs matériaux constitutifs et de prévoir la fiabilité de la structure sollicitée.

Plusieurs méthodes ont été développées pour déterminer les constantes d'élasticité des matériaux massifs et revêtus. Elles peuvent être classées en deux groupes: les techniques statiques et dynamiques. L'essai de traction est l'un des essais statiques le plus utilisé pour caractériser le comportement élastique des matériaux [Hollman 1997, Chen 2009, Huang 2013, Gong 2014, He 2016]. Cet essai permet la détermination de plusieurs caractéristiques mécaniques d'un matériau. Par contre, son application dans le cas des couches minces reste restrictive à cause des différents problèmes rencontrés au cours de l'essai (délamination de la couche, fissuration de la couche au cours de l'essai, etc.). Il est aussi intéressant de noter que la sensibilité de cet essai décroit lorsque le rapport entre l'épaisseur du substrat et celle de la couche croit en raison de la diminution de la sensibilité de la couche à la contrainte appliquée. Par conséquence, cet essai n'est pas adapté à la caractérisation élastique des couches minces ayant une épaisseur de l'ordre du micromètre.

L'essai de flexion est souvent utilisé particulièrement pour tester les matériaux ayant un comportement fragile tel que les céramiques. Plusieurs auteurs ont effectué l'essai de flexion pour déterminer le module d'Young [Rouzaud 1995, Schalko 2011, Grieseler 2016]. Les problèmes rencontrés avec cet essai sont les mêmes que ceux rencontrées avec l'essai de traction et qui ont comme principale cause le niveau de chargement élevé appliqué au cours de l'essai. Parmi les nombreuses techniques statiques disponibles pour mesurer le module d'Young, on trouve l'essai de nanoindentation qui est souvent utilisé pour déterminer les propriétés élastiques des couches minces [Chen 2005, Gerthoffer 2017]. Bien que l'essai de nanoindentation représente l'un des essais les plus utilisés pour déterminer les constantes d'élasticité des couches minces, les résultats issus de cet essai sont influencés par l'interaction élastique entre le substrat et la couche. De plus, étant donné que la majorité des dépôts sont anisotropes, le module d'élasticité déterminé par nanoindentation est une combinaison des modules d'élasticité parallèle et perpendiculaire à la surface de la couche. Il est aussi généralement supposé que le coefficient de Poisson de la couche est connu, ce qui n'est pas toujours vrai.

Parmi les techniques dynamiques, on trouve la méthode par mesure de vitesse de propagation d'ondes ultrasonores. Cette méthode se distingue par son caractère non destructif. Plusieurs auteurs ont utilisé la méthode ultrasonore pour déterminer les constantes d'élasticité de dépôts obtenus par projection thermique [Lima 2005, Tan 2010, Sedmák 2013] ou par pulvérisation cathodique [Thomasovà 2015]. Des excitations de faibles amplitudes sont suffisantes pour effectuer des mesures ultrasonores. Cette caractéristique donne l'avantage d'utiliser la méthode ultrasonore pour les couches minces. De plus, la possibilité de calculer la matrice de rigidité entière à partir d'un spectre unique est un avantage distinct de cette méthode. Malgré le caractère non destructif de cette technique, les résultats peuvent être influencés par la texture et les défauts structuraux présents au sein du matériau [Ledbetter 1988, Liu 2008].

Une technique dynamique connue dans la littérature est la Technique d'Excitation Impulsionnelle (TEI). Le principe de base de cette technique est d'exciter un échantillon

(poutre, cylindre, disque, etc.) par un choc et le laisser vibrer librement. Les fréquences des modes de vibration sont mesurées, et à l'aide de la densité ou de la masse et les dimensions de l'échantillon, on peut remonter aux constantes d'élasticité du matériau testé. Cette technique a été utilisée par plusieurs auteurs pour déterminer les constantes d'élasticité de différents matériaux (métaux, céramiques, polymères, composites, verre, matériaux poreux, dépôts, etc.) [Schrooten 1999, Gadaud 2004, Gadaud 2009, Radovic 2004, Hauert 2009, Vasechko 2016, Slim 2017a, b] et dans une large gamme de températures [Peraud 1997, Gadaud 2009, Raj 2009, Patel 2018]. Grace à son caractère non destructif et aux faibles niveaux de contraintes générées, la TEI est qualifiée comme une prometteuse alternative pour la caractérisation du comportement élastique des couches minces. D'autres techniques expérimentales ont été utilisées pour déterminer les constantes d'élasticité des films minces parmi lesquelles : la microscopie à force atomique (AFM) [Kim 2009, Kopycinska-Müller 2013, Kaman 2014], le micro-essai de gonflage [Tsakalakos 1981, Vlassak 1992, Martins 2009] et la méthode de trou [Sungwoo 2005].

D'autres travaux ont montré que les constantes d'élasticité, la morphologie, la structure, la texture et les contraintes résiduelles dans les couches minces élaborées par pulvérisation cathodique magnétron dépendent des paramètres de dépôt. Shaochen et al. [Shaochen 2018] et Bao et al. [Bao 2018] ont montré que le module d'Young dépends de la pression de dépôt. Choudhary et al [Choudhary 2015] ont rapporté le changement du module d'Young, mesuré par nanoindentation, d'une couche de AlN élaborée par pulvérisation cathodique magnétron, à la tension de polarisation du substrat. Bao et al. [Bao 2018] ont constaté que les couches de SiC déposées à une faible pression inférieure à 0.3 *Pa*, sont délaminées et fissurées. Celles qui ont été déposées à 0.4 *Pa* présentent une morphologie dense. Par contre, les couches de SiC qui ont été déposées à une pression supérieure à 0.8 *Pa* présentent une morphologie colonnaire.

Les couches minces élaborées par pulvérisation cathodique magnétron sont généralement texturées, polycristallines et composées de différentes phases. Etant donné que la pulvérisation cathodique magnétron est une technique d'élaboration hors équilibre, elle favorise la formation des phases métastables : W_β dans des couches de tungstène [Shen 2000, Girault 2013, Slim 2017b], Ti_β dans des couches de Ti-17 [Liu 2018] et Ta_β dans des couches de tantale [Javed 2010, Colin 2017]. Ait-Djafer et al. [Ait-Djafer 2015] ont remarqué que l'apparition d'une phase et la disparition de l'autre est fonction de la pression et de la tension de polarisation du substrat. Achache et al [Achache 2016] ont constaté un changement de la texture des couches de TNTZ sous l'effet de changement de la tension de polarisation du substrat et de la pression du dépôt. Zhang et al. [Zhang 2013] ont constaté un changement de texture en fonction de l'épaisseur des dépôts de TiN élaborés par pulvérisation cathodique magnétron. Les contraintes résiduelles générées dans une couche mince lors d'un dépôt par pulvérisation cathodique magnétron dépendent de différent paramètres comme par exemple la pression de travail durant le dépôt, la température du substrat, l'épaisseur de la couche et la tension de polarisation. Escobar et al [Escobar 2015] ont remarqué que les couches de TiZrN admettent des contraintes en compression qui diminuent de -2.8 *GPa* à 1.05 *GPa* en augmentant la température du substrat jusqu'à 200 °*C*. D'autres études ont examiné l'évolution des contraintes résiduelles en fonction de l'angle d'inclinaison du substrat (α) [Siad 2016, Abadias 2019b].

D'après cette courte synthèse de la bibliographie, on peut constater que les couches minces déposées par pulvérisation cathodique magnétron sont généralement polycristallines, texturées et composées de différentes phases ce qui leurs confèrent un comportement élastique anisotrope. De plus, leurs propriétés élastiques, leurs orientations cristallographiques, leurs morphologies et leurs structures dépendent principalement des paramètres de dépôt. Donc, afin de contrôler le comportement élastique des films élaborés par pulvérisation cathodique magnétron, leurs constantes d'élasticité doivent être évaluées.

D'après la bibliographie, on peut conclure qu'une caractérisation macroscopique des constantes d'élasticité des dépôts élaborés par pulvérisation cathodique magnétron est insuffisante pour prédire son comportement élastique. En conséquence, une caractérisation microscopique des constantes d'élasticité des couches minces est nécessaire qui permettra une meilleure prédiction du comportement élastique de ces couches. Plusieurs modèles de transition d'échelles ont été utilisés pour déterminer les constantes d'élasticité du monocristal et du polycristal.

Le but de cette thèse est de proposer des méthodologies permettant de caractériser le comportement élastique des couches minces anisotropes à deux échelles différentes (Figure I.1). Pour la caractérisation élastique macroscopique des dépôts élaborés, notre choix s'est reposé sur la Technique d'Excitation Impulsionnelle (TEI) étant donné les avantages qu'elle présente par rapport aux autres techniques. Quant à la caractérisation mésoscopique, on a choisi d'effectuer des essais de diffraction des rayons X (DRX). Grâce à son caractère sélectif, la DRX permettra de déterminer les différentes propriétés microstructurales des couches. L'approche microscopique permettra de déterminer le comportement élastique des couches minces anisotropes en tenant compte de leurs propriétés microstructurales (phases, textures morphologique et cristallographiques, porosité). Ces méthodes seront appliquées à des couches minces en multicouches ayant un comportement isotrope (Chapitres II et III) et puis à des couches déposées à incidence oblique ayant un comportement anisotrope (Chapitres IV et V).

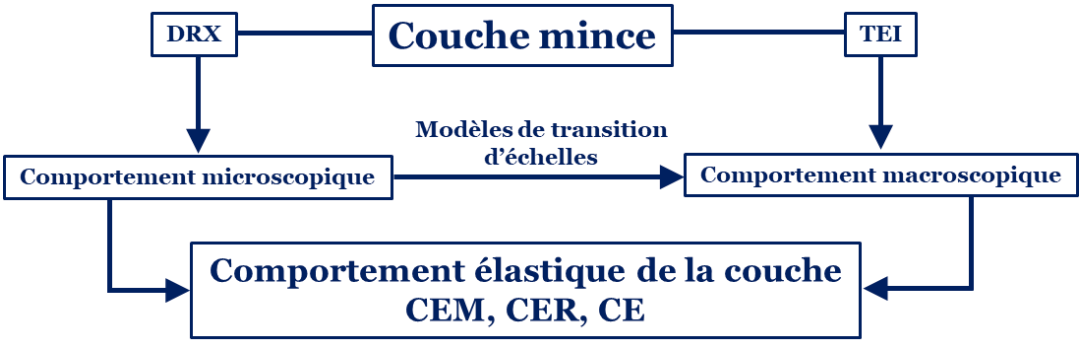

Figure I.1. Représentation schématique de la méthodologie adoptée pour la caractérisation du comportement élastique des revêtements.

Chapitre II Développement analytique pour la détermination des constantes d'élasticité des couches minces en multicouches

La Technique d'Excitation Impulsionnelle (TEI) est une technique non destructive qui peut être facilement utilisée pour déterminer les constantes d'élasticité de divers matériaux [Atri 1999, Radovic 2004, Gadaud 2004, Gadaud 2009]. Grâce à sa grande précision et les faibles niveaux de contraintes qui génère, la TEI peut être utilisée comme une nouvelle alternative pour déterminer le module d'Young et le module de cisaillement des couches minces. En se basant sur différentes théories, plusieurs modèles permettant de déterminer le module de d'Young des revêtements par TEI ont été développés [Berry 1975, Mazot 1998, Gadaud 2004, López-Puerto 2014]. Par ailleurs, pour déterminer le module de cisaillement d'une couche par TEI, des modèles analytiques ont été développés en appliquant le principe d'Hamilton [Gadaud 2009, Slim 2017a]. Pour des multicouches, plusieurs modèles analytiques ont été développés pour déterminer le module d'Young de chaque couche [Cho 1999, López-Puerto 2014] en se basant sur la théorie de rigidité en flexion d'une poutre revêtue (FRCB) ou bien sur la théorie classique des poutres stratifiées (CLBT).

A notre connaissance, aucune étude n'a été faite pour déterminer le module de cisaillement de chaque couche dans un revêtement multicouche. De plus, un manque d'information concernant la détermination du module d'Young à l'aide de différents modes vibratoires mesurés par TEI nous motive à mener une étude approfondie sur le développement de nouveaux modèles qui permettent la détermination des constantes d'élasticité de chaque couche dans un revêtement multicouche.

L'objectif de ce chapitre est d'améliorer les études précédentes en développant de nouveaux modèles permettant la détermination du module d'Young et du module de cisaillement des couches quelle que soit l'épaisseur et les propriétés mécaniques et physiques du substrat et des couches déposées. En vue de guider notre choix de modèle pour déduire les constantes d'élasticité d'un revêtement, nous procéderons de la manière suivante : Premièrement, une représentation des modèles mécaniques existants dans la littérature sera faite pour la détermination de modules d'Young et de cisaillement d'une couche mince. Deuxièmement, des nouveaux modèles seront développés pour la détermination des constantes d'élasticité de chaque couche dans un revêtement multicouche. Troisièmement, une comparaison sera faite entre les modèles analytiques de la littérature, les modèles développés et un modèle éléments finis (MEF) qui sera développé dans ce deuxième chapitre. Cette comparaison permettra d'identifier le modèle le plus fiable parmi les modèles existants dans la littérature et ceux développés en prenant comme référence le MEF.

En se basant sur la théorie des vibrations des poutres classiques d'Euler-Bernoulli qui ne prend pas en compte les effets de cisaillement et d'inertie, l'équation du mouvement d'une poutre soumise à des vibrations en flexion s'écrit comme suit [Rao 2006] :

$$\rho S \frac{\partial^2 w(x,t)}{\partial t^2} + \frac{\partial^2}{\partial x^2}\left(EI_y \frac{\partial^2 w(x,t)}{\partial x^2}\right) = 0 \quad \text{(II.1)}$$

Avec ρ la masse volumique, $w(x,t)$ le déplacement d'un point quelconque appartenant à la structure excite en fonction de sa position et du temps, E le module d'Young, I_y le moment quadratique par rapport à l'axe z de la section droite et S l'aire de la section.

La résolution de cette équation différentielle (équation (II.1)) permet de déterminer les fréquences de résonance $F^{(n)}$ de la structure excitée. Dans le cas de la TEI, les conditions aux limites « libre-libre » sont généralement adoptées. Une solution analytique de l'équation du mouvement peut être déterminée [Rao 2006] :

$$F^{(n)} = \frac{X_n^2}{2\pi L^2}\sqrt{\frac{EI_y}{\rho S}} \quad \text{(II.2)}$$

Avec L la longueur de l'échantillon, n l'ordre du mode de vibration, et X_n la fréquence adimensionnelle qui dépend des conditions aux limites et de l'ordre du mode de vibration. Dans le cas d'une poutre de section rectangulaire, le module d'Young peut être déterminé à partir de la formule suivante [ASTM 2015] :

$$E = k_1 \rho \frac{L^4}{h^2} T_f \left(F^{(1)}\right)^2 \quad \text{(II.3)}$$

Avec $k_1 \approx 0.9465$, $F^{(1)}$ la fréquence fondamentale de résonance de flexion, h l'épaisseur de la poutre et T_f un facteur de correction introduit pour corriger les effets d'inertie et de cisaillement non pris en compte par la théorie d'Euler-Bernoulli.

Par la suite, une poutre composite (substrat + couche) de section rectangulaire sera considérée. Le principe de la mesure est de faire deux mesures de fréquence : une première du substrat nu sans revêtement et une deuxième du substrat revêtu. Puis à l'aide d'un modèle mécanique qui fait intervenir le rapport des deux fréquences, le module d'Young du substrat, la densité du substrat et du dépôt et leurs dimensions on peut remonter au module d'Young de la couche déposée. Les modèles mécaniques existants dans la littérature se basent sur deux différentes théories : modèles basés sur la rigidité en flexion d'une poutre composite (FRCB) et modèles basés sur la théorie classique des poutres stratifiées (CLBT).

La rigidité en flexion d'une poutre composite peut être exprimée comme la somme des rigidités en flexion de chaque matériau (équation (II.4)) [Gere 2003]. La masse volumique multipliée par unité de surface d'une poutre composite peut être exprimée à l'aide de l'équation (II.5) [Gere 2003] :

$$E_t I_t = \sum_{k=0}^{N} E_k I_k \tag{II.4}$$

$$\rho_t S_t = \sum_{k=0}^{N} \rho_k S_k \tag{II.5}$$

Avec les indices *"0"*, *"k"*, *"t"* and *"N"* correspondent respectivement au substrat, à la $k^{\text{ième}}$ couche, à la poutre composite et le nombre total de couches. En substituant les équations (II.4) et (II.5) dans l'équation (II.2), on obtient la fréquence de résonance de la poutre composite $F_N^{(n)}$:

$$F_N^{(n)} = \frac{X_n^2}{2\pi L^2}\sqrt{\frac{E_t I_t}{\rho_t S_t}} \tag{II.6}$$

Parmi les modèles analytiques existants dans la littérature, les modèles de Berry et Lopez [Berry 1975, Mazot 1998] supposent que la fibre neutre reste au centre du substrat et ne se décale pas après dépôt. Par contre, le modèle de Pautrot [Whiting 1995, Mazot 1998, Gadaud 2004] prend en compte le décalage de la fibre neutre après dépôt (Figure II.1).

a) b)

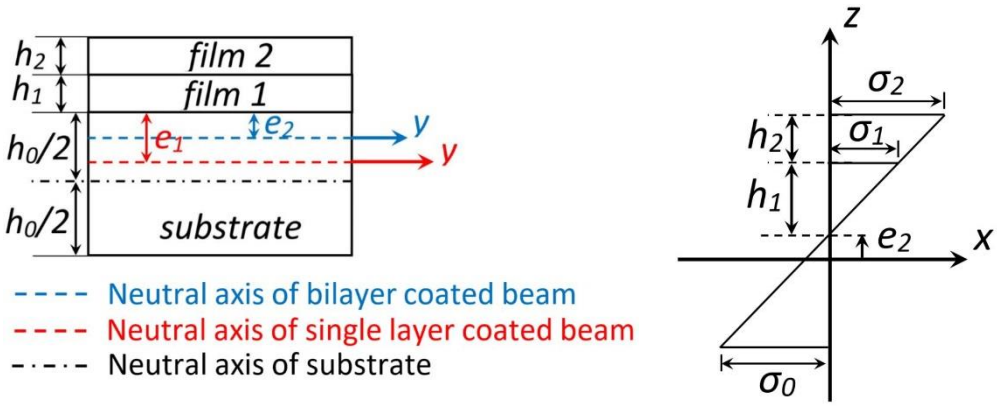

Figure II.1. Représentation schématique du décalage de la fibre neutre a) vue de section, b) répartition de contraintes dans une poutre composée d'un substrat et de deux couches.

Le modèle basé sur la théorie classique des poutres stratifiées (CLBT : Classical Laminated Beam Theory) suppose que la poutre est symétrique [López-Puerto 2014]. Cette hypothèse n'est pas respectée dans la plupart des cas où le film est déposé d'un seul côté du substrat. Cependant, il peut être utilisé comme approximation dans le cas d'une poutre revêtue d'un seul côté. Par ailleurs, plus le rapport des modules et le rapport des épaisseurs augmentent

plus l'erreur commise par ce modèle à cause de cette hypothèse augmente. Dans le cas d'une poutre soumise à des conditions aux limites « libre-libre », le rapport de fréquences en flexion $R_{F1} = \frac{F_1}{F_0}$ de la poutre stratifiée est exprimée comme suit [López-Puerto 2014] :

$$(R_{F1})^2 = \frac{12\rho_0}{E_0 h_0^2}\left(\frac{1}{d_{11}\,(\rho_0 h_0 + \rho_1 h_1)}\right) \tag{II.7}$$

Dans le cas d'une monocouche (substrat + dépôt) [López-Puerto 2014] :

$$d_{11} = \frac{\frac{E_0 K_0}{1-\nu_0^2} + \frac{E_1 K_1}{1-\nu_1^2}}{\left[\frac{E_0 K_0}{1-\nu_0^2} + \frac{E_1 K_1}{1-\nu_1^2}\right]^2 - \left[\frac{\nu_0 E_0 K_0}{1-\nu_0^2} + \frac{\nu_1 E_1 K_1}{1-\nu_1^2}\right]^2} \tag{II.8}$$

$$K_0 = \frac{h_0}{4}\left(\frac{h_0^2}{3} + h_1^2\right) \tag{II.9}$$

$$K_1 = \frac{h_1}{4}\left(\frac{h_1^2}{3} + h_0^2\right) \tag{II.10}$$

L'équation du mouvement de torsion pour des poutres de section rectangulaire a été développée par Timoshenko et Goodier [Timoshenko 1951] et Spinner et Tefft [Spinner 1961]. L'équation qui décrit le mouvement d'une poutre de section prismatique soumise à des vibrations de torsion s'écrit comme suit [Rao 2006] :

$$\begin{aligned}\rho I_p \frac{\partial^2\theta(x,t)}{\partial t^2} - \frac{\partial^2}{\partial t \partial x}\left(\rho I_\psi \frac{\partial^2\theta(x,t)}{\partial x \partial t}\right) - \frac{\partial}{\partial x}\left(C\frac{\partial\theta(x,t)}{\partial x}\right) \\ + \frac{\partial^2}{\partial x^2}\left(EI_\psi \frac{\partial^2\theta(x,t)}{\partial x^2}\right) = 0\end{aligned} \tag{II.11}$$

Avec ρ la masse volumique, $\theta(x,t)$ l'angle de torsion qui dépend de la position x et du temps t, $I_p = \frac{hb^3+bh^3}{12}$ le moment polaire de la section (avec h l'épaisseur et b la largeur), C la rigidité de torsion d'une section non circulaire et $I_\psi = \iint \psi(y,z)^2 dS$ avec $\psi(y,z)$ une fonction décrivant le gauchissement de la section de la poutre. La rigidité de torsion d'une section rectangulaire est définie comme suit :

$$C = \iint_S G\left[\left(\frac{\partial\psi}{\partial y} - z\right)^2 + \left(\frac{\partial\psi}{\partial z} + y\right)^2\right] dS \tag{II.12}$$

Avec G le module du cisaillement.

Dans le cas d'une poutre de section prismatique soumise à des conditions aux limites « libre-libre », le module de cisaillement peut être déterminé à l'aide de la relation suivante [ASTM 2015] :

$$G = 4\rho R L^2 T^2 \tag{II.13}$$

Avec T la fréquence fondamentale de résonance de torsion de la structure excitée, L sa longueur et R un facteur de correction prenant en compte le gauchissement de la section.

En se basant sur le principe de Hamilton [Berdichevsky 2009] qui consiste à minimiser le Lagrangien du système qui est exprimé en fonction de l'énergie potentielle et l'énergie cinétique de la structure en vibration (substrat + dépôt), Gadaud et al. [Gadaud 2009] ont développé un modèle analytique qui permet de déterminer le module de cisaillement d'un film déposé sur une poutre de section rectangulaire. Le modèle de Gadaud ne prend pas en compte le décalage de la fibre neutre après dépôt (Figure II.1). Plus le rapport des épaisseurs, le rapport des densités et les rapports des modules augmentent plus l'erreur commise en utilisant ce modèle augmente à cause de cette hypothèse. Slim et al. [Slim 2017b] ont développé un nouveau modèle analytique qui prend en compte le décalage de la fibre neutre. Par application du principe de Hamilton au Lagrangien, le rapport de fréquences en torsion $R_{T1} = \frac{T_1}{T_0}$ peut s'écrire comme suit :

$$R_{T1} = \left[\frac{\rho_0\, b\, (h_0^2 + b^2)}{3\, G_0\, h_0^2 \left(b - \frac{h_0}{\sqrt{3}} \tanh\left[\frac{\sqrt{3}\, b}{h_0}\right]\right)}\right]^{0.5} \left[\frac{\left[A\left(3bCH_3(h_0E_0 + h_1\, E_1) - H_4\sqrt{3A}\right)\right]}{\left[\left(bCH_3(h_0E_0 + h_1E_1)(H_1\rho_0h_0 + H_2\rho_1h_1)\right)\right]}\right]^{0.5} \tag{II.14}$$

$$\begin{aligned} A = {} & E_0^2 h_0^5 G_0 + E_1^2 h_1^5 G_1 + E_0 h_0^4 h_1 (2E_1 G_0 + 3E_0 G_1) + E_1 h_0 h_1^4 (2E_0 G_1 + 3E_1 G_0) \\ & + 2h_0^3 h_1^2 (3E_0^2 G_1 + 2E_1^2 G_0) + 2h_0^2 h_1^3 (2E_0^2 G_1 + 3E_1^2 G_0) \end{aligned} \tag{II.15}$$

$$B = 2\sqrt{3}\, b\, C\, (E_0\, h_0 + E_1\, h_1) \tag{II.16}$$

$$C = \sqrt{G_0\, h_0 + G_1\, h_1} \tag{II.17}$$

$$H_1 = 3h_0^3 E_0^2 (h_0 + 2h_1) + E_1 h_1 (b^2 + h_1^2)(2h_0 E_0 + E_1 h_1) + E_0^2 h_0^2 (b^2 + 4h_1^2) \tag{II.18}$$

$$H_2 = 3h_1^3 E_1^2 (h_1 + 2h_0) + E_0 h_0 (b^2 + h_0^2)(2h_1 E_1 + E_0 h_0) + E_1^2 h_1^2 (b^2 + 4h_0^2) \tag{II.19}$$

$$H_3 = \frac{B}{e^{\sqrt{A}} + 1} \tag{II.20}$$

$$H_4 = \frac{B}{e^{\sqrt{A}} - 1} \tag{II.21}$$

Comme le modèle de Pautrot est déjà validé dans la littérature [Slim 2017a] pour la détermination du module d'Young d'une seule couche en prenant en compte le décalage de la fibre neutre, on a développé un nouveau modèle noté « Ext-PM » qui est basé sur la théorie FRCB afin de l'utiliser pour des structures multicouches. En appliquant l'équilibre statique des forces axiales d'une poutre en flexion pure, le décalage de la fibre neutre généralisé pour des structures à N couches, peut s'écrire comme suit :

$$e_N = \frac{E_0 h_0^2 - \sum_{i=1}^{N} E_i h_i \left[h_i + 2\delta_i \sum_{j=2}^{i} h_{j-1}\right]}{2\sum_{i=0}^{N} E_i h_i} \tag{II.22}$$

$$\delta_k = \begin{cases} 0 & if\ k = 1 \\ 1 & if\ k \neq 1 \end{cases} \quad (k = 1, \dots, N) \tag{II.23}$$

En développant l'équation (II.6) pour une structure composée d'un substrat et de deux couches (N = 2) avec un décalage e_2, on obtient l'expression du rapport des fréquences R_{F2} en flexion :

$$(R_{F2})^2 = \frac{1 + (R_{h1}^2 R_{E1})^2 + (R_{h2}^2 R_{E2})^2 + 2X_1 R_{E1} R_{h1} + 2X_2 R_{E2} R_{h2}}{(1 + R_{h1} R_{\rho 1} + R_{h2} R_{\rho 2})(1 + R_{E1} R_{h1} + R_{E2} R_{h2})} \tag{II.24}$$

$$R_{hi} = \frac{h_i}{h_0}\ ;\ R_{\rho i} = \frac{\rho_i}{\rho_0}\ ;\ R_{Ei} = \frac{E_i}{E_0}\ ;\ R_{F2} = \frac{F_2}{F_0} \tag{II.25}$$

$$X_1 = 2 + 6R_{h1}(R_{h1} + R_{h2} + 1) + R_{h2}(3 + 2R_{h2}) \tag{II.26}$$

$$X_2 = R_{E2} R_{h2}(2R_{h1}^2 + 3R_{h1} R_{h2} + 2R_{h2}^2) + 2R_{h1}^2 + 3R_{h1} + 2 \tag{II.27}$$

En inversant l'équation (II.24), le module d'Young de la deuxième couche E_2 est déterminé en fonction du module d'Young du substrat E_0 et celui de la première couche E_1, l'épaisseur et la densité du substrat et des deux couches.

Comme dans le case d'une seule couche, le modèle CLBT peut être utilisé pour déterminer le module d'Young de la $k^{\text{ième}}$ couche E_k si les modules d'Young des (k-1)$^{\text{ième}}$, (k-2)$^{\text{ième}}$, … et 1$^{\text{ère}}$ couches sont connus. Par contre, ce modèle ne prend pas en compte le décalage de la fibre neutre. Le nouveau modèle noté « Dev-CLBT » est développé en introduisant ce décalage dans l'expression de la matrice de rigidité en flexion comme suit :

$$D'_{ij} = \int_{-h_0+e_N}^{e_N} \bar{Q}_{ij}^{(0)} z^2 dz + \sum_{k=1}^{N} \int_{Z_1}^{Z_2} \bar{Q}_{ij}^{(k)} z^2 dz \qquad (i, j = 1, 2\ or\ 6) \tag{II.28}$$

$$Z_1 = e_N + \delta_k \sum_{j=1}^{k-1} h_j \qquad Z_2 = Z_1 + h_k \tag{II.29}$$

$$\bar{Q}_{11}^{(k)} = \bar{Q}_{22}^{(k)} = Q_{11}^{(k)} = Q_{22}^{(k)} = \frac{E_k}{1-(\nu_k)^2} \tag{II.30}$$

$$\bar{Q}_{12}^{(k)} = Q_{12}^{(k)} = \frac{\nu_k E_k}{1-(\nu_k)^2} \tag{II.31}$$

$$\bar{Q}_{16}^{(k)} = \bar{Q}_{26}^{(k)} = 0\,;\ \bar{Q}_{66}^{(k)} = Q_{66}^{(k)} = \frac{E_k}{2\,(1+\nu_k)} \tag{II.32}$$

Le moment fléchissant par unité de largeur M_y qui produit un déplacement $w(x,t)$ peut s'écrire comme suit [Hyer 2009]:

$$M_y = -\frac{1}{d_{11}^N}\frac{\partial^2 w}{\partial x^2} \tag{II.33}$$

$$d_{11}^{(N)} = \frac{D_{22}}{det[D]}\ ;\ det[D] = D_{11}D_{22} - D_{12}^2 \tag{II.34}$$

Selon la théorie CLBT, une poutre stratifiée en vibration soumise à un moment fléchissant M_y peut s'exprimer comme suit :

$$\frac{\partial^2 M_y}{\partial x^2} = \rho_{eff}^{(N)}\frac{\partial^2 w}{\partial t^2} \tag{II.35}$$

Avec :

$$\rho_{eff}^{(N)} = \int_{-(\sum_{k=0}^{N} h_k)/2}^{(\sum_{k=0}^{N} h_k)/2} \rho_k dz = \sum_{k=0}^{N} \rho_k h_k \tag{II.36}$$

En substituant l'équation (II.33) dans l'équation (II.35), on obtient l'équation différentielle de vibration pour une poutre stratifiée :

$$\frac{1}{d_{11}^{(N)}\rho_{eff}^{(N)}}\frac{\partial^4 w}{\partial x^4} + \frac{\partial^2 w}{\partial t^2} = 0 \tag{II.37}$$

La résolution de cette équation différentielle permet de déterminer les fréquences de résonance $F_N^{(n)}$ de la structure excitée et par suite le rapport des fréquences :

$$\left(R_{F(N)}\right)^2 = \frac{12\rho_0}{E_0 h_0^2}\left(\frac{1}{d_{11}^{(N)}\rho_{eff}^{(N)}}\right) \tag{II.38}$$

Concernant la détermination du module de cisaillement, le principe de Hamilton peut être appliqué pour une poutre qui présente multicouches en étendant le modèle de Slim [Slim 2017b]. La fréquence de résonance en torsion est donc déterminée et exprimée pour $N = 2$ comme suit :

$$T_2 = \frac{1}{2\sqrt{3}\,L}\operatorname{sech}\left[\frac{B'}{2\sqrt{A'}}\right]\frac{A'(B')^2}{B'(bC')^2(E_t h_t)}\left[\frac{B' + B'\cosh\left[\frac{B'}{\sqrt{A'}}\right] - 2\sqrt{A'}\sinh\left[\frac{B'}{\sqrt{A'}}\right]}{(H'_1\rho_1 + H'_2\rho_2 - H'_3\rho_0) + 2b^2(\rho_t h_t)(E_t h_t)^3}\right]^{0.5} \tag{II.39}$$

$$E_t h_t = \sum_{k=0}^{N} E_k h_k \;;\; \rho_t h_t = \sum_{k=0}^{N} \rho_k h_k \tag{II.40}$$

Les valeurs de A', B', C', H'_1, H'_2 et H'_3 se trouvent dans Chapter II (version anglaise). Le rapport des fréquences en torsion devient :

$$R_{T2} = T_2\sqrt{\frac{\rho_0}{G_0}}\left[\frac{12\,h_0^2\left(b - \frac{h_0\tanh\left[\frac{\sqrt{3}b}{h_0}\right]}{\sqrt{3}}\right)}{b(h_0^2 + b^2)}\right]^{-0.5} \tag{II.41}$$

Les différents modèles analytiques proposés dans la littérature et les nouveaux modèles développés dans ce chapitre sont présentés dans le Tableau II.1.

Tableau II.1
Synthèse de la bibliographie des différents modèles analytiques.

Modèle	Théorie	Nb. of couches	Hypothèses
Lopez [Mazot 1998]	FRCB	Une seule couche	Isotropie
Berry [Berry 1975]	FRCB	Une seule couche	Modèle de Lopez simplifié
Pautrot [Gadaud 2004]	FRCB	Une seule couche	Isotropie et décalage
Whiting [Whiting 1995]	FRCB	Une seule couche	Modèle de Pautrot simplifié
CLBT [López-Puerto 2014]	CLBT	Multicouche	Symétrie et Anisotropie
Nouveau modèle (Ext-PM)	FRCB	Multicouche	Isotropie et décalage
Nouveau modèle (Dev-CLBT)	CLBT	Multicouche	Symétrie, Anisotropie et décalage
Gadaud [Gadaud 2009]	Hamilton	Une seule couche	Isotropie
Slim [Slim 2017b]	Hamilton	Une seule couche	Isotropie et décalage
Nouveau modèle (Ext-Slim)	Hamilton	Multicouche	Isotropie et décalage

La variété des choix faits par les auteurs et le manque d'information sur le domaine de validité de chaque modèle ne permettent pas d'avoir une vision globale de la technique. Afin de vérifier la fiabilité des différentes formulations développées et d'identifier le modèle le plus adapté, une comparaison paramétrique entre les expressions analytiques et un MEF est faite. Le modèle MEF a été développé à l'aide du logiciel de simulation numérique ABAQUS 6.13 [Abaqus 2016]. Le modèle géométrique est composé de deux parties : le substrat et le dépôt. Le substrat est une poutre de section rectangulaire avec une longueur $L = 70\ mm$, une largeur $b = 20mm$ et une épaisseur $h_0 = 0.5\ mm$. Deux différents MEF ont été développés pour une ($N = 1$) et deux couches ($N = 2$) sur le substrat. Afin d'assembler les couches l'une sur l'autre et sur le substrat, la fonction Tie d'Abaqus a été utilisée. Les conditions aux limites « libre-libre » ont été appliquées aux deux poutres composites. Le modèle géométrique a été maillé en utilisant l'élément quadratique C3D20. Le solveur Lanczos du module ABAQUS\Implicit a été utilisé pour extraire les fréquences de résonance de la poutre composite.

D'après la comparaison paramétrique, on a trouvé que les modèles les plus en accord avec les résultats obtenus par éléments finis pour la détermination du module d'Young sont ceux de Ext-PM et de Dev-CLBT. L'accord entre ces nouveaux modèles permet de confirmer la validité de l'hypothèse du décalage de la fibre neutre après dépôt sur laquelle sont fondés ces modèles et de négliger au moins dans le cas de la présente étude les effets de cisaillement et d'inertie (qui sont pris en compte par le MEF). De plus, L'accord entre le nouveau modèle Dev-CLBT et celui MEF montre que l'effet de symétrie sur lequel est basée la théorie CLBT devient négligeable en prenant en compte le décalage de la fibre neutre. D'autre part, le nouveau modèle

Ext-Slim développé pour la détermination du module de cisaillement a été comparé avec un MEF. Un accord entre le MEF et le nouveau modèle nous a permis de le valider sur un large domaine de paramètres plausibles. Dans le chapitre qui suit, ces nouveaux modèles seront appliqués à des multicouches de titane et de niobium déposées par pulvérisation cathodique magnétron.

Chapitre III Mesures expérimentales des constantes d'élasticité des multicouches en utilisant la technique d'excitation impulsionnelle

Après avoir développé des nouveaux modèles qui permettent de déterminer les modules d'élasticité des multicouches, ce chapitre présente l'application expérimentale de ces modèles mécaniques à des multicouches élaborées par pulvérisation cathodique magnétron. Les modèles Ext-PM, Dev-CLBT et Ext-Slim ont été appliqués pour déterminer le module d'Young et le module de cisaillement des multicouches de titane pur et de niobium pur élaborées par pulvérisation cathodique magnétron. Une étude d'incertitude conforme aux recommandations de la norme ISO du Guide pour l'Expression de l'Incertitude de Mesure [JCGM 2008] est faite. La méthodologie d'évaluation des incertitudes de mesure a été développée sur les multicouches de titane pur et de niobium pur élaborées. La morphologie et la structure de chaque couche déposée ont été analysées. Les constantes d'élasticité de chaque couche, sa morphologie et sa structure ont été corrélées. Une comparaison entre les modules réduits déterminés par TEI et par nanoindentation (NI) a été faite.

La technique de dépôt utilisée durant cette thèse est la pulvérisation cathodique magnétron. C'est une technique d'élaboration de couches minces sous basse pression. Les couches de titane et de niobium ont été déposées, à température flottante, par pulvérisation cathodique magnétron, sur des substrats d'acier 316L (échantillon 1), de verre (échantillon 2) et de silicium (Si) par pulvérisation cathodique magnétron en mode continu (DC). Une machine PVD « DEPHIS4 » a été utilisée constituant une enceinte d'un diamètre de 600 *mm* et de 400 *mm* de hauteur. Avant la phase de pulvérisation, un vide de l'ordre de 10^{-4} *Pa* a été créé à l'intérieur de l'enceinte grâce à un système de pompage constitué d'une pompe primaire et une pompe secondaire turbomoléculaire. Après pompage, l'enceinte est remplie d'argon envoyé avec un débit constant égal à 50 *sccm* (sccm : débit volumique de gaz à des conditions standard de température et de pression exprimé en cm^3/min) ce qui ramène la pression dans l'enceinte à une pression égale à 0.2 *Pa*. À l'aide d'un générateur continu pulsé, une décharge d'intensité de 3 *A* a été appliquée sur une cible ayant un diamètre de 200 *mm* et une épaisseur de 6 *mm* (soit le titane comme première couche ou le niobium comme deuxième couche). Afin d'assurer l'homogénéité du dépôt, le porte substrat a été animé en rotation (10 *rpm*) tout en fixant une distance entre les substrats et la cible de l'ordre de 10 cm. Avant d'être mis dans l'enceinte, les substrats ont été nettoyés à l'acétone puis à l'éthanol et séchés à l'air chaud. Sous ces conditions, la vitesse de croissance obtenue sur les dépôts est égale à 16.13 *nm/min* pour la couche de Ti et 18.90 *nm/min* pour la couche de Nb. Les substrats d'acier et de verre ont été utilisés pour les

caractérisations par la TEI, la DRX et la nanoindentation. Les substrats de Si ont été utilisés pour l'imagerie MEB.

La TEI consiste à placer un échantillon sur un support lui permettant de vibrer sans contrainte. L'échantillon est excité, par un coup léger, à l'aide d'un outil d'excitation automatique ou manuelle. Ensuite, on enregistre le signal généré par cette excitation qui est détecté à l'aide d'un microphone ou un transducteur. Ce signal est par la suite analysé afin d'en extraire les fréquences de résonance par transformée de Fourier rapide. Le dispositif expérimental de la TEI est équipé d'un transducteur RFDA, une unité d'excitation automatique, un microphone capable de détecter des fréquences de l'ordre de 100 kHz, un support universel et un ordinateur équipé du logiciel RFDA (Figure III.1). Les mesures de fréquences de résonance ont été faites à l'aide d'un système d'analyse de signal professionnel RFDA (Resonance Frequency and Damping Analysis) construit par l'entreprise IMCE (Genk, Belgique).

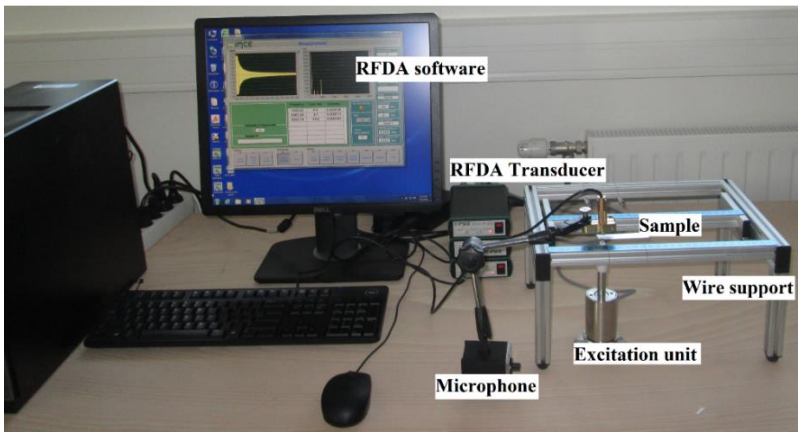

Figure III.1. Dispositif expérimental utilisé pour la TEI.

Avant de lancer l'essai, l'échantillon est placé sur un support au niveau des nœuds naturels de vibration d'une poutre soumise à des conditions aux limites « libre-libre ». Le support doit servir à maintenir et à isoler l'échantillon des vibrations extérieures sans influencer les modes de vibration recherchés. Le matériau du support peut être rigide ou souple. La position des nœuds dépend du mode vibratoire désiré. Enfin, les fréquences de résonance sont utilisées pour déterminer le module d'Young E, le module de cisaillement G et le coefficient de Poisson ν à l'aide des modèles mécaniques développés précédemment. Des explications plus détaillées de la procédure peuvent être trouvées dans la littérature [ASTM 2015].

La fréquence de résonance fondamentale du substrat nu (Acier inoxydable 316L), du substrat revêtu d'une première couche (316L + dépôt de Ti) et du substrat revêtu d'une deuxième couche (316L + dépôt de Ti + dépôt de Nb) est présentée dans la Figure III.2. Elle a été mesurée à l'aide du dispositif présenté sur la Figure III.1. Les mesures vibratoires ont été menées séquentiellement : avant dépôt, les fréquences de résonance du substrat nu ont été mesurées, puis la couche de titane a été déposée sur chaque substrat. Ensuite, les fréquences de résonance de chaque échantillon ont été mesurées. Enfin, la deuxième couche de niobium a été déposée sur l'ensemble (substrat + dépôt de Ti) et les fréquences de résonance de l'ensemble

multicouches (substrat + Ti + Nb) ont été mesurées. D'après la Figure III.2, on peut voir que la fréquence fondamentale est décalée après chaque dépôt. Ces décalages de fréquence ont été utilisés pour calculer le module d'Young et le module de cisaillement à l'aide des nouveaux modèles mécaniques développés.

La fréquence fondamentale de résonance du substrat a été utilisée pour déterminer le module d'Young du substrat à l'aide de l'équation (II.3) et le rapport des deux fréquences a été utilisé pour déterminer le module d'Young des dépôts de titane et de niobium à l'aide des équations (II.6) et (II.38).

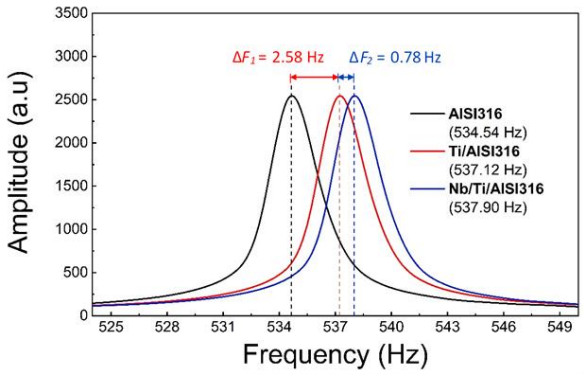

Figure III.2. Fréquences fondamentales de résonance avant et après dépôts.

Le module réduit a été obtenu à l'aide d'un nanoindenteur TI 980-Hysitron. Le nanoindenteur est équipé d'un système CSM (Continuous Stiffness Measurment) permettant de mesurer en continu la raideur de contact en fonction de la profondeur de pénétration. Une pointe Berkovich de module d'élasticité $E_{ind} = 1140\ GPa$ et de coefficient de Poisson $\nu_{ind} = 0.07$ a été utilisée pour les mesures. La moyenne de dix indents a été utilisée pour déterminer le module réduit des couches de Ti et de Nb. Les essais ont été réalisés sous charge contrôlée. Afin de limiter l'effet du substrat, les essais ont été réalisés à une profondeur de pénétration inférieure à 10% de l'épaisseur de la couche déposée [Buckle 1960].

L'analyse structurale des couches déposées a été réalisée à l'aide d'un diffractomètre à rayons X, Bruker D8 Advance, équipé d'une anticathode de cuivre délivrant un rayonnement de longueur d'onde $\lambda = 0.15418\ nm$. Afin de déterminer la structure de chaque couche, des acquisitions sous différents angles d'inclinaison Ψ ont été réalisées dans le but de faire diffracter la plupart des plans cristallographiques. Les données ont été collectées avec un angle de diffraction 2θ qui varie entre 20° et 150°. L'analyse des diffractogrammes a été réalisée à l'aide du logiciel DIFFRAC.EVA.

L'analyse d'incertitude a été effectuée en se basant sur la méthodologie référencée dans les documents de métrologie : le Guide pour l'expression de l'incertitude de mesure (GUM) (Guide to the expression of Uncertainty in Measurment) [JCGM 2008] et la norme de vocabulaire international de métrologie [JCGM 2012]. Dans cette étude, l'incertitude liée à la fréquence quantifiée expérimentalement en étudiant sa répétabilité et d'autres facteurs a été prise de la littérature [Slim 2017a]. Toutes les incertitudes liées aux différentes grandeurs

apparentes dans l'équation (II.3) ont été explicitées. Les incertitudes globales du module d'Young et du module de cisaillement du substrat et des couches ont été calculées à l'aide de l'équation de propagation d'incertitude donnée dans le GUM [JCGM 2008] ou de la méthode de Monte Carlo en générant une dispersion aléatoire sur les valeurs expérimentales.

La morphologie des multicouches a été observée à l'aide d'un microscope électronique Hitachi S3500 SEM-FEG. Une épaisseur régulière des couches peut être observée tout au long de la section (Figure III.3). En plus, la Figure III.3 montre que les deux couches déposées présentent une croissance colonnaire favorisant la formation de pores entre les colonnes. Les analyses de diffraction par rayons X révèlent la présence de deux phases dans la couche de titane : une phase stable de structure hexagonale compacte Ti_{α} et une phase métastable de structure cubique centré Ti_{β}. Par contre, l'analyse structurale de la couche de niobium montre la présence d'une seule phase stable de structure cubique centrée Nb_{α}. La présence de la phase métastable dans la couche de Ti peut être due aux paramètres d'élaboration [Bunshah 1973, Savaloni 2004, Chawla 2008, Chawla 2009, Achache 2016] ou à la formation des phases d'oxydes dues à la présence de quelques traces de gaz résiduelles durant le dépôt [Vijaya 1996].

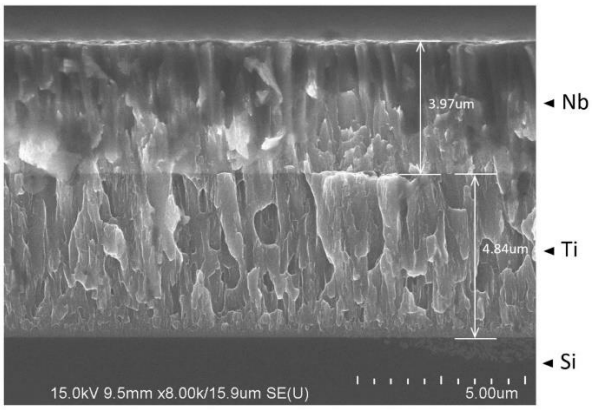

Figure III.3. Image MEB de la section transversale du revêtement multicouches Nb/Ti/Si.

Les valeurs de module d'Young de la couche de titane varient entre 97 *GPa* et 112 *GPa*. Les valeurs rapportées dans la littérature sont très dispersées. Les valeurs calculées dans cette étude sont cohérentes avec certains d'entre eux [Chinmulgund 1995, Tsuchiya 2005, Verkhovtsev 2013] et diffèrent de quelques autres [Kim 1997, Cho 1999]. Les différences peuvent être expliquées par les caractéristiques microstructurales telles que les proportions de phase [Slim 2019], la présence de pores ou par le processus lui-même comme dans la référence [Peraud 1997] où les ions sont implantés dans la structure cristalline pendant le dépôt. Les valeurs de module d'Young de la couche de niobium varient entre 77 *GPa* et 92 *GPa*. Ces valeurs sont proches de celles rapportées dans des études précédentes pour une seule couche de niobium [Seifried 2018, Xu 2019] et sont inférieures à celles données dans d'autres études [Okolo 2004, Czichos 2014]. Cela peut également être dû soit à la présence de pores dans le film, soit à la superposition de différents matériaux qui peuvent faire basculer les résultats et la prédiction du module d'Young d'une couche mince dans une structure multicouche. Une analyse de la fréquence de résonance en fonction du coefficient de Poisson a montré que l'influence de ce dernier sur la détermination du module d'Young en flexion est négligeable

pour les deux modèles Ext-PM et Dev-CLBT. Par suite, les deux modèles peuvent être utilisés pour déterminer le module d'Young d'une couche mince dans une structure multicouche en tenant compte des différentes sources d'incertitude.

Les modules de cisaillement ont été déterminés à l'aide des modèles de Slim (pour la première couche de Ti) et de Ext-Slim (pour la deuxième couche de Nb). Le module de cisaillement de la couche de Ti est égal à 42.84 *GPa* ($\pm$ 1.02 *GPa*) et celui de la couche de Nb est égal à 35.17 ($\pm$ 5.74 *GPa*). La différence entre les modules de cisaillement des deux échantillons (316L et verre) mesurés par TEI est attribuée à l'incertitude de mesure. En supposant que les couches admettent un comportement isotrope et en utilisant le module d'Young et le module de cisaillement déterminés à partir de la TEI, le coefficient de Poisson a été calculé. Le coefficient de Poisson est égal à 0.228 ($\pm$ 0.062) et 0.273 ($\pm$ 0.139) pour les couches de Ti et de Nb respectivement. Une différence entre les valeurs mesurées du coefficient de Poisson et les valeurs trouvées dans la littérature [Brandes 1992, Donachie 2000, Okolo 2004, Zhang 2007] a été observée. Cette différence peut être attribuée à l'incertitude de mesure sur les deux modules. Pour les couches de titane et de niobium, une légère diminution du coefficient de Poisson a été observée par rapport au matériau nu correspondant. L'incertitude de mesure du coefficient de Poisson de la deuxième couche de Nb augmente à cause de l'effet cumulatif des incertitudes du substrat et de la couche de Ti.

Afin de comparer les deux techniques (TEI et NI), une comparaison entre les modules réduits déterminés à l'aide des deux techniques a été faite. Les résultats montrent un module d'Young de 107.26 *GPa* et 87.55 *GPa* par NI et de 105.28 *GPa* et 82.64 *GPa* par TEI pour les couches de Ti et de Nb respectivement. La différence entre les modules d'Young des couches de Ti et de Nb mesurés par NI et TEI est inférieure à l'incertitude de mesure. La faible variation observée entre les valeurs peut être due à la différence de volume analysé par les deux techniques. Le module réduit mesuré par NI dépend des modules parallèles et perpendiculaires à la surface de la couche tandis que le module mesuré par TEI est celui parallèle à la surface de la couche selon l'axe x. Cet argument n'est valable que si les couches présentent une certaine anisotropie liée à sa texture cristalline. Ces questions de texture et d'anisotropie seront analysées en détail au chapitre qui suit. De plus, même si les essais de NI ont été réalisés à une profondeur de pénétration contrôlée inférieure à 10% de l'épaisseur de la couche, les résultats restent influencés par l'interaction élastique entre le substrat et la couche.

Dans le chapitre qui suit, une deuxième étape qui permet la détermination des constantes d'élasticité macroscopiques d'une couche mince anisotrope, sera décrite. L'étude sera étendue pour évaluer macroscopiquement le comportement anisotrope des couches minces. Par rapport à Ext-PM, le modèle Dev-CLBT peut prendre en compte l'anisotropie et va nous permettre de développer la technique vibratoire (TEI) afin de déterminer les modules anisotropes d'un revêtement dans différentes directions.

Chapitre IV Amélioration de la technique d'excitation impulsionnelle pour la détermination des constantes d'élasticité des couches minces déposées à incidence oblique

Comme nous l'avons vu dans le chapitre précédent, les mono ou multicouches élaborées par pulvérisation cathodique magnétron présentent souvent une anisotropie avec des propriétés différentes entre la direction perpendiculaire à la couche (l'axe z) et le plan de la couche (le plan x-y). Cette anisotropie peut être due à la texture cristalline ou bien à la morphologie des grains. En général, il n'y a presque pas une anisotropie dans le plan d'une couche déposée par un procédé PVD classique, du fait de la croissance selon la normale au plan de la couche. L'originalité de cette étude est d'introduire une anisotropie dans le plan de la couche en inclinant des substrats. Cette anisotropie élastique résulte intrinsèquement de la microstructure du film développée pendant le dépôt. Dans ce contexte, un nouveau type de revêtement présentant une large anisotropie, est traité dans ce chapitre dans lequel l'anisotropie de surface est la plus élevée. Dans le but de développer encore plus la technique d'excitation impulsionnelle, une méthodologie est développée. Elle permet de déterminer les constantes d'élasticité d'un revêtement admettant une anisotropie dans son plan en utilisant la TEI.

Tout d'abord, un nouveau modèle a été développé à partir du modèle Dev-CLBT (Eq. (II.38)) en prenant en compte des propriétés anisotropes de la couche. Ce modèle a été validé par comparaison avec un MEF pris comme une référence. Ensuite, le modèle développé a été appliqué pour déterminer les constantes d'élasticité des couches minces de titane élaborées par pulvérisation cathodique magnétron à une incidence oblique (GLAD : GLancing Angle Deposition). La morphologie et la structure des couches déposées ont été analysées et les constantes d'élasticité correspondantes ont été corrélées aux propriétés microstructurales. Cette technique présente une méthode simple pour concevoir diverses architectures colonnaires nanostructurées en utilisant des processus courants tels que la pulvérisation ou l'évaporation.

Le but du processus GLAD est de modifier la microstructure d'une couche en inclinant le substrat. Cette inclinaison permet de contrôler l'ombrage balistique et la croissance d'un film cristallisé durant le dépôt. L'effet balistique devient dominant dans un procédé GLAD étendant les longueurs totales d'ombre grâce à la géométrie oblique du dépôt. Une microstructure de film très poreuse est développée avec une croissance directionnelle des colonnes qui forment un angle β par rapport à la normale de la cible. Dans un procédé GLAD, le substrat est incliné d'un angle d'incidence α (Figure IV.1), créant ainsi une géométrie oblique du dépôt.

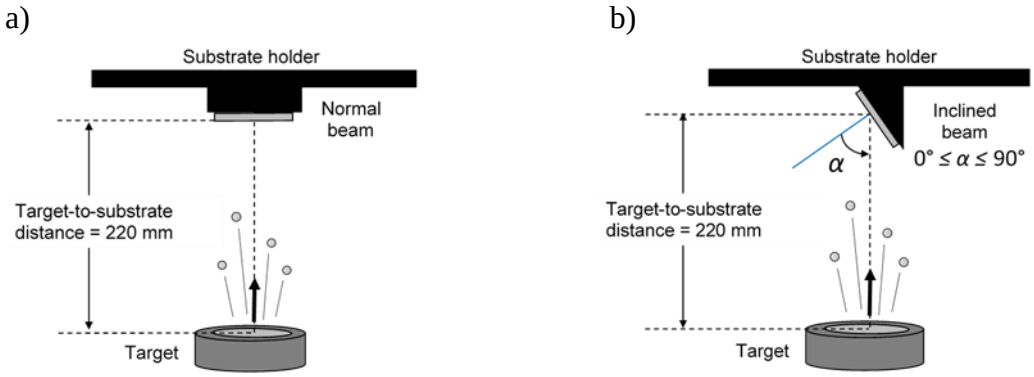

Figure IV.1. Représentation schématique des configurations PVD en : a) pulvérisation conventionnelle et b) pulvérisation à incidence oblique (GLAD).

Lorsque les atomes pulvérisés se condensent sur le substrat incliné, ils forment spontanément des noyaux microscopiques (Figure IV.2(a)). Les noyaux se développent en colonnes inclinées selon la direction de vapeur en raison de l'ombre balistique qui empêche la vapeur entrante de se condenser dans les régions situées derrière les noyaux (Figure IV.2(b)). Ces colonnes sont inclinées d'un angle β connu par l'angle des colonnes. Ces régions d'ombre créées sont ainsi élargies là où aucune croissance ne se produit.

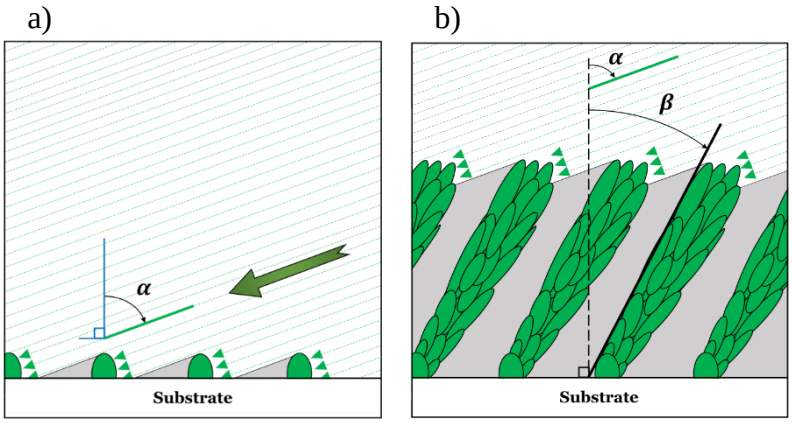

Figure IV.2. Le concept de la croissance d'un film dans le procédé GLAD. Les zones grises sont les régions d'ombre créées où aucune croissance ne se produit.

La théorie classique des poutres stratifiées (CLBT) considère que chaque couche est soumise à un état de contrainte plane. Dans notre cas, cette théorie peut être applicable à des couches minces admettant une anisotropie dans le plan. Cette hypothèse conduit à identifier les constantes d'élasticité selon deux directions perpendiculaires Δ et Π, définies dans la Figure IV.3, sur la surface du film.

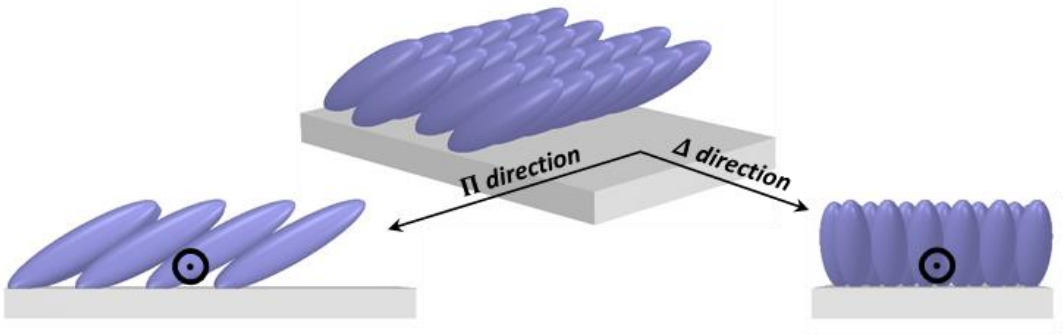

Figure IV.3. Représentation schématique des directions Δ et Π.

Dans ce chapitre, la méthodologie utilisée consiste à déposer différentes paires de revêtements à incidence oblique. L'axe x, défini comme la dimension longitudinale, (resp. l'axe y, défini comme la dimension transversale) du premier échantillon coïncide avec la direction Δ (resp. direction Π). L'inverse est plutôt appliqué au deuxième échantillon où l'axe x (resp. l'axe y) est parallèle à la direction Π (resp. direction Δ), pour obtenir des colonnes inclinées selon deux différentes directions avec un angle d'incidence α constant. De cette manière, chaque paire de poutres est soumise en vibration selon l'axe x conduisant à des mesures fréquentielles différentes. Après vibration, les fréquences de résonance mesurées par TEI sont utilisées avec un modèle 1D simplifié pour chaque paire de poutres afin de déterminer les propriétés élastiques dans chaque direction. Cette méthodologie nous permet de déterminer les constantes d'élasticité inconnues du film anisotrope à l'aide d'un modèle mécanique.

A partir de la relation entre contraintes et déformations pour un état de contrainte plane et en tenant compte du décalage de la fibre neutre après dépôt, la matrice de rigidité en flexion du troisième ordre D_{ij} est exprimée dans l'équation (II.28) avec $N = 1$. Le décalage est calculé en unidirectionnel tout en prenant la composante longitudinale du module d'Young pour chaque paire de poutres, comme suit:

$$\begin{pmatrix} e_x \\ e_y \end{pmatrix} = \frac{1}{2}\begin{pmatrix} \dfrac{E_s h_s^2 - E_x h_c^2}{(E_s h_s + E_x h_c)} \\ \dfrac{E_s h_s^2 - E_y h_c^2}{(E_s h_s + E_y h_c)} \end{pmatrix} \tag{IV.1}$$

Pour un film anisotrope, les éléments de rigidité deviennent :

$$\begin{pmatrix} \bar{Q}_{11}^{(x)} \\ \bar{Q}_{11}^{(y)} \end{pmatrix} = \begin{pmatrix} Q_{11}^{(x)} \\ Q_{11}^{(y)} \end{pmatrix} = \frac{1}{1 - \nu_{yx}\,\nu_{xy}} \begin{pmatrix} E_x \\ E_y \end{pmatrix} \tag{IV.2}$$

$$\begin{pmatrix} \bar{Q}_{22}^{(x)} \\ \bar{Q}_{22}^{(y)} \end{pmatrix} = \begin{pmatrix} Q_{22}^{(x)} \\ Q_{22}^{(y)} \end{pmatrix} = \frac{1}{1 - \nu_{yx}\,\nu_{xy}} \begin{pmatrix} E_y \\ E_x \end{pmatrix} \tag{IV.3}$$

$$\begin{pmatrix} \bar{Q}_{12}^{(x)} \\ \bar{Q}_{12}^{(y)} \end{pmatrix} = \begin{pmatrix} Q_{12}^{(x)} \\ Q_{12}^{(y)} \end{pmatrix} = \frac{\nu_{yx}}{1-\nu_{yx}\,\nu_{xy}} \begin{pmatrix} E_x \\ E_y \end{pmatrix} = \frac{\nu_{xy}}{1-\nu_{yx}\,\nu_{xy}} \begin{pmatrix} E_y \\ E_x \end{pmatrix} \tag{IV.4}$$

$$\bar{Q}_{66}^{(x)} = \bar{Q}_{66}^{(y)} = Q_{66}^{(x)} = Q_{66}^{(y)} = G_{xy} \tag{IV.5}$$

En utilisant le même développement que celui d'un film isotrope (Chapitre II), le rapport de fréquences de résonance devient :

$$\begin{pmatrix} R_{F_x} \\ R_{F_y} \end{pmatrix} = \frac{2}{h_s}\sqrt{\frac{3\rho_s}{E_s\,\rho_{eff}}} \begin{pmatrix} \frac{1}{\sqrt{d_{xx}}} \\ \frac{1}{\sqrt{d_{yy}}} \end{pmatrix} \tag{IV.6}$$

$$\begin{pmatrix} d_{xx} \\ d_{yy} \end{pmatrix} = \begin{pmatrix} \dfrac{\frac{R_x E_s}{1-\upsilon_s^2} + \frac{H_x\,E_y}{1-\nu_{yx}\nu_{xy}}}{\left[\frac{R_x\,E_s}{1-\upsilon_s^2} + \frac{H_x\,E_x}{1-\nu_{yx}\nu_{xy}}\right]\cdot\left[\frac{R_x\,E_s}{1-\upsilon_s^2} + \frac{H_x\,E_y}{1-\nu_{yx}\nu_{xy}}\right] - \left[\frac{\nu_s\,R_x\,E_s}{1-\upsilon_s^2} + \frac{\nu_{yx}\,H_x\,E_x}{1-\nu_{yx}\nu_{xy}}\right]^2} \\ \dfrac{\frac{R_y\,E_s}{1-\upsilon_s^2} + \frac{H_y\,E_x}{1-\nu_{yx}\nu_{xy}}}{\left[\frac{R_y\,E_s}{1-\upsilon_s^2} + \frac{H_y\,E_y}{1-\nu_{yx}\nu_{xy}}\right]\cdot\left[\frac{R_y\,E_s}{1-\upsilon_s^2} + \frac{H_y\,E_x}{1-\nu_{yx}\nu_{xy}}\right] - \left[\frac{\nu_s\,R_y\,E_s}{1-\upsilon_s^2} + \frac{\nu_{xy}\,H_y\,E_y}{1-\nu_{yx}\nu_{xy}}\right]^2} \end{pmatrix} \tag{IV.7}$$

$$\begin{pmatrix} R_x \\ R_y \end{pmatrix} = \frac{1}{3}\begin{pmatrix} e_x^3 - (-e_x + h_s)^3 \\ e_y^3 - (-e_y + h_s)^3 \end{pmatrix} \tag{IV.8}$$

$$\begin{pmatrix} H_x \\ H_y \end{pmatrix} = \frac{1}{3}\begin{pmatrix} -e_x^3 + (e_x + h_c)^3 \\ -e_y^3 + (e_y + h_c)^3 \end{pmatrix} \tag{IV.9}$$

Un modèle éléments finis (MEF) a été développé à l'aide du logiciel de simulation numérique ABAQUS 6.13 [Abaqus 2016] pour vérifier la fiabilité de la formulation développée. Une comparaison entre le modèle développé et le MEF a été réalisée. Le même principe d'assemblage et de maillage que celui utilisé au Chapitre II est appliqué ici. À partir d'une étude paramétrique des deux modèles analytique et numérique, on a remarqué un bon accord entre les résultats calculés et ceux obtenus par éléments finis pour un faible rapport d'épaisseur R_h. La différence entre les deux modèles augmente avec l'augmentation de R_h et plutôt avec l'augmentation du rapport d'anisotropie $AR_E = E_y/E_x$. Avec l'augmentation de AR_E, l'effet de couplage entre les directions augmente. Le modèle développé néglige le couplage avec la troisième direction (l'axe z) qui devient significatif du fait de l'augmentation d'épaisseur. La différence entre le modèle analytique et le MEF reste approximativement constante en augmentant le rapport d'anisotropie. Dans le reste de cette étude, des substrats en verre ont été utilisés et les constantes d'élasticité des couches minces de Ti ayant $R_h < 0.05$ ont été déterminées à l'aide du modèle développé (équation (IV.6)).

Après l'avoir validé pour un film ayant des propriétés élastiques anisotropes, le nouveau modèle a été appliqué expérimentalement à des couches de titane déposées par pulvérisation cathodique à incidence oblique (GLAD). L'élaboration a été faite pendant 180 *min* à une pression de 0.35 *Pa* et un débit d'argon de 30 *sccm*. Une décharge d'intensité de 1.5 *A* a été appliquée sur la cible de titane à l'aide d'un générateur continu pulsé. La distance entre les substrats et la cible était de l'ordre de 22 *cm*. Différents gabarits en aluminium, inclinés par rapport au porte substrat, ont été fabriqués pour faire varier l'angle d'incidence α des substrats. Seulement trois inclinaisons α = 0°, 45° et 80° ont été utilisées dans cette thèse. Ces trois angles d'incidence ont été choisis afin d'analyser différentes configurations critiques.

La morphologie des couches de Ti présente une croissance colonnaire bien définie qui est souvent observée pour les couches de titane [Sit 1999, Barranco 2016, Siad 2016, Alvarez 2016, Dervaux 2017, Pedrosa 2017, Sadeghi-khosravieh 2017, Alvarez 2019]. À une incidence normale (α = 0°), la couche est légèrement poreuse puisqu'aucune ombre significative n'est obtenue et les micro-colonnes ne sont pas séparées. Au fur et à mesure que l'angle d'incidence augmente, l'effet d'ombre augmente progressivement et la structure devient plus poreuse. L'angle entre les colonnes et la normale du substrat est défini par β. Avec l'augmentation de l'angle d'incidence α, l'inclinaison des colonnes par rapport à la normale du substrat augmente (β augmente). Les analyses de diffraction par rayons X ont montré que les couches de Ti admettent une seule phase stable de structure hexagonale compacte Ti_α. Cette structure a été observée sur des films de titane pur élaborés par différentes techniques [Savaloni 2004, Chawla 2008, Sadeghi-Khosravieh 2017, Liedtke 2018].

Afin de connaître la texture cristalline de nos couches, les figures de pôles expérimentales ont été tracées à l'aide du logiciel DIFFRAC.TEXUTRE et mesurées sur deux familles de plans $\{0002\}$ et $\{10\bar{1}1\}$. D'après les figures de pôles expérimentales, on a trouvé que la phase Ti_α admet une texture de fibre d'axe $\{0002\}$. Cette fibre est inclinée de 30° $\pm$ 3° pour α = 45° et de 47° $\pm$ 3° pour α = 80° par rapport à la normale du substrat. Cette inclinaison de l'axe de la fibre par rapport à la normale du substrat a été également présente dans des couches minces de Ti [Sadeghi-Khosravieh 2017], Cr [Elofsson 2014], Mo [Chen 2012, Liedtke-Grüner 2019], Mg [Tang 2007], HfN [Abadias 2019b], TiN [Bouaouina 2018], AlN [Dellas 2006, Deniz 2007] et TiAlN [Shetty 2012].

La résolution des formules du modèle développé (équation (IV.6)) permet de déterminer les modules d'Young E_x et E_y des films de titane en supposant $\upsilon_{xy} = \upsilon_{isotrope}$ = 0.32 [Leonhardt 2004] et $\upsilon_{yx} = \upsilon_{xy}\, E_y/E_x$ [Hyer 2009]. Les modules de cisaillement G_{yz} et G_{xz} des films de titane ont été déterminés en utilisant l'équation (II.14) avec E_x et E_y respectivement. Les modules de cisaillement ont été déterminés en prenant le module d'Young correspondant et en utilisant le modèle isotrope de Slim. En utilisant les composantes x et y, les vibrations en torsion sont produites respectivement dans les plans y-z et x-z. Les valeurs des constantes d'élasticité du film de titane sont inférieures à celles rapportées dans la littérature pour du titane massif et en couche mince [Chinmulgund 1995, Kim 1997, Cho 1999, Leonhardt 2004, Tsuchiya 2005, Verkhovtsev 2013]. Ceci est attribué à l'influence du processus GLAD sur les propriétés élastiques. Cependant, on a remarqué que les constantes d'élasticité d'un film anisotrope sont

en bon accord avec celles calculées en supposant un comportement isotrope du film. Ces résultats nous permettent de conclure que la TEI conduit à une valeur correcte de constantes d'élasticité selon une direction appropriée, par exemple la direction longitudinale pour le module d'Young, même si le module est calculé à partir du modèle isotrope au lieu du modèle anisotrope. En augmentant l'angle d'incidence α, les rapports d'anisotropie $AR_E = E_y/E_x$ et $AR_G = G_{yz}/G_{xz}$ augmentent à cause de différents facteurs parmi lesquels la croissance colonnaire avec des cristallites inclinées selon la direction du flux incident. L'effet de la porosité du film sur les constantes d'élasticité du film de Ti a été évalué. Cependant, les constantes d'élasticité du film de Ti déterminées à l'aide de la TEI étaient différentes de celles calculées théoriquement en tenant compte de la porosité du film. Les résultats confirment l'influence d'autres propriétés microstructurales sur les constantes d'élasticité des films de Ti. La dureté et le module d'Young réduit mesuré par nanoindentation diminuent avec l'augmentation de l'angle d'incidence à cause de l'augmentation de la porosité du film.

La détermination des propriétés élastiques des films déposés par GLAD est importante afin d'utiliser ces films dans le domaine de l'ingénierie et de la science des matériaux. Au niveau de ce chapitre, une première étape de la méthodologie a été atteinte. Dans le chapitre qui suit, une deuxième étape sera abordée et portera sur la détermination des constantes d'élasticité macroscopiques des films de Ti texturés déposés à incidence oblique en tenant compte de ses propriétés microstructurales.

Chapitre V Détermination des constants d'élasticité des couches minces anisotropes en modélisant leurs propriétés microstructurales

L'objectif de ce chapitre est de présenter une méthodologie avancée et développée durant ce travail pour déterminer les constantes d'élasticité macroscopiques d'un film texturé et poreux. Cette méthodologie nécessite l'utilisation des modèles analytiques présentant le comportement élastique macroscopique en fonction de la microstructure du film et des constantes d'élasticité du cristal. Des études antérieures ont été faites pour déterminer les constantes d'élasticité macroscopiques de couches minces à comportement anisotrope [Faurie 2010, Hounkpati 2014a, b]. En revanche, à notre connaissance, aucune étude n'a été faite sur des dépôts anisotropes déposés à incidence oblique. De plus, la plupart des études négligent la texture du film. On s'intéresse ainsi principalement à l'influence de la microstructure (la porosité et les textures cristallographiques et morphologiques) sur les propriétés élastiques du film.

Dans ce chapitre, la microstructure du film a été modélisée analytiquement afin d'atteindre notre objectif. Dans un premier temps, une brève introduction sur la diffraction des rayons X (DRX) a été présentée. Ensuite, nous avons introduit les différents notions et modèles de transition d'échelles utilisés dans la littérature qui permettent de relier les quantités mésoscopiques mesurées par DRX aux quantités macroscopiques. Puis, le tenseur de rigidité effective ainsi que la déformation microscopique mesurée par DRX d'un matériau multiphasé ont été formulés dans le cadre du modèle auto-cohérent de Kröner-Eshelby [Eshelby 1957]. Ce modèle a été utilisé dans ce travail pour déterminer les constantes d'élasticité macroscopiques

de films de titane polycristallin et texturé présentant une seule phase (Ti_α) et déposés à différents angles d'incidence α.

L'influence de la texture morphologique ou/et cristallographique sur les propriétés élastiques a été quantifiée. L'influence de l'angle d'incidence sur la réponse élastique microscopique a également été démontrée et quantifiée. L'état de contrainte résiduelle dans les films de titane a été déterminé en fonction de l'angle d'incidence. En effet, la texture de la phase hexagonale Ti_α, la forme du grain et la porosité du film de titane ont été prises en compte dans la modélisation. Ce travail nous a permet d'avoir un premier jeu de valeurs de constantes d'élasticité d'un film déposé à incidence oblique.

Le principe des modèles de transition d'échelles est de relier l'état mécanique macroscopique à l'état mécanique mésoscopique. Le principe de base du modèle autocohérent a été proposé par Kröner [Kröner 1958]. Il consiste à relier l'état mécanique macroscopique à l'état mécanique mésoscopique à l'aide d'un tenseur de polarisation satisfaisant à la fois la cohérence des déformations et la cohérence des contraintes. Pour déterminer ce tenseur de polarisation, Kröner s'est basé sur les travaux effectués par Eshelby [Eshelby 1957] pour résoudre le problème d'une inclusion plongée dans une matrice infinie et soumise à des chargements mécaniques à l'infini. Le modèle contient des tenseurs de polarisation, un tenseur de localisation des déformations, un tenseur de concentration des contraintes, l'orientation de chaque cristallite dans le repère de l'échantillon et les différentes phases incluses dans le matériau. Le tenseur de rigidité macroscopique C peut être déterminé à partir de l'équation suivante :

$$C = \sum_{i=1}^{n} x_i \ \langle c_\Omega^i : \left[P(C) : \left(c_\Omega^i - C\right) + I_4\right]^{-1} \rangle_{\Omega \in V_i} \tag{V.1}$$

Avec C le tenseur de rigidité macroscopique, c_Ω^i le tenseur de rigidité du monocristal, V_i et x_i le volume et la fraction volumique de la phase i, respectivement et I_4 la matrice d'identité d'ordre 4. L'indice Ω représente l'orientation de chaque cristallite dans le repère de l'échantillon. $P(C)$ représente un tenseur d'ordre 4, appelé tenseur de Morris [Morris 1970], dépend de la forme de l'inclusion et de la rigidité du polycristal. Il peut être déterminé à partir de l'équation suivante [Kocks 1998] :

$$P_{ijkl} = \frac{1}{4\pi} \int_0^\pi \sin\theta \, d\theta \int_0^{2\pi} \gamma_{ikjl} \, d\phi \tag{V.2}$$

Avec :

$$\gamma_{ikjl} = K_{ij}^{-1}(\xi) \, \xi_k \, \xi_l \tag{V.3}$$

$$K_{ip}(\xi) = C_{ijpl} \, \xi_j \, \xi_l \tag{V.4}$$

$$\xi_1 = \frac{\sin\theta\cos\phi}{a_1} \qquad \xi_2 = \frac{\sin\theta\sin\phi}{a_2} \qquad \xi_3 = \frac{\cos\theta}{a_3} \tag{V.5}$$

Les angles $\theta \in [0\,;\,\pi]$ et $\phi \in [0\,;\,2\pi]$ sont les angles qui définissent la direction en coordonnées sphérique du vecteur ξ par rapport aux axes de l'ellipsoïde de longueurs $2a_1$, $2a_2$ et $2a_3$. La texture morphologique du matériau peut être décrite par les trois rapports présentés par l'équation (V.5) [Kocks 1998].

Une machine PVD DEPHIS4 a été utilisée pour déposer des couches minces de titane à température flottante par pulvérisation cathodique magnétron à incidence oblique (GLAD) sur des substrats en verre et en silicium. Une cible circulaire de titane, 200 *mm* de diamètre, ayant une pureté de l'ordre de 99.95 % a été utilisée. Des substrats en verre, ont été utilisés pour déterminer le module d'Young et le module de cisaillement des films par TEI et pour les caractérisations microscopiques par DRX. Les substrats de silicium ont été utilisés pour l'imagerie par microscope électronique à balayage (MEB). Les substrats ont été nettoyés à l'éthanol et à l'acétone puis fixés sur un porte-substrat afin de garantir l'homogénéité du dépôt. La distance cible-substrat a été fixée à 22 *cm*. Un vide poussé de l'ordre de 10^{-4} *Pa* a tout d'abord été créé à l'intérieur de l'enceinte grâce à un système de pompage. Les angles d'incidence α fixés pour une configuration en GLAD sont 0°, 45° et 80°. Le dépôt a été réalisé sous une pression de 0,42 *Pa* avec un débit d'argon de 40 *sccm* et une décharge de 1.5 *A*, appliquée à la cible de titane à l'aide d'un générateur de courant continu pulsé. Le dépôt a été réalisé pendant 240 *min* sur l'une des deux faces des substrats et nous avons obtenu une couche de titane d'une épaisseur h_c qui varie entre 850 *nm* (pour α = 80°) et 1.2 μm (pour α = 0°).

Une morphologie colonnaire a été observée sur les couches de titane avec une inclinaison d'un angle β qui varie en fonction de l'angle d'incidence α. La forme colonnaire des grains a été introduite dans la simulation en utilisant le modèle autocohérent de Kröner-Eshelby (KE) en utilisant les rapports (tenseur de Morris) présentés dans l'équation (V.5). Les grains ont été considérés comme des inclusions ellipsoïdales avec un rayon dans la direction perpendiculaire à la surface du film six fois plus grand que les rayons dans les deux autres directions. L'orientation des grains décrite selon la convention de Bunge [Bunge 1982] est $\Omega \equiv (\varphi_1 = 0°,\ \phi = \beta,\ \varphi_2 = 0°)$ pour les échantillons déposés horizontalement ($B_{0,Y}$, $B_{45,Y}$, $B_{80,Y}$) et $(\varphi_1 = 90°,\ \phi = \beta,\ \varphi_2 = 0°)$ pour ceux déposés verticalement ($B_{0,X}$, $B_{45,X}$, $B_{80,X}$). À partir des figures de pôles expérimentales, la texture de la phase Ti_α a été décrite par une fibre d'axe $\{0002\}$ perpendiculaire à la surface du film. Cette fibre est décalée d'un certain angle d'inclinaison η qui dépend de l'angle d'incidence α. Afin de déterminer les valeurs de l'angle d'inclinaison de la fibre η à différents angles d'incidence α, les échantillons ont été diffractés en mode ψ. La Figure V.1 montre le profil d'intensité du plan diffracté $\{0002\}_\alpha$ pris selon la direction ψ à ϕ = 0° pour les échantillons déposés verticalement ($B_{0,X}$, $B_{45,X}$, $B_{80,X}$) et à ϕ = 90° pour les échantillons déposés horizontalement ($B_{0,Y}$, $B_{45,Y}$, $B_{80,Y}$). Le lissage des données expérimentales a été fait à l'aide d'une fonction pseudo-Voigt et par suite les angles d'inclinaison des fibres avec les incertitudes de mesure ont été déterminés.

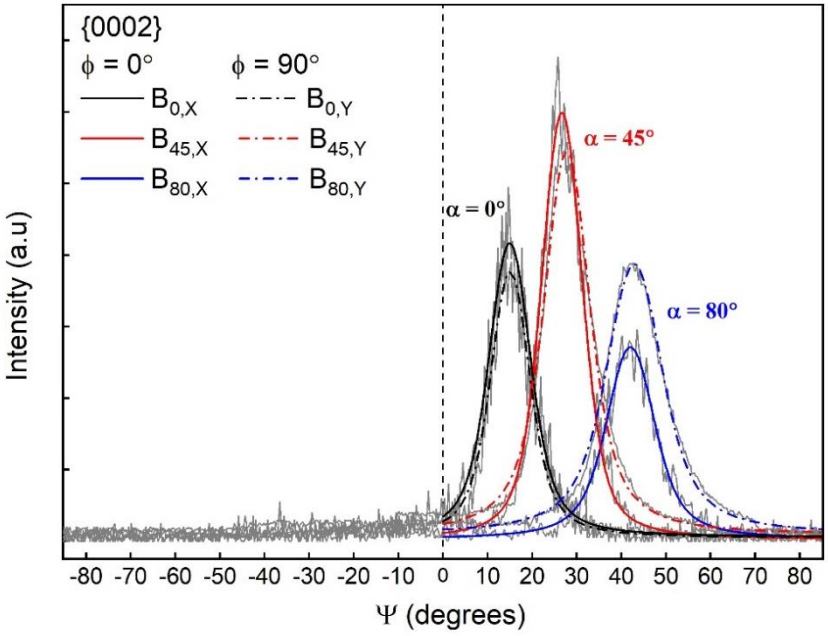

Figure V.1. Profile d'intensité de diffraction du plan $\{0002\}_\alpha$ selon l'axe ψ à $\phi = 0°/90°$ des couches de titane à différents angles d'incidence α (0°, 45° et 80°).

La dispersion de la texture autour des composantes idéales a été négligée. Afin de définir l'orientation cristallographique d'un matériau, deux différents repères sont attribués respectivement au cristal et à l'échantillon. La Figure V.2 représente le repère du cristal et le repère de l'échantillon. Pour décrire une orientation cristallographique, il est nécessaire de relier le repère du cristal au repère de l'échantillon. Pour ce faire, on définit une matrice de passage qui permet le passage du repère du cristal au repère de l'échantillon. Cette matrice peut être définie de différentes manières [Randle 2001, Kocks 1998]. Dans ce travail, les angles d'Euler selon la convention de Bunge [Bunge 1982] ont été utilisés pour décrire l'orientation cristallographique. L'orientation de chaque cristallite est donc définie par $\Omega \equiv (\varphi_1,\ \phi,\ \varphi_2)$.

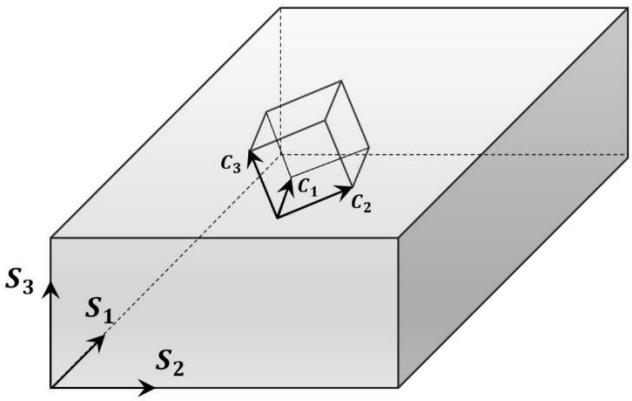

Figure V.2. Repère de l'échantillon (S_1, S_2, S_3) et le repère du cristal (C_1, C_2, C_3).

Dans la modélisation mécanique, la répartition angulaire de la texture autour des composants idéaux est négligée. Cela nous permet de décrire la texture de la phase Ti_α à l'aide

d'une seule orientation. En comparant les figures de pôles simulées avec les figures de pôles expérimentales de la phase Ti_{α}, on a remarqué que les pôles d'intensité sont approximativement situés aux mêmes positions. On peut donc conclure que la texture de la phase Ti_{α} peut être décrite en utilisant les angles d'Euler ($\varphi_1 = 0°,\ \phi = \eta,\ 0 \leq \varphi_2 \leq 360°$) pour les échantillons déposés horizontalement ($B_{0,Y}$, $B_{45,Y}$, $B_{80,Y}$) et ($\varphi_1 = 90°,\ \phi = \eta,\ 0 \leq \varphi_2 \leq 360°$) pour ceux déposés verticalement ($B_{0,X}$, $B_{45,X}$, $B_{80,X}$). Le Tableau V.1 présente les angles d'incidence α, les angles d'inclinaison des micro-colonnes β, les angles d'inclinaison de la fibre η et les constantes d'élasticité macroscopiques calculées à partir du modèle de KE pour les couches de titane. On peut observer que les films présentent un comportement transversalement isotrope avec une faible anisotropie dans le plan du film à α = 80°. La différence entre E_x et E_y peut être attribuée à l'incertitude sur les mesures des angles et sur les constantes d'élasticité du cristal.

Tableau V.1
Les propriétés microstructurales et les constantes d'élasticité macroscopiques déterminées par KE des couches de titane déposées à différents angles d'incidence.

Echantillon	α (± 2°)	β (± 3°)	η (± 0.1°)	E_x (GPa)	E_y (GPa)	E_z (GPa)	G_{xy} (GPa)	G_{xz} (GPa)	G_{yz} (GPa)
$B_{0,X}$	0	0	14.8	90.1	90.4	131.6	31.3	42.0	42.0
$B_{0,Y}$	0	0	15.1	86.1	86.3	129.3	30.0	40.8	40.8
$B_{45,X}$	45	5	27.8	70.1	70.3	111.8	25.4	35.1	35.2
$B_{45,Y}$	45	4	26.7	78.4	78.8	117.0	28.2	37.8	37.9
$B_{80,X}$	80	21	43.0	38.7	39.7	75.6	15.1	22.2	23.4
$B_{80,Y}$	80	21	42.1	48.9	59.3	81.6	20.6	24.6	26.3

En utilisant au moins deux directions de mesure indépendantes, l'état de contraintes résiduelles dans les couches minces déposées en GLAD à différents angles d'incidence α ainsi que l'angle de diffraction de référence $\theta_0^{\{hkl\}_i}$ du plan utilisé ont été déterminés à l'aide de l'équation suivante :

$$\varepsilon_{\phi,\psi}^{\{hkl\}_i} = \ln\left(\frac{\sin\theta_0^{\{hkl\}}}{\sin\theta_{\phi,\psi}^{\{hkl\}}}\right) = \vec{n}\,.\left[\langle\left[P(C) : \left(c_{\Omega}^{i} - C\right) + I_4\right]^{-1}\rangle_{\Omega\in V_i} : C^{-1} : \sigma_R^i\right].\vec{n} \qquad \text{(V.6)}$$

Où $\theta_0^{\{hkl\}}$ et $\theta_{\phi,\psi}^{\{hkl\}}$ représentent respectivement la position du pic de diffraction d'un matériau libre de contrainte (matériau de référence) et la position du pic de diffraction d'un matériau contraint. *h*, *k* et *l* sont les indices de Miller. ϕ et ψ sont respectivement les angles d'azimut et d'inclinaison définissant la direction de la mesure $\vec{n}$ qui s'exprime selon l'équation suivante :

$$\vec{n} = \begin{pmatrix} \cos\phi\sin\psi \\ \sin\phi\sin\psi \\ \cos\psi \end{pmatrix} \qquad \text{(V.7)}$$

Les contraintes résiduelles et l'angle de diffraction de référence $\theta_0^{\{hkl\}_i}$ ont été déterminés sur deux familles de plans différentes $\{11\bar{2}4\}_\alpha$ et $\{20\bar{2}3\}_\alpha$ en utilisant les constantes d'élasticité du cristal Ti_α et les tenseurs de rigidité calculés à partir du modèle KE. Les contraintes résiduelles déterminées à partir des déformations mesurées par DRX ont été comparées à celles mesurées à partir de la méthode de courbure. Un bon accord entre les résultats des deux méthodes a été remarqué, à l'exception des films déposées à 80° d'incidence. Cette différence à 80° d'incidence a bien été présente en comparant les constantes d'élasticité calculées par KE avec celles mesurées par TEI et NI. Cette différence peut être due à l'erreur de modélisation par KE d'une porosité importante dans le film.

D'autres analyses du comportement élastique microscopique des films de titane asymétriquement texturés seront évaluées sous chargement appliqué. Cette analyse nous permet d'étudier la plage de validité du modèle de Kröner-Eshelby en comparant les déformations microscopiques expérimentales et recalculées. Afin de modéliser plus précisément la microstructure des films en GLAD, d'autres modèles de transition d'échelles seront utilisés dans les travaux futurs. De plus, l'amélioration de la qualité des mesures de déformation par DRX est essentielle pour garantir une plus grande précision des résultats.

Conclusion générale

L'objectif de cette thèse est de développer une méthodologie de mesure des constantes d'élasticité macroscopiques des revêtements polycristallins, poreux et texturés. La démarche présentée dans ce travail fait appel à des outils expérimentaux et théoriques ou de simulation. Les outils expérimentaux utilisés durant cette thèse sont la Technique d'Excitation Impulsionnelle (TEI) pour mesurer les constantes d'élasticité macroscopiques du dépôt et la diffraction des rayons X pour déterminer les propriétés microstructurales du dépôt et pour caractériser le comportement microscopique des phases. Les outils théoriques se manifestent par l'emploi des modèles micromécaniques pour la simulation du comportement élastique macroscopique et microscopique des couches.

Nous avons commencé par une caractérisation macroscopique du comportement élastique des multicouches supposant isotropes. Un développement des modèles analytiques (Ext-PM, Dev-CLBT et Ext-Slim) qui permettent de déterminer les constantes d'élasticité des revêtements, a été fait. Les modèles analytiques développés ont été comparés avec un modèle éléments finis pris comme une référence. Nous avons montré que les modèles Ext-PM, Dev-CLBT et Ext-Slim sont fiables pour déterminer les constantes d'élasticité des multicouches. Ceci revient au fait que ces modèles prennent en compte le décalage de la fibre neutre après chaque dépôt.

Les nouveaux modèles ont été appliqués à des couches de titane et de niobium déposées en multicouches sur des substrats d'acier inoxydable et de verre. Les constantes d'élasticité de chaque couche ont été déterminées à partir de la technique d'excitation impulsionnelle. L'étude d'incertitudes sur la mesure du module d'Young et du module de cisaillement a été effectuée dans le Chapitre III. L'étude a montré que l'incertitude sur la mesure du module d'Young et du

module de cisaillement du substrat provient principalement de la mesure de son épaisseur et de sa masse volumique. Alors que dans le cas du module d'Young de la couche de titane, les facteurs les plus influents sont la masse volumique du film, la fréquence de résonnance du substrat et du composite (substrat + dépôt) et le module d'Young du substrat. En déposant la deuxième couche de niobium, le module d'Young de la première couche de titane a été ajouté à la liste des facteurs les plus influents. En augmentant le nombre de modes de vibration, la contribution de la fréquence sur le module d'Young des couches diminue, bien que celle de la masse volumique et du module d'Young du substrat et des couches précédentes augmente.

Par évaluation des incertitudes sur la mesure du module de cisaillement, les sources les plus influentes sur la mesure du module de cisaillement du film sont : la densité des films, les fréquences de torsion du substrat et du composite et les modules de cisaillement des couches précédentes (substrat et premier film de titane). En comparant les deux analyses d'incertitude sur le module d'Young et le module de cisaillement des films, on peut confirmer que les facteurs les plus influents sur la mesure restent les mêmes avec quelques équivalences. Le module d'Young et les fréquences de flexion (pour les modèles Ext-PM et Dev-CLBT) correspondent respectivement au module de cisaillement et aux fréquences de torsion (pour le modèle Ext-Slim). Ces facteurs ont la plus grande influence sur la mesure des constantes d'élasticité des films.

Un nouveau modèle pour déterminer les constantes d'élasticité des films minces déposés à incidence oblique a été développé grâce à l'application de la théorie classique des poutres stratifiées (CLBT). Ce nouveau modèle prend en compte le décalage de la fibre neutre après dépôt et l'anisotropie dans le plan du film. Le modèle a été validé par comparaison avec un modèle éléments finis pris comme une référence. Des dépôts de titane pur ont été élaboré par pulvérisation cathodique magnétron à différents angles d'incidence (α = 0°, 45° et 80°), ses modules d'Young ont été déterminés à l'aide du nouveau modèle et la technique d'excitation impulsionnelle et ses modules de cisaillement à l'aide du modèle de Slim avec le module d'Young correspondant. En augmentant l'angle d'incidence, une baisse du module d'Young et du module de cisaillement du film de titane par rapport à ceux du matériau massif a été observée. L'analyse de morphologie a montré que les couches déposées montrent des morphologies colonnaires inclinées d'un angle β par rapport à la normale pour des angles d'incidence différents de zéro. L'analyse de structure des couches présente une seule phase Ti_{α}, stable de structure hexagonale compacte pour les trois angles d'incidence. La texture de cette phase représente une fibre d'axe $\{0002\}$ inclinée d'un angle η selon la normale à la surface. Selon les calculs faits avec le modèle de Nemat-Nasser, la baisse du module d'Young ne peut pas être attribuée uniquement à la diminution de la masse volumique du dépôt (liée à la porosité) comparée à la masse volumique du matériau massif.

Les constantes d'élasticité macroscopiques ont été recalculées à partir d'un modèle micromécanique. Dans ce travail, nous avons utilisé le modèle de Kröner-Eshelby. La texture des films de titane a été déterminée à l'aide de figures des pôles. L'angle d'inclinaison de la fibre η a été mesuré par diffraction des rayons X. L'angle d'inclinaison des colonnes β a été mesuré sur les images observées par microscopie électronique à balayage. La porosité dans le

film a été mesurée par analyse d'images et par comparaison entre la masse volumique du film et du matériau massif sans pores. À l'aide du modèle autocohérent, nous avons formulé le tenseur de rigidité effectif des dépôts poreux, monophasé (Ti_α) et ayant des colonnes et des fibres inclinées. Puis, les constantes d'élasticité macroscopiques des films de titane ont été déterminées en prenant en compte les propriétés microstructurales (porosité, texture cristallographique et texture morphologique) de chaque film. D'après le calcul, on a trouvé que les films présentent un comportement transversalement isotrope avec une faible anisotropie dans le plan du film déposé à α = 80°. Les différences entre les modules d'Young et de cisaillement mesurés par la technique d'excitation impulsionnelle et recalculés par le modèle autocohérent ont été attribuées aux incertitudes de mesures et de calculs pour les films déposés à 0° et 45° d'incidence. Par contre, pour α = 80°, on a remarqué que cette différence est supérieure aux incertitudes. Ceci peut être due à l'incapacité du modèle autocohérent à modéliser les microstructures présentant une porosité élevée (p > 12%). Les constantes d'élasticité macroscopiques des dépôts de titane présentées dans le Chapitre IV ont été recalculées et la même conclusion a été retrouvée. Nous avons montré que la porosité dans le film a un effet dominant sur les modules d'Young et de cisaillement. L'effet de la texture morphologique ou/et cristallographique sur le comportement microscopique devient dominant. L'influence de l'angle d'incidence sur la réponse élastique microscopique a également été démontrée et quantifiée. Ce travail nous a permet d'avoir un premier jeu de valeurs de constantes d'élasticité d'un film déposé à incidence oblique.

Dans ce travail, le comportement élastique des films GLAD n'est pas bien décrit par le modèle KE. Le modèle KE peut ne pas être bien adapté aux matériaux très poreux, où une interaction significative des pores peut probablement être obtenue. L'anisotropie élastique macroscopique peut être étudiée en utilisant d'autres modèles de transition d'échelle comme celui de Mori-Tanaka qui pourrait simuler plus précisément la microstructure des films en GLAD.

Afin de déterminer les constantes d'élasticité macroscopique des films de titane, nous avons utilisé les constantes d'élasticité de la phase Ti_α de la littérature. Alors qu'il peut être possible que le comportement de notre phase Ti_α soit différent. Une détermination du tenseur de rigidité de cette phase, nous permettra de comparer les coefficients c_{ij}^{α} calculés avec celles qui existent dans la littérature et ne pas imposer un jeu de valeurs qui peut ne pas correspondre à notre cas. Pour cela, il conviendra d'effectuer des mesures de déplacement des pics de diffraction de la phase Ti_α sous chargement imposé.

La méthode des blocs de texture a été utilisée dans la mesure des déformations par diffraction des rayons X et dans le modèle autocohérent. La texture des dépôts a été prise en compte en idéalisant les orientations cristallographiques de la phase Ti_α. Cependant, la texture du dépôt peut être décrite plus précisément à l'aide de fonctions de distributions des orientations.

Appendix C Publications and communications

International publications in peer-reviewed journals

1. **Elia Zgheib**, Akram Alhussein, Mohamed Fares Slim, Khaled Khalil, Manuel François, Elastic behavior of anisotropic coatings sputter-deposited at oblique incidence, International Journal of Mechanical Sciences 191 (2021) 106050.

2. **Elia Zgheib**, Akram Alhussein, Mohamed Fares Slim, Khaled Khalil, Manuel François, Multilayered models for determining the Young's modulus of thin films by means of impulse excitation technique, Mechanics of Materials 137 (2019) 103143.

3. Mohamed Fares Slim, Akram Alhussein, **Elia Zgheib**, Manuel François, Determination of single-crystal elasticity constants of the beta phase in a multiphase tungsten thin film using impulse excitation technique, X-ray diffraction and micro-mechanical modeling, Acta Materialia 175 (2019) 348-360.

International conferences

1. **Elia Zgheib**, Akram Alhussein, Mohamed Fares Slim, Khaled Khalil, Manuel François, Determination of the Elasticity Constants of Textured and Architectured Thin Films by means of Impulse Excitation Technique and X ray Diffraction, 46th International Conference of Metallurgical Coating and Thin Film ICMCTF, May 19 to 24, 2019, San Diego, CA, USA (Oral presentation).

2. **Elia Zgheib**, Akram Alhussein, Mohamed Fares Slim, Khaled Khalil, Manuel François, Determination of elasticity constants of multilayer anisotropic coatings using a vibrational technique, European Materials Research Society E-MRS Spring meeting, May 28 to 30, 2019, Nice, France (Oral presentation).

National congress

1. **Elia Zgheib**, Akram Alhussein, Mohamed Fares Slim, Khaled Khalil, Manuel François, Towards a new methodology for measuring the macroscopic Young's modulus of multilayer thin films using impulse excitation technique, 24ème Congrès Français de Mécanique, August 26 to 30, 2019, Brest, France (Oral presentation).

2. **Elia Zgheib**, Akram Alhussein, Mohamed Fares Slim, Khaled Khalil, Manuel François, Caractérisation multiéchelle de l'élasticité des couches minces anisotropes déposées à incidence oblique, Contraintes résiduelles : de nouveaux outils pour de nouveaux défis, January 20 to 24, 2020, Aussois, France (Poster).

Appendix D

Abstract

In this work, a methodology to determine the macroscopic elasticity constants of thin films was proposed. Different analytical models were developed to determine the macroscopic elasticity constants of multilayer coatings using the Impulse Excitation Technique (IET). The proposed methodology was used to determine the macroscopic elasticity constants of titanium and niobium multilayer coatings and titanium anisotropic thin films sputter-deposited at oblique incidence. An enhanced formulation to determine the elasticity constants of anisotropic thin film was developed. The elastic behavior of anisotropic thin films was investigated theoretically by different analytical models, and experimentally by several complementary techniques, namely X-ray diffraction, nanoindentation and IET. The elastic behavior of anisotropic films deposited at oblique incidence represents an aspect that is not well known in the literature. The anisotropy can be attributed to the crystallographic and morphological textures of the grains. The macroscopic elasticity constants of titanium anisotropic films were also determined using the Kröner-Eshelby micromechanical model. The porosity within the film, and the morphological and crystallographic textures of the Ti_{α} phase were taken into account in the modeling for a proper analysis of the elastic behavior of the film.

Keywords: Thin films, Elasticity, Vibration, Titanium, Anisotropy, Microstructure, Texture (Crystallography), Multiscale analysis.

Résumé

L’objectif de ce travail est de développer une méthodologie qui permet de déterminer les constantes d’élasticité d’un dépôt à une échelle macroscopique. Différents modèles analytiques ont été développés pour déterminer les constantes d’élasticité d’un revêtement multicouches à l’aide de la Technique d’Excitation Impulsionnelle (TEI). La méthodologie que nous avions développée a permis de déterminer les constantes d’élasticité macroscopiques d’un revêtement multicouches de titane et niobium et des couches minces de titane déposées à incidence oblique par pulvérisation cathodique magnétron. Une formulation améliorée pour déterminer les constantes d'élasticité d’un revêtement anisotrope a été développée. Le comportement élastique des couches anisotropes a été étudié théoriquement par différents modèles analytiques et expérimentalement à l’aide de la diffraction des rayons X, la nanoindentation et la TEI. Le comportement élastique des couches anisotropes déposées à incidence oblique s’agit d’un aspect qui n’est pas bien connu dans la littérature. L'anisotropie peut être attribuée à la texture cristalline et la morphologie des grains. Les constantes d'élasticité macroscopiques des couches anisotropes de titane ont également été déterminées à l'aide du modèle micromécanique de Kröner-Eshelby. La porosité au sein de la couche, et les textures morphologiques et cristallographiques de la phase Ti_{α} ont été prises en compte dans la modélisation pour une analyse exacte du comportement élastique de la couche.

Mots clés : Couches minces, Élasticité, Vibrations, Titane, Anisotropie, Microstructure (Physique), Texture (Cristallographie), Analyse multiéchelle.

Elia ZGHEIB

Doctorat : Matériaux, Mécanique, Optique, Nanotechnologie

Année 2020

Modélisation et caractérisation multiéchelle du comportement élastique des couches minces anisotropes

L'objectif de ce travail est de développer une méthodologie qui permet de déterminer les constantes d'élasticité d'un dépôt à une échelle macroscopique. Différents modèles analytiques ont été développés pour déterminer les constantes d'élasticité d'un revêtement multicouches à l'aide de la Technique d'Excitation Impulsionnelle (TEI). La méthodologie que nous avions développée a permis de déterminer les constantes d'élasticité macroscopiques d'un revêtement multicouches de titane et niobium et des couches minces de titane déposées à incidence oblique par pulvérisation cathodique magnétron. Une formulation améliorée pour déterminer les constantes d'élasticité d'un revêtement anisotrope a été développée. Le comportement élastique des couches anisotropes a été étudié théoriquement par différents modèles analytiques et expérimentalement à l'aide de la diffraction des rayons X, la nanoindentation et la TEI. Le comportement élastique des couches anisotropes déposées à incidence oblique s'agit d'un aspect qui n'est pas bien connu dans la littérature. L'anisotropie peut être attribuée à la texture cristalline et la morphologie des grains. Les constantes d'élasticité macroscopiques des couches anisotropes de titane ont également été déterminées à l'aide du modèle micromécanique de Kröner-Eshelby. La porosité au sein de la couche, et les textures morphologiques et cristallographiques de la phase Ti ont été prises en compte dans la modélisation pour une analyse exacte du comportement élastique de la couche.

Mots clés : couches minces – élasticité – vibrations – titane – anisotropie – microstructure (physique) – texture (cristallographie) – analyse multiéchelle.

Multiscale Modeling and Characterization of the Elastic Behavior of Anisotropic Thin Films

In this work, a methodology to determine the macroscopic elasticity constants of thin films was proposed. Different analytical models were developed to determine the macroscopic elasticity constants of multilayer coatings using the Impulse Excitation Technique (IET). The proposed methodology was used to determine the macroscopic elasticity constants of titanium and niobium multilayer coatings and titanium anisotropic thin films sputter-deposited at oblique incidence. An enhanced formulation to determine the elasticity constants of anisotropic thin film was developed. The elastic behavior of anisotropic thin films was investigated theoretically by different analytical models, and experimentally by several complementary techniques, namely X-ray diffraction, nanoindentation and IET. The elastic behavior of anisotropic films deposited at oblique incidence represents an aspect that is not well known in the literature. The anisotropy can be attributed to the crystallographic and morphological textures of the grains. The macroscopic elasticity constants of titanium anisotropic films were also determined using the Kröner-Eshelby micromechanical model. The porosity within the film, and the morphological and crystallographic textures of the Ti phase were taken into account in the modeling for a proper analysis of the elastic behavior of the film.

Keywords: thin films – elasticity – vibration – titanium – anisotropy – microstructure – texture (crystallography) – multiscale analysis.

Thèse réalisée en partenariat entre :

Ecole Doctorale "Sciences pour l'Ingénieur"